TECHNISCHE UNIVERSITÄT MÜNCHEN

Fakultät für Chemie – Lehrstuhl für Technische Elektrochemie

Electrochemical and structural investigations on lithium-ion battery materials and related degradation processes

Irmgard Hedwig Buchberger

Vollständiger Abdruck der von der Fakultät für Chemie der Technischen Universität München zur Erlangung des akademischen Grades eines

Doktors der Naturwissenschaften (Dr. rer. nat.)

genehmigten Dissertation.

Vorsitzender:		Prof. Dr. Tobias A. M. Gulder
Prüfer der Dissertation:	1.	Prof. Dr. Hubert A. Gasteiger
	2.	Priv.-Doz. Dr. Christoph P. Hugenschmidt

Diese Dissertation wurde am 05.07.2016 bei der Technischen Universität München eingereicht und durch die Fakultät für Chemie am 01.08.2016 angenommen.

Abstract

The introduction of the lithium-ion battery technology in the automotive field has boosted the renaissance of electromobility over the last decade. To improve the energy density and durability of the battery system, analytical approaches have to be developed, which help to understand novel electrode materials and degradation phenomena. In this work, an *in situ* XRD cell for reflection and transmission geometry was established to investigate the structural changes in $LiCoPO_4$ and Li_2S during the first cycle. By combing (*in situ*) XRD with neutron-induced prompt-gamma activation analysis and positron annihilation spectroscopy, the kinetic origin of the first-cycle capacity loss of NMC-111 and the main degradation processes in graphite-NMC-111 cells under different operating conditions could be identified.

Kurzfassung

Die Einführung der Lithium-Ionen-Batterie-Technologie in die Automobilbranche führte in den letzten Jahrzehnten zu einer Renaissance der Elektromobilität. Zur Verbesserung der Energiedichte und Langlebigkeit des Batteriesystems müssen analytische Ansätze entwickelt werden, die dabei helfen neuartige Elektrodenmaterialien als auch Degradationserscheinungen zu verstehen. In dieser Arbeit wurde eine *in situ* Röntgendiffraktionszelle für die Reflektions- und Transmissionsgeometrie eingeführt, um die strukturellen Veränderungen von $LiCoPO_4$ und Li_2S im ersten Zyklus zu untersuchen. Durch die Kombination von (*in situ*) Röntgendiffraktometrie mit neutronen-induzierter prompte-Gamma Aktivierungsanalyse und Positronenannihilationsspektroskopie, konnte so der kinetische Ursprung des Kapazitätsverlustes von NMC-111 im ersten Zyklus und die Hauptalterungsprozesse in Graphit-NMC-111 Zellen unter verschiedenen Betriebsbedingungen identifiziert werden.

Danksagung

Die vorliegende Arbeit fasst die wissenschaftlichen Ergebnisse meiner Promotionszeit zusammen. Tatsächlich wäre diese ohne Hilfe und Unterstützung wohl nie entstanden, und so bedanke ich mich hier bei meinen zahlreichen Wegbegleitern:

Ich bedanke mich herzlich bei meinem Doktorvater **Prof. Dr. Hubert A. Gasteiger** für die freundliche Aufnahme in seine Arbeitsgruppe, für die vielfältigen und spannenden Forschungs- und Arbeitsmöglichkeiten und die großartige Unterstützung. Besonders dankbar bin ich für die konstruktiven Diskussionen, in denen er sein fundiertes Wissen und seine Ideen teilte, sowie die kritischen Fragen, um auch jegliches Problem in seiner Ursache zu verstehen.

Mein Dank für die finanzielle Unterstützung der Promotionszeit gilt dem Bundesministerium für Bildung und Forschung (BMBF) im Rahmen des **ExZellTUM-Projektes**. Dies ermöglichte mir, durch die Zusammenarbeit verschiedener Projektpartner, wertvolle Erfahrungen über den Lehrstuhl hinaus zu sammeln. Der Dank geht insbesondere an die Teilnehmer vom **EES**, **iwb** und **FRM II**.

In diesem Zusammenhang danke ich meinen geschätzten Arbeitskollegen und Bürokumpanen **Johannes Hattendorff** und **Dr. Jörg Schuster**. Mit euch wurde das Verbundprojekt mit all seinen Facetten gestemmt. Danke für die lockere und produktive Arbeitsatmosphäre. Ein außerordentliches Dankschön geht hierbei an **Dr. Stefan Seidlmayer**, der mir bei der Auswertung und Interpretation der XRD-Daten sehr behilflich war und von dessen Erfahrung ich enorm profitieren konnte. Dazu zählen auch die gemeinsamen, zahlreichen Versuchsplanungen, Messungen und Diskussionen an der Neutronenquelle.

Ich bedanke mich zudem bei **Dr. Michele Piana**, der mir bei der Entwicklung der *in situ* XRD-Zelle eine große Unterstützung war, sowie all meinen Bachelor- und Masterstudenten (**Chiara Donadel**, **Aneil Pokharel**, **Steffen Garbe**, **Artur Kupczak**) für deren Motivation und experimentellen Beiträge.

Ein liebes Dankeschön geht an **Veronika Pichler**. Ohne dich würd hier nix laufen. Vielen Dank für die großartige administrative Organisation unserer Gruppe und vor allem die interessanten Mittagspausen, in denen mal zur Abwechslung Nicht-Wissenschaftliches diskutiert wurde.

Ich danke **Dr. Petra Kudejova**, **Dr. Ralph Gilles, Thomas Gigl, Markus Reiner** und **Dr. Christoph Hugenschmidt** für deren Beitrag zum Gelingen der Neutronen- und Positronenmessungen.

Außerdem bedanke ich mich bei allen Mitarbeitern der Feinmechanik-Werkstatt, die meine diversen, teils wirren Zeichenpläne stets zu meiner vollen Zufriedenheit umsetzen konnten.

Allen Mitarbeitern der TEC-Gruppe gebührt ein herzliches Dankschön. Es war eine tolle Zeit mit euch.

Zum Schluss bedanke ich mich von Herzen bei all meinen Freunden und meiner Familie. Danke für euer Vertrauen, die tolle Unterstützung und die Abwechslung im Alltag. Dabei gilt natürlich ein besonderer Dank meinen Eltern und Geschwistern, die immer an mich geglaubt haben, sowie meinem Mann für seine Hilfe, Freundschaft und Liebe, trotz so manch anstrengender Zeit.

Contents

List of acronyms

AC	alternating current
BET area	surface area determinedby N_2 adsorption according to Brunauer, Emmet and Teller
BEV	battery electric vehicle
BOPP	bi-axially oriented polypropylene
CC	constant current
CDBS	coincidence Doppler broadening spectroscopy
CMC	carboxymethyl cellulose
CV	constant voltage
DBS	Doppler broadening spectroscopy
DMC	dimethyl carbonate
DME	dimethoxyethane
DOL	1-3 dioxalane
EC	ethylene carbonate
EDX	energy-dispesive X-ray spectroscopy
EIS	electrochemical impedance spectroscopy
EMC	ethyl-methyl carbonate
EV	electric vehicle
FEC	fluoroethylene carbonate
FEP	fluorinated ethylene propylene
FKM	fluoroelastomer, originally developed by DuPont (Viton)
GITT	galvanostatic intermittent titration technique
HDPE	high-density polyethylene
HE	high energy
HEV	hybrid electric vehicle
HFR	high frequency resistance
HPGe	high-purity germanium
HV	high voltage
ICL	irreversible capacity loss
ICP-OES	inductively-coupled plasma optical emission spectrometry
IR	infrared
LCP	lithium cobalt phosphate
LFP	lithium iron phoshate
LiTFSI	lithium bis(trifluoromethanesulfonyl)imide
LMR	lithium- and manganese-rich

NAA	neuton activation analysis
NCA	lithium nickel coblat aluminum oxide
NEPOMUC	neutron-induced positron source Munich
NMC	lithium nickel manganese cobalt oxide
NMP	N-methyl pyrrolidone
OCV	open-circuit voltage
OEMS	online electrochemical mass spectrometry
PALS	positron annihilation life time spectroscopy
PAS	positron annihilation spectroscopy
PDF	powder diffraction file
PE	polyethylene
PEIS	potentioelectrochemical impedance spectroscopy
PFA	perfluoroalkoxy alkane
PGAA	prompt-gamma activation analysis
PTFE	polytetrafluoroethylene (teflon)
PVdF	poly(vinylidenedifluoride)
SEI	solid electrolyte interphase
SEM	scanning electron microscopy
UHV	ultra-high vacuum
VC	vinylene carbonate
XRD	x-ray diffraction
XRF	X-ray fluorescence

1 Introduction

Electromobility has become a significant political issue in the context of global warming and climate change. In 2012 the US Department of Energy spent more than US$120 million on battery research and development,[1] one and half times higher than in 2010. Along with Japan, they lead the world in national funding, whereas Japan is also strong in industrial funding, since many of the established battery manufacturers are Japanese companies. More recently, South Korea and China have been setting up government and industrially funded research labs to push forward cost and performance related targets in the battery sector.[2]

Besides American and Asian countries, the German government also took up the global challenge and in 2010 started a national program to develop electromobility, called *Nationaler Entwicklungsplan Elektromobilität.*[3] The goal is to reduce greenhouse gases such as CO_2 and to mitigate the dependence on fossil fuels, through which an important step towards climate protection is achieved. Since transportation is responsible for 30% of today's energy consumption, a key to success is the electrification of the drive system in order to replace the petroleum based combustion engine.[4] Linked to this, a strict change to renewable energy sources such as wind and solar would be required to essentially eliminate CO_2 emissions, while powering the new electric vehicle system. In 2014, there were 24000 electrical vehicles (EVs) on German roads.[5] The ambitious aim of the German government is to increase this number to 1 million by 2020.

To meet these targets, highly efficient EVs based on either hybrid-, battery- or fuel cell technology is necessary. The latter two represent supplemental and complementary routes, both of which are supported by the German government.[3,6] The main difference between batteries and fuel cells is related to the locations of *energy storage and conversion.* While batteries are closed systems, in which energy storage and conversion occur in the same compartment, fuel cells constitute open systems, in which the electrodes are only chemical-to-electrical energy converters and the fuel (*e.g.*, hydrogen) is provided by an external tank.[7] In this context, questions regarding the electrical and hydrogen infrastructure arise, in which both systems must be based on renewable energy sources to meet the demands of sustainability and reduced CO_2 emissions. Furthermore, the consumer's expectations and requirements concerning cost and driving range have to be addressed in order to achieve a broad market acceptance. In consideration of all the political efforts, the answer to this market-acceptance question will hopefully soon be learned, presenting a great opportunity for research and development in various areas of expertise.

2 State of the art

2.1 Lithium-ion battery technology

The renaissance of electromobility was boosted over the last decade mainly by the introduction of lithium-ion batteries in the automotive field. Although a large variety of batteries have been utilized to power EVs, lithium-ion seems to be the only battery technology to potentially meet the future requirements of the automotive industry in terms of both *energy* and *power density*.[8] The *specific energy* of a battery pack, which determines the driving range of a car, is the amount of electrochemical energy per mass in units of Wh/kg (or in J/kg):

$$\text{Specific energy} = Q \cdot U \tag{2.1}$$

where Q is the specific capacity of the battery in Ah/kg, and U is the voltage in V. In some cases the *energy density* defined as energy per volume (Wh/l) is considered the more important parameter as the energy storage system has to fit into the limited space of a car. Mass, volume and cell voltage are specifications that are directly linked to the chemistry of the system. Thus, it is not surprising that lithium batteries offer the best prospects for developing high energy batteries, since they are based on the third lightest element, lithium, which also has the most negative potential in the galvanic series (-3 V against the standard hydrogen potential). By combining metallic lithium with more positive materials, high cell voltages can be achieved in order to maximize specific energy. Goodenough *et al.* first recognized that lithium can be electrochemically removed from $LiCoO_2$ at cell voltages of around 3.8 V *vs.* Li/Li^+, which outperformed the at that time existing $Li\text{-}TiS_2$ system,[9] and therefore proposed the family of layered oxide compounds that are still popular in today's lithium-ion batteries. It was then the discovery of the reversible, low-voltage lithium intercalation into carbonaceous materials[10] that circumvented safety issues with metallic lithium, and finally led to the commercialization of the lithium-ion battery by Sony in 1991:[11]

$$LiCoO_2 + 6\,C \underset{discharge}{\overset{charge}{\rightleftharpoons}} Li_{1-x}CoO_2 + Li_xC_6 \tag{2.2}$$

The electrochemical reaction is based on the *reversible intercalation* and *deintercalation* of lithium-ions into the graphitic and layered oxide host structure as shown

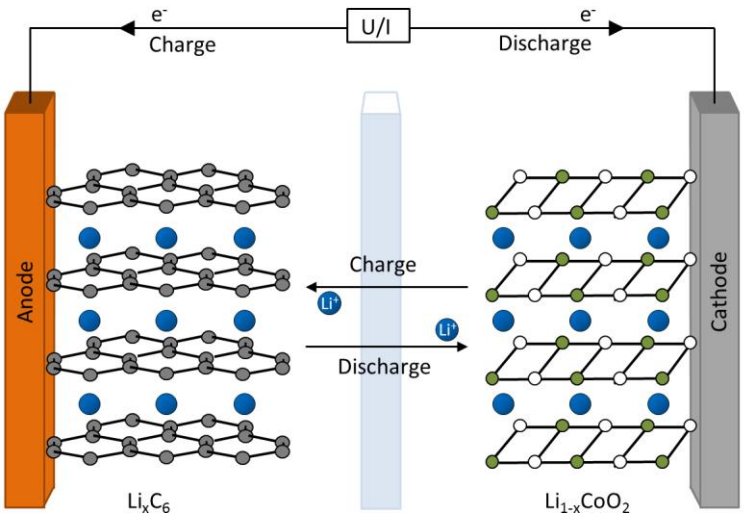

Figure 2.1: Schematic illustration of the working principles of a non-aqueous $Li_xC_6/Li_{1-x}CoO_2$ lithium-ion cell. During charge, lithium ions diffuse from the lithiated layered oxide $Li_{1-x}CoO_2$ (the cathode) into a delithiated graphite Li_xC_6 structure (the anode) with concomitant oxidation and reduction of the two electrodes, respectively. The reverse process occurs during discharge.

schematically in Figure 2.1. Since $LiCoO_2$ is the source of lithium in the cell, the charging process has to proceed via lithium extraction and the oxidation of Co^{3+} to Co^{4+} at the *positive electrode* (*cathode*), while at the same time lithium-ions are inserted into graphite and are reduced at the *negative electrod*e (*anode*). During discharge the reaction proceeds *vice versa*. Due to the development of stable, liquid organic carbonate solvents, it was possible to operate the cell at high voltages, at least up to 4.2 V *vs.* Li/Li^+.[12] This was the moment when the $LiCoO_2$ cathode revolutionized the portable electronics market. Although offering a specific capacity of 140 mAh/g_{LiCoO_2}, which is achieved by extracting $x = 0.5$ lithium, it falls far behind the current target of automotive companies. To achieve a driving range of 300 miles (≈480 km, defined by the US Department of energy), the cathode material has to provide a specific energy of about 800 $Wh/kg_{cathode}$,[13] which is clearly above the 530 Wh/kg_{LiCoO_2} for $LiCoO_2$. The further improvement of this material – also related to attempts to reduce the amount of Co due to limited availability, cost and safety issues[14] – resulted in structurally similar mixed-layered-oxides such as $LiNi_{1/3}Mn_{1/3}Co_{1/3}O_2$ (NMC-111) and $LiNi_{0.8}Co_{0.15}Al_{0.05}O_2$ (NCA) with specific energies of 600-650 $Wh/kg_{NMC\text{-}111}$ and 700-750 Wh/kg_{NCA},[13] respectively. These two materials are therefore commercially utilized in several full EVs such as the BMW i3, the Nissan leaf (blended NMC-111), the Daimler Smart EV (NMC-111), or in the Tesla Model S (NCA).

Currently, three types of novel oxide cathode materials are considered as the next generation to power EVs by providing either higher voltages or capacities: Ni-rich NMCs,[15,16] so-called high-energy (HE) NMC, which is an overlithiated layered-layered oxide of the general composition $xLi_2MnO_3(1\text{-}x)LiMO_2$ (M=Ni, Mn, Co),[17] and high-voltage (HV) spinels, *e.g.*, $LiNi_{0.5}Mn_{1.5}O_4$.[18] However, most of these oxide materials often encounter increased structural instability and reactivity towards the electrolyte, which

currently impedes their commercial application. By substantially improving these systems, the chances are good to meet the above mentioned target of automotive companies.

In addition to the cathode material, the anode also provides opportunities to increase the specific energy of the battery pack by reducing the mass of the electrode. At present, conventional graphite is the dominating anode material, with an average voltage of 0.1 V *vs.* Li/Li^+ and a theoretical specific capacity of 372 mAh/g_C (LiC_6). By increasing the specific capacity, less anode material is required to incorporate the same cathode capacity. In this regard, silicon is the most attractive candidate because it provides a theoretical specific capacity of 3580 mAh/g_{Si} ($Li_{15}Si_4 \approx Li_4Si$) while maintaining a low average voltage of 0.4 V *vs.* Li/Li^+.[19] But due to its large volume expansion of ≈300% during Li-Si alloying and the concomitant electrode disintegration,[20] only blends of graphite and 20% silicon are generally considered for practical use, which offer a specific capacity of 1100 mAh/g_{C+Si}.[13]

For a more realistic estimation of the proposed target, both anode and cathode have to be included in the calculation of the specific energy. Therefore, a final value of 250 $Wh/kg_{battery}$ needs to be achieved on a system level (battery pack) in order to have a

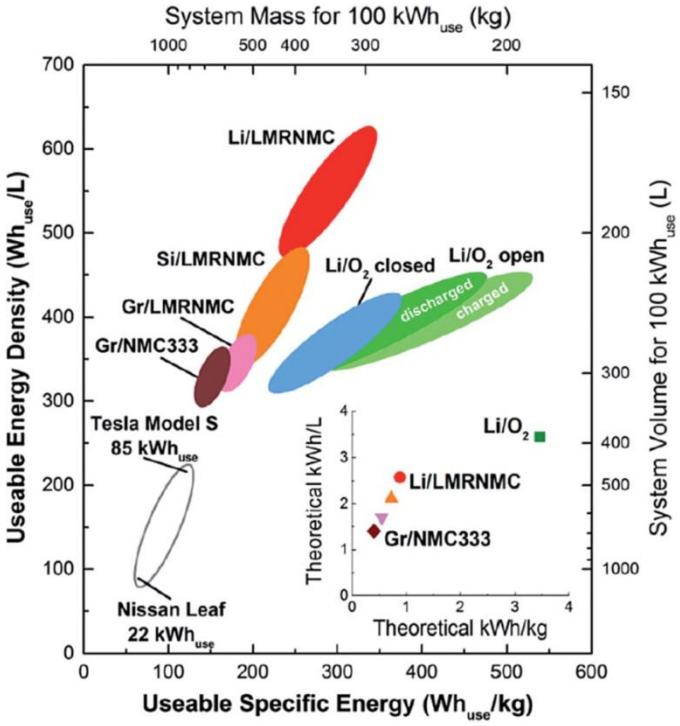

Figure 2.2: Calculated system level energy density (Wh_{use}/l) and specific energy (Wh_{use}/kg) for different lithium-ion battery pack systems with 100 kWh of useable energy and 80 kW of net power at a nominal voltage of 360 V. The already commercially available graphite/NMC333 (also called NMC-111) is compared to a lithium- and manganese-rich NMC (LMR-NMC, which is the same as HE-NMC) paired with the advanced anode materials silicon and lithium. (inset) Theoretical specific energy and energy density considering both anode and cathode active materials. Reproduced from Ref.[21] with permission from The Royal Society of Chemistry.

driving range of 300 miles as suggested by BMW;[13] whereby the total mass of the lithium-ion battery pack compromises ≈25% for the cathode, ≈15% for the anode, ≈10% for the electrolyte and ≈50% for the pack components.[22] A rigorous analysis by Gallagher *et al.*[21] is summarized in Figure 2.2. It compares the attainable specific energies and energy densities on a system level for different lithium-ion battery technologies, which is consistent with the later projections of BMW. Both conclude that next generation cathode materials (Ni-rich NMC, HE-NMC or HV-spinels) have to be combined with a silicon-carbon composite anode to be able to meet the required target value. To significantly exceed the 250 $Wh/kg_{battery,}$ the only option would be the use of lithium metal anodes. But due to unfavored morphological changes during cycling, which result in dendrite formation and internal shorts,[23] this system is still far from commercialization. While so-called *post* or *beyond* lithium-ion batteries, *i.e.*, lithium-oxygen and lithium-sulfur, have been assumed to revolutionize battery energy storage due to their amazing material-based storage capacities of up to 2500 Wh/kg_{Li_2S}[24] and 3460 $Wh/kg_{Li_2O_2}$[25] (see also inset in Figure 2.2), their system level specific energies and energy densities are very sobering (*e.g.*, 450-500 $Wh/kg_{battery}$ for Li-S and 300-500 $Wh/kg_{battery}$ for Li-O_2)[26] compared to advanced lithium-ion batteries (see Figure 2.2). Thus, Li-S and Li-O_2 batteries are currently regarded as unfeasible for use in automotive cars and only interesting with respect to a potential material cost advantage.[26]

During the last 25 years, since the first lithium-ion battery was commercialized, the number of patent activities in the field of lithium-ion battery has exploded: Starting with the establishment of the fundamental technology and the development of consumer electronics, a second boost of activities emerged in the last few years due to new opportunities in large-scale systems such as transportation and stationary storage.[27] As one might expect, electrodes and electrolyte, with an average annual growth rate of ≈25-30%, account for the largest number of patent families.[27] Driven by cost targets and performance requirements, not only improvements to energy density should be considered, but also issues concerning safety, durability and cycle life.

2.2 Cell failure and analytics

The current goal of the battery community in developing new electrode materials is not just to increase the energy density, *i.e.*, to increase the driving range of the EV, but also to maintain the performance of the material, *i.e.*, to sustain the cycle lifetime of the battery and hence the durability of the EV. For a battery lifetime that satisfies consumer expectations, 2000 to 3000 discharges and a calendar life of 10 to 15 years with a maximum of 20% deterioration in key performance metrics (*e.g.*, capacity) are required according to the International Energy Agency (IEA).[28] Therefore, it is crucial to understand and identify the main aging and degradation mechanisms in current lithium-ion batteries in order to

find strategies to counter overall cell failure, which is considered to be the most challenging task.

In general, the degradation of a lithium-ion battery is quantified at two levels, *i.e.*, cell aging during storage of the cell (*calendar aging*) and cell fatigue during operation (*cycle aging*).[29] Since both conditions influence cell behavior and response differently, the experiment has to be carefully planned according to the investigated phenomena.[30] The degradation under both conditions, however, is based on two principal observations, which are mainly characterized by *capacity fade* due to irreversible capacity losses and *power fade* due to increased cell impedance and coupled voltage losses.[31] The underlying fundamental processes on the material level are not easy to define or to distinguish, therefore a sophisticated combination of various electrochemical and analytical methods is absolutely necessary for an in-depth understanding.[31–37] To start with, most of the research refers to aging mechanisms that are well established, given *e.g.*, the sound review by Vetter *et al.* in 2005.[38] Since the anode and cathode differ in chemical composition and operate at different potentials, the observed degradation processes are often separated according to the individual electrodes, whereas electrolyte degradation is included in the corresponding electrode/electrolyte interfaces.[39,40]

At the graphite negative electrode, the development of the so-called *solid-electrolyte-interphase* (SEI) is the main aging factor with time. Due to the thermodynamic instability of the organic carbonate-based electrolyte against electrochemical reduction at potentials below ≈0.8 V *vs.* Li/Li$^+$,[45] a passivating surface film at the electrode/electrolyte interface during the first lithiation process is formed. Peled *et al.* first described the SEI as a lithium-ion conductive, but electronically insulating layer, which in an ideal case prevents further electrolyte decomposition.[41] The proposed model of the SEI is shown in Figure 2.3, in which the SEI consists of multiple layers: A dense layer of inorganic components

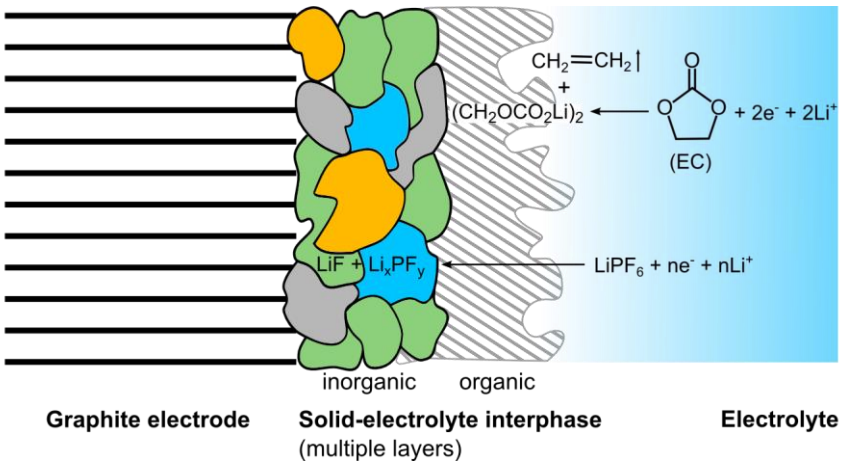

Figure 2.3: Model of the solid-electrolyte interphase (SEI) on graphite based on a concept first introduced by Peled *et al.* and refined later by different groups.[41–44] The SEI consists of multiple layers, with the innermost being more "inorganic" and the outermost being more "organic". Exemplary reactions of the electrolyte (EC = ethylene carbonate) decomposition are provided.

(*e.g.*, LiF, Li_2O and Li_2CO_3) close to the carbon phase, followed by a porous organic or polymeric layer (*e.g.*, $(CH_2OCO_2Li)_2$, ROLi and $ROCO_2Li$, where R is an organic group that depends on the solvent) close to the electrolyte phase.[42–44] The identified products in the layer result either from electrolyte solvent decomposition or from salt degradation, which involves the irreversible consumption of active lithium-ions (see exemplary degradation reactions in Figure 2.3).[46]

The initial stability of the SEI depends, of course, on the electrolyte system used. Furthermore, it was found that the SEI growth continues as the cell cycles. The according growth rate and concomitant parasitic reactions at the electrode surface, however, slow at a rate d*x*/d*t*, which is due to the passivating nature of the SEI:[47]

$$\frac{\mathrm{d}x}{\mathrm{d}t} = \sqrt{\frac{k}{2}}\, t^{-1/2} \tag{2.3}$$

where k is a constant depending on the given electrolyte/electrode system and temperature, x is the hypothetic thickness of the SEI, and t is the time since the beginning of cycling. Thus, the total amount of lithium incorporated into the SEI (irreversible capacity loss), which is directly proportional to the layer thickness $x = \sqrt{2kt}$, increases approximately as $\propto \sqrt{t}$, leading to a steady loss of cyclable lithium during cell operation independent from cycle number.[47,48]

Additionally, if the SEI layer is not elastic enough to accommodate the volume change of graphite during lithiation/delithiation, micro-cracks could emerge, exposing fresh graphite surface to the electrolyte which is reduced again. At elevated temperatures, these degradation processes and hence the SEI growth are accelerated inducing a break down or dissolution of the SEI. But also the morphology and chemical composition of the SEI changes, which is caused by the decomposition of metastable SEI components and the predominant LiF formation due to the instability of the electrolyte salt at higher temperatures.[49,50] All these mechanisms may lead to partially uncovered graphite surfaces which further react with the electrolyte components to form an additional SEI layer. The consequence is an accelerated loss of active lithium and capacity degradation of the cell. Furthermore, the SEI growth induces a gradual contact loss within the composite anode as well as a possible electrode delamination, which result in an impedance rise of the cell.[51] At low temperatures or high rates, metallic lithium plating is induced causing possible short circuits between anode and cathode.

At the positive electrode, however, structural and mechanical changes during cycling are the predominant aging factor.[52] Since the degradation is strictly dependent on the state of charge (degree of delithiation) of the cathode material, further chemical decomposition/transition metal dissolution or surface modifications are provoked.[36] In particular, successive extraction/insertion of lithium ions leads to volumetric changes of the material inducing mechanical stress, possible electrode disintegration/delamination or even cracks within the particle.[53] Irreversible phase changes, structural disordering or transition metal

dissolution reduce the amount of active material and reversible lithium-ions,[31,54–56] whereas electrolyte decomposition at the cathode/electrolyte interface results in surface film formation.[40,44] These effects are very sensitive to the individual cathode active-material and are strongly influenced by cycling and storage conditions.

In a complete battery, however, additional effects and aging processes due to the interaction between anode and cathode by transport of degraded electrolyte species or transition metal ions have to be considered.[57] Due to this complexity, the main challenge in lithium-ion battery research consists of the identification of the individual aging mechanisms and their origins, which are influenced by different cycling and storage conditions. Thus, various analytical methods and approaches have been used to investigate degradation at different levels such as spectroscopic methods (*e.g.*, electrochemical impedance spectroscopy (EIS), Raman spectroscopy, infrared spectroscopy (IR), X-ray photoelectron spectroscopy (XPS)), microscopic methods (*e.g.*, scanning electron microscopy (SEM)) and diffractometric tools (*e.g.*, X-ray diffraction (XRD), neutron diffraction (ND)) as well as elementary and gas phase analysis.[31–37,58] But due to novel electrode materials, new technologies and different application requirements of the lithium-ion battery, a critical reevaluation of existing degradation processes and also the establishment of advanced investigative methods and approaches are continually necessary to promote strategies for durable lithium-ion batteries.

2.3 Objectives of this work

High specific energies, durability and a key understanding of individual electrode processes in lithium-ion batteries are closely linked. By developing analytical approaches, insights to the system can be achieved, which help to explain complex correlations not only related to material improvements but also to aging phenomena. This thesis focuses on analytical techniques primarily based on *in situ* X-ray diffraction and novel applications of neutrons and positrons in lithium-ion battery investigations.

Since commercial electrochemical cells for *in situ* XRD analysis using laboratory diffractometers are very scarce and often restricted to the supplied diffractometer system, *in situ* XRD cells have been developed during this work. To perform reliable structural analysis, particularly for longer timescales, a comparable electrochemical performance to standard laboratory cells is necessary. The development and performance of an *in situ* XRD cell for Bragg-Brentano geometry (reflection mode) is the topic of Chapter 4.2, whereas a standard single-layered pouch cell design, utilized for transmission geometry, is discussed in Chapter 4.7.

First applications of the *in situ* XRD cell are provided in Chapter 4.3 for the high-voltage material $LiCoPO_4$ (LCP) and in Chapter 4.4 for the Li-Li_2S system. Experiments on LCP proved to be very valuable, since only with this approach could the existence of the moisture-sensitive phase "$CoPO_4$", which was first proposed by Bramink *et al.* in

2007,[59] be confirmed. In the case of Li_2S, the complete reaction of Li_2S to crystalline sulfur during the first activation charge was demonstrated, which was not obvious based on contradictory literature data.[60,61] This chapter is further complemented by comparison of the performance between Li-Li_2S and Si-Li_2S cells.

By combining *in situ* XRD with neutron-induced prompt gamma activation analysis (PGAA) and potentiostatic electrochemical impedance spectroscopy (PEIS), the main aging mechanism in a graphite-$LiNi_{1/3}Mn_{1/3}Co_{1/3}O_2$ (NMC) cell under different operating conditions was identified. This is outlined in Chapter 4.5 which in addition deals with the kinetic origin of the first cycle capacity loss of NMC and its influence on cell balancing.

Finally, in Chapter 4.6, the defect evolution in NMC and its influence on the first cycle capacity loss are probed with defect-sensitive positron annihilation spectroscopy (PAS). In contrast to *in situ* XRD analysis and electrochemical charge calculations, PAS unambiguously showed that elevated temperatures are more beneficial for capacity-recovery treatments than low potentials.

The entire Chapters 4.4 and 4.5 have already been published as articles in peer-reviewed journals,[62,63] whereas Chapter 4.6 is in preparation for publication.

3 Theoretical concepts and experimental methods

3.1 Fundamentals on battery electrochemistry

3.1.1 Battery thermodynamics

A *battery* is by definition a device consisting of one or more electrically connected electrochemical cells which convert chemical energy into electrical energy.[7,64] It is generally classified into either *primary batteries*, which are assembled in the charged state and discarded after delivering the electrical energy during discharge, or into *secondary (rechargeable) batteries*, which may be restored during charge to their original condition by passing an electric current opposite to the direction of the discharge current. The latter can therefore be used as a storage device for electrical energy. In principle, the electrical energy is provided by chemical redox reactions occurring at the electrode/electrolyte interfaces:

$$\nu_{ox}\,\mathrm{Ox} + n\mathrm{e}^- \underset{oxidation}{\overset{reduction}{\rightleftharpoons}} \nu_{red}\,\mathrm{Red} \tag{3.1}$$

where at the *anode* oxidation takes place via release of electrons into the external circuit and at the *cathode* reduction takes place via acceptance of electrons from the external circuit. Charge balance is achieved by the transportation of positive ions via the internal ion-conductive circuit of the electrolyte solution. The terms *positive* and *negative electrode*, however, refer to electrochemical reactions characterized by higher and lower electrode potentials, respectively, and therefore are independent of the current flow. By convention, the negative electrode is often assigned as "the anode" of the battery, and the positive electrode as "the cathode" of the battery, even though this terminology only applies for the discharge direction. Accordingly, electrode materials are called "anode material" and "cathode material", respectively.[64]

In lithium-ion battery cells, *e.g.*, the overall electrochemical reaction given in Equation 2.2 can therefore be divided into two half-cell reactions:
At the cathode/positive electrode

$$\mathrm{LiCoO_2} \underset{discharge}{\overset{charge}{\rightleftharpoons}} \mathrm{Li_{1-x}CoO_2} + x\mathrm{Li^+} + x\mathrm{e^-} \tag{3.2}$$

and at the anode/negative electrode

$$6\ C + x Li^+ + x e^- \underset{discharge}{\overset{charge}{\rightleftharpoons}} Li_xC_6 \tag{3.3}$$

The electrochemical redox reaction is mainly driven by the electrode potential, in addition to pressure and temperature, which are driving forces for all chemical reactions. The equilibrium potential, also named reversible potential E_{rev}, is dependent on the chemical activity of the oxidized a_{ox} and the reduced a_{red} species as given by the Nernst equation:

$$E_{rev} = E^0 + \frac{RT}{nF}\ ln\frac{a_{ox}^{v_{ox}}}{a_{red}^{v_{red}}} \tag{3.4}$$

where E^0 is the electrode potential at standard conditions, R is the universal gas constant (8.3145 $JK^{-1}mol^{-1}$), T is the temperature in K, n is the number of electrons transferred according to Equation 3.1 and F is the Faraday constant (96485 $Cmol^{-1}$).[65]

Since absolute electrode potentials cannot be measured directly, potentials are determined relative to a second electrode, the so-called *reference electrode*, whose potential must be known and stable during the experiment. In lithium-ion battery research, potentials are commonly reported to the Li/Li^+ potential (E_{rev}= 0 V *vs.* Li/Li^+) which corresponds to -3.04 V *vs.* standard hydrogen electrode.[66]

The equilibrium cell voltage U is given by the potential difference of anode and cathode. It represents the maximum cell voltage that can be delivered by the active materials in the cell and depends on the change in free energy ΔG of the electrochemical couple:[64]

$$U = E_{cathode} - E_{anode} = -\frac{\Delta G}{nF} \tag{3.5}$$

The *open-circuit voltage* (OCV) is the voltage of a cell or battery without an external current flow and is usually a close approximation of the theoretical thermodynamic cell voltage in batteries. Slight variations can occur due to surface effects.

For a proper functioning of the cell, the two half-cell reactions must occur separately. The electrodes must be electronically insulated to prevent short circuits, but also ionically connected to allow current flow. This is achieved by a porous polymer membrane (electronic insulation), which is soaked with electrolyte (ion conduction).

3.1.2 Battery kinetics and voltage losses

Thermodynamics describe reactions at equilibrium condition, whereas kinetics describe the system when a current is flowing. The additional voltage that is needed to drive a reaction during discharge or charge at a certain current is called voltage *polarization* or *overpotential* η and is determined by the difference between the equilibrium voltage OCV and the operating cell voltage $U_{ch/dis}$:[65]

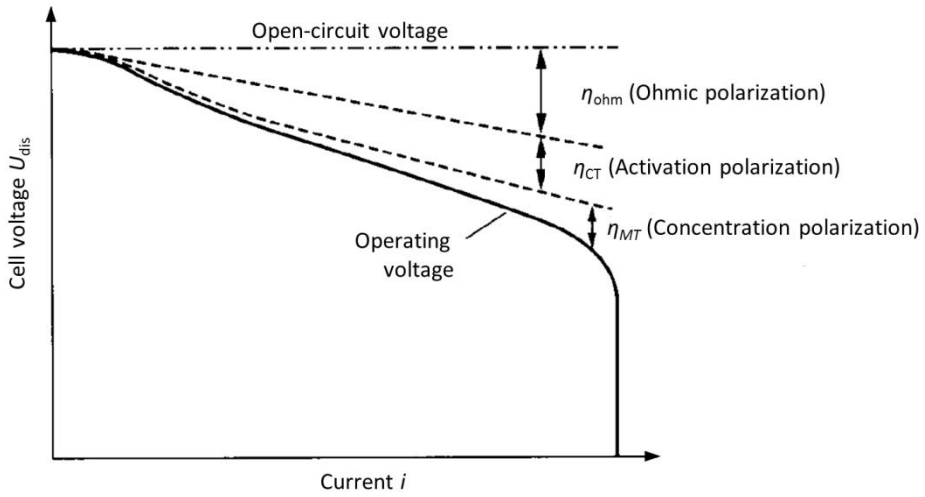

Figure 3.1: Cell polarization as a function of operating current. The operating voltage is influenced by ohmic, activation and concentration polarization. Adapted from Ref.[64]

$$\eta_{ch/dis} = U_{ch/dis} - OCV \tag{3.6}$$

An overpotential arises due to kinetic limitations of the reactions and is generally devided into three main contributions: the *activation*, the *concentration* and the *ohmic polarization.*[64] Figure 3.1 illustrates the relationship between cell polarization and discharge current.

The activation polarization η_{CT} is related to the kinetics of the charge-transfer reactions at the electrode/electrolyte interface. The current flow i of a charge-transfer-controlled battery reaction is given by the Butler-Volmer equation:[67]

$$i_{(T,\, a_{ox},\, a_{red})} = i_0 \cdot \left[exp\left(\frac{\alpha n F}{RT}\, \eta_{CT}\right) - exp\left(-\frac{(1-\alpha) n F}{RT}\, \eta_{CT}\right)\right] \tag{3.7}$$

where i_0 is the exchange current density, which depends on the specific reaction rate constant and activities of the reactants at a given temperature and α is the transfer coefficient of the charge-transfer reaction, which describes the energy barrier symmetry and the number of electrons in the rate determining step. For battery applications, electrode reactions with high exchange current densities at room temperature are favored, since reactions with larger i_0 have a lower overpotential for a given current density and are therefore more reversible.

The concentration polarization η_{MT} arises from mass-transport limitations at the electrode surface due to hindered diffusion of active species. In lithium-ion batteries, most battery electrodes are porous structures filled with electrolyte, which extend the available surface area and thus lower the current density for a more efficient operation.[7] The ohmic polarization η_{ohm} is related to the internal impedance R_{int} of the cell and is proportional to the current drawn from the system following Ohm's law:[64]

$$\eta_{ohm} = i \cdot R_{int} \tag{3.8}$$

The total internal impedance is the sum of the ionic resistance of the electrolyte, the electronic resistances of the active mass, the current collectors and the electrical tabs, and the contact resistance between the active mass and the current collector.

3.1.3 General terms and definitions

(a) Specific capacity

The theoretical capacity of an electrode material for lithium-ion batteries dependent on the amount of lithium is called *specific capacity* C_{spec}. It is characteristic for each active material and is defined as

$$C_{spec} = \frac{n \cdot F}{M} \tag{3.9}$$

where n is the number of electrons per reaction, F the Faraday constant and M the molar mass of the active material. By convention, the mass of lithium is only included in the molar mass of the cathode active material, because it introduces the lithium ions into typical lithium-ion battery cells during assembly. Generally, the specific capacity gives the amount of charge which can be stored in a certain mass of active material. In some cases, the lithium cannot be extracted completely from the active material. Thus, the value for n is not always set to one, *i.e.*, $n = 0.6$ for $LiCoO_2$.

(b) C-rate

In describing lithium-ion batteries, the charge and discharge current is often expressed as *C-rate* in order to normalize against battery capacity. A C-rate is therefore a measure of the rate at which a battery is charged or discharged relative to its nominal cell capacity.[68] This means that at a C-rate of τ, the nominal cell capacity (measured in Ah) is delivered in $1/\tau$ hours; *e.g.*, for a 5 Ah cell, a discharge at C/10 signifies a 10 h discharge with a current drain of 0.5 A. The C-rate is typically given in units of 1/h. Kinetic losses due to fast charges or discharges reduce consequently the required time.

(c) Coulombic efficiency

The *coulombic efficiency* η_C for the charge/discharge cycle of a lithium-ion cell is defined by

$$\eta_C = \frac{Q_{dis}}{Q_{ch}} = \frac{\int_0^t i_{dis} dt}{\int_0^t i_{ch} dt} \tag{3.10}$$

where *Q* is the capacity transferred during charge and discharge of the cell. This value is determined by the current flow *i* and the required time *t* for a complete charge or discharge. Coulombic efficiency is generally used to measure the reversibility of the cell reaction. Since secondary reactions such as electrolyte degradation and irreversible lithium consumption occur upon charge, the coulombic efficiency is smaller than 100%. For state-of-the-art lithium-ion batteries, a coulombic efficiency of 99.99% is achieved during cycling.[64] *E.g.*, in order to accomplish 1000 cycles with a capacity loss of less than 20%, which equates to 0.02% loss per cycle, a coulombic efficiency of more than 99.98% would be required, unless no other losses occur.

3.2 Electrode preparation

3.2.1 Requirements on electrode formulation

Lithium-ion battery electrodes are an extremely complex mixture of different materials optimized to meet a number of requirements. Each single component needs to be chemically and electrochemically stable in the battery environment to achieve a good performance of the cell. Furthermore, mechanical stability of the electrode is equally important for extended cycle life and is largely influenced by the electrode processing techniques. A typical industrial lithium-ion electrode consists of the redox-*active material*, *conductive carbon*, and a *polymeric binder*. While the conductive carbon increases the electronic conductivity by providing good contact to every particle and to the current collector, the polymeric binder glues all particles together and ensures adherence to the current collector as well as mechanical integrity during battery operation.[69] The electrode components are mixed in a solvent and the resulting slurry is cast either on an aluminum foil, commonly used as cathode current collector, or on a cupper foil, commonly used as anode current collector. To minimize the contribution to the electrode weight and still maintain a good processability, the foil thickness usually ranges from 8 to 15 µm for copper and from 15 to 25 µm for aluminum. For high energy density electrodes, the active material content needs to be as high as possible and the electrode needs to be compressed after drying to decrease porosity and improve the inter-particle contact and hence the electrical conductivity. The amount of conductive carbon, however, should be as low as possible, to reduce the surface area and related parasitic reactions with the electrolyte during cycling. The binder content is also kept very low to avoid the formation of closed pores due to swelling and associated increase in electrode impedance.[70]

Poly(vinylidenedifluoride) (PVdF) is widely used as binder for both anode and cathode in commercial lithium-ion batteries due to its good electrochemical stability and high adhesion to electrode materials and current collector. This polymer is insoluble in commonly used electrolyte solutions such as alkyl carbonates, but can be processed in the organic solvent N-methyl pyrrolidone (NMP).[71] Recently, aqueous binders have been

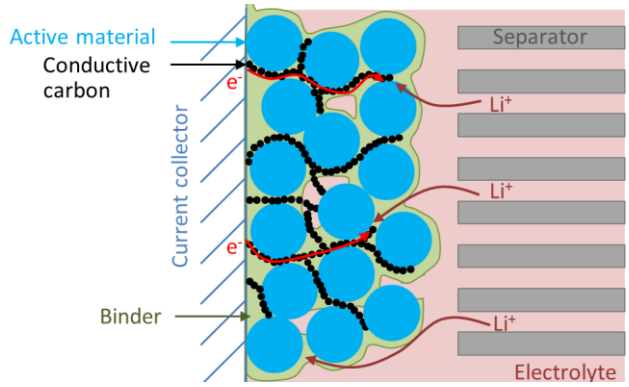

Figure 3.2: Schematic illustration of a typical lithium-ion porous electrode. Function of individual components: (i) the active material is used as the Li^+ inter-/deintercalation host, (ii) the electrolyte transports Li^+ ions between anode and cathode, (iii) the conductive carbon transports e^- to/from the active material, (iv) the binder provides mechanical integrity of the electrode and adhesion to the current collector.

gradually replacing PVdF for the anode, since they are environmentally friendlier and cheaper due to a water-based processing of the slurries. Among them, carboxymethyl cellulose (CMC) is the most promising substitute.[72] As conductive additive, carbon black with a particle size of 15 to 100 nm is usually utilized to fill the spaces between the larger particles and hence increase the conductivity of the electrode.[73] To minimize side reactions, carbon blacks with a relative specific surface area below the 100 m^2/g are preferred, such as Super C65 (62 m^2/g, TIMCAL). A schematic drawing of a typical lithium-ion porous electrode with its individual components is shown in Figure 3.2.

The typical commercial electrode contains ≈96 wt% active material and ≈2 wt% of both conductive carbon and binder.[69] Since active materials behave differently due to differences in their intrinsic properties, the electrode composition needs to be optimized accordingly.

3.2.2 Electrode fabrication

The preparation method for the lithium-ion-cell electrodes used in this thesis followed a procedure described by Marks *et. al.*, which was derived from industrial standards.[69] Main steps include mixing of the electrode-material powders in a solvent, coating of the final slurry onto the current collector foil, solvent evaporation, calendering and electrode cutting as illustrated in Figure 3.3.

Electrode slurries were prepared using appropriate ratios of the active material, PVdF binder (Kynar® HSV 900, Arkema) and conductive carbon black (Super C65, TIMCAL) in NMP solvent. All components were mixed together in a plastic container in a planetary centrifugal vacuum mixer (ARV-310, Thinky corporation). By applying both *revolution* and *rotation* motion, *i.e.*, the sample container *revolves* clockwise about the central axis while the container itself *rotates* counter-clockwise, a uniform dispersion of solvent, binder, active material and carbon black could be achieved, even up to high-viscosity

mixtures. The revolution speed was therefore set to 2000 rpm for 5 min and the whole cycle was repeated again. Final slurries had a solid content in the range of 50-65% depending on the materials used. To further increase the solid content and thus to reduce the amount of solvent while maintaining the same viscosity of the previous slurry, a sequential-dilution process was introduced by Jörg Schuster in our group. In this process, the material powders were first mixed without any solvent, followed by a stepwise dilution of the mixture with NMP solvent to the defined solid content. For the three-step dilution, one third of the total NMP amount was added in each step of mixing. The mixing parameters were adjusted to 1000 rpm for two times at 2 min for each step in order to minimize heat generation by friction, whereas in the last step the speed could be increased up to 2000 rpm. Thus, the final amount of solid could be increased to 55-70% and was mainly applied in the production of electrodes for single-layered pouch cells.

The resulting slurries were then cast onto the respective current collector foils using an electrically driven coating machine (Modell 624, K-control-coater, Erichsen). The metallic foils were cleaned with ethanol and adhered to a sheet of float glass that fitted into the coater. Different wet-film thicknesses in the range of 100 to 500 µm could be adjusted by the commonly used Doctor-blade technique, in which a gap between the support and the blade determined the active material loading. By setting the coating speed to 2 m/min, very homogeneous coatings with reproducible loadings were accomplished.

After evaporating the solvent at 50°C in a drying oven, the coating was either calendered to a defined thickness/porosity or directly forwarded to the electrode-cutting step without any compression. For the calendering process, the electrode sheet was passed

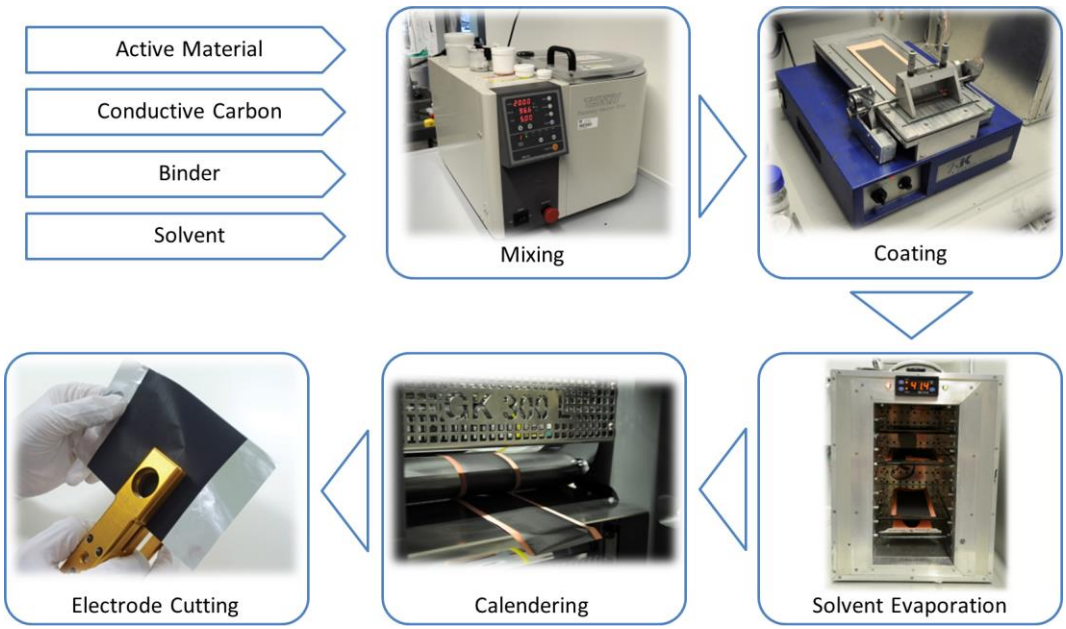

Figure 3.3: Overview of the electrode fabrication steps. Main steps include mixing of the electrode-material powders in a solvent, coating of the final slurry onto the current collector foil, solvent evaporation, calendering and electrode cutting.

through the compression rollers of a laboratory calender (GK 300L, Saueressig). The roller gap was adjusted by distance using a feeler gauge. The final disk-shaped electrodes were then punched from the electrode sheet using a hand-held punching tool (Hohsen) with typical diameters of 10 mm for the cathode and 11 mm for the anode. Prior to cell assembly, electrodes were dried under dynamic vacuum at least 3 h at 120°C and directly transferred to an argon filled glovebox. For pouch cells, the prepared electrode sheets were either cut into 30x30 mm squares for the cathode or into 33x33 mm squares for the anode, both equipped with a 10x40 mm tab on the upper left side of the electrode. The residual coating must therefore be carefully scraped off from the tab.

3.2.3 Electrode characteristics

In order to adjust porosity as well as discharge current and to determine the electrode capacity, it is important to characterize the prepared electrodes prior to cell assembly. For this purpose, the thickness and mass of each electrode were accurately measured. The dry-film thickness of the electrode coating d_{coating} was obtained by subtracting the current-collector-foil thickness from the total electrode thickness. The active-material *loading* in mg_{AM}/cm^2 was calculated in a similar manner by using following formula:

$$Loading_{AM} = \frac{\left(m_{electrode} - m_{support}\right) \cdot f_{AM}}{A} \tag{3.11}$$

where $m_{\text{electrode}}$ and m_{support} represent the total electrode mass and the mass of the pure current collector foil, respectively, f_{AM} is the active material mass fraction in the dried coating and A is the surface area of the electrode.

The data were then used to determine the electrode *porosity* by calculating the difference between the actual coating volume $V_{\text{actual}} = A \cdot d_{\text{coating}}$ and the nominal solid volume V_{solid}, which is defined by the bulk material densities $\rho_{\text{i,bulk}}$ and the material masses m_i, if the porosity were zero.

$$V_{\text{solid}} = \sum_{i}^{\text{components}} \frac{m_i}{\rho_{i,\text{bulk}}} \tag{3.12}$$

which finally results in

$$Porosity = \frac{V_{actual} - V_{solid}}{V_{actual}} \cdot 100 \tag{3.13}$$

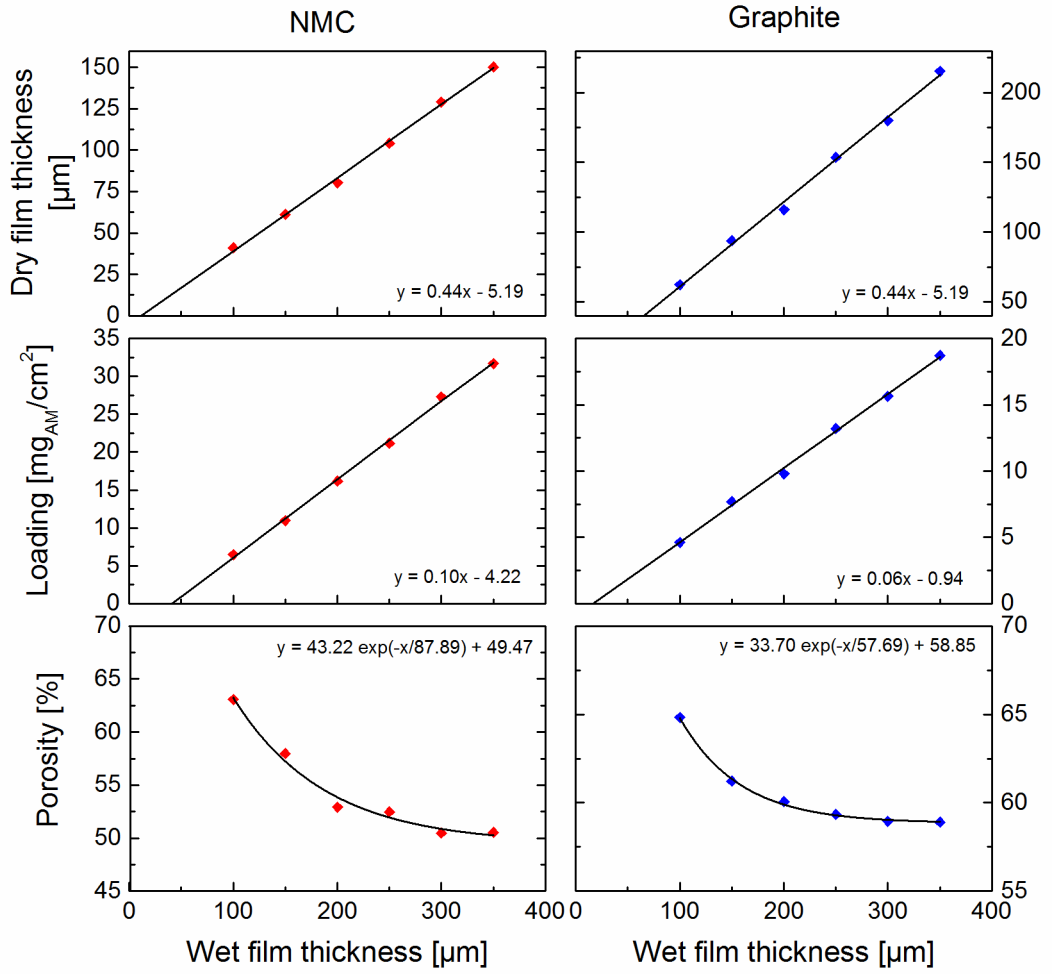

Figure 3.4: Electrode characteristics for non-calendered $LiNi_{1/3}Mn_{1/3}Co_{1/3}O_2$ (NMC) and graphite electrodes. NMC electrodes consisted of 96 wt% NMC, 2 wt% Super C65 and 2 wt% PVdF binder. The corresponding slurry had a solid content of 65%. Graphite electrodes consisted of 95 wt% graphite and 5 wt% PVdF binder. The corresponding slurry had a solid content of 50%. Both slurries were mixed according to the one-step mixing procedure.

Figure 3.4 provides electrode characteristics for non-calendered electrodes prepared with different wet-film thicknesses. These values are based on $LiNi_{1/3}Mn_{1/3}Co_{1/3}O_2$ (NMC) and graphite electrodes, which are mainly used throughout this thesis. Standard NMC electrodes were typically prepared with a wet-film thickness of 200 µm resulting in an active material loading of ≈15 mg_{NMC}/cm^2 and ≈55% porosity, whereas standard graphite electrodes were prepared with 150 µm resulting in ≈8 mg_C/cm^2 and ≈60% porosity. Since dry-film thickness and loading show a linear dependency on the wet-film thickness, this relationship can be easily used to adjust the desired electrode characteristics for defined purposes such as electrode balancing.

3.2.4 Full-cell capacity and electrode balancing

The capacity of lithium-ion full cells is given by the capacity of its electrodes and the active lithium which is available in the cell during cycling. Lithium is primarily stored in the cathode active material, since handling of lithiated graphite is difficult due to its sensitivity to air and it would react rigorously upon first contact with the electrolyte during assembly causing severe safety risks. Thus, the amount of active lithium introduced into the cell is limited by the cathode capacity. Furthermore, a part of the lithium is irreversibly consumed on the anode side during the formation of the SEI. Consequently, only a part of the cathode capacity is used during cycling leading to a decreased full cell capacity.

The cell capacity is further influenced by the relation between cathode and anode capacity, known as *electrode balancing*. Usually, the anode capacity is significantly higher than the cathode capacity to prevent metallic lithium deposition and related side reactions with the electrolyte, which would further consume active lithium. These reactions are correlated to the SEI built up to passivate the freshly exposed lithium surface, similar to the processes described for graphite surfaces in Chapter 2.2. Figure 3.5a demonstrates the correlation between electrode balancing, available active lithium and the characteristic voltage profile of the full and half cells. Half-cell data are shifted and scaled against each other to match the full-cell data.[75] The grey areas indicate the electrode capacity, which is not used in the arranged cell configuration. In the present example, a large part of the graphite anode remains unused (second area), whereas only a small part of the cathode capacity is not used (first area). The cathode losses almost equal the SEI losses of the anode. Depending on the anode-to-cathode areal-balancing, the SEI losses can be greater than the cathode losses and hence determine the reversible full-cell capacity as illustrated in Figure 3.5. Here, the absolute first-cycle capacity loss in mAh of the full cell is com-

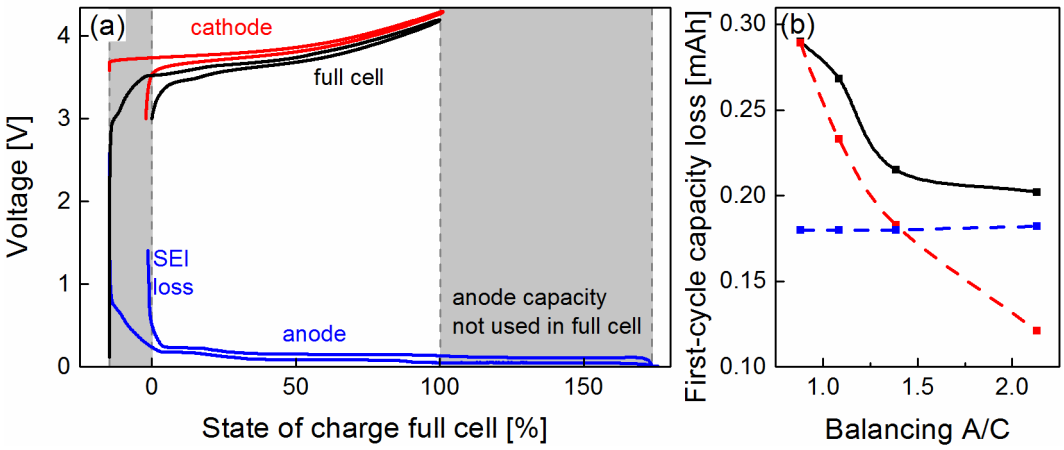

Figure 3.5: (a) Full-cell voltage profile for a graphite-$LiNi_{1/3}Mn_{1/3}Co_{1/3}O_2$ cell compared to corresponding half-cell voltage profiles for Li-graphite and Li-$LiNi_{1/3}Mn_{1/3}Co_{1/3}O_2$ cells. Anode-to-cathode areal capacity ratio = 1.1. (b) First-cycle-capacity loss depending on different anode-to-cathode (A/C) areal-capacity ratios (mAh cm^{-2}/mAh cm^{-2}). Data is based on Ref.[74]

pared to the calculated losses of the corresponding anode and cathode, which depends on the active material mass and an experimentally determined specific-capacity loss for each electrode (27.6 mAh/g_{NMC} for NMC, 19.8 mAh/g_C for graphite, half-cell configuration).[74] To keep the irreversible capacity as small as possible and still maintain a safe cycling of the full cell, typical anode-to-cathode areal capacity ratios are close to 1.1.

3.3 Electrochemical testing

3.3.1 Laboratory test cell designs and assembly

The investigation of new battery materials is usually done in experimental cells for lithium-ion battery research. The advantage of such cells is their easy assembly and the small amount of required material due to small electrode geometries in the range of a few cm^2. Furthermore, they allow the assembly of various cell configurations by combing different kinds of electrodes, electrolytes and separators. All experimental cells used in this thesis were assembled in an argon-filled glovebox (MBraun, < 0.1 ppm H_2O and O_2) to prevent reactions of metallic lithium, electrodes and the electrolyte with oxygen or water.

*(a) Swagelok T-cell*s

A commonly utilized cell design, which can be built in a three-electrode configuration with an additional reference electrode, is based on Swagelok® parts. This cell type was first introduced to our group by Rebecca Bernhard and further improved to enable a reproducible cell assembly and sealing as well as to prevent short circuits.[76] A detailed overview of the principal components of the Swagelok T-cell is provided in Figure 3.6. The central part represents the T-shaped cell housing which easily accommodates and aligns the stainless-steel current-collector rods for anode, cathode and reference electrode. Each rod is sealed by a combination of two perfluoroalkoxy alkane (PFA) ferrules, which exhibit excellent electrochemical stability. A stainless-steel compression spring with a spring rate of 3.71 N/mm is used to apply a homogeneous and constant pressure of ≈0.19 MPa to the cell stack by compressing it to ≈4 mm at a given contact area of 0.79 cm^2 (cathode area). To prevent any short circuits with the stainless-steel cell housing, the cell stack is encased in an insulating HDPE (high-density polyethylene) tube, while the reference electrode is separated by a HDPE ring.

The cell assembly is performed according to following procedure:

1. The anode current-collector rod equipped with the HDPE tube is fixed to the cell housing.
2. The negative electrode (Ø11 mm) is placed inside the tube on top of the anode rod with the coating facing upwards.

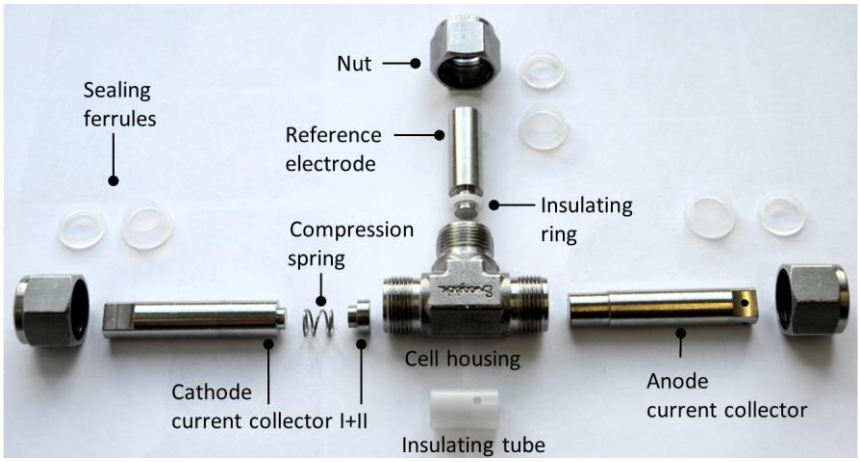

Figure 3.6: Photo of the electrochemical test cell based on Swagelok® stainless-steel parts.

3. Two porous separators, usually glass fiber (Ø11 mm, Grade 691, VWR International GmbH), are placed on the negative electrode.
4. 80 µl of electrolyte are added.
5. The positive electrode (Ø10 mm) with the coating facing downwards is placed on the two separators.
6. The cathode current-collector parts comprising part I, spring and part II are placed on the positive electrode and fixed to the cell housing.
7. The spring is compressed to ≈4 mm using a custom-built cell holder with a micrometer-screw adjustment described in Ref.[76]
8. For a two-electrode setup, the reference side is closed with a face seal fitting.
9. For a three-electrode setup, metallic lithium (Ø6 mm) is put on top of the reference-electrode rod. The HDPE tube has a small hole on the side to allow ionic conduction between the reference and the main cell compartment. The ionic conduction is facilitated by a specially-cut separator which has a little extension (Ö) that fits through the hole of the HDPE tube and connects to the reference electrode. Before fixing the reference-electrode rod to the cell housing, an additional piece of separator is placed between the tube and the lithium and 20 µl of electrolyte are added.

(b) Pouch cells

Another experimental cell is based on the design of commercially available pouch cells. In contrast to Swagelok T-cells, single-layered pouch cells are very flexible in electrode geometry and size, since the cell housing is an aluminum-composite foil (*pouch foil*) which can be adapted to the desired design of the electrode. The pouch foil used (type

D-EL40H(3), DNP Europa GmbH) consists of a polypropylene layer of 45 µm thickness for sealing purposes, an aluminum layer of 40 µm thickness, to provide a barrier against moisture intrusion, and an oriented-nylon layer of 25 µm thickness, to protect the aluminum layer from scratches.

The pouch-cell fabrication steps, exemplified on a full-cell configuration, are illustrated in Figure 3.7. Most steps can be performed outside an argon-filled glove box (steeps 1-5), whereas the electrolyte filling and the final sealing must be performed in inert-gas atmosphere (steps 6-8).

1. The pouch foil (70x140 mm) is folded to divide it into two parts with the polypropylene layer facing upwards (this becomes later the inside of the pouch cell).
2. The negative electrode (33x33 mm) is centered on the right side of the folded pouch foil with the coating facing upwards and fixed with a small piece of green BOPP tape (bi-axially oriented polypropylene tape with an acrylic adhesive, type 854PA, 3M company).
3. A sheet of porous separator (36x36 mm) is centered on the negative electrode and fixed with BOPP tape.
4. The positive electrode (30x30 mm) is centered on the separator and fixed with BOPP tape.
5. The pouch foil is closed along the fold and the electrode tabs are heat-fixed to the pouch foil after adding an additional tab sealing tape (type PPa-F(100), DNP Europa GmbH) on the front and back side of the tabs. The fixation is accomplished with heat sealing tongs (type HPL WSZ 200, hawo GmbH).

The tab sealing tape is used to enhance the sealing at the electrode feedthroughs and hence to prevent possible short circuits with the aluminum layer of the composite foil. The cell assembly is then dried under vacuum at 95°C below the melting temperature of the polypropylene layer of the pouch foil for at least 12 h and afterwards transferred to an argon-filled glovebox equipped with a vacuum sealer (C100, Multivac). The sealing parameters of the device are set to a pressure of 50 mbar and a sealing time of 3.5 s:

6. The electrode tabs and the opposite edge of the pouch are sealed double-sided leaving one side open for electrolyte filling.
7. The amount of electrolyte added is depending on the void volume of the electrodes and the separator, and calculated with an excess of 50%:

$$V_{electrolyte} = 1.5 \sum V^{void} \tag{3.14}$$

8. The pouch cell is finally evacuated and sealed.

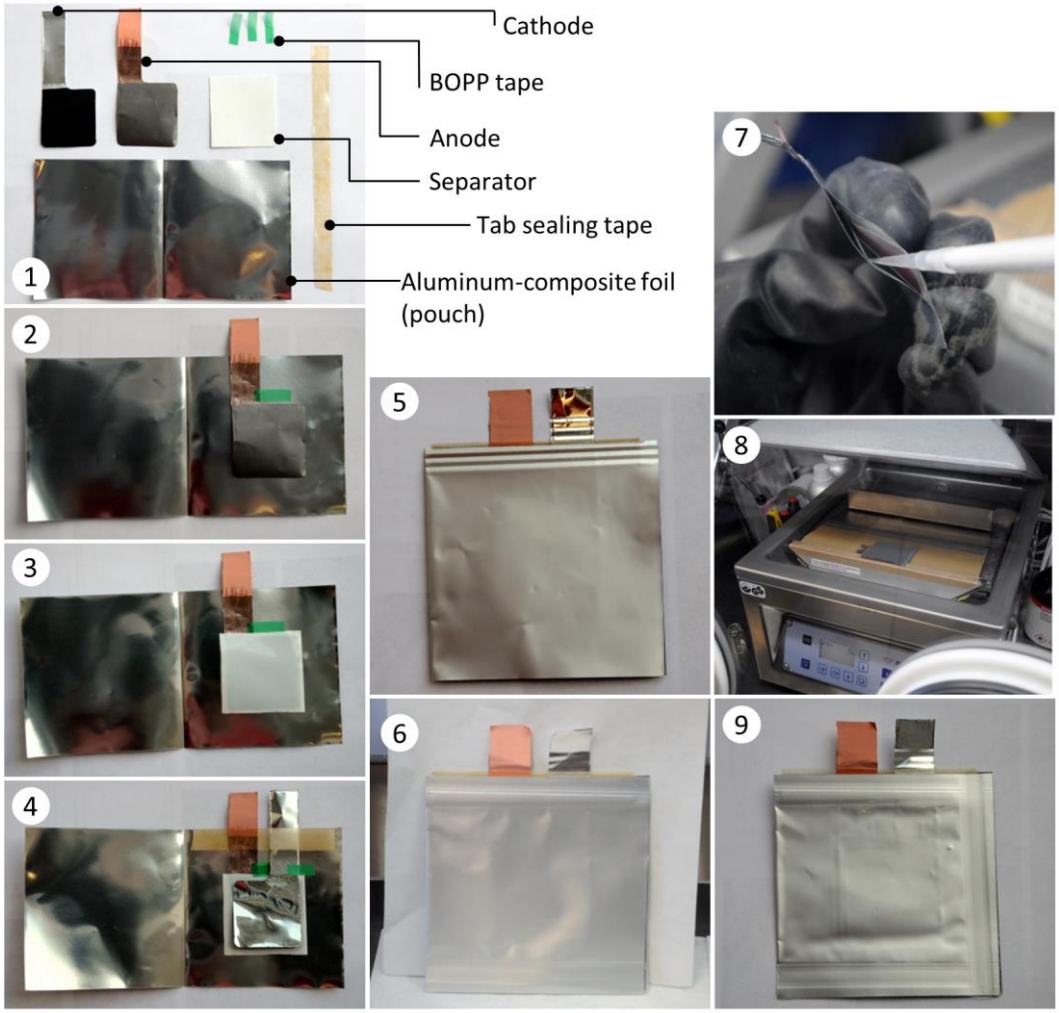

Figure 3.7: Photos of the pouch cell fabrication steps exemplified on a full-cell configuration.

The fabrication of pouch cells in half-cell configuration follows a slightly modified procedure because the negative electrode (lithium metal) can only be handled in the glovebox. For this purpose, steps 1-5 proceed without the negative electrode and only the tab of the positive electrode is heat-fixed, leaving space for the negative electrode-tab. In the glovebox, the lithium metal (33x33 mm) is added and connected to a copper-foil strip (10x60 mm). Sealing and electrolyte filling are in accordance with steps 6-8. A reference electrode can be added in a similar manner to the pouch cell. A small piece of lithium is therefore put beside the electrode stack, but still in contact with the separator and the electrolyte, and connected to an additional copper-foil strip. In this thesis, two types of separator material, namely glass fiber separator (grade 691, VWR International GmbH) and Celgard® separator (type H2013, Celgard, LLC), were used.

3.3.2 Battery Cycling

Degradation processes of lithium-ion batteries can be either investigated during storage of the cell at a certain state of charge or during operation of the cell (cf. Chapter 2.2). During operation, the cell is charged and discharged multiple times, which is called *cycling*. The *cycle life* of a battery defines the cycle number that a battery can achieve before the capacity falls below a certain threshold value at a given C-rate (typically 80% of the initial capacity at 1C). The cycling can be either conducted in a galvanostatic (constant current, CC) or in a potentiostatic (constant voltage, CV) mode. In most instances, the galvanostatic cycling is preferred, but also a combination of galvanostatic and a subsequent potentiostatic mode is commonly used to achieve the full nominal discharge or charge capacity.

A standard cycle procedure to investigate lithium-ion cells in this thesis is shown in Figure 3.8, which includes a CCCV charge followed by a CC discharge. By applying a positive current, the cell is charged until the upper cut-off voltage is reached. This voltage is then kept constant and the current is recorded. When the current drops to a set limit, the discharge is initiated by applying a current in the inverse direction, and is stopped when the lower cut-off voltage is reached. The transferred charge Q can be determined by the integral of the current I and the corresponding time t for the charge and discharge, respectively:

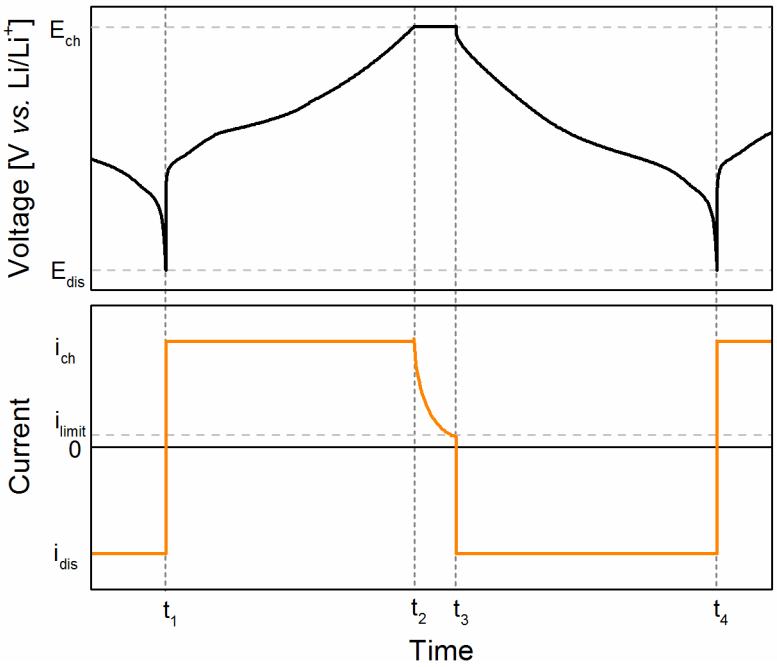

Figure 3.8: Typical cycle procedure of an experimental cell with a constant current (CC) and constant voltage (CV) charge followed by a constant current (CC) discharge. (top) Voltage profile with corresponding cut-off voltages E_{ch} and E_{dis}, and (bottom) respective current profile with charging/discharging currents i_{ch} and i_{dis} and the cut-off current i_{limit} for the CV step.

$$Q_{ch} = \int_{t_1}^{t_3} I(t)dt \qquad \text{or} \qquad Q_{dis} = \int_{t_3}^{t_4} I(t)dt \tag{3.15}$$

Battery cycling can be conducted at various C-rates, temperatures and voltage windows to investigate different degradation processes.

3.3.3 Electrochemical impedance spectroscopy (EIS)

Electrochemical impedance spectroscopy (EIS) operates with a sinusoidal alternating-current or voltage at varying frequencies ω to determine the frequency dependent *impedance Z* (alternating-current/voltage resistance) of an electrochemical system.[77,78] Similar to a pure ohmic resistance, impedance is the ratio between voltage and current, but it further takes the phase shift ϕ between the voltage and current signal into account. Thus, impedance is defined as a complex resistance in an alternating-current circuit, which has the ability to resist the flow of electrical current, represented by the *real impedance* Z_{RE} term, but also to store electrical energy, reflected in the *imaginary impedance* Z_{IM} term, with i = $\sqrt{-1}$:

$$Z(\omega) = \frac{U(\omega)}{I(\omega)} = |Z|e^{-i\phi} = |Z|\cos\phi + i|Z|\sin\phi = Z_{RE} + iZ_{IM} \tag{3.16}$$

The data is usually represented in a so-called Nyquist plot, in which the imaginary part is plotted as a function of the real part. A simplified graph of the impedance response of a lithium-ion cell is given in Figure 3.9a. These data are analyzed by simulating the electrochemical system with an equivalent circuit model as shown in Figure 3.9b, which possesses a similar frequency depending impedance. For most batteries, individual processes are assigned to different frequency ranges and are generalized as follows:[79] At very

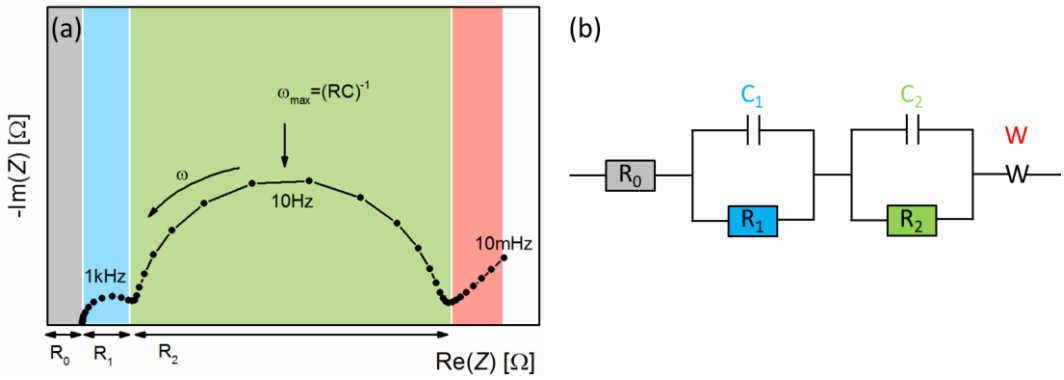

Figure 3.9: (a) Idealized Nyquist plot of an electrochemical lithium-ion cell with typical frequency regimes and (b) corresponding equivalent circuit model. Resistances R_0, R_1 and R_2 can be attributed to solution, contact, charge-transfer or film resistances. C reflects the capacitance and W is the Waburg-element for solid diffusion processes.

high frequencies (>100 kHz), electronic conduction through the particles and ionic conduction through the electrolyte dominate the impedance spectrum and are represented by a series resistance R_0, also called high frequency resistance HFR. The subsequent semicircle at high frequencies (100 kHz-5 kHz) can be related to contact resistances between the electrode and the current collector, which is described by the R_1C_1-element. At medium frequencies (5 kHz–10 Hz), a combination of charge transfer, *i.e.*, the electron transfer between the particle surface and the ions in solution, and Li^+ ion transport through a passivating film is the dominating process, which can be expressed by two additional RC-elements (the graph simplifies these processes to only one R_2C_2-element). Solid state diffusion can be described by the Warburg impedance *W* and is measured at frequencies below 10 Hz.

In a practical lithium-ion cell, the impedance spectrum is a superposition of differently contributing processes at the anode and cathode. To separate and define the main cause for cell impedance, EIS measurements are either conducted via a reference electrode, in which the reference must be placed between the anode and the cathode,[80] or in a symmetrical cell, in which cells are assembled from two equal electrodes.[81] The Swagelok T-cell design used in this thesis, however, was found not to be suitable for impedance analysis via reference electrode, since the point-like reference leads to artifacts in the impedance spectrum arising from geometrical and electrical asymmetries.[82] Thus, impedance spectra were measured in a two-electrode setup and analyzed by qualitatively comparing them. Furthermore, EIS was conducted usually before cell cycling to check the assembled cells. The analysis of the HFR, *e.g.*, reveals if the electrodes or the separator are properly wetted by the electrolyte.

3.4 Analytical methods

3.4.1 Leak test with pressure transducer

When searching for leaks, the analysis can be conducted by monitoring the pressure change of a system using a pressure gauge. Based on the direction of flow for the medium, it is distinguished between the *overpressure* method (referred to as an *inside-out* leak), where the medium flows from the inside to the outward, since the pressure inside the test specimen is greater than ambient pressure, and the *vacuum-decay* method (known as an *outside-in* leak), where the direction of flow is into the test specimen, since the pressure inside is less than ambient pressure.[83]

In this thesis, the leak test was performed on the *in situ* XRD cell according to the latter method using a Baratron® absolute capacitance manometer (Type 627D, MKS instruments). The experimental setup is shown in Figure 3.10. The cell is connected to the pressure transducer and a rotary vane vacuum pump. After evacuation of the system, the valve to the pump is closed and the pressure is monitored every 10 s by the pressure

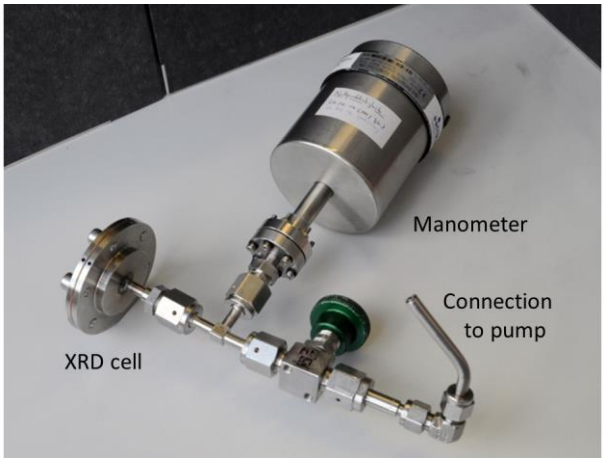

Figure 3.10: Photo of the experimental setup of the leak test using a Baratron® absolute capacitance manometer for measuring the vacuum decay.

transducer. The according data (in torr) is recorded by a multifunction data acquisition module (USB-6281, National Instruments) interfaced to a computer via a Labview program developed by our group.

3.4.2 X-ray powder diffraction (XRD) on battery materials and cells

(a) Principles of X-ray powder diffraction (XRD)

X-ray diffraction (XRD) techniques are widely used in the area of lithium-ion battery research due to the crystalline nature of the active materials. From the recorded X-ray diffractograms of the investigated material, structural information regarding phase composition, space group, lattice parameters and site occupancies can be obtained. This not only facilitates the development of new battery active materials, but also helps to reveal the exact lithium intercalation and de-intercalation process, as well as the overall cell failure mechanism of fatigued battery active materials.

In principle, X-rays are diffracted at the lattice planes of a crystal, which can be expressed by the Bragg equation:

$$n\lambda = 2d\sin\theta \tag{3.17}$$

where λ is the wavelength of the incident beam, d is the inter-planar spacing, θ is the angle between the incident beam and the relevant crystal planes, and n is an integer. When Bragg's Law is satisfied, the additional distance a coherent beam has to travel is a multiple of λ, which results in a constructive interference of the diffracted waves and its characteristic diffraction pattern.[84]

X-rays are scattered by the electron cloud of atoms, which define the crystal plane. Therefore, elements with many electrons scatter more X-rays and give stronger signals than light elements. All these interactions lead to a material specific XRD pattern that

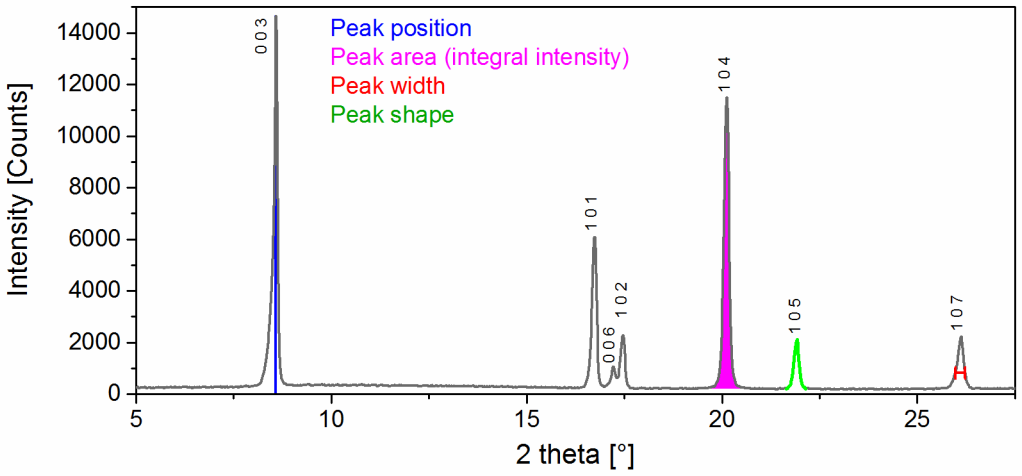

Figure 3.11: Characteristic features of a powder diffraction pattern. $LiNi_{1/3}Mn_{1/3}Co_{1/3}O_2$ was used as an exemplary powder sample. Miller indices (*h k l*) for $R\bar{3}m$ space group describe the crystallographic lattice planes, at which diffraction occurs according to Bragg´s Law.

contains all the structure-related information of the investigated material. An exemplary XRD pattern is shown in Figure 3.11. In general, the number of reflections and their position define the symmetry of the structure (*space group*), allowing for qualitative phase identification. Each reflection is related to the diffraction of a particular lattice plane, of which the *d*-spacing and Miller indices (*h k l*) are defined and thus the lattice parameters, which describe the size and symmetry of the unit cell. In the reflection area, expressed as the integral intensity, resides the information on the content of the *unit cell*, *i.e.*, type, position, and occupancy of atoms in the crystal structures. If different phases are present in one pattern, the comparison of relative intensities enables accurate quantitative phase analysis. Further pattern characteristics are the reflection shape and width, which are related to the crystallite size or strain. All this information can be separately obtained from the different characteristics of the pattern, carrying out a pattern fitting.

(b) The Rietveld method

All the characteristic features of a diffractogram can also be extracted by refining the crystallographic parameters using the popular *Rietveld method*. In this work, Rietveld refinement was primarily used to accurately determine the lattice constants of the battery active material. To do this, however, a known structure and a proper description of the pattern profile are necessary. The advantage of the Rietveld method, in contrast to previously applied reflection profile fitting procedures, is the use of individual intensity data points of the diffractogram instead of the integrated intensity of the reflections. This method was introduced by the physicist Hugo M. Rietveld to refine structures recorded by neutron diffraction[85] and was later extended for X-ray diffraction patterns. Since then it has become a major tool in structure determination.

In order to evaluate the diffraction pattern, the intensities of a mathematical model y_{ic} of the investigated structure are compared to the intensities y_{io} of the experimental diffraction data at the *i*th step (data point). By refining the initial structure model, the calculated pattern y_{ic} is fitted to the observed pattern y_{io}, by minimizing the quantity S in a least-squares procedure:

$$S = \sum_{i}^{N} w_i |y_{io} - y_{ic}|^2 \tag{3.18}$$

where w_i is a weighting factor assigned to each data point.[84,86]

The calculated intensity y_{ic} is described as the sum of various contributions plus the background intensity y_{ib}:

$$y_{ic} = s \sum_{k} m_k L_k |F_k|^2 G(\Delta\theta_{ik}) + y_{ib} \tag{3.19}$$

where s is the scale factor, m is the multiplicity factor for the Bragg reflection k, L is the Lorentz-polarization factor, F is the structure factor that describes the reflection intensity dependent on scattering ability and position of a given atomic species, $\Delta\theta_{ik} = 2\theta_i - 2\theta_k$ is the calculated position of the Bragg reflection at $2\theta_k$ corrected for the zero-point shift of the detector, and $G(\Delta\theta_{ik})$ is the reflection profile function.[84,86]

When the method is applied, many parameters are refined, such as lattice constants (affecting the position of each reflection), atomic positions, occupancy and the thermal factor (affecting the reflections intensities) as well as the profile functions G and y_{ib}. Since the Rietveld method is designed to *refine* a structure and not to *solve* it, the 'input' structure needs to be a close approximation of the final structure in order to properly index the Bragg reflections of the pattern.

For refinement of the diffractogram, many software packages have been developed over the years, *e.g.*, STOE's WinX^{POW}, Topas (commercial) or Jana2006 and GSAS-II (freely available). In this work, the diffraction data were either analysed by the commercial software High Score plus[87] or by the freely available FullProf suite, written by J. Rodríguez-Carvajal.[88,89] In all used programs the quality of the refinement can be easily assessed by visually evaluating the difference plot between measured and calculated intensities, however, it is also important to describe the quality numerically by so-called *R*-values.[90] *R*-values are fundamental to follow the effect of small changes in the structural model (*i.e.*, improved or deteriorated models), but one has to be careful not to overestimate such small changes when comparing different samples or measurement setups.

(c) Experimental setup for ex situ or in situ XRD analysis

Battery materials are polycrystalline and thus, powder diffractometry is the first method of choice. With our laboratory diffractometer (Stadi P, STOE & Cie GmbH, Germany)

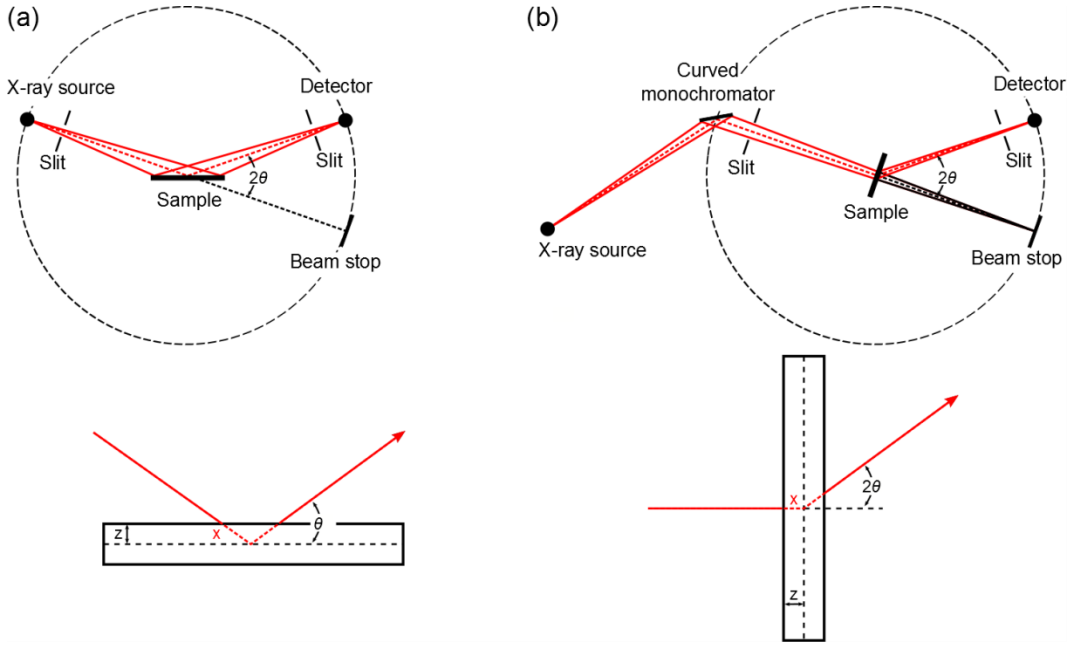

Figure 3.12: Geometry of focusing diffractometers used in our laboratory. (a) Reflection/Bragg-Brentano geometry and according beam path through the planar sample. (b) Transmission/Debye-Scherrer geometry with curved monochromator and according beam path through the flat sample. The dotted-circle centered on the sample position represents the goniometer circle. Upper figures were adapted from the user's manual STOE transmission diffractometer system Stadi P incl. Bragg-Brentano diffractometer system.

two different configurations were accessible to perform the diffraction experiments, namely: *Transmission/Debye-Scherrer* or *reflection/Bragg-Brentano* geometry. The Debye-Scherrer mode is used for cylindrical samples (capillaries) with a very small sample quantity. Therefore, it is only suitable for measuring the active material powder directly, *e.g.*, material scraped off from battery electrodes. In contrast, the transmission or Bragg-Brentano mode is applied to thin films or planar samples and thus is appropriate for electrodes or even entire battery cells, with the advantage of reducing errors in sample preparation or even completely removing them.

Ex situ XRD measurements on as-prepared electrodes and electrodes disassembled from battery cells were conducted in transmission mode (Figure 3.12b). To prevent any undesired reaction of electrodes at high state of charge with moisture, an air tight flat sample holder, developed by our group, was used.[91,92] This sample holder consists of a stainless steel body, two aluminum foils and a PTFE sealing. Since aluminum already exists as current collector in the cathode samples, no additional reflections were introduced by the sample holder. Electrode samples (< Ø 11 mm) were prepared in an Ar-filled glove box.

For *in situ* XRD analysis on operating battery cells, both reflection and transmission geometry can be utilized. However, one has to be aware of their particular benefits and limitations. The relative diffraction intensity depends on the total path length travelled by

the incident and diffracted X-rays as illustrated in the lower panel of Figure 3.12a and b. This can be described by the exponential attenuation:

$$\frac{I}{I_0} = \mathrm{e}^{-\mu'\rho x} \tag{3.20}$$

where I is the emerging beam intensity after passing through a thickness x of material, I_0 is the incident beam intensity, μ' is the mass attenuation coefficient ($\mu' = \mu/\rho$), in which the linear attenuation coefficient μ depends on the material and energy of the incident X-ray photons, and ρ is the density for the specific material.

In *reflection mode* the attenuation depth z_{att}, at which the diffraction signal is attenuated by a factor e^{-1}, can be calculated from the angle dependent path length x:

$$x = 2z_{att}/\sin\theta \tag{3.21}$$

$$z_{att} = \frac{1}{2\mu'\rho}\sin\theta \tag{3.22}$$

These equations also show that the probed area within a certain 2θ range depends on the absorption characteristics of the material as well as the energy of the X-ray source (included in tabulated values for μ' or μ [93]), which consequently restricts the cell design for reflection geometry. By using the current collector of the electrode as a window for the X-ray beam, only cathode materials with an aluminum current collector are accessible in Bragg-Brentano configuration due to the good X-ray transmission characteristics of thin aluminum foils. *E.g.*, at 17.5 keV (Mo source, $\mu_{Al} = 13.70\ cm^{-1}$) the penetration depth z_{att} equals 32 µm at $2\theta = 10°$, which is certainly sufficient for analysis when compared to a foil thickness of 18 µm. The copper current collector, however, cannot be penetrated by X-rays in reflection mode. At 17.5 keV ($\mu_{Cu} = 435.81\ cm^{-1}$) and $2\theta = 10°$, it merely shows a penetration depth of 1 µm compared to a foil thickness of 10 µm. This consequently prevents the analysis of anode materials (cf. Table 3.1 for calculations on different diffraction angles). The primary advantage of this setup, however, lies in the simplicity of the diffractogram, showing only reflections from the investigated electrode without any interference from the underlying separator or the counter electrode.

Table 3.1: Penetration depth z in µm of the X-ray beam in reflection mode for the applied current collector materials aluminium and copper at various incident angles. The corresponding linear absorption coefficient at an energy of ≈17.5 keV (Mo-Kα radiation) is $\mu_{Al} = 13.39\ cm^{-1}$ and $\mu_{Cu} = 438.62\ cm^{-1}$.[93–95]

Incident angle ϑ [°]	2ϑ [°]	z_{Al} [µm]	z_{Cu} [µm]
5	10	33	1
15	30	97	3
25	50	158	5
Foil thickness		18	10

In *transmission geometry* the path length of the X-ray beam is independent of *z*, so the spectra are completely normalized over the bulk of the electrode. Yet, the beam has to travel through both electrodes, separator, electrolyte, and the cell housing, leading to the necessity of highly penetrating X-rays from a Mo source for this type of experiments. Since the beam enters all cell components normal to the sample surface ($\theta = 90°$), anode materials on thin copper current collectors, which show in this configuration a penetration depth of 23 µm ($x = 2z_{att}$), were also accessible and could be measured simultaneously with the cathode. The resulting diffractogram therefore becomes rather complex.

Due to the complementary information, both types of diffraction geometries were employed in this thesis. The experiments were conducted on a two-circle goniometer, in which both transmission and reflection mode could be used independently while sharing one Mo source (Kα_1, λ_1 = 0.70930 Å, Kα_2, λ_2 = 0.71354 Å, 50kV, 40 mA). A focusing monochromator Ge(1 1 1) is used at the transmission side, while no monochromator is chosen at the reflection side in order to maintain high beam intensity. Both setups are equipped with a DECTRIS Mythen 1K one-dimensional silicon strip detector. Diffraction data were collected with the STOE powder diffraction software package WinX^{POW} (STOE & Cie GmbH, Darmstadt, Germany).

3.4.3 Neutron-induced prompt gamma activation analysis (PGAA)

(a) Theory and basic principles

Neutron-induced prompt gamma activation analysis (PGAA) is a nuclear-analytical technique for non-destructive determination of elemental and isotopic compositions. The sample is activated in a neutron beam and the emitted prompt γ-rays from the radiative capture are detected. This multi-elemental technique is used for the detection of a broad range of elements simultaneously and is independent of the shape of the sample due to the highly penetrating nature of both neutrons and γ-rays. Apart from bulk solid samples, also liquids and gaseous samples can be measured in special containers. Therefore, it has been

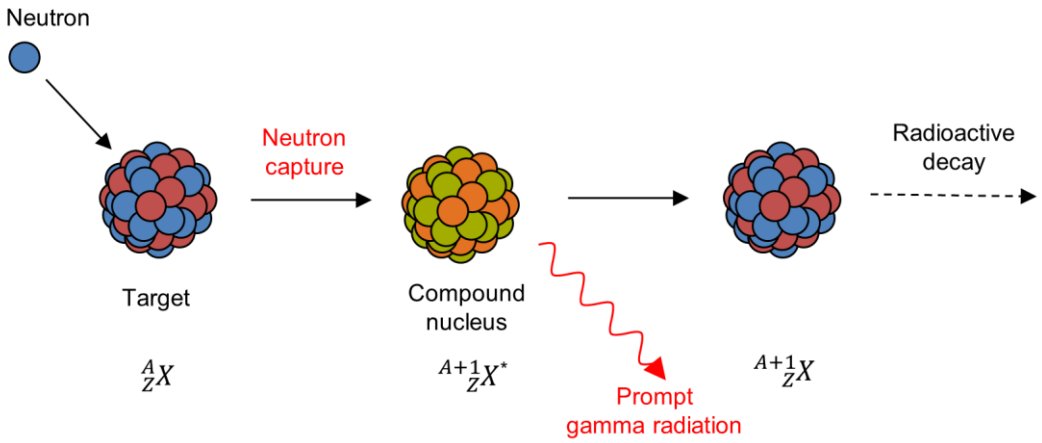

Figure 3.13: Scheme of the basic reaction in prompt gamma activation analysis after neutron capture.

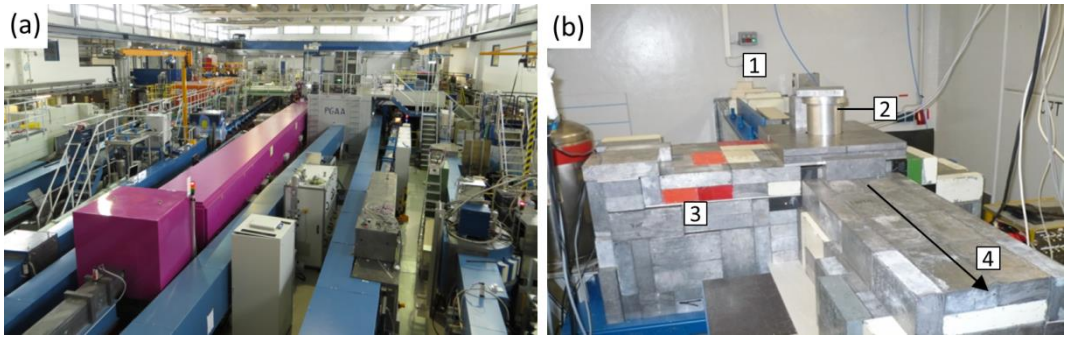

Figure 3.14: Photos of the experimental set-up at the FRM II. (a) Neutron guide hall with the PGAA facility. (b) Instrument PGAA with shielding from the direction of the beam stop: (1) guide chamber, (2) central chamber with access to sample chamber, (3) detector chamber and (4) beam-stop chamber.

applied in a broad range of research, *e.g.*, material science, archaeology, geology, environmental research, food analysis, research of semiconductors and superconductors, medicine and fundamental research.[96] Elements can be quantitatively determined down to the ppm range but the specific detection limit of each element is dependent on the sample matrix. The advantage of PGAA in contrast to conventional delayed gamma neutron activation analysis (NAA) or X-ray fluorescence methods (XRF) is its suitability for light elements like hydrogen, boron, lithium or sulphur. In addition, it represents a rapid method as irradiation and detection proceeds simultaneously.[97]

The neutron capture is a basic nuclear reaction, in which in principle every isotope is involved except ^{4}He. Preferentially, low energy, cold neutrons are used for PGAA measurements, since the neutron capture cross section increases with decreasing energy. Whenever a target nucleus (^A_ZX) captures a neutron (^1_0n), a compound nucleus ($^{A+1}_ZX*$) is formed. After typically 10^{-12}-10^{-09} s the nucleus reaches its ground state ($^{A+1}_ZX$) by emitting specific γ-rays (see Figure 3.13). With the γ-radiation a qualitative and quantitative analysis is possible, since the energy of the γ-rays is specific for an element or isotope and their intensities are proportional to the amount of atoms. About 25 peaks per element are appropriate to allow a distinctive and unambiguous identification with high precision.[98]

If the ground state is not stable, radioactive decay by emission of β-rays is the most prominent reaction. This is commonly followed by further emission of γ –radiation, which can also be used for chemical analysis and is applied in delayed gamma NAA.

(b) Experimental setup

PGAA was performed at the Forschungsneutronenquelle Heinz Maier-Leibnitz (FRM II) in Garching, Germany.[99–101] The corresponding instrument scientists are Dr. P. Kudejova and Dr. Z. Revay. A picture of the PGAA facility inside the neutron guide hall is shown in Figure 3.14a, whereas in b the PGAA instrument is illustrated. The instrument is located approximately 51 m from the reactor core at the end of a curved neutron guide. Cold neutrons with an average energy of 1.83 meV (6.7 Å) are provided by the neutron source

(liquid deuterium at 25 K) and are guided to the target. Depending on the size of the sample, two measuring conditions with varying beam size are provided, while the neutron flux can be tuned by a set of attenuators from $1 \cdot 10^9$ neutrons/cm^{2}s to $6 \cdot 10^{10}$ neutron/cm^{2}s (thermal equivalent = equivalent to a defined thermal neutron flux with 25 meV energy), which is the highest reported beam flux.[100,101] The instrument consists of four units as depicted in Figure 3.14b: the guide chamber (1), the central chamber containing the sample (2), the detector chamber perpendicular to the beam direction (3), and the beam-stop chamber (4). Each unit is shielded with lead to attenuate γ-radiation, while boron- and ^{6}Li-containing shielding material (*e.g.*, B_4C, ^{6}LiF-loaded polymer) is used to stop cold neutrons. Measurements are usually conducted at a low vacuum (0.2 mbar) to remove ambient air in order to reduce interfering signals from nitrogen in the spectrum. For the detection of γ-rays a high-purity germanium (HPGe) detector is applied, which is cooled by liquid nitrogen to 77 K to eliminate the formation of electron-hole pairs by thermal excitation.

(c) Sample and data treatment

For PGAA, a vertical sample holder with six positions allows the automated measurement of six samples in a batch. Electrode samples are fixed in a grid of polymeric fibers of 0.3 mm thickness, which are attached to the sample holder frame as shown in Figure 3.15a to c. The frame as well as the fiber consists of fluorinated ethylene propylene (FEP), a copolymer of tetrafluoroethylene and hexafluoropropylene, which provides a low background signal in the measurement due to its very low neutron capture cross sec-

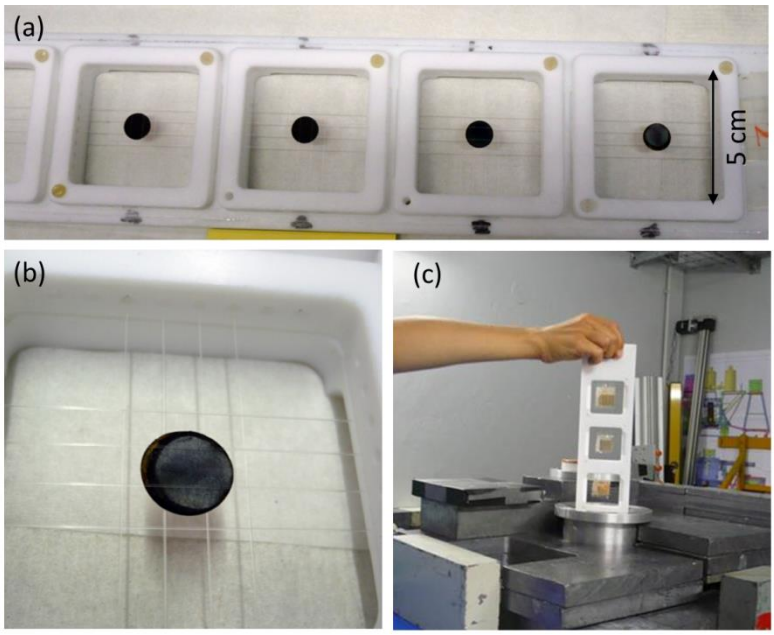

Figure 3.15: Photos of the PGAA sample holder with attached electrode samples. The vertical sample holder allows the automated measurement of six samples in a batch. Figures were provided by Petra Kudejova.

tion. According to the size of the frame of 50 x 50 mm^2 (Figure 3.15a) the sample dimensions are restricted to 40 x 40 x 40 mm^3, so that the complete neutron beam is always bigger in size than the sample. This set-up enables sample weights ranging from 0.1 mg to 10 g.[101,102]

The qualitative elemental identification is based on a comparison of the sample spectrum with the γ-ray database. For this purpose, energies of the most intense prompt γ-peaks are chosen.[103] A common source of background comprises nitrogen in the air, which is drastically reduced by applying vacuum, and carbon/fluorine from the FEP sample holder. The quantification of the elements is done on an average of selected γ-peaks according to following formula:

$$A = \frac{m}{M} N_A \sigma_\gamma \phi \varepsilon t \tag{3.23}$$

where A is the net peak area, m is the mass of the emitting nuclide, M is its atomic weight, N_A is the Avogadro number, σ_γ is the partial γ-ray production cross section, ϕ is the thermal equivalent neutron flux, ε is the counting efficiency, and t is the measurements time (live time).[103] The evaluation is conducted on relative peak intensities, in which the mass ratios are calculated from ratios of the peak areas, while at the same time systematic errors can be avoided:

$$\frac{m_1}{m_2} = \frac{A_1}{A_2} \frac{\varepsilon(E_2)}{\varepsilon(E_1)} \frac{\sigma_{\gamma,1}}{\sigma_{\gamma,2}} \frac{M_1}{M_2} \tag{3.24}$$

Numbers in indices refer to two different chemical elements, whereas one is represented by copper. Copper is used as an internal standard for mass determination, since it is included as current collector foil in the investigated electrode. The mass of copper is known to a precision of 0.02 mg.

(d) Validation

The validation of PGAA for the analysis of graphite electrodes is demonstrated on samples spiked with little amounts of transition metal ions. For this purpose, a standard graphite slurry consisting of graphite, 95 wt%, and PVdF, 5 wt%, was prepared by adding a predefined amount of $LiNi_{1/3}Mn_{1/3}Co_{1/3}O_2$ (NMC) powder with each transition metal equates to a concentration of either 500 or 5000 ppm with respect to copper. The respective slurries were cast onto a thin cupper foil and after drying at 50°C in a drying oven, electrodes of 11 mm diameter were punched. Pure copper current collectors (Ø=11 mm) had a mass of 8.514 ±0.016 mg. The aim of the validation process is to recover the amount of transition metals with PGAA. In this way background problems and peak overlap can be explored in order to select suitable peaks for the quantitative analysis of transition metal deposition on aged graphite electrodes (cf. Chapter 4.5). In Figure 3.16 the amount of transition metals $x_{(\text{weighed sample})}$ ("Standard"), based on a calculated value on

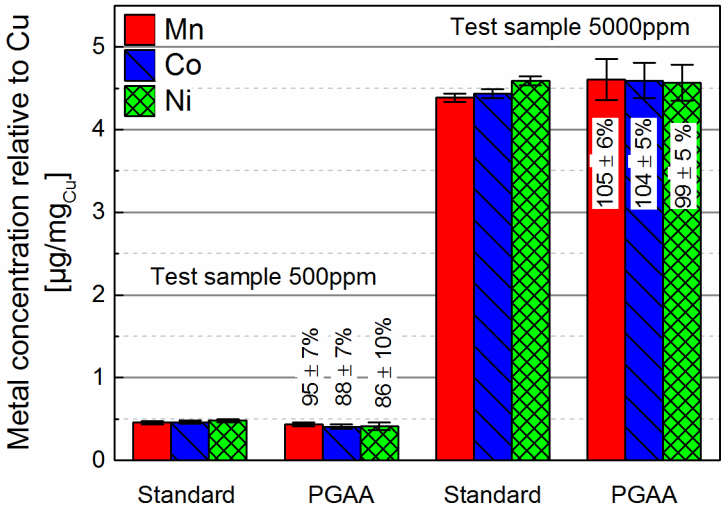

Figure 3.16: Validation of PGAA for elemental analysis on graphite electrodes loaded with either 500 ppm or 5000 ppm transition metals relative to copper. Numbers in percent indicate the recovery rate of PGAA compared to the weighed samples referred to as "Standard". The standard consists of graphite electrodes mixed with defined amounts of NMC powder.

weighed graphite electrodes, is compared to the amount measured by "PGAA" $x_{(PGAA)}$. The determined recovery rate ($r = x_{(PGAA)}/x_{(weighed\ sample)}$) is excellent over the wide transition metal concentration range and equals almost 100% within the error range. While samples with low concentrations are slightly underestimated, high concentrations can be determined with good precision.

The analysis was conducted in cooperation with researchers from the Forschungsneutronenquelle Heinz Maier-Leibnitz (FRM II): Dr. Petra Kudejova (experiment and fitting of spectra) and Dr. Stefan Seidlmayer (data analysis). Measurements were performed within the assigned beam-time according to the rapid access proposal 9123 submitted on the 19th of December 2013.

3.4.4 Positron annihilation spectroscopy (PAS)

(a) Theory and basic principles

Positron annihilation spectroscopy (PAS) is a non-destructive characterization method for probing the local electron density and in particular defects in solids due to the electrostatic interaction of positrons with their environment. The method relies on the propensity of positrons to get localized at open-volume regions of a solid and the emission of annihilation γ-rays.[104] When positrons are implanted into condensed matter (cf. Figure 3.17a), they rapidly lose kinetic energy by interaction with the material. With decreasing energy, positrons participate in several ionization processes, e^--hole excitations, and phonon scattering until they reach thermal equilibrium with the medium. After thermalization, positrons diffuse over many lattice spacings in the order of 100 nm before they annihilate

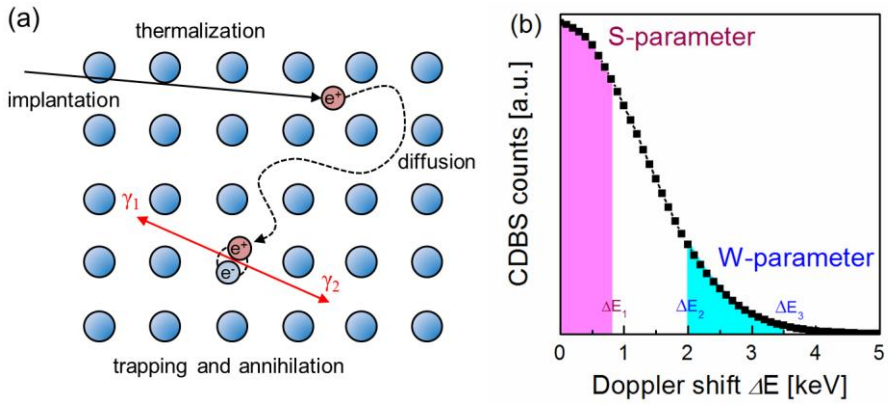

Figure 3.17: (a) Principle of positron annihilation spectroscopy. (b) Evaluation of a CDB spectrum at the 511 keV annihilation line (="0"), which is symmetrically around the center. The observed line shapes are usually characterized by integral parameters: The *S*-parameter is defined as the ratio of counts in the central part to the total area of the annihilation line and reflects mainly interactions of positrons with low momentum electrons. The *W*-parameter is defined as the ratio of counts in the wing region to the total area of the annihilation line and reflects mainly interactions of positrons with high momentum electrons.

with electrons. During diffusion, the positron can get trapped in an open-volume defect such as monovacancies, vacancy clusters or dislocations, *etc*. The transferred information of these interactions is investigated by the detection of the respective annihilation radiation.[105]

PAS measurements for defect characterization utilize several observables: (i) positron life time, (ii) Doppler broadening, and (iii) angular correlation of annihilation radiation. The positron annihilation life time spectroscopy (PALS) is sensitive to the electron density at the annihilation site. It is capable of distinguishing different kinds of vacancies (size and type) but provide no direct information on chemical surrounding. With coincident Doppler broadening spectroscopy (CDBS) the momentum distribution of positron-electron annihilation radiation is investigated. This allows both the detection of open-volume defects and their chemical composition. Angular correlation of annihilation radiation (ACAR) is based essentially on the same measurement principle as CDBS. While the resolution of this technique is superior to CDBS, the count rates are much lower.[106]

In Doppler broadening spectroscopy (DBS) the positron annihilation line shape is analyzed, which directly reflects the momentum distribution of electron-positron pairs. The momentum itself is expressed by the amount of Doppler shift ΔE of the emitted γ-rays. Since during annihilation two γ-quanta are emitted with an energy of 511 keV in the center of mass system of the annihilating pair, the energy of one γ-ray can be upshifted while the other is downshifted from the center of energy:

$$E_{1,2} = m_e c^2 \pm \Delta E \tag{3.25}$$

where $E_{1,2}$ is the energy of the two γ-rays, m_e is the electron mass, c is the velocity of light, and $\Delta E = p_L c/2$ is the Doppler shift including the longitudinal momentum component of the electron-positron pair p_L in the direction of the emitted γ-rays.[104] For

quantitative evaluation, the line shape parameters *S* and *W*, where parts of the annihilation peak are integrated, are used to characterize the 511 keV annihilation line. This is shown in Figure 3.17b and represented by following equations:

$$S = \int_{-\Delta E_1}^{\Delta E_1} I(\Delta E)dE \; / \int_{-\infty}^{+\infty} I(\Delta E)dE \tag{3.26}$$

$$W = \left(\int_{\Delta E_2}^{\Delta E_3} I(\Delta E)dE + \int_{-\Delta E_2}^{-\Delta E_3} I(\Delta E)dE \right) / \int_{-\infty}^{+\infty} I(\Delta E)dE \tag{3.27}$$

where *I* is the intensity (CDBS counts) of the annihilation radiation.

The *S*-parameter in the central region mainly corresponds to interactions with low momentum valence e^- which reflects the annihilation in open-volume defects. The *W*-parameter in the wing-region is sensitive on the annihilation with high momentum core e^- and thus includes information about the chemical surrounding. The analysis of the rare events in the wing-region is significantly improved by a two-detector system which detects both annihilation photons and selects only coincident events while the sum of both annihilation quanta energies must be 1022 keV. Thus, random background counts are eliminated and the peak-to-background ratio is improved.[105,106]

(b) Experimental setup

CDBS was performed at the neutron-induced positron source Munich (NEPOMUC) at the Forschungsneutronenquelle Heinz Maier-Leibnitz (FRM II) in Garching, Germany.[108,109] Corresponding instrument scientists are Dr. C. Hugenschmidt and Dr. C. Piochacz. A pic-

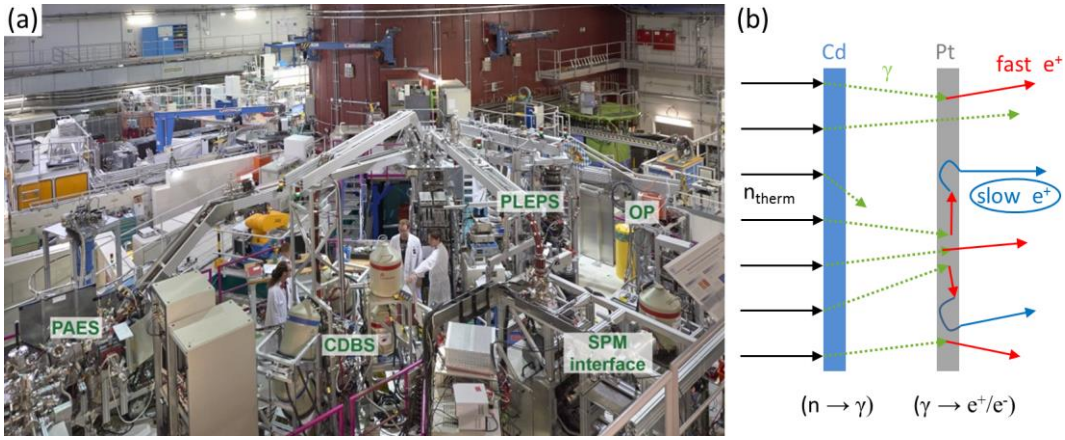

Figure 3.18: (a) Photo of the positron beam facility and instrumentation at NEPOMUC (FRM II): PAES (positron-induced Auger-electron spectrometer), CDBS (coincident Doppler broadening spectrometer), PLEPS (pulsed low-energy positron system), SPM interface (scanning positron microscope), and OP (multi-purpose open beam port).[107] (b) Principle of neutron-induced positron formation at NEPOMUC.[108]

ture of the positron beam facility is shown in Figure 3.18a, which gives an overview of the instrumentation at NEPOMUC. NEPOMUC provides a high-intensity low-energy positron beam with $>10^9$ moderated positrons per second at a beam energy of 1 keV. The positrons are generated by pair production from absorption of high-energy prompt γ-rays after thermal neutron capture in Cd (see Figure 3.18b). First, high-energy γ-rays are produced by the neutron-capture reaction of ^{113}Cd in a cadmium cap of the in-pile positron source (^{113}Cd(n,γ)^{114}Cd). A structure of Pt foils mounted inside the cadmium cap converts the released γ-radiation into positron-electron pairs. Pt is also applied as positron moderator, which leads to the emission of mono-energetic positrons directly into ultra-high vacuum. Positive high voltage is needed in order to extract the moderated positrons and a magnetic guide field of typically 7 mT transports the positrons into a remoderator outside the biological shield of the reactor. Finally, the positron beam passes a magnetic beam switch to the corresponding positron experiments.[108–110]

Like the beamline, the sample chamber of the CDB spectrometer applies ultra-high vacuum (UHV) to prevent the interaction of positrons with residual gas before they reach the sample. Several electrical lenses focus the positron beam with an adjustable size between 0.3 and 3 mm onto the target. The sample holder itself is connected to a negative voltage power supply, which defines the positron implantation energy between 0.2 and 30 keV. Thus, a mean positron implantation depth up to several µm can be achieved. For the detection of γ-rays, a high-purity germanium (HPGe) detector is applied, which is cooled by liquid nitrogen to 77 K to eliminate the formation of electron-hole pairs by thermal excitation. The energy resolution is 1.4 keV at 511 keV.[111]

(c) Sample and data treatment

For CDBS, an aluminum sample holder equipped with a titanium fixture and a size of 20x25 mm is used. The beam size is in the order of several mm as no space-resolution is required, which would extend measurement time. Each sample must therefore be greater than 5x5 mm to get completely irradiated by the positron beam and to prevent any inter-

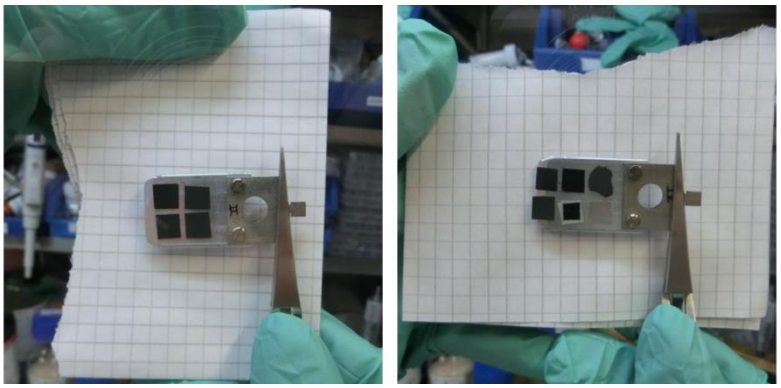

Figure 3.19: Photos of the PAS sample holder with attached samples for CDBS measurement. Up to six samples with a minimum size of 5 x 5 mm^2 and a distance of 1 mm between each sample can be accommodated on the aluminum sample holder with titanium fixture.

action of positrons with the support during data acquisition. Due to measurement requirements, the maximum number of samples is restricted to six samples per sample holder. The distance between each sample must be at least 1 mm, so that each sample position can be exactly determined by a quick line scan in *x*- and *y*-direction. This is based on a distinct signal change between sample and aluminum support, which gives the *x*-*y*-coordinates for sample access. The sample arrangement is shown in Figure 3.19. The additional distance between the edge of the aluminum support and the sample is necessary to accommodate a guide rail on the long side of the support. Samples must be properly dried before entering the UHV of the CDB spectrometer. Adhesion and electronic conductivity to the support is achieved by a carbon tape, which has to be smaller in size than the sample.

Emitted γ-rays are detected in coincidence by two collinear HPG-detectors. These events are summed up in a two-dimensional plot, where the axes represent the energy scale of each detector. The projection of the annihilation line from the two dimensional plots is then performed for data analysis.

The measurement and analysis was conducted in cooperation with researchers from the Forschungsneutronenquelle Heinz Maier-Leibnitz (FRM II): Thomas Gigl (experiment and data analysis), Dr. Markus Reiner (experiment and data analysis), Dr. Stefan Seidlmayer (experiment and data analysis), and PD Dr. Christoph Hugenschmidt (experiment and data discussion). Measurements were performed within the assigned beam-time according to proposal 10428 submitted on the 16th of January 2015.

4 Results and Discussion

4.1 *In situ* XRD on lithium-ion cells

4.1.1 State of the art

Driven by the need for high-performance lithium-ion batteries for portable electronics and electric vehicles, much work within battery materials research today focuses on developing and improving the understanding of new electrode materials. In this context, *in situ* XRD studies on electrochemical cells have proven to be a powerful tool for investigating lithium-ion insertion processes in electrode materials. In contrast to *ex situ* and *post mortem* investigations, *in situ* XRD has the ability to monitor structural changes in the electrode material directly in the cell under investigation at certain steps of the lithiation and delithiation process. Combined with the electrochemical measurement, valuable information about the relationship between structure and electrochemical properties can be obtained. In order to investigate the reversibility of the intercalation process of the electrode material or its structural capability for long-term cycling in a battery, various *in situ* XRD measurement techniques have been realized over the last decades, specific to different instruments and problems.

The first publication on *in situ* XRD observations of an insertion electrode material was released in 1978 by Chianelli *et al.*[112] The cell was used in a conventional X-ray powder diffractometer in Bragg-Brentano geometry (reflection-mode) and consists of a rigid cell body with a sealed beryllium window, which enables X-ray diffraction from the backside of the positive electrode to be measured. In the subsequent years variations of such reflection-mode cells have emerged to study battery materials.[113–120] Later designs also included modifications of conventional coin cells[121,122] or replacement of the beryllium window.[32,33,123–125]

In 1992, Gustafsson *et al.* reported the first XRD study of a battery at preset voltage limits in transmission geometry.[126] The electrochemical cell, commonly described as a *coffee-bag cell* or *pouch cell*, consists of a stack of thin electrode layers and a polymeric electrolyte enclosed in a polymer-coated aluminum foil. With the invention of a similarly constructed cell based on *Bellcore* plastic lithium-ion technology (PLiON™),[127] *in situ* measurements at the synchrotron have become extremely popular and were not merely restricted to pouch bag designs.[128–141]

Most of the designs described in the literature were constructed either for implementation at a laboratory diffractometer in reflection mode or for implementation at the synchrotron in transmission mode. Some exotic designs also involve the use of a micro-battery incorporated in a capillary commonly used for powder XRD.[142] In the last years, this topic has attracted so much interest, that even commercial solutions for laboratory *in situ* XRD cells have been provided by different companies.[143–146]

4.1.2 Design requirements of an electrochemical *in situ* XRD cell

Although X-ray synchrotron radiation presents some major advantages over the conventional laboratory sources (*e.g.*, high intensity X-ray beam, tunable wavelength, and fast acquisition times), the limited experimental beam time and its very high costs still makes the laboratory diffractometer an attractive system. Based on the large number of existing designs for *in situ* XRD on lithium-ion batteries, an electrochemical cell for reflection mode as well as a pouch cell for transmission mode, both suitable for our laboratory diffractometer, will be introduced. The planning and design of these cells must meet distinct criteria for both electrochemical and XRD characterization:

- The cell needs to be *airtight* to prevent any exposure of the cell components to water and air.
- The cell needs to fit into the *STOE diffractometer system* for Bragg-Brentano or transmission geometry.
- The cell should be *easy to assemble* in a glove-box environment.
- The cell body and the materials for sealing the cell need to be *resistant* to swelling or chemical attack from the organic electrolyte as well as stable against the lithium potential.
- For the cells in transmission mode, since the beam crosses the complete cell stack including cell housing, all inactive cell components need to be as *thin* as possible to reduce additional absorption of the X-ray beam.
- Both the cathode and the anode must be *electronically connected* by current collectors:
- In transmission mode, aluminum and copper foils can be used as current collectors for the cathode and anode, respectively; whereas copper demonstrates a higher absorption of X-rays.
- In reflection mode, the current collector acts also as a *conductive X-ray window*. For this purpose, only aluminum foil is suitable due to its low absorption characteristic regarding the angle dependent penetration depth of X-rays at this geometry. The analysis is therefore restricted to cathode materials (cf. Section 3.4.2 for details).

- The cell components need a *uniform compression* to keep the electrodes in place and to maintain a good electrochemical performance. A spring is used in the reflection mode, whereas the external atmospheric pressure is applied on a vacuum-sealed pouch cell in transmission mode.

For reflection mode, it was decided against the use of a beryllium window because it is not completely stable against corrosion at potentials higher than 4.2 V.[117] This would consequently prevent the investigation of novel high voltage materials. Additionally, beryllium is a very toxic and carcinogenic metal, which presents a serious health risk and thus has to be handled very carefully. Since it is a light element with very few electrons, it shows weak Bragg reflections in the diffraction pattern, in addition to beryllium oxide reflections.

In addition to continuously improving laboratory diffractometer systems, highly intense X-ray sources are also available on the market, which in the last decade especially benefited the analysis of single-layered pouch cells in transmission mode. In combination with the highly penetrating X-rays from a Mo source, measurements can be easily conducted with a laboratory setup to obtain a sufficient signal-to-noise ratio for data analysis.

All these requirements and conditions led finally to the development of three generations of electrochemical *in situ* XRD cells. The first design, adapted for Bragg-Brentano geometry, was replaced during the supervision of a master's thesis[147] by a more advanced *in situ* XRD cell design. This second version features a good performance while being easy to assemble, but within 200 cycles a higher capacity fade compared to laboratory Swagelok® T-cells is observed, which in the end prevents the investigation of long-term cycling experiments. Nevertheless, the *in situ* XRD cell was very useful to identify insertion mechanisms and to establish structural-electrochemical relationships, which will be demonstrated in the subsequent chapters. With the introduction of a single-layered pouch cell, a stable and comparable system is adjusted to transmission geometry and preliminary results obtained with this setup will be given at the end of this thesis.

4.2 Development of an *in situ* XRD cell for Bragg-Brentano geometry

4.2.1 Experimental setup

The Bragg-Brentano *in situ* XRD cell consist of several principal components: a rigid stainless-steel body, comprising bottom and top current-collector plates, an elongated hole in the top current-collector plate for X-ray reflection, two O-rings, an electrically insulating sealing unit, a spring, and a stainless-steel plate. An exploded illustration is given in Figure 4.1 for both developed cell versions. In the beginning, the development of the design is explained on the basis of version 1, which represents the origin of relevant improvements for version 2.

One of the most important parts of the cell is the design of the *X-ray window* to allow for reflection of the incident and outgoing X-rays. Due to the application of highly penetrating Mo X-rays (λ=0.7093 Å), diffraction occurs at much smaller angles compared to commonly used Cu sources (λ=1.5406 Å) with about twice the wavelength (cf. Equation 3.17 in Section 3.4.2). In order to measure, for example, the (0 0 3) reflection of NMC-111 at $2\theta_{Mo} \sim 8.6°$ ($2\theta_{Cu} \sim 19.0°$), the beam has to enter the sample at an angle smaller than $\theta \sim 4.3°$ relative to the surface. To ensure, however, proper stack pressure and stiffness, the opening of the top plate should be as small as possible. Therefore, a length of 17.5 mm has been chosen, which conveniently enables XRD measurements at angles greater than $2\theta_{Mo} \sim 6.8°$. The thickness of the top plate (500 µm) and the aluminum current collector (18 µm) is included in this calculation (see cross section in Figure 4.1). To further narrow the size of the window, but to sustain good alignment between beam and cell, the width of the window was adjusted to 8 mm, which easily accommodates a beam width of 4 mm. With this design, however, the cell cannot rotate in the sample holder of the diffractometer and preferred orientation might become an issue.

A thin aluminum foil (18 µm, MTI Corporation, USA) was selected as an *X-ray window*, which is used simultaneously as a current collector for the cathode material. This material demonstrates a good barrier against moisture (no permeation of H_2O, O_2, and N_2) and reasonable transmission of X-rays at low angles for reflection mode (cf. Equations 3.20 to 3.22 in Section 3.4.2). *E.g.*, with an 18 µm thick foil and an incident angle of $\theta \sim 4.3°$, a transmission of 50% of the incident beam intensity is achieved, which allows the detection of diffracted X-rays at the cathode surface at these small angles.

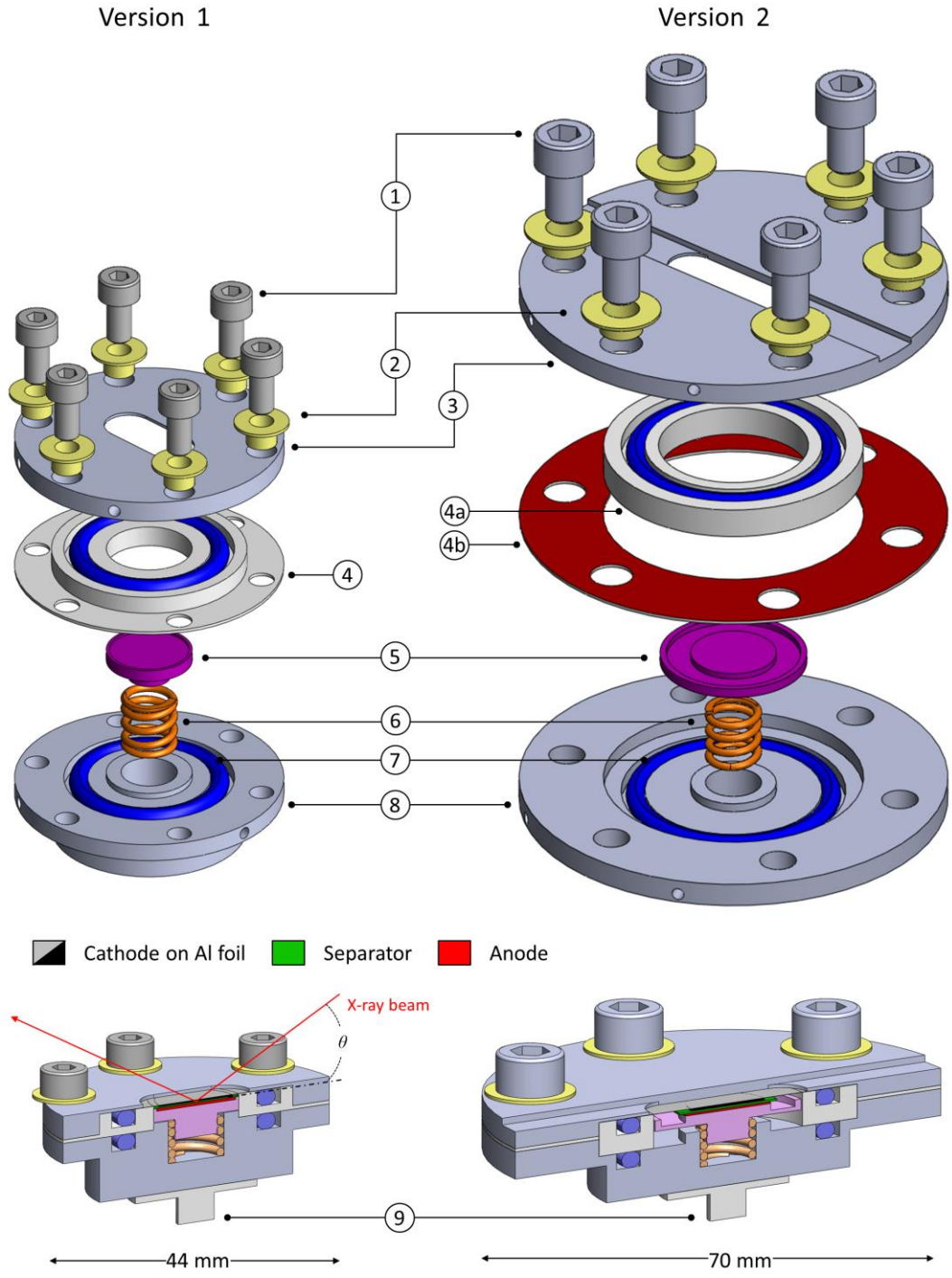

Figure 4.1: Exploded illustration and cross section of the first and second generation electrochemical *in situ* XRD cells with same scale: (1) Stainless-steel screws, (2) insulating polyethylene ferrules, (3) stainless-steel top positive current-collector plate with an elongated hole for X-ray reflection, (4) insulating PTFE sealing unit to electrically separate the top and bottom current collectors, and to incorporate the O-rings, (4a) PE sealing unit to incorporate the O-rings, (4b) insulating silicon rubber to electrically separate the top and bottom current collectors, (5) stainless-steel plate, (6) stainless-steel compression spring, (7) O-rings, (8) stainless-steel bottom negative current-collector plate, and (9) adapter to fix the cell to the Bragg-Brentano sample holder. The electrode stack comprises a cathode-coated aluminum foil facing the X-ray hole, glass-fiber separators, and a lithium metal or anode-coated cupper foil counter-electrode. Technical drawings of the *in* situ XRD cell are provided in the appendix.

The *sealing* of the aluminum window is accomplished with an O-ring, which is pressed against the aluminum foil and the top current-collector plate. For this purpose the inner diameter of the O-ring must be greater than the opening of the plate, and the diameter of the aluminum foil must be greater than the outer diameter of the O-ring. Thus, a 3 x 20 mm O-ring and a Ø 30 mm aluminum foil were chosen for this design. Since the O-ring is in direct contact with electrolyte due to its immediate proximity to the cathode and separator, a standard FKM O-ring (fluoroelastomer with carbon black fillers, Viton®) was avoided. It was found that FKM O-rings adsorb the electrolyte solvent and are prone to carbon oxidation at high potentials due to the high surface area of the carbon filler. Instead, an O-ring with an elastic FKM core and a protective FEP-shell (FEP-O-Seal, Angst+Pfister AG, Switzerland) was selected, but only for the upper sealing.

The *rigid cell body* and the anode plate are composed of stainless steel that provides excellent corrosion resistance against the electrolyte and potentials used. Therefore, the austenitic steel 1.4571, also known as 316Ti or X6CrNiMoTi17-12-2 is most suitable for this requirement as the addition of Mo and Ti stabilizes the alloy. The cell body, divided into top and bottom plates, also acts as a current collector for the electrodes. By inserting small drill holes at the side of the plates, a potentiostat can be directly connected via banana jacks to the negative and positive poles. To electronically insulate the top plate from the bottom plate, a polytetrafluoroethylene (PTFE) sealing unit with a cylindrical cavity for the integration of the cell stack and the anode plate is utilized as shown in Figure 4.1 component (4).

Before cell assembly, the cathode-coated aluminum window has to be prepared according to a *mask-coating procedure*. Since the standard preparation of battery electrodes via doctor-blade method delivers electrodes completely covered with active material, the

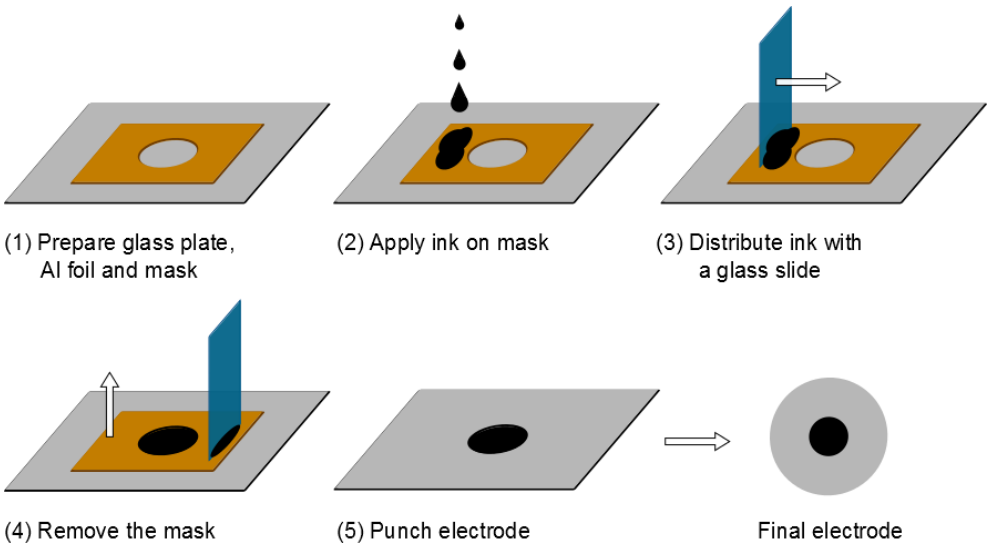

Figure 4.2: Schematic illustration of the mask-coating process to produce electrodes suitable for the *in situ* XRD cell in Bragg-Brentano configuration.

mask coating leaves some empty space at the edges of the aluminum foil. The active-material free edge-region is necessary because it is used to seal the cell via contact with the O-ring. However, one has to recognize that with this method the aluminum foil is much bigger in size than the active-material coating, which could introduce some errors in the calculation of the mass loading. The inks for the mask-coating procedure are prepared similarly to inks used for the doctor-blade technique (see Chapter 3.2) and must be of high viscosity to prevent creeping. The process of mask coating is illustrated in Figure 4.2 and can be divided up into five steps: (1) Preparation of a cleaned glass plate as support for the aluminum foil and a punched mask with a hole the size of the final electrode coating (Ø 12 mm). The mask consists of a PTFE coated glass fabric (Fiberflon GmbH & Co. KG, Germany), which is available in various thicknesses to adjust the desired mass loading of the coating. Additionally, this material features a superior non-stick surface, which is easy to clean. In a first step, the aluminum foil is smoothed with ethanol and a lint-free tissue onto the glass plate; then the mask is put on top of it and fixed with tape. Next, (2) the viscous ink is applied and (3) uniformly distributed with a glass slide. Then, the mask is removed (4). After drying the coating at 50°C for at least 1 h, (5) electrodes with the coating centered on the aluminum disc are punched. Prior to cell assembly the electrodes are dried under dynamic vacuum at 120°C in a Büchi oven for at least 3 h.

All *in situ* XRD cell components are assembled in an argon filled glovebox. Beginning with the top current-collector plate, the cathode is centered on the X-ray opening of the plate with the coating facing upwards, followed by the PTFE sealing unit already equipped with the FEP sealing O-ring. The cavity of the PTFE sealing unit facilitates the stacking of two glass fiber separators (Ø 14 mm, 250 µm thickness) and the lithium-loaded anode plate, all centered on top of the cathode coating. Before placing the anode plate, ≈100 µl of electrolyte are added, which can easily be taken up by the soft separators. The use of Celgard separators is not recommended here as they show poor

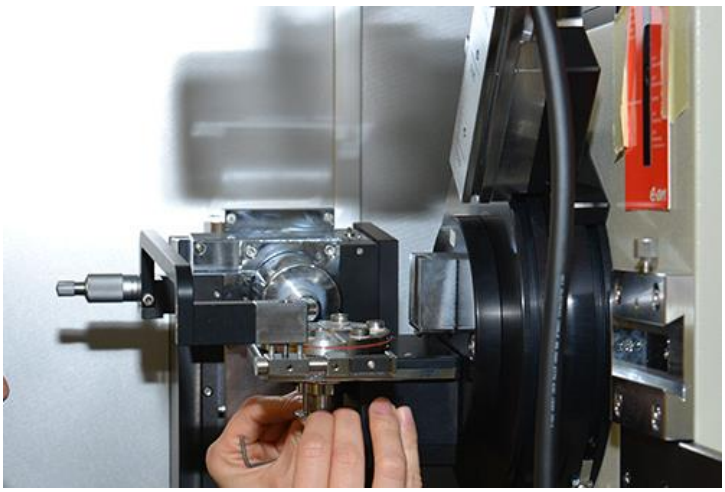

Figure 4.3: Photo of the *in situ* XRD cell mounted on the sample holder of the Bragg-Brentano diffractometer system. The cell must be properly aligned in height (1) and according to the beam direction (2).

compressibility and therefore cannot guarantee a homogeneous pressure distribution across the cell stack. Before closing the cell with the bottom current collector plate, a compression spring (LC 032E0S316, 3.71 N/mm, Lee Spring GmbH, Germany) and the remaining FKM O-ring are added. The assembled cell is then transferred from the glovebox to the Bragg-Brentano diffractometer system and mounted via the adapter onto the sample holder (see Figure 4.3), with the X-ray window aligned along the beam direction. The height of the cell is adjusted by taking the aluminum foil as a reference and measuring the correct position of the (0 2 2) reflection ($2\theta = 28.7°$). Detailed technical drawings of the electrochemical *in situ* XRD cell are provided in the appendix.

4.2.2 Performance and benchmarking of the *in situ* XRD cell version 1

To demonstrate the functionality of the described cell, performance and benchmarking tests were first conducted on the Li-$LiNi_{1/3}Mn_{1/3}Co_{1/3}O_2$ (Li-NMC) system. For this purpose, an *in situ* XRD cell was built, which contained a cathode with 96 wt% NMC, 2 wt% PVdF binder and 2 wt% Super C65 conductive carbon (17.7 mg_{NMC}/cm^2, 2.65 mAh/cm^2). Two glass fiber separators (500 µm thickness each) soaked with 100 µl electrolyte (1 M $LiPF_6$ in a mixture of ethylene carbonate (EC) and ethyl-methyl carbonate (EMC), EC:EMC, 3:7 v:v, LP57, BASF) and a lithium metal anode (Ø13 mm, 450 µm thickness) were added. For comparison to laboratory test cells, the same cell components were adapted for the Swagelok® T-cell: cathode (Ø10 mm): 16.7 mg_{NMC}/cm^2, 2.51 mAh/cm^2, two glass fiber separators (Ø11 mm), lithium anode (Ø11 mm) and 80 µl electrolyte.

Before testing the electrochemical behavior of the cell, an XRD pattern was collected in the pristine state of the assembled cell. The result is shown in Figure 4.4. By comparing the observed reflection positions of the coated NMC to the standard capillary measurement of the pure NMC powder, a good agreement between both diffraction patterns can be recognized, whereas all additional reflections in the upper pattern can be assigned to the aluminum current collector (indicated with an asterisk in the graph). One obvious difference, however, is the strongly reduced beam intensity at very low diffraction angles ($2\theta < 10°$). One reason could be the low transmission of X-ray intensity through the aluminum foil due to the increased path length at these small angles. Therefore, the angle-dependent X-ray transmission for aluminum was calculated and illustrated in Figure 4.4 to show its impact on the pattern (cf. Equation 3.20 in Section 3.4.2). At $2\theta \approx 8.6°$, an intensity loss of 50% can be determined, which can explain the weak reflection to a certain extent. Another reason could be the closely confined opening of the window which might truncate the beam, especially at low angles, and thus reduce the measurable sample volume of the active material. Due to this observation, XRD analysis with this cell is only performed in a qualitative manner by analyzing the reflection position and assigning phases or by determining the unit cell parameters.

In addition to attaining XRD data with sufficiently high signal-to-noise ratio and acceptable 2θ range, a reliable electrochemical performance in good agreement with our standard laboratory test cells is necessary for the analysis of lithium-insertion mecha-

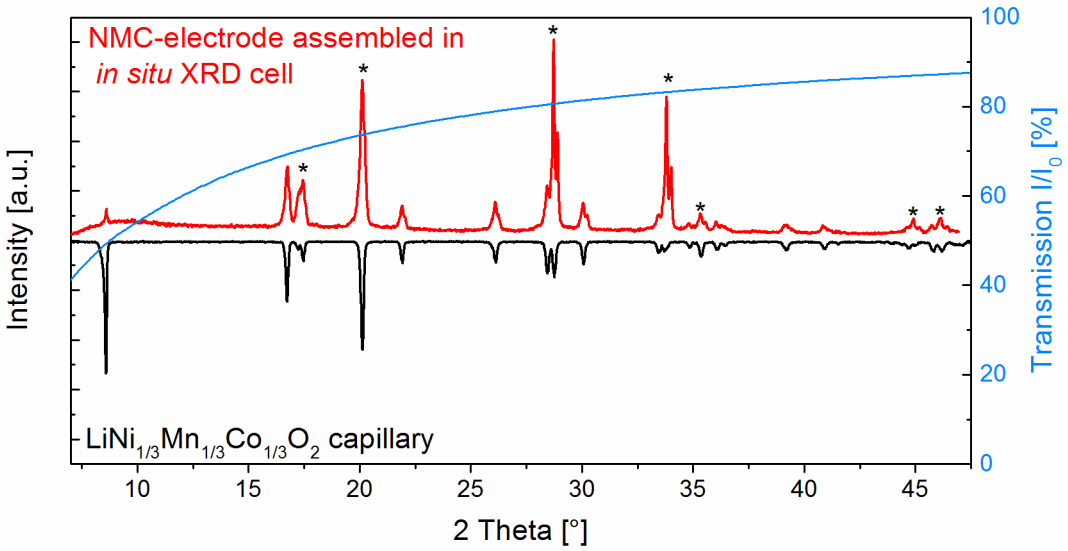

Figure 4.4: Comparison of the diffractogram of a capillary measurement of the pure NMC powder to the diffractogram of the NMC-electrode assembled in the *in situ* XRD cell (Version 1). The Li-NMC cell contains a cathode with 96 wt% NMC, 2 wt% PVdF binder and 2 wt% Super C65 conductive carbon, two glass fiber separators soaked with electrolyte (1 M $LiPF_6$ in EC:EMC, 3:7 v:v, LP57, BASF), and a lithium metal anode. The asterisk marks the position of the reflections from the aluminum window. Additionally, the transmission of the X-ray beam in reflection geometry for the 18 µm aluminum foil at 17.5 keV is given in dependence on 2θ (see Equation 3.20).

nisms or degradation studies. Only when these requirements are satisfied, a good correlation between structural and electrochemical properties can be assumed. In Figure 4.5a the rate and cycling performance of the *in situ* XRD cell is compared to the performance of a Swagelok T-cell assembled with an identical cell stack. In the rate capability test, both cells cycle similarly up to a rate of 0.2C, but at high C-rates a strong deviation in capacity retention occurs. The same behavior is also reflected in the discharge potential profiles in Figure 4.5b. Although care was taken to ensure a uniform pressure distribution in the *in situ* XRD cell, the opening in the top plate and thus the slight bending of the soft aluminum window may result in a lower local compression. The resulting inhomogeneous current distribution and locally increased ohmic resistance could therefore cause the deviation in rate performance at currents higher than 0.2C. This could also be an explanation for the reduced cycling performance at 0.5C that directly followed the rate capability test. Consistent with this assumption is also the fact that no severe leaks between the internal parts of the cell and the ambient air could be detected, which would result in a rapid capacity fade during the cycling of the cell. Thus it is concluded that the cell is properly designed and assembled, and that it can be reliably used within the first few cycles up to a rate of 0.2C.

Given the good performance of the *in situ* XRD cell within these constraints, first investigations were conducted on the Li-Li_2S and Si/C-Li_2S system that belongs to the next generation of lithium-ion batteries, namely lithium-sulfur batteries. The results of a measurement series on the first charge of a Li-Li_2Si cell served as a basis to explain the

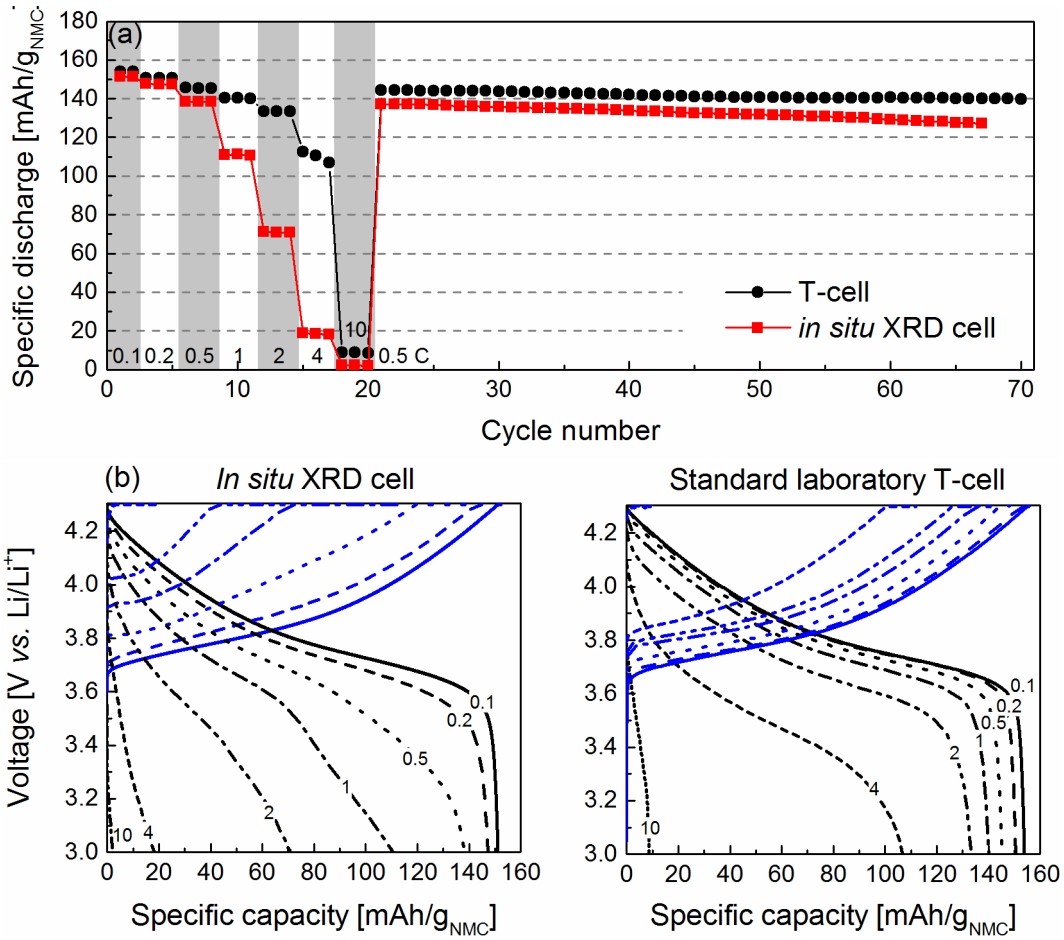

Figure 4.5: Electrochemical performance of the *in situ* XRD cell (version 1). The Li-NMC cell contains a cathode with 96 wt% NMC, 2 wt% PVdF binder and 2 wt% Super C65 conductive carbon, two glass fiber separators soaked with electrolyte (1 M $LiPF_6$ in EC:EMC, 3:7 v:v, LP57, BASF), and a lithium metal anode. (a) Comparison of rate and cycling performance of the *in situ* XRD cell to a standard laboratory T-cell, and (b) comparison of their voltage profiles during the rate test. The numbers in the plot indicate the C-rate (h^{-1}), at which the cell is cycled.

reaction mechanism of Li_2S in a lithium-ion battery. Details on the Li-Li_2S system and its comparison to the performance of a Si/C-Li_2S will be discussed in Chapter 4.4.

4.2.3 Improvements in cell design (version 2)

In order to tackle issues with XRD data quality and electrochemical performance, some slight variations on cell version 1 were performed (see Figure 4.1). Some of this work as well as experiments discussed in Chapter 4.2.4 were conducted during the supervision of a master's thesis.[147]

The most obvious feature is the overall enlargement of the cell dimensions due to the further elongation of the X-ray opening in the top plate to 26 mm. This should, primarily, increase the sample volume of the active material at angles around $2\theta_{Mo} \sim 6.6°$ because in the former version the divergent beam might be truncated by the closely confined opening

of the cell accompanied by a reduction in beam intensity. The size of the O-rings and the diameter of the aluminum current collector needed to be adjusted accordingly. Thus, a 3 x 27 mm O-ring and a Ø42 mm aluminum foil were chosen for this design. Furthermore, the top plate was increased in thickness (2 mm) to maintain a reliable compression of the O-ring, since in the former design a slight curvature of the 500 µm thick stainless-steel plate had been observed. The area along the beam direction, however, had to be kept at 500 µm to allow for proper X-ray access at low angles.

The sealing unit was separated in two parts to further promote the functionality of each unit. The outer ring composed of an insulating silicon rubber, which electrically separated the top and bottom current-collector plates and provided an additional sealing. Due to the reactivity of the PTFE material towards metallic lithium, it had to be replaced with the more resistant polyethylene (PE). Thus, the inner part consisted of a PE component, which could incorporate the FEP sealing O-ring and had a cavity for the cell stack and the anode plate.

To improve cell compression, a higher spring rate (23.21 N/mm, LC 047D01S316, Lee Spring GmbH, Germany) and two additional glass-fiber separators were added. A 25 µm thick punched Kapton foil was inserted between the top plate and the aluminum window to protect the aluminum foil from being punctured by the X-ray opening. The hole in the Kapton foil was the size of the active material coating, thus no additional signals from the Kapton foil were expected in the diffraction pattern. No changes were made to the diameter of the cathode coating (Ø12 mm), the separator (Ø14 mm) and the anode (Ø13 mm). Overall, the handling and assembly in the glovebox could be slightly improved compared to cell version 1. Detailed technical drawings of the electrochemical *in situ* XRD cell version2 are provided in the appendix.

4.2.4 Towards a long-term cycling *in situ* XRD cell?

Due to the changes in cell design, which were mostly directed to enhance the X-ray diffraction, cell compression and sealing around the X-ray opening, improvements in the capability for long-term cycling are expected. The aim is to analyze the active material inside the cell and correlate structural changes with cycling performance without having to dismantle the cell. The clear benefit would be less sample preparation and the elimination of related errors. The cycling procedure can be continued after an intermediate XRD check-up has been conducted, so that structural changes will be monitored on one system. Nevertheless, the XRD cell has to fulfil distinct electrochemical requirements in order to certainly correlate structural and electrochemical performance.

For this benchmarking process, well-characterized cell chemistries such as Li-$LiNi_{1/3}Mn_{1/3}Co_{1/3}O_2$ (Li-NMC) and Li-$LiFePO_4$ (Li-LFP) were chosen. These materials were well established in our laboratory and thus provided a suitable basis for analysis and comparison. NMC cathodes consisted of 96 wt% active material, 2 wt% PVdF binder, and 2 wt% Super C65 conductive carbon, whereas LFP cathodes comprised 80 wt% active material, 10 wt% PVdF binder, and 10 wt% Super C65 conductive carbon. All electrodes were prepared according to the mask-coating procedure. LFP electrodes were

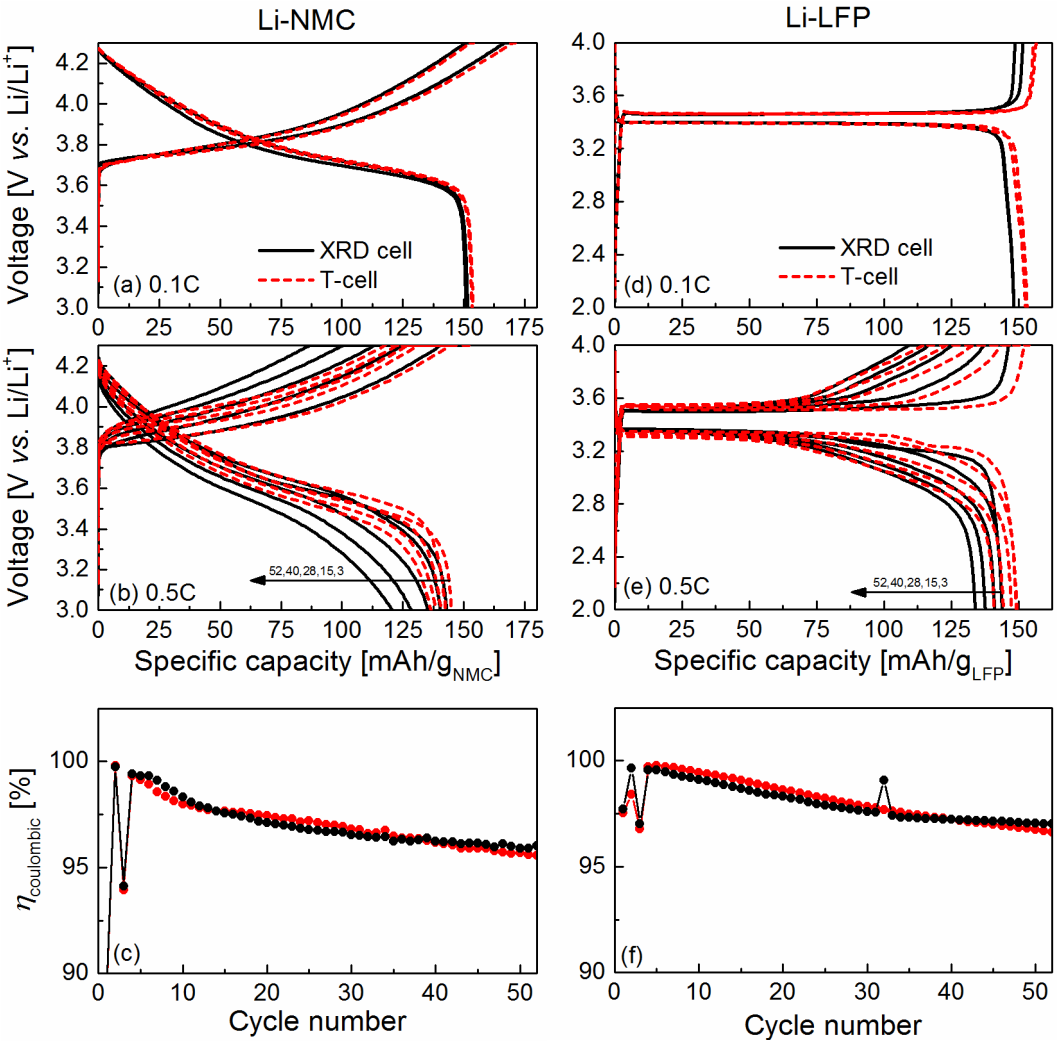

Figure 4.6: Comparison of the electrochemical performance of the *in situ* XRD cell (version 2) to a laboratory Swagelok T-cell for Li-NMC and Li-LFP systems. Li-NMC cells contain a cathode with 96 wt% NMC, 2 wt% C65, and 2 wt% PVdF, four glass fiber separators soaked with electrolyte (1 M $LiPF_6$ in EC:EMC, 3:7 v:v, LP57, BASF), and a lithium metal anode, whereas the Li-LFP system contains a cathode with 80 wt% LFP, 10 wt% C65, and 10 wt% PVdF. (a)-(c) Voltage profile and coulombic efficiency of Li-NMC cells during cycling at 0.1C and 0.5C, respectively (Loading XRD cell: 19.5 mg_{NMC}/cm^2, Loading T-cell: 18.6 mg_{NMC}/cm^2), (d)-(f) Voltage profile and coulombic efficiency of Li-LFP cells during cycling at 0.1C and 0.5C, respectively (Loading XRD cell: 8.3 mg_{LFP}/cm^2, Loading T-cell: 7.2 mg_{LFP}/cm^2). Numbers in the plot indicate shown cycle numbers.

additionally pressed at 430 MPa (modified KBr-press, PerkinElmer) to achieve good electrochemical contact between particles, which is necessary for this type of material. For T-cells, electrode samples with 10 mm diameter were punched from the aforementioned electrodes. The exact individual loadings of each electrode are specified in each of the figure captions. In all cells, glass fiber separators were used, whereas 1 M $LiPF_6$ in EC:EMC (3:7, v:v, LP57, BASF) electrolyte was chosen for Li-NMC and 1 M $LiPF_6$ in EC:DMC (1:1, v:v, LP30, BASF) electrolyte was chosen for Li-LFP, unless stated otherwise. The typical electrochemical test contained two formation cycles at 0.1C and 50 cycles at 0.5C, whereby the constant current (CC) charge was followed by a constant voltage (CV) period at the upper cut-off potential with 0.05C as cut-off current. Li-NMC cells were cycled between 3.0 and 4.3 V, whereas Li-LFP cells were cycled between 2.0 and 4.0 V.

Figure 4.6 shows the voltage profiles and coulombic effciency arising from the XRD cell and the comparable T-cell at different C-rates and cycle number for the respective cell chemistries. At low C-rates of 0.1C, Figure 4.6a and d, the performance of the XRD cell with respect to voltage and capacity is almost identical to the T-cell, which makes the XRD analysis very reliable at this C-rate. For long-term experiments with high cycle numbers, however, one has to use faster rates in order to accelerate the experiment or promote active material fatigue, while maintaining a similar performance of the XRD cell compared to a Swagelok T-cell. Analogous to cycling experiments using the previous XRD cell design (version 1), the rate was increased to 0.5C, whereas the cycle number was restricted to 50 cycles. This served as a precaution because metallic lithium counter electrodes tend to easily form dendrites, which would consequently impede proper cycling due to short circuits.[46]

The results of the cycling test on both cell chemistries are shown in Figure 4.6b and e. Apparently, the XRD cell exhibits an increased capacity fade accompanied with higher overpotentials in the voltage curve compared to the T-cell. Such performance losses, which have already been observed for the previous cell version, can be caused by mass transport limitations or increased ohmic resistances, and may be related to the still uneven compression of the cell stack by the thin aluminum X-ray window. Possible effects of this uneven compression could be inhomogeneous lithium deposition followed by additional electrolyte reduction on the anode side due to freshly exposed lithium surfaces. The resulting surface films would therefore add to the existing cell impedance and decrease cycling performance. In Figure 4.6c and f, the coulombic efficiency between the two different cell designs and cathode active materials is compared. In both XRD and T-cell design, the reversibility of the cell reaction seems to be equal, whereas slightly improved coulombic efficiencies can be observed for the Li-LFP cells compared to the Li-NMC cells. In all systems, the coulombic efficiency decreases to almost 95%, which indicates increasing side reactions during the charge of the cell. This would be in accordance with the previous assumption, in which an uneven lithium deposition causes additional electrolyte reduction. Since the extent of parasitic reactions must be the same in both cell

systems according to the results in Figure 4.6c and f, the performance loss of the XRD cell observed in Figure 4.6b and e would be most likely related to the consequences of an inhomogeneous compression encountered in the XRD cell.

To further investigate this assumption and to reveal the main cause for the observed performance drop, several tests regarding leakage, lithium plating, and compression were performed, which, in the end, may offer a cell-design solution for prolonged cycling stability.

(a) Leakage test

First of all, the leak-tightness of the XRD cell had to be proven, as this is the most crucial parameter concerning cell reliability. The reactivity of cell components with water and oxygen, arising from a leak, causes parasitic currents which would affect the coulombic efficiency. Furthermore, the resulting parasitic reaction products could affect the observed electrochemistry or XRD pattern and therefore lead to a misinterpretation of results. For this reason, two different leakage tests were performed: i) a water-proof test and ii) a vacuum-decay test.

The *water-proof test* on the XRD cell was based on a similar test on a modified pouch cell described in the literature.[141] In this report, metallic lithium was used as an indicator for moisture as it easily reacts in contact with air to form white residues (LiOH, Li_2O, Li_2CO_3, Li_3N (reddish)): After they had placed a piece of lithium inside the sealed pouch cell, the cell was immersed in water for three weeks and then the surface color of lithium was examined. The water-proof test on the XRD cell, however, was slightly extended compared to the aforementioned method. In this case, a completely assembled and operational XRD cell was immersed in ultrapure water (resistivity of 18 MΩ cm) overnight. A very low conductivity of water was essential to prevent any short circuits of the cell by conducting ions. Furthermore, the closed container (with XRD cell and water) was purged with inert gas to suppress CO_2 dissolving back into the pure water which would raise its conductivity. With this setup, any water penetrating the cell would immediately react with metallic lithium or the conducting salt $LiPF_6$, which would drastically reduce the cell performance after the water immersion test.

The experiment was conducted on Li-LFP XRD cells with LP30 electrolyte and the results of cells cycled with and without water proof test are shown in Figure 4.7. The spike in the plot of the standard XRD cell aroused from a short circuit, which had no further implications on cell cycling. Obviously, the capacity of the immersed cell is lower than the capacity of the dry cell. This offset, however, is not linked to any leak, as the immersed XRD cell already showed a capacity as low as 140 mAh/g_{LFP} at 0.1C cycling before the test. A reasonable explanation might be some error in determining the exact electrode mass of this specific cell. Despite this discrepancy, the immersed cell exhibits a similar cycling stability as the dry cell. A drastic decline in cycling capacity is not observed, which would indicate the intrusion of water via a leak. Thus it is concluded that the *in situ* XRD must be leak-tight within the scope of this experiment.

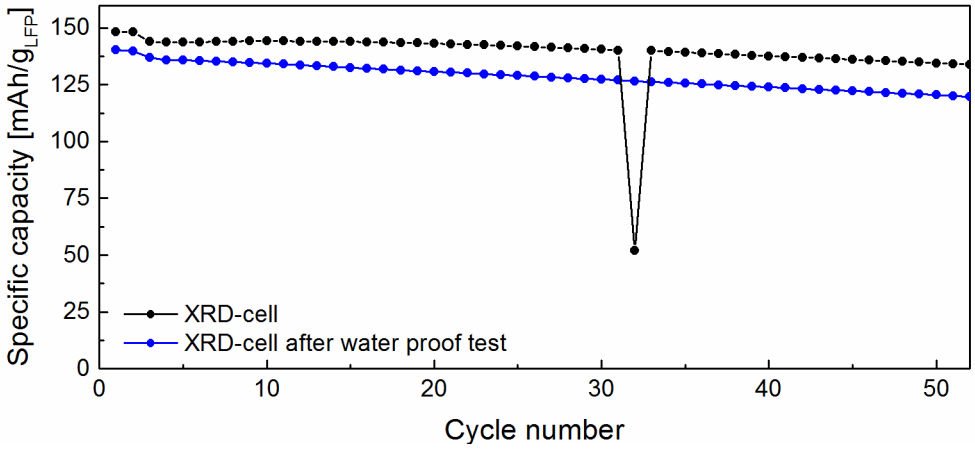

Figure 4.7: Electrochemical cycling of Li-LFP *in situ* XRD cells at 25°C with/without a previous water-proof test. Charge-discharge cycles were conducted between 2.0 - 4.0 V two times at 0.1C and 50 times at 0.5C with CCCV charge procedure. The loading of the cells were 7.7 mg_{LFP}/cm^2 (water-proof test) and 8.3 mg_{LFP}/cm^2 (no water-proof test). The applied current was calculated from a theoretical capacity of 170 mAh/g_{LFP}.

In order to verify this finding, an additional leakage test was performed on the XRD cell. For this purpose, the XRD cell comprised only the stain-less steel cell body, insulation-sealing unit, O-rings and the aluminum window. The bottom plate was specially adapted for this experiment by a welded VCR® gland to the bottom part of the cell, which could then be connected to a vacuum pump and a Baratron capacitance manometer (cf. Section 3.4.1 for experimental details). After evacuation of the XRD cell, the pressure was monitored over time. This kind of leakage test is called the *vacuum-decay method*.

Two XRD cells were assembled for this experiment and the result of the pressure measurement is illustrated in Figure 4.8. The fist cell (black curve) was only evacuated for 1 h and thus surface outgassing was predominant in the beginning of the pressure record indicated by a rapid pressure increase. Afterwards, the pressure adopted a steady behavior with a small slope. For the second cell (red curve) the evacuation process was extended to 8 h. This time, no initial rapid pressure increase was observed, which showed that, indeed, adsorbed surface molecules were the reason for the outgassing. The pressure curve of the second cell exhibits a similar slope as the long-term slope seen for the first cell.

Since no device is absolutely tight, a little pressure increase can always be detected. It is essential that these leaks are as small as possible to verify a proper operation of the XRD cell. In order to quantify the leakage, its rate has to be calculated according to the following equation:

$$q_L = \frac{\Delta p\, V}{\Delta t} \tag{4.1}$$

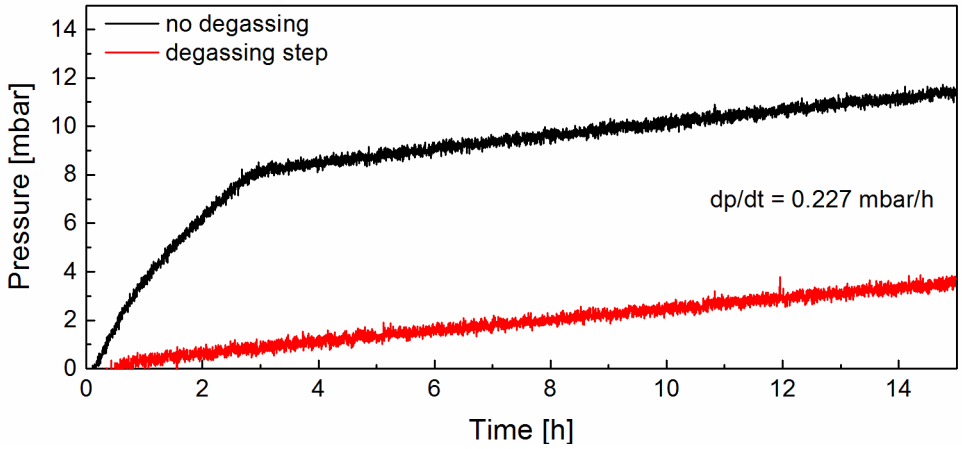

Figure 4.8: Vacuum-decay test performed on the *in situ* XRD cell using a Bratron capacitance manometer. Cells were evacuated prior to measuring the pressure increase either for 1 h (black line) or for 8 h (red line).

where q_L is the leakage rate in mbar l s^{-1}, Δp is the observed pressure increase in mbar, V is the internal volume of the test object in liters, Δt is the measurement period in seconds. With the slope from Figure 4.8 and the internal system volume of ≈13 ml (cell ≈2.7 ml + pressure transducer ≈7 ml + connections ≈3ml, determined from the geometry of the designs) a leakage rate of $\approx 8 \cdot 10^{-07}$ mbar l s^{-1} is determined. A leakage rate of $<10^{-06}$ mbar l s^{-1} is generally considered as "very tight" or "gas tight" in vacuum technology.[83] According to the vacuum decay method, a severe leak could not be detected for the XRD cell. Since we do not apply vacuum to our cell during operation nor do we want to maintain a vacuum, the XRD cell can be regarded as leak-tight during the operation at atmospheric pressures.

In summary, both applied leak tests, *i.e.*, the water-proof test and the vacuum-decay method, do not give any hint of a severe leak in the XRD cell. This also supports the findings of the measured coulombic efficiency in Figure 4.6c and f, in which both XRD and T-cell exhibit the same reversibility of the cell reaction.

(b) Inhomogeneous lithium plating

After extended charge-discharge cycles and several lithium plating and stripping processes, it is generally accepted that the lithium deposit is inhomogeneously distributed and easily forms a mossy/dendritic-like structure on the metallic lithium surface.[46] The formation of micro-structured lithium leads to higher surface area, irreversible electrolyte reduction at freshly deposited lithium surfaces and premature lithium decomposition.[43,148–150] These are some of the reasons why metallic lithium is not used as anode material in lithium-ion batteries, in addition to its low rate capability, the formation of dendrites and associated safety risks.[151]

In order to investigate this subject, the lithium anode was harvested inside a glove box from a Li-LFP XRD cell cycled for 50 cycles (see Figure 4.10, black line) and SEM pictures at different position of the lithium electrode were taken. The results are shown in

Figure 4.9a and b. The dark grey area in both pictures corresponds to pure metallic lithium surface, whereas the light grey area reflects the lithium deposit. After 50 cycles a clear micro-structured (mossy) and bulky lithium deposition can be observed, which must be very loose due to the easy formation of cracks. Apparently, these structures exhibit a high surface area, which when freshly exposed to electrolyte enhances electrolyte degradation. During electrochemical cycling this process can be related to a reduced coulombic efficiency (discharge capacity divided by charge capacity), as additional charge is added to the actual delithiation/charging reaction of LFP. Indeed, a low coulombic efficiency of ≈96% at the end of the cycling test can be measured for both XRD and Swagelok T-cells (see black line in Figure 4.10b). This reveals that mossy lithium plating is not restricted to the XRD cell but rather an inherent property of cycling lithium electrodes in a battery cell.

By employing 10vol% fluoroethylene carbonate (FEC) as an electrolyte additive in the previously used LP30 electrolyte (1 M $LiPF_6$ in EC:DMC, 1:1, w:w), improvements in cycling stability and coulombic efficiency are expected due to its stabilizing effect on anode materials such as lithium, graphite, and silicon.[152–155] FEC is a derivative of the commonly used electrolyte component ethylene carbonate (EC) with one fluorine atom replacing a hydrogen atom in the structure. Although both components are reduced on the anode to form a protective solid electrolyte interface (SEI), the beneficial effect of FEC

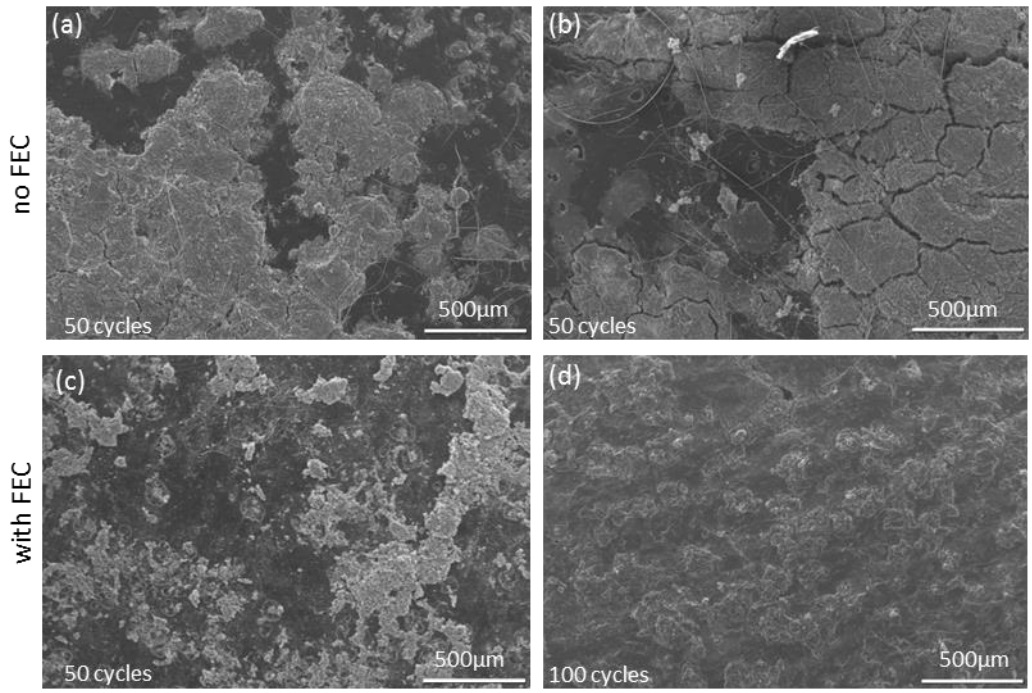

Figure 4.9: SEM micrographs of lithium counter electrodes cycled with/without 10vol% FEC as electrolyte additive. (a)(b) Lithium surface at two different positions of the electrode (the lithium electrode was harvested after 50cycles from the *in situ* XRD cell without additive). (c)(d) Lithium was harvested after 50cycles and after 100 cycles from the *in situ* XRD cell with FEC additive.

supposedly lies in its selective de-fluorination pathway, thus forming a highly cross-linked polymeric matrix on the outer SEI layer with increased ionic conductivity.[153,155–157] As a consequence, the formed SEI layer is more stable against volumetric changes and the current is more evenly distributed on the anode surface leading to a more homogeneous and compact lithium deposit in FEC-containing electrolyte.[158] In contrast, the SEI that forms in standard carbonate-based electrolyte is less cross-linked (less flexible) and mainly consists of deposited lithium salts (*e.g.*, LiF, Li_2CO_3, and Li_2O).[43,46] Due to these properties, the SEI cannot withstand the stress induced by volumetric changes during non-uniform lithium plating-stripping and eventually ruptures by exposing fresh reductive lithium surface to the electrolyte. This cracking-repairing process finally causes the growth of micro-structured (mossy) lithium and leads to poor coulombic efficiency of the cells as demonstrated in Figure 4.9a, b and Figure 4.10b.

The use of FEC-containing electrolyte should therefore significantly influence cycling

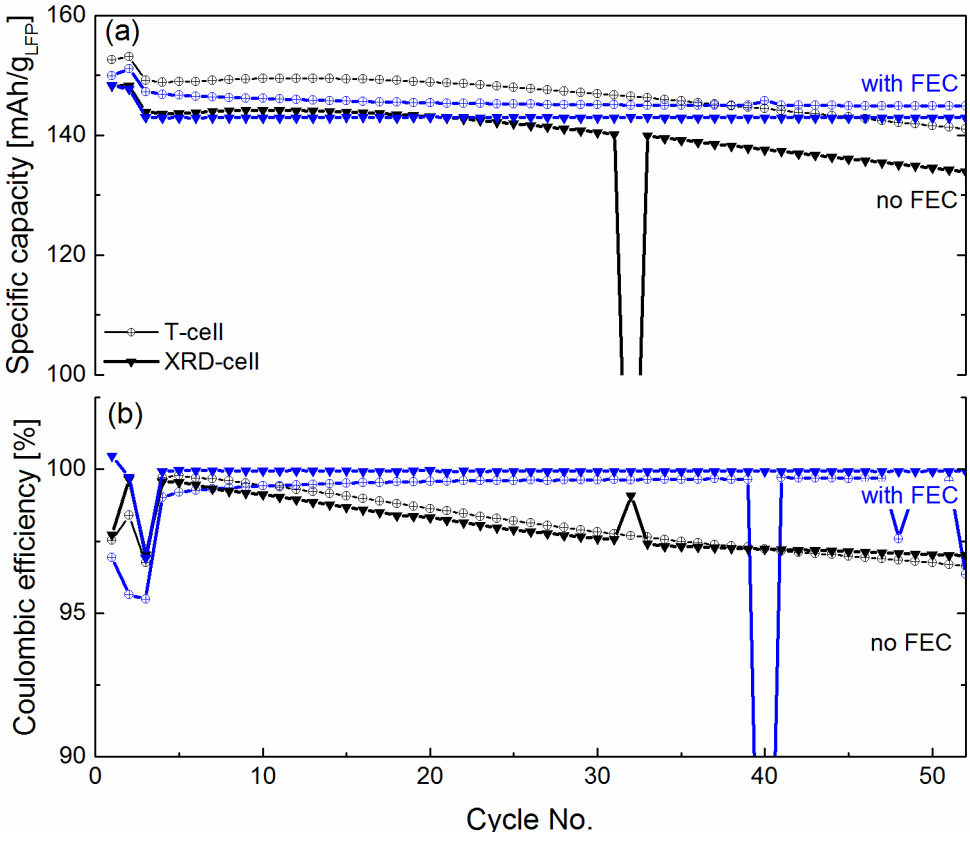

Figure 4.10: Comparison of the electrochemical cycling performance of Li-LFP *in situ* XRD cells and Swagelok T-cells with/without 10 vol% FEC in LP30 (1 M $LiPF_6$ in EC:DMC, 1:1, w:w). (a) Charge-discharge cycles of all cells were conducted between 2.0 - 4.0 V two times at 0.1C and 50 times at 0.5C with CCCV charge procedure. (b) Coulombic efficiency (%) of the cells (discharge devided by previous charge). Spikes in the positive direction indicate a possbile disconnection of the cell, whereas spikes in the negative direction reveal a short-circuit of anode and cathode due to lithium dendrite formation. Loadings for T-cells: 7.2 mg_{LFP}/cm^2 and 9.2 mg_{LFP}/cm^2 (FEC); loadings for XRD cells: 8.3 mg_{LFP}/cm^2 and 9.1 mg_{LFP}/cm^2 (FEC). Cells without FEC are the same as used in Figure 4.6 d-f.

stability and coulombic efficiency due to its crucial effect on SEI properties. Indeed, SEM images of harvested lithium electrodes cycled in FEC-containing electrolyte show a reduced formation of mossy lithium (Figure 4.9c) and even after 100 cycles a dense and compact lithium deposition can be observed for the XRD-cell (Figure 4.9d), which confirms the aforementioned assumptions. Furthermore, the stabilizing effect of FEC on the SEI can be directly monitored by an improved cycling performance with increased coulombic efficiency as illustrated for both XRD and T-cell in Figure 4.10a and b.

With the application of FEC as electrolyte additive, it was effectively demonstrated that inhomogeneous lithium plating plays an important role in the cycling performance, not only restricted to the XRD cell. The cycling stability and coulombic efficiency could be significantly improved so that the XRD cell is applicable for more than 50 cycles. Nevertheless, the use of additives is not always suitable and the problem of dendrite formation at high cycle numbers or rate still exists. Furthermore, the effect of FEC was less pronounced when cycling Li-NMC cells (not shown here for clarity), which indicates that other parameters besides micro-structured lithium-plating play a crucial role, which will be addressed next.

(c) Cell compression

Another notable source of weakness of the *in situ* XRD cell is related to a reduced compression of the cell stack by the thin aluminum X-ray window, which slightly yields to the pressure of the cell stack at the cell opening. Simultaneously, the cathode coating also bends, as it is directly attached to the aluminum foil. The elongated opening in the top plate, however, is mandatory to allow X-rays to interact with the cathode material in reflection mode. Thus, non-uniform current distribution and restricted cathode utilization might be the result of this design, especially at higher C-rates, which would be in accordance with the observed performance loss for the XRD cell already shown in Figure 4.6. Since an uneven compression also affects lithium plating – *e.g.*, high compressive forces increase the compactness of micro-structured lithium deposits as discussed by Gireaud *et al.*[148] – the use of FEC-containing electrolyte might have addressed this issue as well by stabilizing the deposited lithium structure. Hence, the superposition of both effects (inhomogeneous lithium deposition and reduced cell compression) can be present in the XRD cell.

To further investigate the effect of compression, an adapter was constructed for the XRD cell. This adapter fitted perfectly into the X-ray opening, so that the cell could be operated in a closed configuration as illustrated in Figure 4.11c. The main purpose of the adapter was to counteract the reduced cell compression at the X-ray opening by offering resistance to the cell stack and providing uniform pressure distribution during cycling at higher rates. For XRD analysis, the adapter could be removed. Experiments were conducted on the Li-NMC system using LP57 electrolyte (1 M $LiPF_6$ in EC:EMC, 3:7, w:w). Before assembling the cell, the adapter had been mounted on the top plate of the XRD cell.

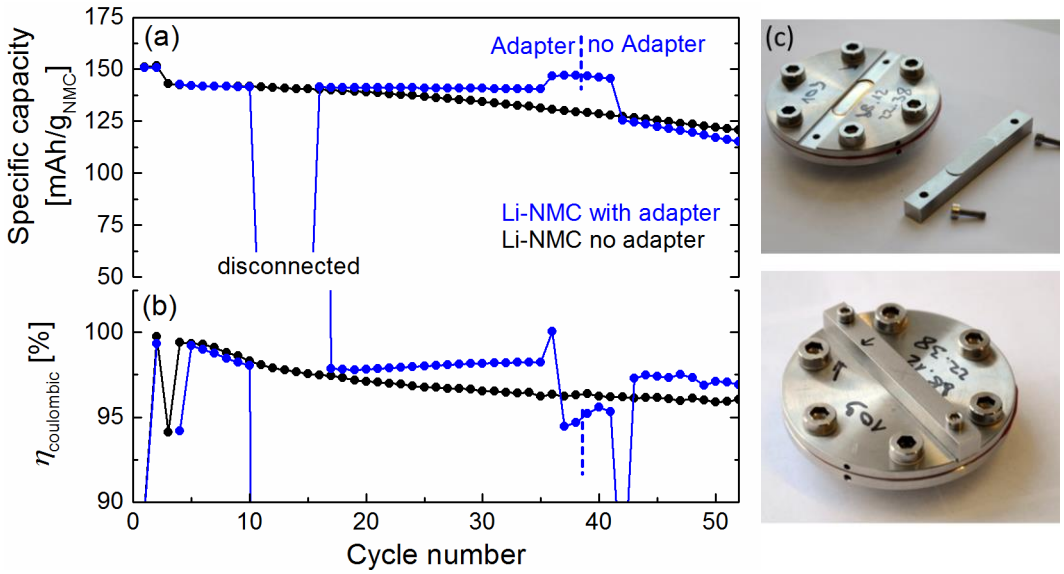

Figure 4.11: (a) Electrochemical cycling of Li-NMC *in situ* XRD cells at 25°C with/without an additional adapter. Charge-discharge cycles were conducted between 3.0 - 4.3 V two times at 0.1C and 50 times at 0.5C with CCCV charge procedure. (b) Coulombic efficiency of the cells. The loading of the cells were 19.5 mg$_{NMC}$/cm^2 (no adapter) and 18.3 mg$_{NMC}$/cm^2 (with adapter). The applied current is calculated from the reversible capacity of 150 mAh/g$_{NMC}$ at 0.1C. (c) Adapter mounted on the XRD cell (closed configuration).

The result of cells cycled with and without adapter are shown in Figure 4.11a by plotting the discharge capacities against cycle number. During initial cycling at 0.1C, both cells achieve a reversible discharge capacity of 150 mAh/g$_{NMC}$. It has already been shown in the beginning of this chapter that at this low rate the performance of the XRD cell is very similar to that of the T-cell. During cycling at 0.5C, however, the XRD cell without adapter starts to deviate from the XRD cell with adapter at around 20 cycles. It should be noted that during the experiment the latter cell was disconnected for a short time, as demonstrated by the abrupt capacity decline, but no crucial impact on the further cycling behavior was observed. Apparently, the application of the adapter improves cycling stability as well as coulombic efficiency, which is demonstrated in Figure 4.11b. After 35 cycles, the closed XRD cell was cycled again at 0.1C before detaching the adapter and repeating the cycling experiment. Both conditions at 0.1C (before and after adapter removal) show similar capacity retentions with slightly increased charge capacities, which can be evidenced by a lower coulombic efficiency. At 0.5C, when the adapter is removed, the capacity rapidly drops and the performance becomes similar to that cell, which is cycled completely without adapter. Again, the importance of the adapter is demonstrated here. While at 0.1C the cell can be operated without adapter to perform *e.g.*, XRD measurements, at 0.5C the adapter is necessary to maintain a good cycling stability.

According to these observations, the slight bending of the aluminum X-ray window seems to be the main reason for the performance drop of the XRD cell. To circumvent this issue, an adapter has been suggested, which should be used for extended cycles at higher rates, and which has to be removed for XRD analysis. However, the process of

attaching/detaching the adapter leads to additional stress on the thin aluminum window, which in the long-term might cause damage to the foil and affects its stability.

(d) Full cell configuration

The experience obtained from previous results of cycling XRD half cells is now transferred to a full cell configuration. By exchanging the lithium counter electrode with a graphite electrode, formation of dendrites and excessive electrolyte reduction can be avoided, which enables experiments at higher cycle number. However, the use of graphite restricts the lithium inventory as no excess lithium can be provided, contrary when using metallic lithium. All lithium-ions have therefore to be provided by the cathode material, which requires an adequate capacity balancing between the electrodes (cf. Section 3.2.4 for experimental details). Accordingly, an areal-capacity ratio of ≈1.1 between anode and cathode was chosen. Since FEC-containing electrolyte was only used to demonstrate the effect of non-uniform lithium plating, it was not considered for these experiments. Although it is reported that FEC shows some improvements on graphite,[152,159] it is not a common additive used with graphite electrodes such as vinylene carbonate (VC).[39,160] For this reason, the long-term cyclability of XRD full cells were only tested with the adapter approach. Experiments were performed with the graphite-NMC system using LP57 electrolyte (1 M $LiPF_6$ in EC:EMC, 3:7, w:w). The anode consisted of 95 wt% graphite active material and 5 wt% PVdF binder and was prepared according to the Doctor-blade method described in Section 3.2.2.

Figure 4.12a compares first results on the rate performance of XRD cells without adapter to XRD cells with adapter and Swagelok T-cells. As expected, the rate capability of the XRD cell without adapter lags behind that of the other cells and only up to a rate of 0.5C similar capacities can be achieved. This again demonstrates the limitations introduced by the soft aluminum X-ray window. By utilizing the adapter, these limitations could be tackled and the XRD cell accomplished the same capacities as the T-cell up to a rate of 5C. At high rates (3C and 5C) the XRD cell slightly outperformed the T-cell in capacity, which was probably due to a higher compressive force in the XRD cell. In the XRD cell, *e.g.*, the spring was compressed by ≈3 mm, which resulted at a given spring rate of 23.2 N/mm and a contact area of $1.13 \cdot 10^{-4}$ m^2 (Ø12 mm cathode coating) in a stack pressure of ≈0.6 MPa. Whereas in the T-cell a three times smaller stack pressure of ≈0.2 MPa was obtained, given a spring compression of ≈4 mm, a spring rate of 3.7 N/mm and a contact area of $0.79 \cdot 10^{-4}$ m^2 (Ø10 mm cathode coating). The higher compressive force in the XRD cell might have further reduced the thickness of the soft glass fiber separator or improved the contact resistance of the electrodes, which both led to a lowered cell resistance that eventually resulted in the slightly better rate capability at higher rates. It has to be noted that despite a three times higher stack pressure of the XRD cell, the gain in capacity is not that much pronounced, and that pressures of 0.2 MPa (compression in a T-cell) are therefore completely sufficient for testing these materials.

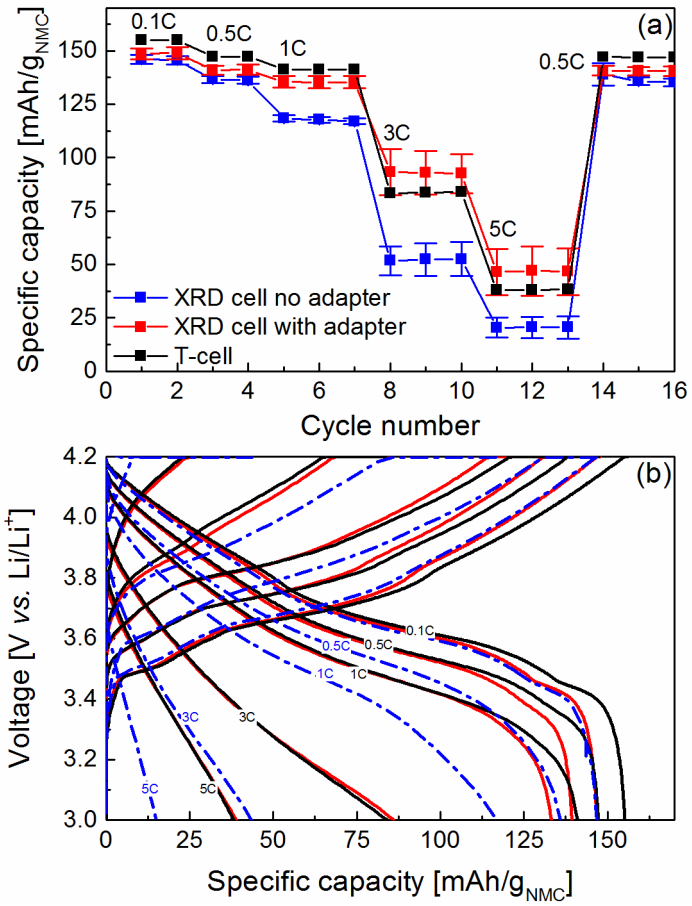

Figure 4.12: Electrochemical rate performance of the *in situ* XRD cell in full cell configuration with graphite-NMC. (a) Comparison of the capacity between XRD cell (no adapter), XRD cell (with adapter), and T-cell. Error bars illustrate the standard deviation using two normally identical cells. (b) Comparison of the respective voltage profiles during the rate test. Numbers in the plot indicate the C-rate (h^{-1}), at which the cell was cycled. All cells had an average NMC loading of 18.1 ±0.3 mg/cm^2 and a graphite to NMC areal-capacity ratio of 1.09 ±0.01.

However, a closer look at the voltage profile of the rate test (Figure 4.12b; for clarity only one cell for each cell system is shown) reveals that at 0.1C both XRD-cell systems (with and without adapter) show slightly lower discharge capacities than the T-cell (147 mAh/g_{NMC} *vs.* 155 mAh/g_{NMC}), which was not as obvious as in the previous plot. Since kinetic limitations can be neglected at this slow rate, differences in electrode-cell design are therefore considered more closely. It is known that electrode capacity balancing can have a great influence on the first-cycle capacity loss and the related irreversible lithium consumption by forming the SEI (see experimental Section 3.2.4). Due to a similar anode-to-cathode areal-capacity balancing between all cells (see figure caption of Figure 4.12), these losses are adjusted to the same size so that issues with balancing can be neglected. Also the areal overlap of the graphite electrode relative to the cathode is similar in all cell systems, *viz.*, ≈17% for the XRD cell and ≈21% for the T-cell. Thus, possible reasons for the observed capacity difference are thought to be a loss in the cath-

ode utilization of the XRD cell, in which the full capacity of the cathode material is not completely used, or a systematic error in electrode mass determination, in which the mass of the active material must be overrated in the order of 5%. While cathode utilization should be improved with the adapter and also be directly evidenced by a loss in performance at higher rates, a systematic error of 5%, introduced by the oversized aluminum window (ten times bigger in size than the actual active-material coating) or by the mask-coating process, is more likely with respect to the XRD cell.

Despite this capacity discrepancy, the voltage curve of the XRD cell with adapter and the voltage curve of the T-cell are in good agreement, whereas the voltage curve of the XRD cell without adapter demonstrates increased overpotentials at rates higher than 0.5C. This again confirms that the X-ray window is the weak point of the *in situ* XRD cell when it comes to electrochemical performance. The use of the adapter therefore appears to be very promising as similar rate performances compared to the T-cell were obtained.

To prove the practicality of this concept the long-term experiments, cells were cycled for more than 170 cycles at 0.5C. At certain points, the C-rate was changed to 0.1C while the adapter of the XRD cell was removed to mimic an XRD measurement. During 0.5C cycling the adapter was again attached to the XRD cell. The results of this experiment are shown in Figure 4.13a and b. The black line in Figure 4.13a corresponds to the cycling capacity of the reference Swagelok T-cell, whereas the red and blue line refer to the XRD cell with and without adapter, respectively. These are the best performances obtained for the XRD cell so far. With the adapter a drastic improvement in cycling stability is obtained when compared to the performance without adapter. Furthermore, the detachment/attachment of the adapter during 0.1C/0.5C cycling does not affect further cycling, so the XRD analysis could be constantly performed during cycling. The capacity fade of the XRD cell with adapter, however, is still more pronounced than in a T-cell. After 170 cycles only 85% of the initial capacity at 0.5C could be recovered, while the T-cell still offers 96%. Additionally, when comparing the voltage profile in Figure 4.13b, the decline in capacity is also accompanied by a slight increase in overpotential, visible in the voltage difference between successive cycles of the XRD cell with adapter. This discrepancy in performance, however, excludes the use of the XRD cell for long-term studies as no reliable correlation between electrochemical data and structure analysis can be expected with respect to a standard laboratory test cell.

Despite all improvements, the *in situ* XRD cell does not meet the electrochemical requirements. It is possible that issues with cell leak-tightness still exist, as with the previous tests on XRD half cells only a rough estimation of long-term stability could be given. The consequence would be an enhanced irreversible lithium consumption at the SEI due to water intrusion and its effect on SEI stability.[43,161] However, cycling tests in inert gas atmosphere (inside a glove box) did not show any improvements in capacity retention, so therefore moisture intrusion could be excluded from consideration. The origin of the poor performance of the *in situ* XRD still remains unclear, although the most obvi-

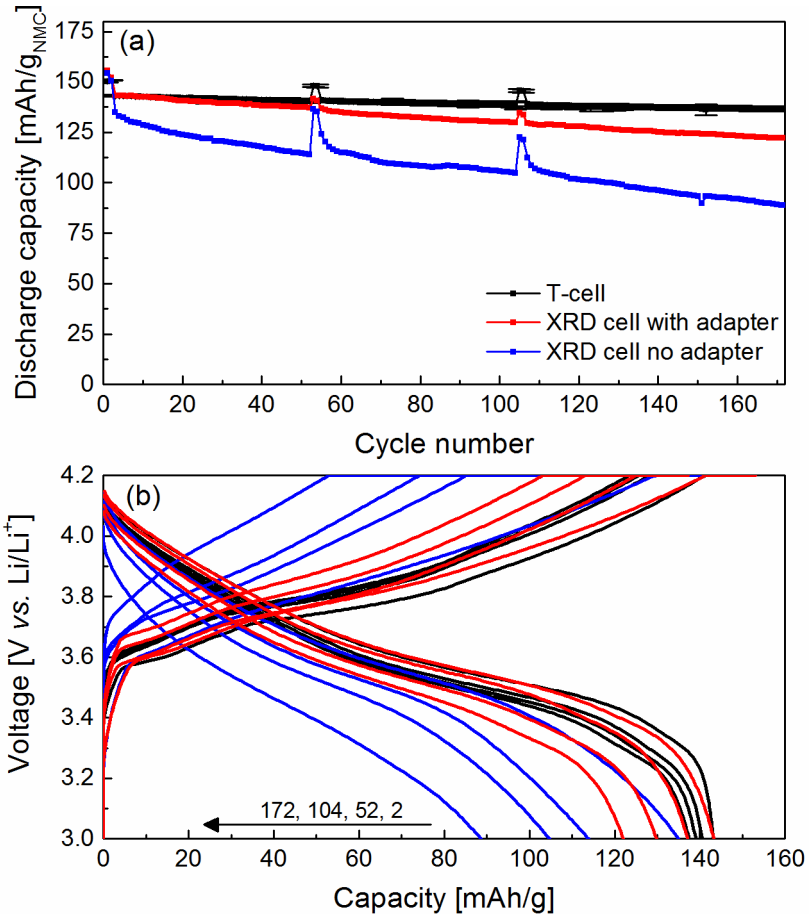

Figure 4.13: Electrochemical cycling performance of the *in situ* XRD cell in full cell configuration with graphite-NMC at 0.5C and 25°C (a) Comparison of the cycling capacity between XRD cell (no adapter), XRD cell (with adapter), and T-cell. Jumps in capacity indicate a rate change to 0.1C, at which the adapter is removed from the closed XRD cell. (b) Comparison of the respective voltage profiles at 0.5C during the cycling test. Numbers in the plot indicate shown cycle numbers. The cells have an average NMC loading of 18.3 ±0.8 mg/cm^2 and a graphite to NMC areal capacity ratio of 1.05 ±0.06.

ous difference between XRD and T-cell regarding compression has been amply discussed and tackled.

4.2.5 Summary and conclusion

The *in situ* XRD cell established in this chapter has been under critical examination regarding electrochemical and structural investigations in Bragg-Brentano geometry with a Mo source. With this setup, only cathode materials are feasible for XRD analysis, since a copper current collector foil, which is necessary for anode materials, would be essentially impenetrable to X-rays under grazing incidence conditions required for the Bragg-Brentano geometry. Electrodes need to be specially fabricated via mask-coating process, so that the aluminum current collector of the cathode can simultaneously be used as an X-ray window. During the development of a suitable design, the first version was soon

replaced by a more reliable and efficient second version. This version could be operated in half- and full-cell configuration, whereas the cycling stability of half-cells was drastically improved by using FEC-containing electrolyte due to its beneficial effect on lithium plating.

The main drawback of this design, however, concerns the X-ray opening in the top plate. Due to the slight bending of the soft aluminum window, the compression of the cell stack is not uniform, which can be observed in a poor rate and cycling performance. With the adapter approach, this issue could be resolved to a large extent, but discrepancies between XRD cell and a reference laboratory cell still exist during prolonged cycling. Thus, the *in situ* XRD cell does not meet the electrochemical requirements for long-term studies as correlating structural investigations would be doubtful.

Nevertheless, the *in situ* XRD cell behaved very reliable during the initial cycles at 0.1C and was therefore successfully utilized in several studies to reveal distinct electrochemical-structural relationships. In Chapter 4.3 the first charge/discharge of the high voltage material $LiCoP_4$ is discussed, in which three phases could be identified and correlated to the charging profile. In Chapter 4.4 the charging mechanism of Li_2S in a Li-sulfur battery is investigated, whereas Chapter 4.5 deals with the aging phenomena occurring in a graphite-$LiNi_{1/3}Mn_{1/3}C_{1/3}O_2$ system.

4.3 *In situ* XRD investigation on the first cycle of $LiCoPO_4$

4.3.1 Introduction

$LiCoPO_4$ (LCP) belongs to the phospho-olivine family Li*M*PO_4 (*M* = Mn, Fe, Co, Ni), which has received much attention in lithium-ion battery research since the development and commercialization of the low-cost and stable $LiFePO_4$ (LFP) by Goodenough's group in 1997.[162,163] Due to the strong P-O bond, which prevents O_2 release at high potentials and/or temperatures in contrast to layered oxide materials, LFP shows remarkably good safety characteristics with high lithium-ion intercalation reversibility. Although LFP has a theoretical specific capacity of 171 mAh/g_{LFP} at a mean voltage of 3.45 V *vs.* Li/Li^+, the resulting specific energy of ≈590 Wh/kg_{LFP} is very limiting and presents no improvements over $LiCoO_2$. One approach towards higher specific energies, required for electric vehicle application, would be an increase in cell voltage. This can be achieved by the use of Co- instead of Fe-ions in the Li*M*PO_4 structure. Based on an average charge/discharge voltage of ≈4.85 V *vs*. Li/Li^+ and a theoretical specific capacity of 167 mAh/g_{LCP}, LCP would achieve a theoretical specific energy of ≈800 Wh/kg_{LCP}.[164]

The mechanism of lithium extraction-insertion of LCP is expected to be similar to the mechanism of the isostructural LFP (both crystalize in the *Pnma* space group), which shows a two-phase mechanism with the two phases $LiFePO_4$ and $FePO_4$ resulting in a flat plateau in the charge and discharge curves.[165,166] In the literature, however, contradictory mechanisms are proposed for the LCP material. One is in accordance with the above-described process. The reported cyclic voltammetry confirmed only one oxidation and one reduction peak at 5.1 V *vs.* Li/Li^+ and 4.8 V *vs.* Li/Li^+, respectively, which are characteristic for a reversible two-phase transition.[167,168] Later on, *in situ* synchrotron structural investigations by Ehrenberg's group revealed a second plateau in the voltage profile dependent on the synthesis condition, on different particle sizes and/or on different morpholgies.[59,169] Excluding electrolyte degradation in the high-voltage region,[170] the new potential plateau was assigned to the two-phase mechanism of an intermediate phase "$Li_{0.7}CoPO_4$" and $LiCoPO_4$.[59] At that time, it was also evidenced by *ex situ* XRD on LCP samples that a distinct amorphization of the cathode material after electrochemical delithiation can take place.[171]

In this section, the electrochemical extraction-insertion mechanism of LCP is investigated with *in situ* XRD on a laboratory diffractometer to shed some light on the lithium extraction process as well as on the large capacity fade during the first cycle. The utilization of *in situ* techniques is of great importance here, especially when dealing with moisture-sensitive phases such as "$CoPO_4$", which is expected to be the final charge product. From the literature it is known that this phase undergoes amorphization when in contact with air.[59]

4.3.2 Experimental

$LiCoPO_4$ was synthesized by the group for Synthesis and Characterization of Innovative Materials (Prof. Dr. Tom Nilges) at the Chemistry Department of the Technische Universität München. The synthesis followed a conventional solid state route which was described by Freiberg *et al.*[172]In order to achieve a homogeneous and viscous slurry for electrode preparation, the standard method for ink preparation in a planetary centrifugal mixer cannot be applied because the present forces are not enough to break up particle agglomerates. The synthesized LCP, 80 wt%, was mixed with Super-C65 (TIMCAL), 10 wt%, and PVdF (Kynar HSV 900, ARCHEMA), 10 wt%, in NMP (Sigma Aldrich) by ball milling (Fritsch Pulverisette 7) in a 20 ml ZrO_2 jar with 10 mm diameter ZrO_2 balls at 180 rpm for 1 h. The final ink was then coated onto aluminum foil using the mask-coating procedure described in the previous chapter. After drying at room temperature, the electrodes were punched according to the requirements for the *in situ* XRD cell and pressed at 430 MPa (modified KBr-press, PerkinElmer) to achieve good electrochemical contact between particles, which is necessary for this type of material. Finally, the electrodes were dried at 120°C under dynamic vacuum in a Büchi oven. The LCP loading of the prepared electrodes was ≈9.4 mg_{LCP}/cm^2 (1.57 mAh/cm^2), which is higher than the usual achieved loadings for tests in Swagelok T-cells (≈4.0 mg_{LCP}/cm^2). This high loading was intentional in order to increase the amount of active material in the X-ray beam and thus to improve signal intensity.

The *in situ* XRD cell (version2) is then assembled according to the procedure described in Section 4.2.1. Four glass fiber separators (Ø14 mm, 250 µm, VWR International GmbH) were used to separate the metallic lithium counter electrode (Ø13 mm, 450 µm, Rockwood Lithium) from the LCP working electrode and 220 µl electrolyte (1 M $LiPF_6$ in EC:DMC, 1:1, w:w, LP30, BASF) were added. The cell was galvanostatically cycled in a potential window between 3.0 and 5.0 V *vs.* Li/Li^+ at a rate of 0.1C. For diffraction analysis of evolving phases, the cell was stopped consistently after a pre-defined time and kept at OCV for 1 h to allow for equilibration. Afterwards, the charging or discharging process was continued. At the upper cut-off potential, the voltage was kept constant (constant voltage or CV step) until the current dropped to almost zero.

XRD patterns were taken in repetition mode, *i.e.*, each diffraction pattern was continuously measured with a 3.0 s step time and a 0.30° step size in a 2θ-range of 5.0 – 34.7°, which results in a collection time of 10 min per pattern. For the analysis of evolved phases during the OCV period, corresponding diffraction patterns were summed up by the software $WinX^{POW}$ raw data handling.[173]

4.3.3 Results and discussion

The first charge-discharge cycle of the *in* situ XRD cell with LCP at a current of 0.1C is depicted in Figure 4.14. The specific charge capacity including the constant voltage period equals 190 mAh/g_{LCP}, which is higher than the theoretical capacity of this material

(167 mAh/g_{LCP}). This is not surprising as electrolyte oxidation and parasitic reactions easily occur at potentials higher than 4.5 V, which to a certain extent contributes additional charge to the electrochemical reaction of LCP. During discharge, however, the cell delivers only 110 mAh/g capacity, which corresponds to 66% of its theoretical capacity. This value is consistent with results obtained from Swagelok T-cells tested in our laboratories and cycled with similar LCP material.[172] Limited mass transport at the cathode/electrolyte interface is possibly the main reason for the observed capacity loss due to degraded electrolyte species on the cathode surface, whereas irreversible phase transitions upon cycling can be excluded.[167] This will also be shown in the subsequent XRD data analysis. Up to now the theoretical capacity of LCP has not been recovered and the highest reported first discharge capacity is in the order of 150 mAh/g_{LCP} at a C-rate of 0.05C (90% of theoretical capacity).[174]

The characteristic feature of two plateaus appearing upon charge at ≈4.8 V and ≈4.9 V, respectively, is present in this data and less pronounced during discharge. Similar behavior has already been mentioned.[174,175] Since the complete charging process is associated with lithium extraction and Co^{2+}/Co^{3+} oxidation as shown by X-ray absorption spectroscopy,[170] the origin of the two plateaus is not related to side reactions but rather to the inherent property of electrochemical oxidation of LCP. By comparing the data with results from Ehrenberg's group,[59] it can be assumed that a two two-phase redox reaction also takes place in our system and that each plateau might be linked to a two-phase transition.

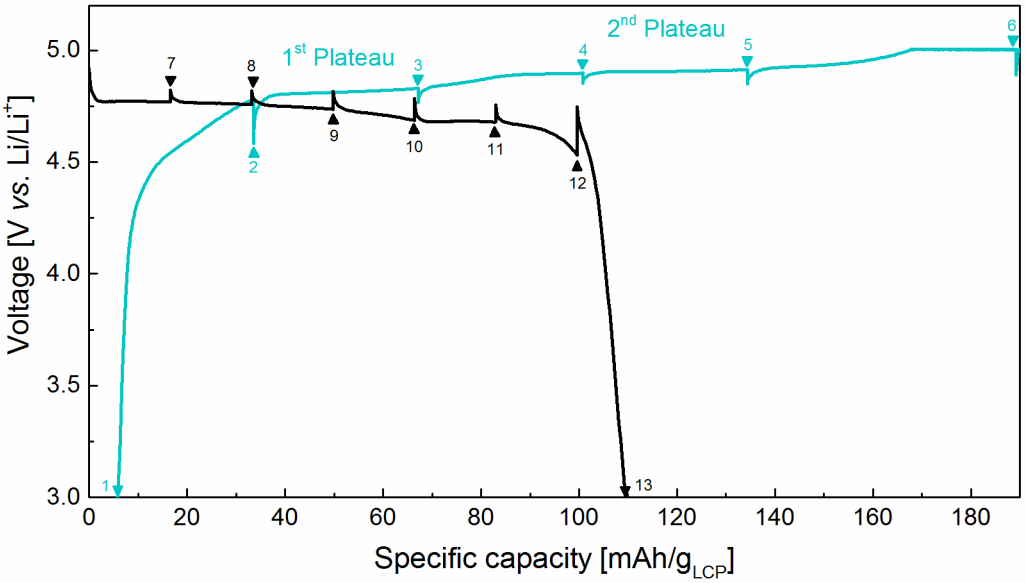

Figure 4.14: Voltage profile during the first galavonstatic (0.1C) charge-discharge cycle of $LiCoPO_4$ measured with the *in situ* XRD cell (version2). Metallic lithium was used as anode. The cell was cycled between 3.0 V and 5.0 V. At 5.0 V the voltage was kept constant until the current dropped down to almost zero (≈C/250). Spikes and small triangless mark the positions, at which the cell was in OCV for 1 h to take XRD patterns in an equiblrated state. LCP has a theoretical capacity of 167 mAh/g_{LCP}

In order to confirm this reaction mechanism, *in situ* XRD measurements were performed at different stages of lithium extraction and insertion. Figure 4.15a shows the succession of the diffraction patterns collected during OCV periods of the first charge-discharge cycle of $LiCoPO_4$. As charging (de-lithiation) proceeds, additionally to the $LiCoPO_4$ a second phase appears, which is best represented by the (2 0 0) reflection at $2\theta \approx 8.0°$. The reflections of the new phase (phase "2") are slightly shifted from those of

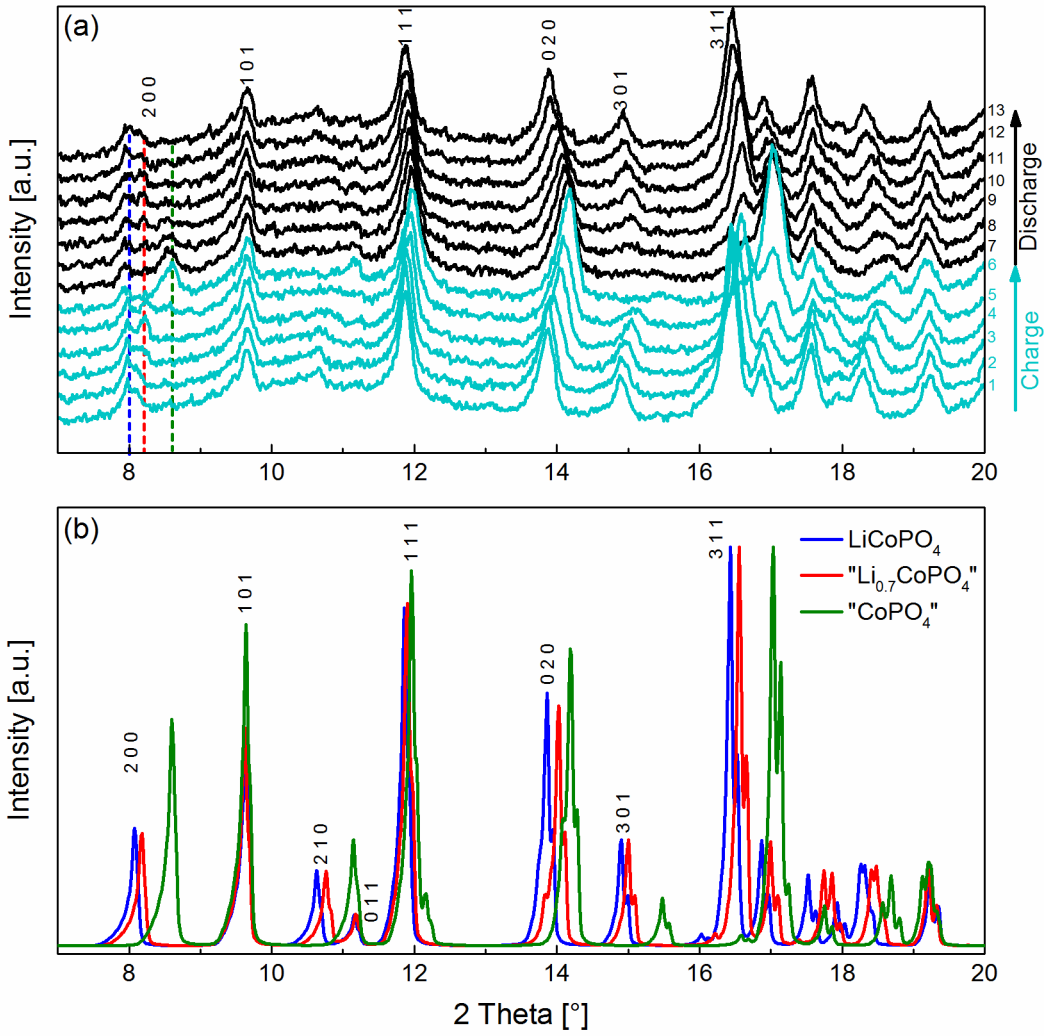

Figure 4.15: (a) Selected region in the diffraction patterns taken *in situ* during the first charge-discharge cycle of LCP (λ = 0.70930 Å). Numbers on the right side refer to labels in Figure 4.14. Vertical dashed lines are guide to the eyes to follow the phase change during cycling exemplified on the 2 0 0 reflection. (b) Theoretical patterns of the phases $LiCoPO_4$ (a=10.1955 Å, b=5.9198 Å, c=4.6971 Å), "$LiCo_{0.7}PO_4$" (a=10.070 Å, b=5.851 Å, c=4.717 Å), and "$CoPO_4$" (a=9.567 Å, b=5.7860 Å, c=4.7636 Å) with spacegroup *Pnma* according to Bramnik *et al.*[59] Pattern parameters for the theoretical calculation were chosen to mimic the pattern of the *in situ* reflection measurement (Pseudo-Voigt profile function with Gauss component, generation of $K\alpha_2$ reflections from non-monochromatized radiation, reflection asymmetry) by using the $WinX^{POW}$ software package. The Miller indices $h\ k\ l$ are given only for the phase $LiCoPO_4$ and can be accordingly adopted for the other phases due to identical space group symmetry.

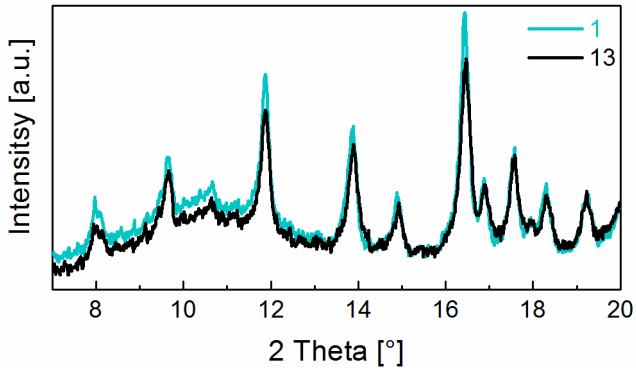

Figure 4.16: Comparison of the first and last XRD pattern of pristine and discharged LCP, respectively.

pristine $LiCoPO_4$ (phase "1"). Towards the end of the charging process phase "1" and "2" gradually vanish and a third phase is formed ($2\theta \approx 8.5°$). By comparing the reflection position of each phase with theoretical generated patterns based on data by Bramnik *et al.*,[59] who proposed the two two-phases transition for LCP for the first time, the unknown phases "2" and "3" can be assigned unambiguously to the intermediate lithium-deficient phase "$Li_{0.7}CoPO_4$" and the composition corresponding to"$CoPO_4$", respectively (see Figure 4.15b). During discharge these phase transitions are qualitatively reversed.

Furthermore, the reflections of the last pattern in the discharged state are in good agreement with the reflections of the first pattern of pristine $LiCoPO_4$ (see Figure 4.16). Since reflection intensity and broadening seems to be unaffected, it is concluded that the LCP material exhibits good structural reversibility during the first cycle. At 2θ-angles below 12°, however, a deviation in background intensity can be observed. This can be attributed to a change in electrolyte composition due to the strong oxidizing conditions at 5.0 V *vs.* Li/Li^+, which eventually influences the background at low angles.

By correlating observed phase transitions during charge to electrochemical data, it is shown that the reaction from $LiCoPO_4$ to "$Li_{0.7}CoPO_4$" is not fully completed when the second voltage plateau emerges (see diffraction pattern 1-4 and reflection (2 0 0) at $2\theta \approx 8.0°$ in Figure 4.15a). Furthermore, there is still some "$Li_{0.7}CoPO_4$" phase present at the end of the second voltage plateau when the "$CoPO_4$" phase starts to form (pattern 5) and only during prolonged charge at 5.0 V (constant voltage period) a complete transition to "$CoPO_4$" can be recognized (pattern 6). Obviously, there seems to be a lag between the two voltage plateaus and the two-phase reaction regions, which is also discussed in the literature.[59,174] Strobridge *et al.*[174] mainly ascribed this behavior to the overpotential occurring during a phase transition in order to drive the energetically unfavorable decrease in unit cell volume in $LiCoPO_4$. Their assumption was based on the comparison between open circuit voltages obtained from galvanostatic intermittent titration technique (GITT) experiments and the voltage curve obtained from galvanostatic cycling and *in situ* XRD.

4.3.4 Conclusion

The *in situ* XRD cell presented in this chapter proved to be very reliable in revealing the electrochemical extraction-insertion mechanism of LCP. It was found that the material synthesized by a solid-state route exhibits two plateaus at ≈4.8 V *vs.* Li/Li^+ and ≈4.9 V *vs.* Li/Li^+ in the voltage profile during galvanostatic charge and discharge. This behavior, however, differs from the well-known one voltage plateau characteristic for the isostructural LFP (*Pnma* space group) and therefore deviations from a pure two-phase transition can be considered. Indeed, the delithiation of $LiCoPO_4$ commences via an intermediate phase identified as "$Li_{0.7}CoPO_4$" until it reaches the final state "$CoPO_4$" during a prolonged charge. Upon re-lithiation, the reversibility of the whole process was demonstrated. Although two two-phase transitions ($LiCoPO_4$ ↔ "$Li_{0.7}CoPO_4$" and "$Li_{0.7}CoPO_4$" ↔ "$CoPO_4$") can be assumed for our system, a clear assignment for the observed two-voltage plateaus could not be established due to a lag arising from possible overpotentials during phase transition.

All in all, with the *in situ* XRD cell operating in reflection mode it was possible to successfully catch the moisture-sensitive phase "$CoPO_4$" and prove its existence during prolonged charging of the cell. This is not possible with *ex situ* XRD except under special sample preparation conditions, because this material undergoes amorphization when exposed to air. In such a case *in situ* XRD should be favored over *ex situ* XRD to unambiguously determine this instable phase. Additionally, the cell was operated in the high voltage region of 4.5-5.0 V *vs.* Li/Li^+ without any visible corrosion of the current collector/XRD window, which resulted in a stable performance that makes the cell comparable to our laboratory Swagelok T-cell as well as to the literature.

4.4 Li-S batteries with Li_2S cathodes and Si/C anodes

The article entitled *Li-S batteries with Li_2S cathodes and Si/C anodes* by Himendra Jha, Irmgard Buchberger, Xueyin Cui, Stefano Meini, and Hubert A. Gasteiger, which was published in the *Journal of The Electrochemical Society*, 2015, Volume 162, Issue 9, Pages A1829-A1835, is presented in this section. This is an open access article distributed under the terms of the Creative Commons Attribution 4.0 License (permanent weblink: http://dx.doi.org/10.1149/2.0681509jes).

With the goal to increase energy density, researchers are pursuing alternative cathode materials compared to the ones currently used in lithium-ion batteries, which are based on an insertion mechanism. Among these so-called post or beyond lithium-ion batteries, the lithium-sulfur (Li-S) system promise improved capacities that could exceed those of conventional lithium-ion batteries. Sulfur, one of the most abundant elements on earth, is an electrochemically active material that can accept up to two electrons per atom according to following reaction:[176]

$$S + 2Li^+ + 2e^- \underset{charge}{\overset{discharge}{\rightleftharpoons}} Li_2S \qquad \approx 2.1\ V \qquad (4.2)$$

As a result, sulfur cathode materials have a high theoretical capacity of 1675 mAh/g_S, which would allow energy storage up to $\approx 2500\ Wh/kg_{Li_2S}$.

Metallic lithium is commonly used as anode material in this system, but it shows morphological changes during cycling, which results in dendrite formation and internal shorts.[46,148] The use of silicon anodes might therefore offer better safety and durability characteristics for the cell, since lithium is incorporated in the silicon structure by an alloying instead of a plating process.[177] However, by replacing metallic lithium with silicon, the lithium must be introduced either on the anode or on the cathode to enable an operational system. In this study, Himendra Jha, the main author of this article, and Xueyin Cui prepared Li_2S cathodes in combination with Si/C anodes (*i.e.*, Si/C-Li_2S full-cells) to investigate both the processes during initial charging/activation of Li_2S cathodes and the effect of Li_2S cathode activation on the cycling performance of Si/C-Li_2S full-cells. It was observed that the initial activation requires a substantially higher charging potential than for the subsequent cycles.

My role in this work was the structural analysis of the first charging process of Li_2S. For this purpose, an *in situ* XRD cell according to version 1 was assembled in half-cell configuration (Li-Li_2S). The resulting diffraction analysis of the cathode during the first cycle clearly indicated the gradual transformation of Li_2S to polysulfides and finally to crystalline sulfur, *i.e.*, even large Li_2S particles ($\approx 20\mu m$) could be charged completely. I also investigated the structural changes in the Si/C-Li_2S full-cell system, which gave similar results compared to the half-cell data and thus were not discussed in this article.

The complete conversion of Li_2S was further confirmed by *ex situ* SEM/EDX analysis, which revealed the formation of large sheets of sulfur at the cathode/separator interface. Comparable cycling performance of Si/C-Li_2S full-cells was observed both at 0.1C and 1C rates, a clear advantage over Li/Li_2S half-cells, which suffer from severe dendrite formation at 1C in the case of high Li_2S loadings.

4.4.1 Introduction

High capacity energy storage systems are needed for various applications ranging from portable electronic devices to automotive applications. For the latter, a safe onboard energy storage system that can provide sufficient driving range is needed. However, the specific energy of current intercalation based lithium ion batteries (≈250-280 Wh/kg_{cell}) substantially limits the driving range compared to that of conventional fuel vehicles[22,178] so that batteries offering higher specific energy are required.

Lithium-air (Li-O_2)[179] and lithium-sulfur (Li-S)[180,181] batteries are among the most widely explored so-called post-lithium ion technologies, for which the lithium ions in the cathode react with either oxygen or sulfur during discharge, resulting in Li_2O_2 or Li_2S discharge product, respectively. Considering the high theoretical specific energy of these post-lithium ion cathodes on the *active materials level* (viz., ≈3.5 kWh/kg_{Li2O2} for Li-O_2 and ≈2.5 kWh/kg_{Li_2S} for Li-S[178]), they are very promising for use in electric vehicles, even though the specific energy gains over lithium ion batteries if compared on the *battery system level* are substantially lower.[21] However, there are still several major issues to be resolved. In the case of Li-O_2 batteries, these include the poor charge/discharge reversibility[182,183] as well as the poor stability of electrolytes[184–186] and of the catalyst support.[187] Similarly, Li-S batteries are still plagued by an irreversible loss of active sulfur species, by polysulfide shuttling, and by the continuous electrolyte consumption at the lithium electrode.[149,188] Nevertheless, Li-S battery performance/durability has improved significantly over the last few years, mainly by optimizing composite cathodes prepared of sulfur and carbon nanostructures,[189] carbon fibers,[190] and metal oxides like MnO_2 and titanium sub-oxides[191,192] as well as by optimizing electrolytes.[193,194] With these improvements, Li-S half-cells have reached reversible capacities of > 800 mAh/g_S after several hundreds of cycles.[195]

Studies in the field of Li-S batteries have mostly been demonstrated by using metallic lithium as anode, which typically is not used in commercial rechargeable batteries with liquid electrolytes because of safety issues.[196] Alternatives to the metallic lithium anode have been widely investigated during the last three decades, focusing mainly on carbon, silicon, and tin.[197] Among these, graphite is widely used as anode material in current lithium-ion batteries, but it has a relatively low specific capacity (≈372 mAh/g_C)[196] and is thus not suitable in combination with high capacity cathodes such as sulfur. In contrast, Si offers a high specific capacity (3580 mAh/g_{Si} for the electrochemically reversible $Li_{15}Si_4$), but due to its large volume expansion during charging, it suffers from both me-

chanical degradation and continuous electrolyte consumption due to the instability of the SEI (solid electrolyte interface) on the expanding/contracting silicon surface during charge/discharge. The latter can be partially mitigated by using nanostructured Si (nanowires, nanotubes, nanoparticles, etc.).[198,199]

One approach to use silicon anodes instead of metallic lithium is to use Li_2S (lithium sulfide) rather than S cathodes.[60,200,201] Unfortunately, there are very few studies on full-cells with Li_2S cathodes and high capacity Si or Sn anodes. In one study, Li_2S/C composites were prepared by milling commercially available Li_2S with carbon and testing it in a full cell with a Sn/C composite anode using a polymer electrolyte.[201] Another frequently employed approach to prepare a full-cell with a Si anode and a S cathode is through electrochemical pre-lithiation of the Si anode prior to full-cell assembly with a S cathode, as demonstrated by Elazari *et al.*[202] On the other hand, Lui *et al.* pre-lithiated silicon nanowire electrodes by physically contacting them with metallic lithium and subsequently assembling them into full-cells using S cathodes.[203] More recently, Brückner *et al.* pre-lithiated Si-coated carbon and cycled it against a S cathode with a remaining capacity of ≈400 mAh/g_S after >1000 cycles.[204]

In the present study, we have demonstrated full-cell cycling of a Li_2S cathode coupled with a Si/C anode, examining the effect of the initial Li_2S cathode activation process and comparing full-cell performance with that of Li_2S half-cells (*i.e.*, using a metallic lithium anode). *In situ* XRD and post-mortem SEM/EDX in combination with three-electrode measurements are used to elucidate the Li_2S activation process.

4.4.2 Experimental

(a) Preparation & characterization of Li_2S cathodes

Commercially available Li_2S powder (Sigma Aldrich) was used as-received to prepare Li_2S cathodes. The Li_2S particle size ranged from few hundreds of nanometers to more than 20 micrometer, as shown by the SEM image in Figure 4.17a; particle size analysis by laser scattering (not shown) indicated a median diameter of ≈10 µm (volume-averaged distribution). The ink for the electrode coating was prepared by mechanically mixing the Li_2S powder with commercial Vulcan®XC72 carbon (≈30 nm primary particles and ≈200-300 nm primary agglomerates) using a mortar and pestle, followed by dispersion in a solution of N-Methyl-2-pyrrolidone (NMP) with dissolved polyvinylidene fluoride (PVDF) for two hours using a high speed magnetic stirrer. The solids content of the ink was approximately 150 mg (Li_2S+C+PVDF) per milliliter of NMP, with a solids composition of 60 %wt. Li_2S, 30 %wt. C, and 10 %wt. PVDF. The ink was coated onto an 18 µm thick aluminum foil using a 300 µm gap doctor-blade. Because of the high reactivity of Li_2S with moisture, all the processing steps were carried out inside an Ar-filled glove box (MBRAUN; <1 ppm H_2O & <1ppm O_2). After drying inside the glove box, 10 mm diameter electrodes were punched out and further dried at 80°C under dynamic vacuum in a Büchi oven for 2 hours. For all the measurements, the Li_2S loading in the

cathode was maintained at ≈2.0 ±0.1 mg_{Li_2S}/cm^2 (≡ 2.3 ±0.1 mAh/cm^2 theoretical capacity). Morphological characterization of the cathode electrodes was carried out using SEM-EDX (Jeol, JSM 6000 equipped with EDX) using an air-tight specimen holder to transfer samples from the glove box to the SEM chamber.

(b) Silicon/carbon anodes

The Si anodes used in this study contained 20 %wt. nano-silicon particles, 60 %wt. graphite, 12 %wt. conductive carbon-black, and 8 %wt. Na-CMC binder, supported on a Cu-foil current collector (Si anodes were provided by Wacker Chemie AG). The areal weight of the anode electrodes was 2.2 mg/cm^2 (including Si, graphite, carbon-black, and binder). Assuming specific capacities of 3580 mAh/g_{Si},[19,205] 372 $mAh/g_{graphite}$, and 150 $mAh/g_{carbon\text{-}black}$,[206] the theoretical capacity of the Si/C anodes equates to 2.1 mAh/cm^2. Anodes were punched out with a diameter of 10 mm (*i.e.*, 0.785 cm^2).

(c) Electrochemical characterization

All electrochemical testing was conducted in a Swagelok type cell using DOL:DME (1:1 v/v) with 1M LiTFSI and 0.5M $LiNO_3$ electrolyte; the amount of electrolyte was normalized to ≈40 µl/cm^2 for Li/Li_2S or Li/Si half-cell measurements, and to ≈35 µl/cm^2 for Si/Li_2S full-cell measurements. Three layers of Celgard® C480 were used as a separator. Most experiments were conducted in a two-electrode configuration, except in few specifically mentioned instances when a three-electrode configuration with a metallic lithium reference electrode was used. The cells were cycled galvanostatically (BioLogic VMP3 potentiostat) at different currents (rates) between 1.7 and 3.0 V_{Li} for Li/Li_2S half-cells, between 0.02 and 1.5 V_{Li} for Li/Si half-cells, and between 1.3 and 2.6 V_{cell} for Si/Li_2S full-cells. Before cycling the cells, the Li_2S cathodes were initially activated by charging them up to 4.0 V_{Li} for half-cells (Li/Li_2S) and 3.8 V_{cell} for the full-cells (Si/Li_2S). All cells were cycled in a climatic chamber at 25°C.

(d) In situ XRD measurements

A specially designed cell was used for the *in situ* X-ray diffraction measurements, in which the aluminum current collector of the cathode electrode served as X-ray window. X-ray diffraction (XRD) patterns were recorded using a STOE Stadi P diffractometer equipped with a linear position-sensitive detector (Dectris Mythen 1K) and a Mo K_α source (50 kV of tube voltage and 20 mA current) in a Bragg-Brentano configuration. Each diffraction pattern was measured in three ranges with a step size of 15° (2θ = 4-18°, ω = 6.5° fixed). The 2θ range was chosen so that the reflections from the aluminum window do not interfere with the reflections of the Li_2S. The exposure time for each range was 180s, equating to an acquisition time of 9 minutes for a complete *in situ* diffractogram.

4.4.3 Li/Si half-cell characterization

Commercially available Li_2S powder with particle size up to ≈20 µm (Figure 4.17a) was used to prepare the cathode electrodes. Since the ink for the cathode was prepared by stirring, *i.e.*, without exposing to strong shear forces during mixing, one would expect a similar Li_2S particle size distribution in the cathode. This is indeed the case, as illustrated by the electrode surface morphology shown in Figure 4.17b, where large particles are ascribed to non-fractured Li_2S particles.

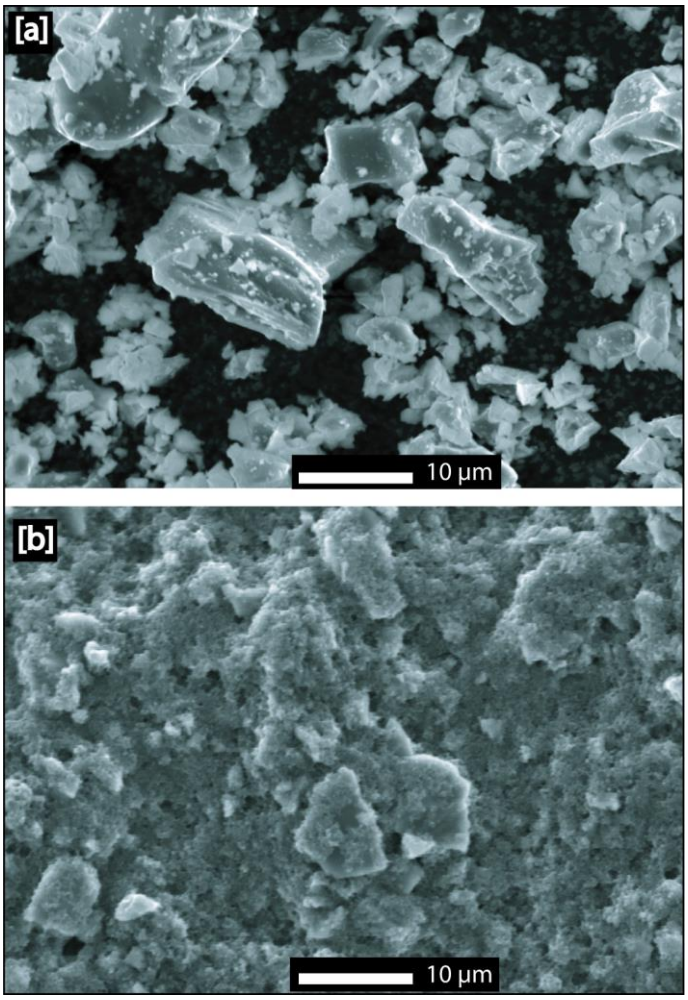

Figure 4.17: SEM images of (a) commercial Li_2S particles used in this study; (b) surface morphology of a dried Li_2S cathode. The scale-bar in the images corresponds to 10 µm.

Figure 4.18a shows the initial five charge/discharge cycles of the Si anode in a Li/Si half-cell at a rate of C/4.5 (referenced to the theoretical Si/C anode areal capacity of 2.1 mAh/cm^2, and corresponding to a geometric current density of 0.46 mA/cm^2). It can be observed that the very first lithiation capacity (red dashed line in Figure 4.18a) reaches the calculated theoretical capacity (see experimental section), following a potential profile which is characteristic of crystalline silicon.[205] After the first lithiation and delithaiation cycle, the specific lithiation and delithiation capacity decreases to a constant value of

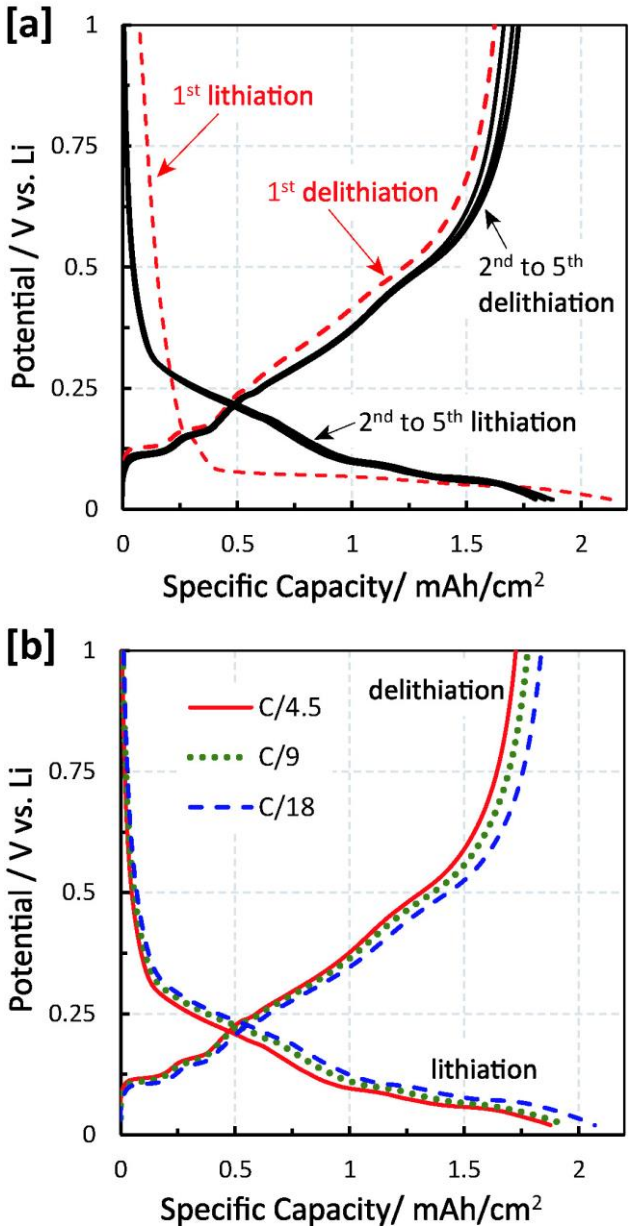

Figure 4.18: Galvanostatic lithiation and delithiation of the Si/C composite anode electrode (Li/Si half-cells). (a) 5 cycles of lithiation and delithiation at C/4.5, and (b) comparison of the 2nd cycle at C/4.5, C/9, and C/18. The C-rates are calculated based on the theoretical capacity of 2.1 mAh/cm^2 for the Si/C anode. The cells were cycled in DOL:DME (1:1 v/v) with 1M LiTFSI and 0.5M $LiNO_3$.

≈1.8 mAh/cm^2, corresponding to ≈85% of the theoretical areal capacity of the composite anode. The higher capacity observed in the first lithiation is attributed to SEI formation on the Si surface. The potential profile of the subsequent lithiation cycles is different from the first one, reflecting the typical lithiation profile of amorphized silicon.[205] As shown in Figure 4.18b, the 2nd cycle lithiation/delithiation capacities for these Si/graphite composite anodes is nearly independent of rate between C/18 and C/4.5. Overall, from these results it can be concluded that the reversible capacity of the Si anodes in our study is ≈1.8 mAh/cm^2 (within the first four cycles after the initial formation) and does not change significantly within the measured range of C-rates.

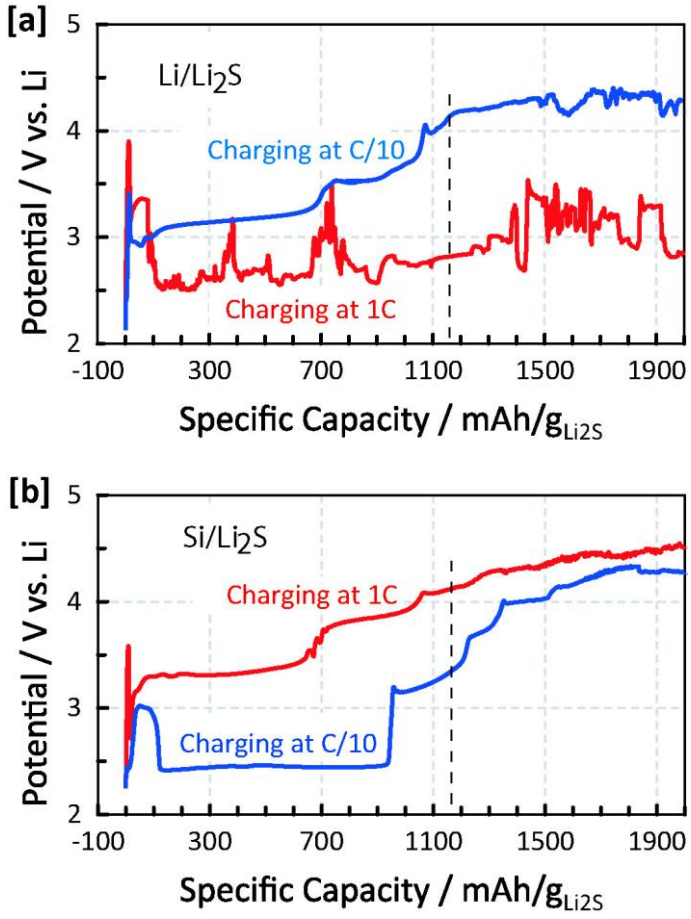

Figure 4.19: Initial galvanostatic charging of Li/Li_2S half-cells (a), and Si/Li_2S full-cells (b) at rates of C/10 and 1C without imposing an upper potential limit. The y-axis (potential) is referenced in both cases against lithium, whereby a two-electrode cell was used in the Li/Li_2S half-cell experiments and a three-electrode cell with a lithium reference electrode was used in the Si/Li_2S full-cell experiments. The vertical dashed line indicates the theoretical capacity of Li_2S. The C-rates are calculated based on $C_{theoretical}$ = 1165 mAh/g_{Li_2S} for the Li_2S cathode. The cells were cycled in DOL:DME (1:1 v/v) with 1M LiTFSI and 0.5M $LiNO_3$.

4.4.4 Activation of Li_2S in Li/Li_2S and Si/Li_2S cells

Similar to the initial high-potential activation required during charging of Li_2O_2 pre-filled cathodes in the case of Li-O_2 batteries,[207] we found that the initial charging of Li_2S cathodes also requires activation at higher potentials. This observation was reported also by Yang *et al.*,[60] who showed that a ≈1 V overpotential is required during the first charge of a Li/Li_2S half-cell in comparison to charging a discharged Li/S cell, which they ascribed to the initial barrier of forming soluble polysulfides in the electrolyte, which in turn serve as an electron shuttle between the electronically conductive carbon matrix and the Li_2S particles. Consistent with this hypothesis, Meini *et al.*[208] found that the high potential re-

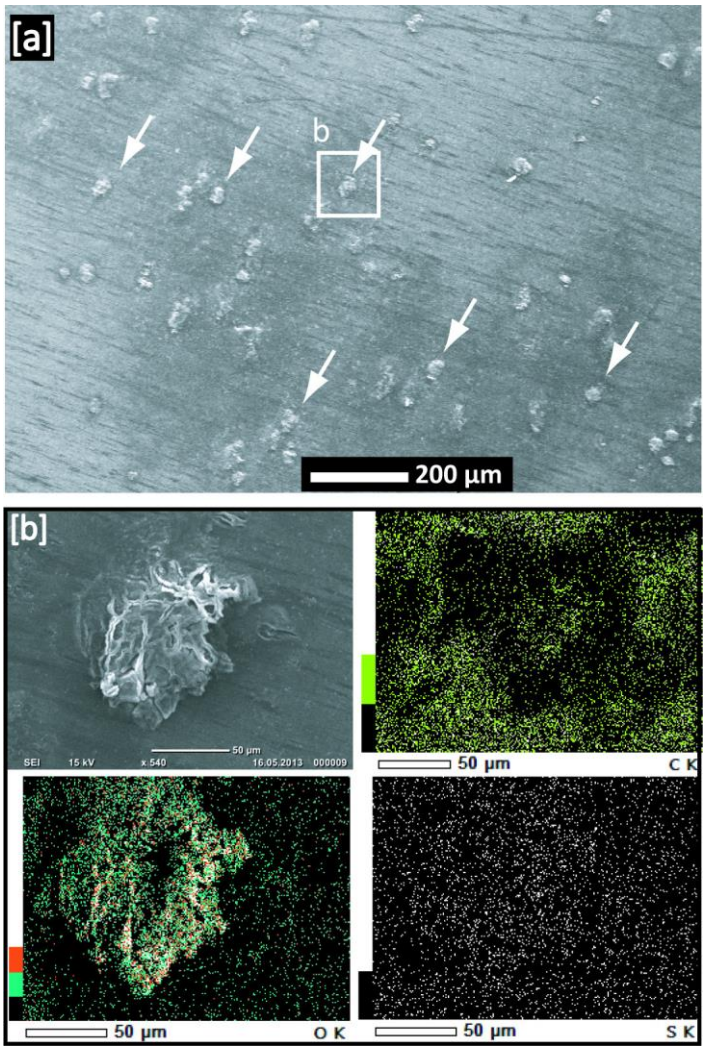

Figure 4.20: (a) SEM image of the middle separator (out of three layers) of a Li/Li_2S half-cell after initial charging at 1C as shown by the red curve in Figure 4.19a. (b) EDX mapping of carbon, oxygen, and sulfur of a lithium dendrite feature in the separator, whereby the high oxygen signal at the location of the dendrite originates from lithium which was deliberately exposed to air in order to oxidize it. The C-rates are calculated based on $C_{theoretical}$ = 1165 mAh/g_{Li2S} for the Li_2S cathode.

quired in the first charging step of Li_2S cathodes can be eliminated in the presence of redox-active additives.

Figure 4.19a shows the initial charging of a Li_2S cathode against a Li anode (Li/Li_2S half-cell) at rates of C/10 (blue line) and 1C (red line), with the voltage initially increasing to potentials of ≈3.4 V_{Li} and ≈3.9 V_{Li}, respectively, followed by a sharp decrease to a lower voltage plateau region. At the rate of C/10 (blue line), two charging plateaus at ≈3.2 and at ≈3.5 V_{Li} are observed until the charging capacity approaches its theoretical value of 1165 mAh/g_{Li_2S}, at which point the voltage increases to ≈4.2 V_{Li}, where the current is sustained by the continuous oxidation of the DOL/DME electrolyte. On the other hand, at a rate of 1C, the charging voltage strongly fluctuates and the charging process continues indefinitely between 2.5 and 3.5 V_{Li}, which we ascribe to the intermittent formation of lithium dendrites at this rather high current density of 2.3 mA/cm^2 (dendrite formation was shown to occur by Aurbach *et al.*[46] at >1 mA/cm^2). This is evidenced by SEM/EDS analysis of the middle separator removed from the Li/Li_2S cell after 1C charging (s. Figure 4.20a): the separator was severely penetrated by lithium dendrites with a spot-size of 50μm or more, and EDX mapping shows that these spots have a high oxygen content, indicating lithium oxides, hydroxides, or carbonates formed during air exposure of the separator (the separator was intentionally exposed to air to oxidize metallic lithium dendrites). These results confirm that the high current density during 1C charging (2.3 mA/cm^2) leads to severe dendrite formation if metallic lithium used as anode.

As one would expect, lithium dendrite formation at high C-rate can be avoided during initial charging of a Li_2S cathode in Si/Li_2S full-cells, as evidenced by the smooth charging profile at 1C in full-cells shown in Figure 4.19b (red line), where the potential is referenced against a metallic lithium reference electrode (using a three-electrode cell). Again, the capacity obtained as the potential reaches 4 V_{Li} is close to the theoretical capacity of the Li_2S cathode.

In order to confirm that Li_2S is oxidized completely during the first activation cycle and to determine whether the lower and upper plateaus at the C/10 charging profile in the Li/Li_2S half-cell (blue line in Figure 4.19a) are indeed related to Li_2S charging, *in situ* XRD analysis was carried out with a Li_2S cathode and a lithium metal counter electrode. Figure 4.21a shows the charging potential profile (vs. lithium) for a Li_2S cathode at C/10 in the *in situ* XRD cell, which is in excellent agreement with the charging profile obtained with a standard Swagelok cell (see Figure 4.19a, blue line). The labels placed along the charging curve (letters a - i in Figure 4.21a) mark the collection of the XRD diffractograms shown in Figure 4.21b (note that the diffractograms were acquired over a time of 9 minutes during cell charging). As expected, sharp peaks corresponding to the (111) and (200) diffractions of Li_2S are observed at the beginning of the charging process (a in Figure 4.21b), then gradually decrease during the first charging plateau at ≈3.2 V_{Li} (b – d in Figure 4.21b), and remain visible throughout the second charging plateau of ≈3.5 V_{Li} (e and f in Figure 4.21b). The Li_2S diffraction peaks only disappear after the second charging plateau, *i.e.*, after having reached 85-90% of the theoretical Li_2S charge capacity (g - i

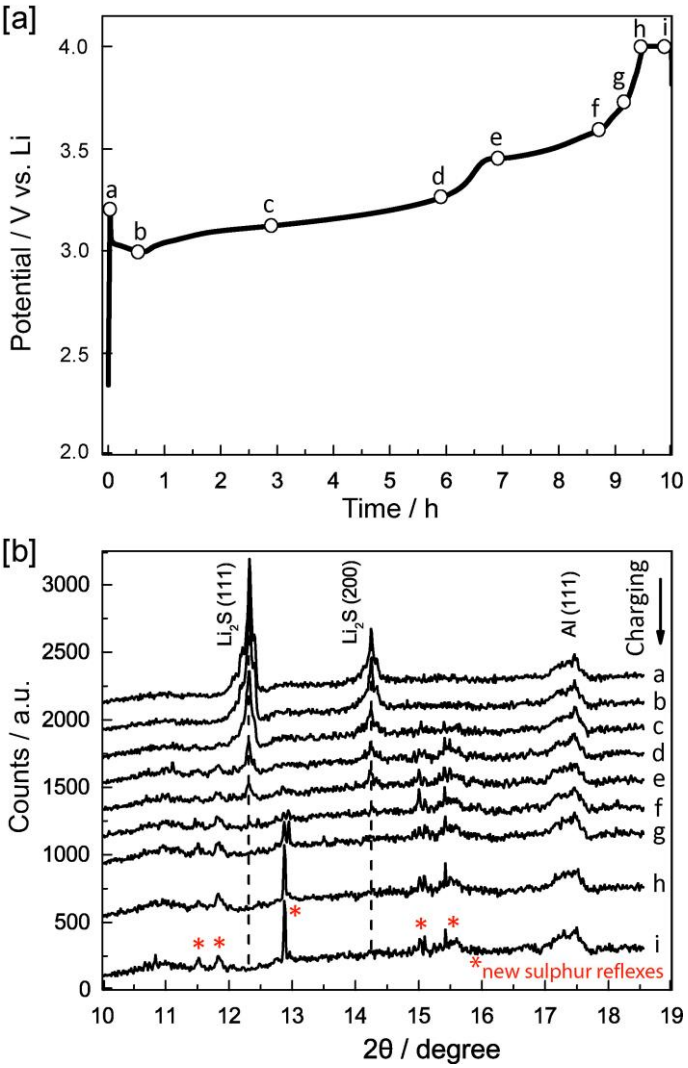

Figure 4.21: *In situ* XRD analysis of a Li_2S cathode (vs. lithium metal) during initial activation/charging at a rate of C/10 (The C-rate is calculated based on $C_{theoretical}$ = 1165 mAh/g_{Li_2S} for the Li_2S cathode). (a) Potential vs. charge profile and (b) diffractograms acquired at the positions marked in the charging curve (a – i), with an acquisition time of 9 min.

in Figure 4.21b). This may be compared to the study by Cañas *et al.*,[125] who observed the disappearance of Li_2S diffractions during the charge of a discharged S cathode at already ≈50% of the charging capacity, which is most likely due to the much smaller Li_2S particles formed during S cathode discharge compared to the ≈20 µm large Li_2S particles in our electrodes.

The appearance and growth of new diffraction peaks (marked by * in Figure 4.21b) can be observed at already ≈60% of charging (d in Figure 4.21b), developing into sharp diffraction peaks after ≈90% of charging (g in Figure 4.21b), which suggests the formation of large crystallites. These peaks must be related to the formation of crystalline sulfur, even though their positions do not exactly match the PDF database, indicating the

formation of a new crystalline phase of sulfur. A similar observation was reported by Cañas *et al.*,[125] who reported sulfur reflections after ≈90% of charge of a previously discharged sulfur cathode, with diffraction patterns which were also different from the PDF database. Furthermore, Nelson *et al.*[61] also observed the formation of crystalline sulfur after ≈80% charging of a discharged sulfur cathode. These findings, however, contradict the *in situ* XRD study by Yang *et al.*,[60] where no crystalline sulfur is observed even after complete charging of their Li_2S cathode; the origin of this discrepancy is unfortunately not clear.

In summary, the analysis of Figure 4.21 suggests that the charging process in the first plateau at ≈3.2 V_{Li}, which extends to ≈60% of the charging, can be assigned to the transformation of Li_2S to lithium polysulfides and possibly small amounts of sulfur, as the potential is sufficiently high to oxidize polysulfides to sulfur. After the second charging plateau (g in Figure 4.21), all Li_2S diffraction peaks have vanished and sharp diffraction peaks related to crystalline sulfur appear (at around 2θ = 12.8°), indicating the formation of large sulfur crystallites in the charged Li_2S cathode.

The formation of large crystalline sulfur domains after charge of the Li_2S cathode was verified by *ex situ* SEM/EDX analysis of the Li_2S cathode after charging to a cut-off potential of $4V_{Li}$ at C/10, *i.e.*, after nearly 100% of the theoretical charge was obtained. For this investigation, the cell was disassembled inside a glove box, washed with DME to remove any residual polysulfides from the cathode, and then the electrode transferred into ambient air in order to convert potentially remaining Li_2S into Li_2CO_3, LiOH, and Li_2O; subsequently, the sample was transferred into the SEM. Strikingly, as shown in Figure 4.22a, the surface of the cathode was covered with large sheets of sulfur, as confirmed by the EDX elemental mapping: the sulfur map matches the SEM image (compare Figure 4.22a and c), while no common patterns are observed between the oxygen map and the SEM image (compare Figure 4.22a and d), which after air exposure could only be the case for elemental sulfur. The sulfur sheets extend over several hundreds of micrometers across the cathode surface, whereby imprints from the separator can be observed on the sulfur sheets. The cross-section of the cathode was examined after bending of the electrode, as shown in Figure 4.22b. Empty pockets inside the cathode electrode can be clearly seen, the sizes of which are consistent with the initial size of the Li_2S powder used to prepare the Li_2S cathode, which is consistent with the absence of Li_2S diffraction peaks after charging (s. Figure 4.21).

Analogous to our study, the formation of large crystalline sulfur domains at the cathode/separator interface upon charging of a discharged sulfur electrode was also observed by Cañas et.al.,[125] albeit with different shapes/morphology. We believe that the accumulation of sulfur at the cathode/separator interface during the last stages of the charging process is most likely due to the oxidation of dissolved polysulfides (solubility of 0.1 to 1 mol/l in the electrolyte) contained inside the separator (rather than inside the cathode) during the final stages of charging: under this condition, the high cathode potential will cause the rapid and highly localized oxidation of polysulfides which are stored inside the

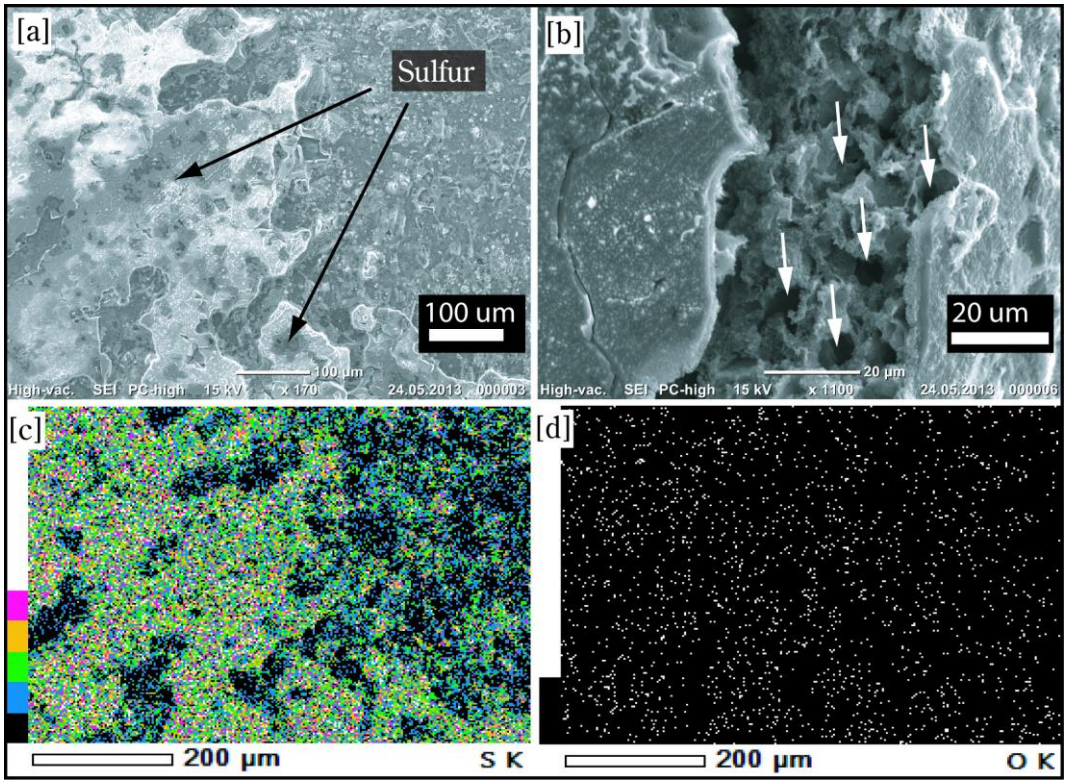

Figure 4.22: SEM/EDX analysis of a Li_2S cathode after charging to 4.0 V at C/10 vs. a Li-anode. (a) SEM image of the cathode, showing a compact sheet of sulfur covering the surface. (b) SEM image inside a crack (made intentionally by bending the cathode) of the cathode electrode, showing empty pockets in the cathode electrode layer. EDX elemental mapping of the surface shown in (a) is given for sulfur and oxygen in (c) and (d), respectively (the C-rate is calculated based on $C_{theoretical}$ = 1165 mAh/g_{Li_2S} for Li_2S cathode).

separator region once they reach the cathode/separator interface, thereby forming a deposit at this very interface.

4.4.5 Activation and cycling of Si/Li_2S full-cells

The activation and subsequent cycling of Si/Li_2S full-cells was investigated using Si/C anodes and Li_2S cathodes of theoretical capacities of ≈2.1 and ≈2.3 mAh/cm^2, respectively. In order to monitor the charge/discharge behavior of each electrode, the Si/Li_2S full-cells were assembled with a metallic lithium reference electrode in a three-electrode cell. The questions to be addressed were: *i)* whether the polysulfide shuttling currents would be low enough to allow for a complete charging of the Si/C anodes; *ii)* whether the high voltages at 1C activation (≈3.3/≈3.5 V_{Li} in the 1st/2nd charging plateau; red line in Figure 4.19b) compared to C/10 activation (≈2.5/≈3.1 V_{Li} in the 1st/2nd charging plateau; blue line in Figure 4.19b) would affect the subsequent cycling stability, as activation at lower potentials was suggested to improve cycle-life;[208] and, *iii)* whether the long-term cycling stability of Si/Li_2S full-cells would be comparable with that of Li/Li_2S half-cells.

The Si/Li_2S full-cells were subjected to an initial activation from OCV (≈0.3 V_{cell}) to a cell voltage of 3.8 V_{cell} at two different rates, viz., C/10 (Figure 4.23a) and 1C (Figure 4.23b), followed by continuous cycling between 1.3 and 2.8 V_{cell} at C/5 rate. Figure 4.23a and b show the potential variation of the Li_2S cathodes vs. Li reference (curve 1, dashed blue line), the cell potential of the Si anodes vs. the Li_2S cathodes (curve 2, black line), and the potential of the Si anodes vs. Li reference (curve 3, dashed red line). Examining the first activation cycle at both C/10 and 1C (initial charging panels in Figure 4.23a and b, respectively), it is clear that the potential of the Si anodes is gradually lowered to <0.5 V_{Li}, where lithium ion intercalation will occur. The fact that the Si anode potential decreases faster to below 0.5 V_{Li} at 1C (at ≈120 mAh/g_{Li_2S}; dotted red line in Figure

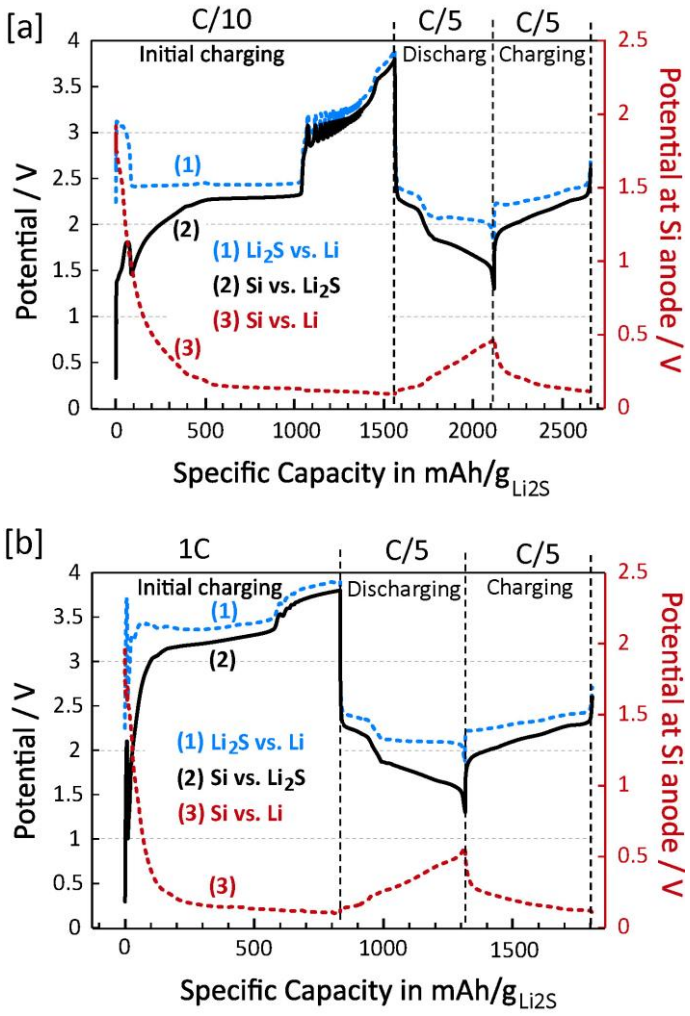

Figure 4.23: Cell voltage (left axis) vs. charge (black solid line) of a Si/Li_2S full-cell during activation at (a) C/10 and (b) 1C, followed by cycling at C/5. The experiment was conducted in a three-compartment cell with a Li reference electrode, and the potentials referenced to Li are shown for the Li_2S cathode (blue dashed line) on the left axis and for the Si anode (red dotted line) on the right axis. The C-rates are calculated based on $C_{theoretical}$ = 1165 mAh/g_{Li_2S} for the Li_2S cathode.

4.23b) compared to charging at C/10 (at ≈320 mAh/g_{Li_2S}; dashed red line in Figure 4.23a) is ascribed to the polysulfide shuttling current, which consumes a larger fraction of the charging current at the lower C-rate. At the end of the activation cycle, the Si anode potentials reach ≈0.1 V_{Li}, which according to Figure 4.18b would correspond to a ≈50% charge of the Si anode (≈1 mAh/cm^2). The missing charge compared to the expected ≈2.1 mAh/cm^2 (s. above) must be caused by the irreversible lithium loss for SEI formation.

This is consistent with the only ≈50% theoretical cell capacity obtained in the second discharge/charge cycle at C/5 shown in Figure 4.23: ≈550 mAh/g_{Li_2S} corresponding to ≈1.1 mAh/cm^2 at C/10 and ≈500 mAh/g_{Li_2S} corresponding to ≈1.0 mAh/cm^2. If compared with the Si anode half-cell data at the same current density (red lines in Figure 4.23b), a charge/discharge capacity of ≈1.0-1.1 mAh/cm^2 is consistent with the observed Si anode potentials in the 2nd cycle, ranging between ≈0.12 and ≈0.5 V_{Li} (s. C/5 segments in Figure 4.23). These results clearly indicate that the capacity of the cell is limited by the Li_2S cathode due to a large irreversible lithium loss during the first charging cycle, while only about ≈50% of the anode's capacity is used. Consequently, we expect that the Si/Li_2S full-cell performance will improve by applying an excess cathode capacity of Q_{Li_2S}/Q_{Si} between 1.5/1 and 2/1, which we will explore in future experiments.

The Li_2S cathode potential profiles during activation (blue dashed lines in Figure 4.23) are essentially identical to those shown in Figure 4.19b, except that potential oscillations are observed toward the end of the C/10 charging curve (dashed blue line in Figure 4.23a). Indeed, we have frequently observed these potential oscillations during charging at low C-rates, and Figure 4.23a clearly shows that it is caused by the Li_2S cathode and not the anode electrode. The fact that these oscillations appear in the second charging plateau, where we had observed the onset of the formation of crystalline sulfur phases (see Figure 4.21) suggests that they are related to the formation of current-blocking sulfur domains at the separator/cathode interface (see Figure 4.22). The absence of these oscillations at the higher rate of 1C would then suggest that the formation of large sulfur sheets might be suppressed at higher rates, which could be explained by fact that the cathode potential in that case is far above the potential required for the complete reduction of polysulfides to sulfur, so that the polysulfide concentration in the separator will remain low (see above discussed hypothesis for the sulfur sheet formation at the separator/cathode interface).

The long-term cycling performance of Si/Li_2S full-cells is shown in Figure 4.24a (showing the average and the standard deviation of two cells for each test sequence), exploring the effect of C-rate during activation and during long-term cycling on capacity retention: *i)* initial activation at 1C followed by cycling at C/5; *ii)* initial activation as well as cycling at 1C; and, *iii)* initial activation at C/10 followed by C/5 cycling. It can be seen that the cells that were activated at C/10 followed by C/5 cycling show somewhat higher capacities (red line in Figure 4.24a) compared to the cells which were activated at 1C and

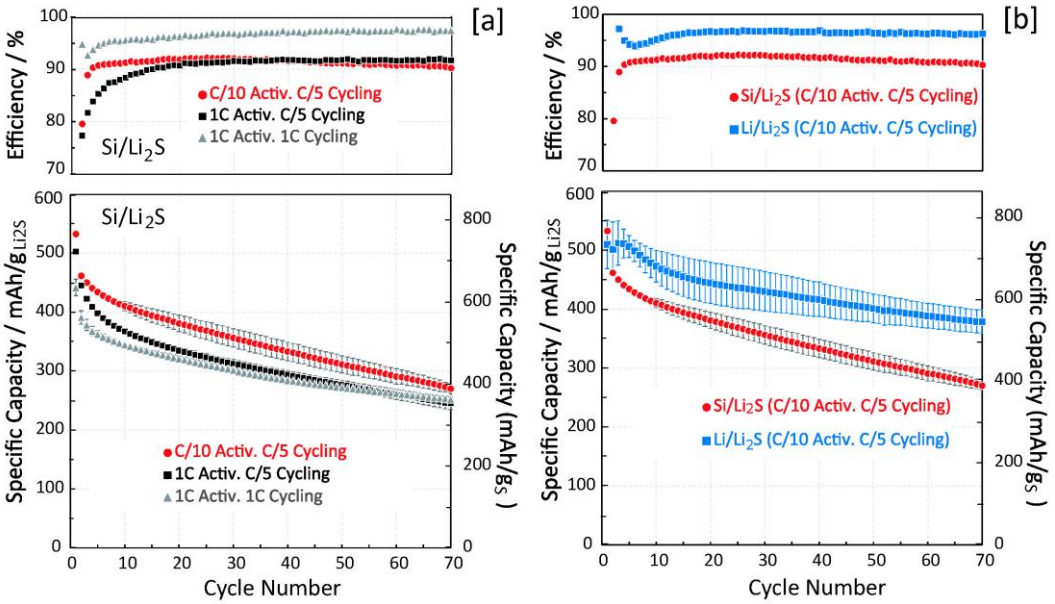

Figure 4.24: (a) Activation and cycling performance of Si/Li_2S full-cells at different rates for the 1st cycle charge ("activation") and different subsequent cycling rates: Comparison of Si/Li_2S full-cells at different activation and cycling rates; (b) Comparison of the cycling performance of Si/Li_2S and Li/Li_2S cells after initial activation at C/10 and subsequent cycling at C/5. The upper panels of each graph indicate the Coulombic efficiency ($\equiv Q_{discharge}/Q_{charge}$). The C-rates are calculated based on $C_{theoretical}$ = 1165 mAh/g_{Li_2S} for the Li_2S cathode. The error bars represent the standard deviations of two cells in each case. Capacities are referenced to either Li_2S (left y-axes) or S (right y-axes).

cycled at either C/5 or 1C (black and grey lines in Figure 4.24a). While the difference is small, it might be related to the much lower charging voltages if the initial activation step (*i.e.*, the very first charging cycle) is done at C/10 instead of at 1C (see Figure 4.23), which might prevent the formation of electrolyte decomposition products at the initially high voltages that could compromise cycle-life. The higher coulombic efficiency of the cells cycled at 1C (grey lines in top panel of Figure 4.24a) compared to the cells cycled at C/5, independent of the activation procedure (red and black lines in Figure 4.24a), is indicative of significant polysulfide-shuttle currents, which play a lesser role at the higher C-rate. After 70 cycles, the cells activated at C/10 and cycled at C/5 have a remaining capacity of 280 mAh/g_{Li_2S}, (≡400 mAh/g_S). To our knowledge, our study is the first to examine the long-term stability of Si/Li_2S full-cells based on Li_2S powder based cathodes and Si based anodes. The only related study is the work by Yang *et al.*,[209] who cycled Si anodes with Li_2S cathodes obtained by lithiation of a sulfur cathode with n-butyllithium, observing mych higher capacity fading (to ≈250 mAh/g_{Li_2S} after only 20 cycles at a similar rate of C/3).

On the other hand, Si/S full-cell data have been obtained combining electrochemically pre-lithiated Si anodes with S cathodes. For the latter configuration, Elazari *et al.*[202] demonstrated ≈380 mAh/g_S after 60 cycles at C/5, and Brückner *et al.*[204] showed ≈400 mAh/g_S after 1400 cycles at C/2 (≈700 mAh/g_S after 70 cycles at C/2). They also

showed increased capacity fading with increasing C-rate for Li/S half-cells, while high C-rates of a large number of cycles could be maintained with Si/S full-cells based on S cathodes and pre-lithiated Si anodes, which they ascribed to both a larger irreversible electrolyte loss at the lithium anode and/or lithium dendrite formation. Without providing any proof, their hypothesis would suggest that the rate capability of Si/S or Si/Li_2S full-cells would be higher than that of Li/S or Li/Li_2S half-cell. That this is indeed the case is shown by our Si/Li_2S full-cell tests, which demonstrate the same capacity retention of 350 mAh/g_S (≡250 mAh/g_{Li_2S}) after 70 cycles, independent of whether cells were cycled at 1C or C/5 (grey and black lines in Figure 4.24a, respectively). Thus, we can provide for the first time an unambiguous proof that the poor rate capability in Li/S or Li/Li_2S half-cells is caused by the lithium anode and that the kinetics of the sulfur cathode is much faster than previously assumed based on half-cell data.

Furthermore, the fact that the capacity retention of Si/Li_2S full-cells is the same at C/5 and 1C demonstrates that capacity fading is not related to total time, but to the number of cycles, which points towards irreversible lithium loss, originating from SEI expansion/contraction during each cycle. This is indeed supported by a comparison of the capacity retention between Si/Li_2S full-cells and Li/Li_2S half-cells at C/5 (s. Figure 4.24b): while the initial capacities are quite similar for half-cells and full-cells, the capacity retention of half-cells is superior (≈550 vs. ≈400 mAh/g_S after 70 cycles), which supports the above hypothesized active lithium loss into the SEI. Here it may be noted that the capacity retention of our Li/Li_2S half-cells compares reasonably well with that shown previously by Yang *et al.*[60] (≈650 mAh/g_S after 50 cycles at C/10) and Cai *et al.*[210] (≈550 mAh/g_S after 45 cycles at C/5).

4.4.6 Conclusion

Li_2S cathodes were prepared from as-received Li_2S powder (≈20µm particle size) and *in situ* XRD half-cell measurements clearly showed that Li_2S could be completely decomposed during the first charge and that crystalline sulfur was being formed. This was confirmed by *ex situ* SEM/EDX, revealing the presence of very large sulfur sheet (>100 µm) located at the separator/cathode interface, which we believe is caused by the oxidation of dissolved polysulfides present in the separator.

Li_2S cathodes were also tested in full-cells using Si/C composite electrodes without any pre-treatment. While Li/S and Li/Li_2S half-cells have been shown in the literature to have a poor capacity retention at high C-rates, we could demonstrate for the first time that the capacity and the capacity fading of Si/Li_2S full-cells is identical for C/5 and 1C. This suggests that the apparently poor rate capability of sulfur cathodes tested in half-cells is caused by the lithium electrode and that the intrinsic charge/discharge kinetics of sulfur cathodes are much larger than previously thought.

Acknowledgment: The authors would like to acknowledge funding of this work from the Federal Ministry of Education and Research (BMBF) under agreements number 03X4627A ("LiSSi" project) and number 03X4633A ("ExZellTUM" project) and to acknowledge Wacker AG for providing the Silicon anodes used in this study. Furthermore, we would like to thank Stefan Haufe, Jürgen Stohrer, and Robert Maurer from Wacker AG as well as and Oliver Gröger from Volkswagen AG for valuable discussions. S.M. would like to acknowledge financial support from BASF SE through the framework of its Scientific Network on Electrochemistry and Batteries. The authors would also like to thank Anna Eberle for her help with cell building and testing.

4.5 Aging analysis of graphite/$LiNi_{1/3}Mn_{1/3}Co_{1/3}O_2$ cells using XRD, PGAA, and AC impedance

The article entitled *Aging analysis of graphite/$LiNi_{1/3}Mn_{1/3}Co_{1/3}O_2$ cells using XRD, PGAA, and AC impedance* by Irmgard Buchberger, Stefan Seidlmayer, Aneil Pokharel, Michele Piana, Johannes Hattendorff, Petra Kudejova, Ralph Gilles, and Hubert A. Gasteiger, which was published in the *Journal of The Electrochemical Society*, 2015, Volume 162, Issue 14, Pages A2737-A2746, is presented in this section.

For this comprehensive study, the performance degradation of graphite/NMC lithium ion cells charged and discharged up to 300 cycles at different operating conditions of temperature and upper cut-off potential (4.2V/25°C, 4.2V/60°C, and 4.6V/25°C) was investigated. A combination of electrochemical methods with X-ray diffraction (XRD) both *in situ* and *ex situ* as well as neutron induced Prompt-Gamma-Activation-Analysis (PGAA) allowed us to elucidate the main failure mechanisms of the investigated lithium ion cells.

Preliminary *in situ* XRD investigations of the NMC material revealed that the first cycle "irreversible" capacity is the cause of slow lithium diffusion kinetics. In full-cells, however, this "lost" lithium ions can be used to build up the solid electrolyte interface (SEI) of the graphite electrode during the initial formation cycle. Hence, NMC stays the charge delivering and thus the capacity limiting electrode. By determining the *c*/*a* ratio of harvested NMC cathodes in the discharged state using *ex situ* XRD, the loss of active lithium can be determined.

Besides loss of active lithium, transition metal dissolution/deposition on graphite strongly effects cell aging, especially at elevated temperatures and high upper cut-off potentials. In close collaboration with the neutron source (FRM II, Heinz Maier-Leibnitz Zentrum (MLZ) in Garching involving Stefan Seidlmayer, Petra Kudejova, and Ralph Gilles) the deposition of transition metals on graphite was quantified with PGAA. In contrast to other elemental analysis methods like ICP-OES, this non-destructive method allowed us to recycle the graphite electrodes and use them for further analysis, *e.g.*, half-cell studies.

Due to the combination of different electrochemical and analytical techniques, it was found that loss of active lithium, transition metal dissolution/deposition and growth of cell impedance strongly affect cell aging, especially at elevated temperatures and high upper cutoff voltages.

My part in this work comprised all electrochemical and structural experiments on the graphite/NMC system as well as the preparation of samples for *ex situ* XRD and PGAA

analysis. The evaluation of the diffraction patterns resulting from both *ex situ* and *in situ* XRD data was conducted in close collaboration with Stefan Seidlmayer. For *in situ* XRD analysis, cell version 2 was utilized. Being the main author, I organized the experiments, guided the discussion of experimental results and prepared the manuscript for this article.

4.5.1 Introduction

Besides their current use in portable power electronics, lithium ion batteries have recently been used for battery electric vehicles (BEV) and are envisioned for large-scale energy storage. For the latter applications, life times of >10years are required so that it is essential to understand and quantify the mechanisms that contribute to battery failure. Among the commercially available lithium-ion battery chemistries,[13,211] the graphite/$LiNi_{1/3}Mn_{1/3}Co_{1/3}O_2$ (NMC) system is one of the materials currently envisioned for automotive applications.[21] This cathode material demonstrates high capacity, good structural stability due to its small volume changes (<2%) during Li insertion and extraction, and high thermal stability in the charged state.[212–214] In addition, this material could theoretically be operated with high charge cut-off potentials up to 5.0 V, as its bulk structure is claimed to be stabilized by the presence of Mn^{4+},[215] even though other authors suggest that irreversible structural changes occur at these very high potentials and at high temperature.[216] Due to its sloped potential profile, the capacity and also the average cell voltage increase with increasing charging potential.[215,217]

Despite the improved safety and cycling performance of NMC material, operating NMC based cells (full-cells or half-cells) at elevated temperatures or at high charge potential leads to poor cycle life.[55,218–220] During cycling of graphite/NMC full-cells, transition metal dissolution from the NMC material is found to be a crucial factor controlling capacity fade.[219,220] In one of these studies, Zheng *et al.* demonstrated that upper cut-off potentials of >4.3 V lead to transition metal dissolution from NMC and thus compromise cycling performance.[220] Based on half-cell experiments, Gallus *et al.* proposed that transition metal dissolution is promoted by an acidic corrosion reaction due to the presence of HF,[55] suggested to be produced by the reaction of $LiPF_6$ salt with trace water in standard electrolytes.[221] Removal of transition metals from the NMC structure not only affects cathode performance (loss of active material and/or structural changes of the particle surface), but also strongly influences the anode through the deposition of dissolved transition metals on the graphite surface. Already small amounts of Ni, Mn, and Co on the anode can result in enhanced electrolyte decomposition and impedance rise of the cell.[222–225]

In addition to increased anode impedance, it is also hypothesized that part of the capacity loss observed in full-cells in the presence of dissolved manganese is due to the continuous loss of active lithium.[226,227] This is explained by the incorporation of manganese into the solid electrolyte interface (SEI) of the anode (see, *e.g.*, Xiao *et al.*[228]), where it is believed to catalyze solvent reduction with a concomitant loss of active lithium,[229] The latter is confirmed by model experiments with a copper electrode,[224] demonstrating

an increase in electrolyte reduction charge with increasing manganese content of the SEI layer on the copper anode. It is hypothesized by Burns *et al.*[227] that these two different capacity fading phenomena can be discerned in the capacity versus cycle life features in graphite/NMC full-cells: a gradual capacity loss caused predominantly by active lithium loss and a more sudden capacity loss (referred to by the authors as "rapid rollover capacity loss") caused predominantly by anode impedance growth. While the latter can be reasonably well quantified by AC impedance in full-cells, quantification of active lithium loss currently cannot be done without cell disassembly followed by building half-cells with the harvested electrodes.

In this study, we examine the cycling stability of graphite/NMC full-cells at different operating temperatures (25°C, 60°C) and with different positive cut-off potentials (4.2 V, 4.6°V), seeking to deconvolute the above discussed aging mechanisms, viz., transition metal dissolution, active lithium loss, and impedance growth. The main diagnostic focus is put on structural analysis via X-ray diffraction (XRD), which will be used to quantify both the irreversible capacity loss (ICL) of NMC during the first cycle and the active lithium loss over extended charge/discharge cycling: first, *in situ* XRD measurements are used to establish a correlation between lithium content in NMC; subsequently, post-mortem *ex situ* XRD of aged NMC cathodes is used to quantify the active lithium loss. The latter will be confirmed by half-cell measurements on harvested aged NMC cathodes. AC impedance on full-cells and rate capability curves of half-cells built with harvested aged graphite and NMC electrodes are used to examine the impedance build-up during aging, which is most pronounced for cycling at high positive cut-off potential. Neutron based prompt gamma activation analysis (PGAA) of harvested graphite electrodes is used to quantify the amount of deposited transition metals. Our study confirms that the gradual capacity loss at low positive cut-off potentials both at 25 and 60°C is indeed caused by active lithium loss while the "rapid rollover capacity loss" is caused mostly by an increase in anode and cathode impedance.

4.5.2 Experimental

(a) Electrode preparation

Cathodes based on commercial $LiNi_{1/3}Mn_{1/3}Co_{1/3}O_2$ (NMC) active material were prepared by dispersing NMC (96 wt%), polyvinylidene difluoride (PVdF, Kynar HSV 900, Arkema, France) (2 wt%), and carbon black (Super C65, TIMCAL, Switzerland) (2 wt%) in N-methyl-2-pyrrolidone (NMP, Sigma Aldrich, Germany) and mixing them altogether in a planetary centrifugal vacuum mixer (Thinky, USA) at 2000 rpm for 10 min. The resulting viscous slurry with a solids content of 1.8 g/ml_{NMP} was cast onto a thin aluminum foil (thickness 18µm, MTI corporation, USA) using the doctor-blade method (RK Print Coat Instruments, UK). After drying at room temperature, electrodes with 10 mm diameter were punched and then dried at 120°C for 3 h under dynamic vacuum in a glass oven

(Büchi oven, Switzerland). The NMC loading of all tested electrodes was 15.0 ±0.2 mg_{NMC}/cm^2 with an electrode thickness of ≈90 µm. For the *in situ* XRD measurements, NMC cathodes with 18.4 ± 1.1 mg_{NMC}/cm^2 (thickness of ≈110 µm) were prepared by applying the slurry through a mask (12 mm diameter circle) onto an aluminum foil with a diameter of 42 mm, whereby the aluminum foil serves both as current collector and X-ray window.

Graphite electrodes were produced analogously, using a mixture of 95 wt% graphite (SGL Carbon, Germany) and 5 wt% PVdF binder in NMP (solids content of 0.88 g/ml). Copper foil was used as a current collector (10µm, MTI corporation, USA) from which electrodes with a diameter of 11 mm diameter were punched out. For graphite/NMC cells cycled between 3.0 and 4.2 V_{cell}, the graphite loading was 7.4 ± 0.2 $mg_{graphite}/cm^2$ (thickness of ≈90 µm), while it was 9.3 ± 0.2 $mg_{graphite}/cm^2$ (thickness of ≈100 µm) for cells cycled between 3.0 and 4.6 V_{cell}. The different graphite loadings were necessary to adjust the areal capacity of the graphite anodes to the voltage dependent areal capacity of the NMC cathodes, so that a constant capacity balancing factor of 1.2 $(mAh/cm^2_{anode})/(mAh/cm^2_{cathode})$ could be achieved (assuming capacities of 150 and 190 mAh/g_{NMC} at 4.2 and 4.6 V_{cell}, respectively).

(b) Electrochemical characterization

For the graphite/NMC full-cell cycling studies, Swagelok T-cells were assembled in an argon filled glove-box (H_2O and O_2 content < 0.1 ppm, MBraun, Germany) using two glass fiber separators (glass microfiber filter, 691, VWR, Germany; 11 mm diameter). For three-electrode measurements (e.g., in Figure 4.31a), a 450 µm thick lithium foil (Rockwood Lithium) was used as reference electrode. The cells were filled with 80 µl LP57 electrolyte (1 M $LiPF_6$ dissolved in EC:EMC 3:7 wt% <20 ppm H_2O, BASF, Germany). Electrochemical tests were carried out in a climatic chamber (Binder, Germany) using a battery cycler (Series 4000, Maccor, USA). Two formation cycles between 3.0 and 4.2 V were performed at C/10 at 25°C to produce a stable SEI on the graphite electrode. To study the effect of temperature and upper cut-off voltage during long-term cycling at 1C for both charge and discharge, cells were cycled under three conditions: between 3.0 V and 4.2 V at 25°C (referred to as 4.2V/25°C), between 3.0 V and 4.6 V at 25°C (referred to as 4.6V/25°C), and between 3.0 and 4.2 V at 60°C (referred to as 4.2V/60°C). The charging process is always accompanied by a constant voltage step with current limitation at C/20. Under each condition, two cells were tested for up to 300 cycles.

Electrochemical Impedance Spectroscopy (EIS) experiments were conducted after the formation cycle and at the end of the cycling experiment in the discharged state after an OCV period of 3h at 25°C. Impedance spectra (500 kHz to 10 mHz, 5 mV perturbation) were recorded using a VMP-3 potentiostat (Biologic, France).

At the end of the cycling tests, the cells were dissembled in a glove box and both anode and cathode were harvested. In one set of experiments, anodes and cathodes (without washing step) were assembled in half-cells to evaluate their electrochemical performance.

These experiments were carried out in two-electrode Swagelok cells with lithium foil as counter electrode (11 mm diameter) and new glass fiber separators wetted with 80 µl fresh LP57 electrolyte. The rate performance test for both electrodes consists of an intercalation step at a maximum rate of C/2 followed by a constant voltage step with current limitation (C/20) and a deintercalation step at rates of C/10, C/2, 1C, 2C, 3C, 5C, and 10C, respectively. Each rate setting was conducted three times. For NMC half-cells, a voltage window of 3.0 – 4.3 V was applied; for graphite half-cells, the voltage window was 0.01 – 1.5 V.

(c) Prompt gamma activation analysis (PGAA)

PGAA was performed at the neutron source FRM II of the Heinz Maier-Leibnitz Zentrum (MLZ) in Garching.[100] Harvested graphite electrodes before and after the long-term cycling test were analyzed to get information about the amount of deposited transition metals. Prior to the PGAA analysis, the electrodes were rinsed with dimethyl carbonate (DMC, Sigma Aldrich, Germany), which was dried and stored at room temperature over a molecular sieve. The samples were then placed into an evacuated chamber and irradiated with cold neutrons at the NL4b beam guide for about 6 h each at a neutron flux of $4x10^{10}$ neutrons/(cm^2·s) thermal equivalent (equivalent to a defined thermal neutron flux with 25 meV energy). The whole sample was immersed into the neutron beam and the copper signal coming from the copper current collector of the graphite electrodes (exactly known mass) was used as an internal standard for the determination of transition metal concentrations.

(d) X-ray diffraction (XRD) studies

The ex situ XRD patterns of the harvested NMC cathodes before and after the long-term cycling experiment were obtained in transmission mode with a STOE STADI P diffractometer (STOE, Germany) using Mo-$K_{\alpha 1}$ radiation (λ = 0.70932 Å, 50 kV, 40 mV) and a Mythen 1K detector. The diffraction patterns were measured in repetition mode with two repetitions per sample. The patterns were collected in a 2θ-range between 6.5-52° with a step size of 0.015° and a time of 5 s per step. To prevent any contact with moisture, the electrodes were put in an airtight sample holder with aluminum windows as reported in a previous work of our group.[207]

The *in situ* XRD cell, custom designed by our group, was used to follow the structural changes of NMC during electrochemical tests. In this cell, the aluminum of the cathode acts both as a current collector and X-ray window. Lithium metal is used as counter electrode and 4 glass fiber separators (14 mm diameter) wetted with 160 µl LP57 electrolyte are placed between cathode and anode. The *in situ* XRD patterns were collected with non-monochromatized Mo-K_α radiation to allow for higher flux and thus faster data collection. Bragg-Brentano geometry (reflection mode) was used in this set-up. During the experiments, the cell was connected to a SP200 potentiostat (SP200, Biologic, France). All

XRD patterns were collected during intermittent OCV periods during the cycling procedure. Data analysis was performed using either WinXPow program package (WinXPow software version 3.0.2.1, 2011, by STOE & Cie GmbH, Darmstadt, Germany) or Highscore Plus[87] (HighScore(Plus) software version 4.1, 2014, by PANalytical B.V., Almelo, Netherlands).

4.5.3 Electrochemical performance

To examine the effect of different operating conditions on the long-term cycling performance, graphite/NMC full-cells were assembled and tested with different upper cut-off potentials (4.2 V and 4.6 V) and at different temperatures (25°C and 60°C). The results are shown in Figure 4.25. The cells 4.2V/25°C demonstrated a negligible capacity fade after 300 cycles, while the capacity of the cells 4.2V/60°C fades more severely. Changing the upper cut-off potential leads to a different failure mechanism and rapid capacity decay after 150 cycles can be observed in the cells 4.6V/25°C. While it is well known that higher cut-off potentials yield substantially higher initial NMC capacities[214,215,220] (see 4.2V/25°C *vs.* 4.6V/25°C in Figure 4.25), higher initial capacities at 1C are also observed at elevated temperatures (see 4.2V/25°C vs. 4.2V/60°C in Figure 4.25), which is due to increased charge transfer kinetics and electrolyte conductivity (also evidenced by the

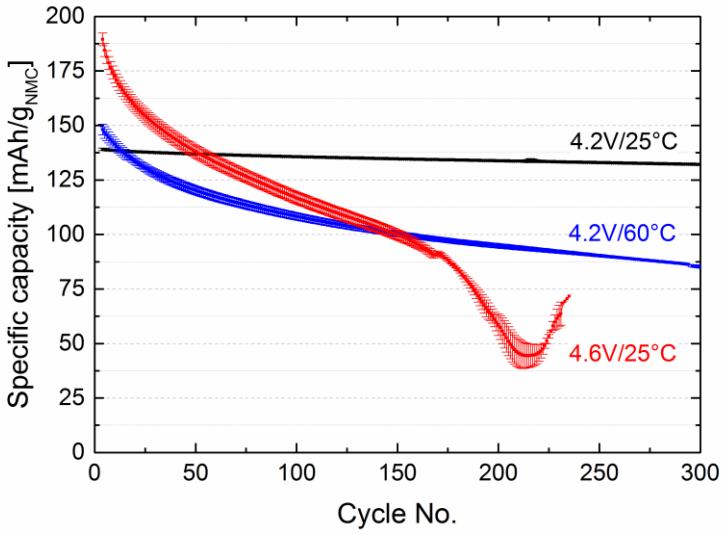

Figure 4.25: Specific discharge capacities *vs.* cycle number for graphite/NMC full-cells operated with different upper cut-off voltage limits (4.2 V, 4.6 V) and at different temperatures (25°C, 60°C) in EC/EMC (3/7) with 1 M $LiPF_6$. The cycling was performed at a rate of 1C for discharge and discharge with a lower cut-off potential of 3.0 V. Cathode loadings are 15.0 ±0.2 mg_{NMC}/cm^2, while anode loadings were 7.4 ±0.3 $mg_{graphite}/cm^2$ (3.0-4.2 V) and 9.3±0.3 $mg_{graphite}/cm^2$ (3.0-4.6 V) to maintain an areal capacity ratio of graphite/NMC=1.2. Results are averaged over two cells and the error bars represent the standard deviation between the two cells.

much lower charge/discharge hysteresis shown for the first cycle after formation in Figure 4.32).

Unfortunately, higher cut-off voltages and temperature may also accelerate undesired side reactions, like changes in the surface structure of NMC, active lithium loss through anode SEI growth triggered by transition metal dissolution, and enhanced electrolyte oxidation due to the restricted anodic stability of carbonate based electrolytes.[230] For example, NMC half-cell data with 1 M $LiPF_6$ in EC/DMC (1/1) at 25°C by Gallus et al.[55] showed similarly strong capacity loss at 4.6 V cut-off potential (15% capacity loss over 50 cycles), which was ascribed to transition metal dissolution. Furthermore, similar cycling profiles were reported in the literature, showing that gradual capacity losses can be caused by loss of active lithium ions, whereas a "rapid rollover" failure is commonly linked with increasing cell impedance, mostly ascribed to the anode.[226,227] In order to understand the fundamental reasons for cell failure at different operating conditions shown in Figure 4.25, electrochemical techniques were combined with XRD measurements and elemental analysis using PGAA.

4.5.4 *Ex situ* XRD analysis of aged NMC electrodes

Figure 4.26a shows the XRD patterns of a pristine NMC electrode and electrodes harvested in the discharged state after the cycling experiment shown in Figure 4.25. Other than diffractions from the aluminum current collector and the XRD cell window, no additional bulk phases besides those for NMC, which can be indexed and refined in the hexagonal $R\bar{3}m$ space group, are found in the XRD pattern, thus indicating the absence of any severe structural damage to NMC after long-term cycling (note that possible surface structural changes would not be detectable in this analysis). Furthermore, investigation of the profile parameter *W* (see caption of Figure 4.26) reveals that only a minor peak broadening occurs between pristine and aged NMC electrodes, most prominent for the cells cycled at 4.6 V cut-off at 25°C (see Figure 4.26b). This is consistent with previous reports, where the bulk structure of NMC was retained after chemical[231] or electrochemical[215] delithiation as well as after 500 cycles to 4.6 V[220] (again, surface structural changes might occur, but would not have been detectable in these measurements).

However, compared to the pristine electrode, the reflections of the harvested electrodes deviate from their original position, *e.g.*, as clearly seen in the splitting of the (1 0 8) and (1 1 0) peaks as well as in the shift of the (1 1 3) peak to higher angles in Figure 4.26b. These shifts can be correlated with the lattice shrinkage along *a* and *b* direction and the expansion along *c*. Pattern fitting of the 4.6V/25°C sample reveals that the *a*-parameter decreases from 2.859 to 2.840 Å, while the c-parameter increases from 14.219 to 14.454 Å. The main reason for these structural changes is the below discussed variation in Li content of the aged NMC material, which affects the interlayer distance and thus the lattice parameter *a* and *c*. In the literature, various methods have been applied to show that the lattice parameters are correlated to the lithium content of the

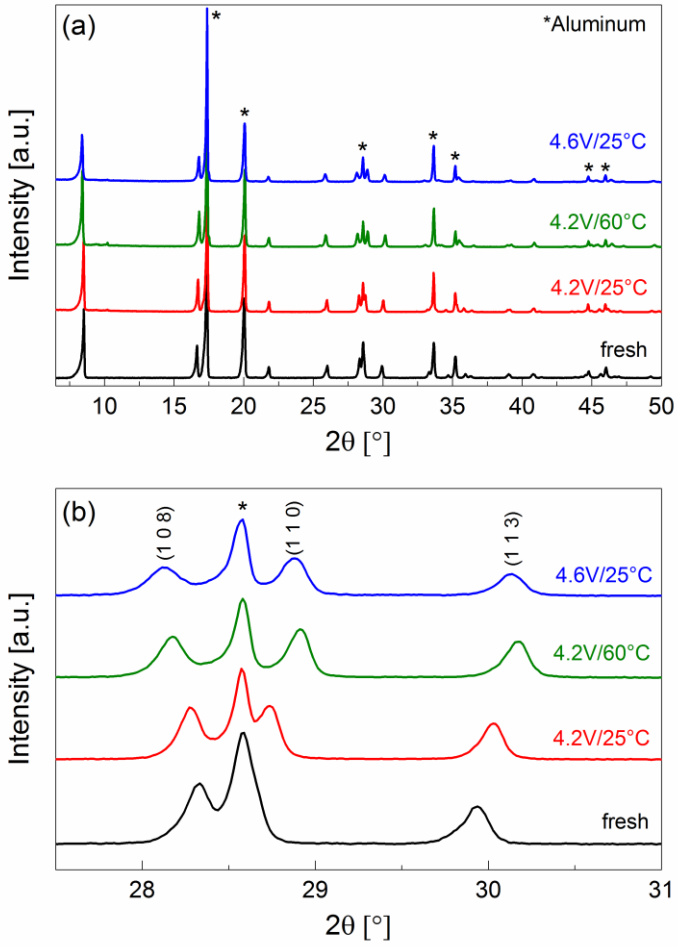

Figure 4.26: XRD patterns of the fresh NMC electrode and electrodes harvested in the discharged state after the cycling experiment: (a) complete diffractogram; (b) expanded view of the (1 0 8), (1 1 0), and (1 1 3) reflections. The fitted lattice parameters are: fresh NMC electrode: a = 2.859 Å, c = 14.241 Å, W = 0.0109; after 4.2V/25°C cycling: a = 2.854 Å, c = 14.320 Å, W = 0.0102; after 4.2V/60°C cycling: a = 2.836 Å, c = 14.426 Å, W = 0.0142; after 4.6V/25°C cycling: a = 2.839 Å, c = 14.448 Å, W = 0.0181. The diffractions from the Al window of the *ex situ* XRD holder are marked by an asterisk.

NMC electrode (x in $Li_{1-x}Ni_{1/3}Mn_{1/3}Co_{1/3}O_2$), *e.g.*, chemical or electrochemical delithiation combined with ICP-OES, XRD, neutron diffraction, or combinations of these methods.[214,215,232–234] In our study, we aim to quantify the Li-loss after long-term cycling as a function of cycling condition directly from the XRD data. For this purpose, a calibration curve is needed, which correlates the transferred electrochemical charge to the Li content of NMC and its lattice parameters. As was shown previously,[215] this can be done using *in situ* XRD during charging and discharging of an NMC electrode.

4.5.5 *In situ* XRD study of NMC

Figure 4.27 shows a comparison of the diffractograms and the Rietveld refinement obtained with pristine NMC electrodes collected either with the in situ XRD cell (Figure 4.27a) or the ex situ XRD sample holder (Figure 4.27b). The in situ pattern, measured in Bragg-Brentano geometry, contains a more sloping background compared to the ex situ pattern measured in transmission geometry (Debye-Scherrer). This is due to the additional electrolyte and separator contained in the in situ XRD cell. Furthermore, intensities differ due to the different impact of preferred orientation and the inability to rotate the in

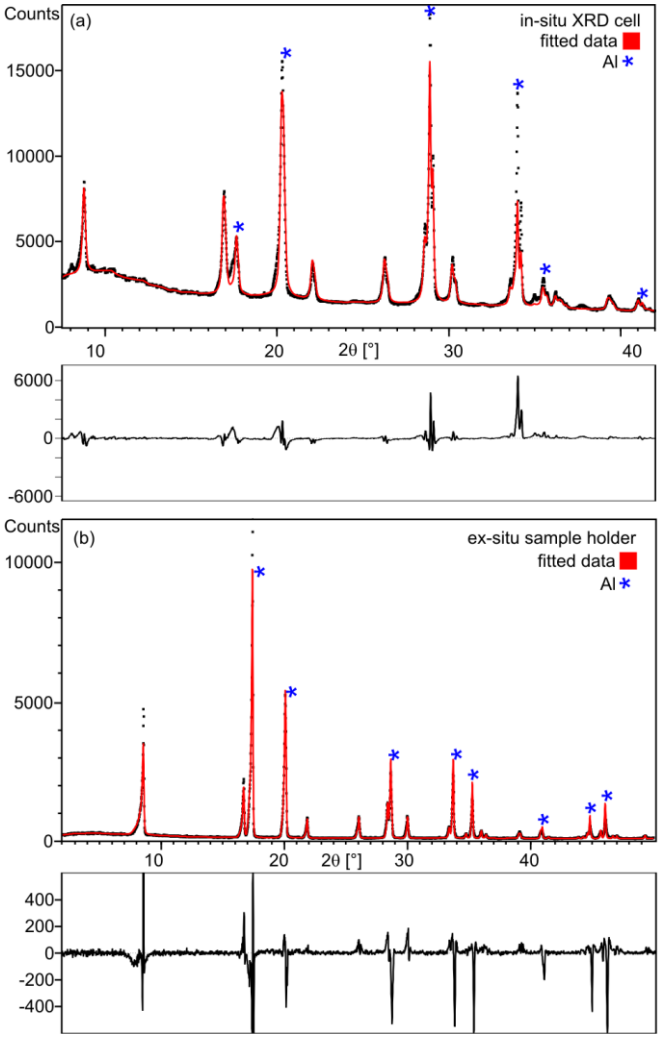

Figure 4.27: Comparison of the X-ray diffraction data and Rietveld refinement of pristine NMC electrodes collected (a) with the *in situ* XRD cell in Bragg-Brentano geometry and (b) with the *ex situ* sample holder in transmission geometry. Circles and lines correspond to the observed and calculated intensities, respectively. The difference between the observed and calculated patterns is indicated below each graph. The asterisks mark the diffraction peaks originating from the aluminum window(s).

situ XRD cell. The transmission geometry shows more peak asymmetry, the Bragg-Brentano in situ cell though shows broader peaks and less asymmetry. In both cases the data quality was sufficient to get reliable cell constants from the fit.

Figure 4.28shows the results from *in situ* XRD measurements of a Li/NMC half-cell at room temperature cycled between 3.0 and 4.3 V during the 1st charge and discharge (black lines) as well as the 2nd charge and discharge (red lines). From the transferred charge, the amount of extracted lithium was calculated and used to establish a correlation between lattice parameters and the lithium content (1-*x*) in $Li_{1-x}Ni_{1/3}Mn_{1/3}Co_{1/3}O_2$ (see Figure 4.28b-d), analogous to previous literature studies.

A Vegard's law type linear fit[235–237] is only possible in the range $x = 0 - 0.5$. Beyond that, a clear deviation from linearity suggests a phase transformation mechanism which has been discussed by Hwang *et al.*, Koyama *et al.*, and others[215,238,239]; it has been linked with a change in the electronic state (hybridization of Co and O orbitals). While in the linear region the extraction of Li directly affects the interlayer distance due to repulsive interactions of negative charges (elongation of the *c*-axis), further oxidation of NMC leads to a more covalent character of the metal-oxygen bond, hence decreasing the inter-layer repulsion. The best fit for *x* versus structural parameters is obtained when using the *c*/*a* value as a measure of the lattice distortion induced by the Li extraction and insertion (Figure 4.28d).[215]

According to the NMC charging reaction, the process of Li extraction can be described as:

$$Li_1Ni_{1/3}Mn_{1/3}Co_{1/3}O_2 \rightarrow Li_{1-x}Ni_{1/3}Mn_{1/3}Co_{1/3}O_2 + x\,Li^+ + x\,e^- \quad (4.3)$$

The first charge and discharge data of the Li/NMC half-cell shown in Figure 4.28a (black lines) indicates an irreversible capacity loss (ICL) of ~23.4 mAh/g_{NMC}, and the accompanying *in situ* XRD data (black lines in Figure 4.28b-d) suggest that the cathode material is not returning to its fully lithiated state after the first charge/discharge cycle. In these measurements, the upper cut-off potential of 4.3 V corresponds to a minimum lithium content of $(1-x) = 0.35$ (*i.e.*, $x = 0.65$), assuming that the first delithiation reaction proceeds from $Li_{1.00}$NMC to $Li_{0.35}$NMC as deduced from the transferred charge using the above reaction. It is also obvious that relative to the initial material composition only a re-lithiation to ~$Li_{0.916}$NMC is achieved in the first cycle (s. black lines in Figure 4.28a). Therefore, 0.084 moles of lithium per mole of $Li_{1.00}$NMC correspond to the irreversible capacity loss (ICL) of ~23.4 mAh/g_{NMC}. According to the lattice parameters obtained in the 2nd cycle in the *in situ* XRD cell, NMC can only be cycled reversibly back to a maximum lithium content corresponding to $Li_{0.916}$NMC, as the initial state under these conditions is not recovered.

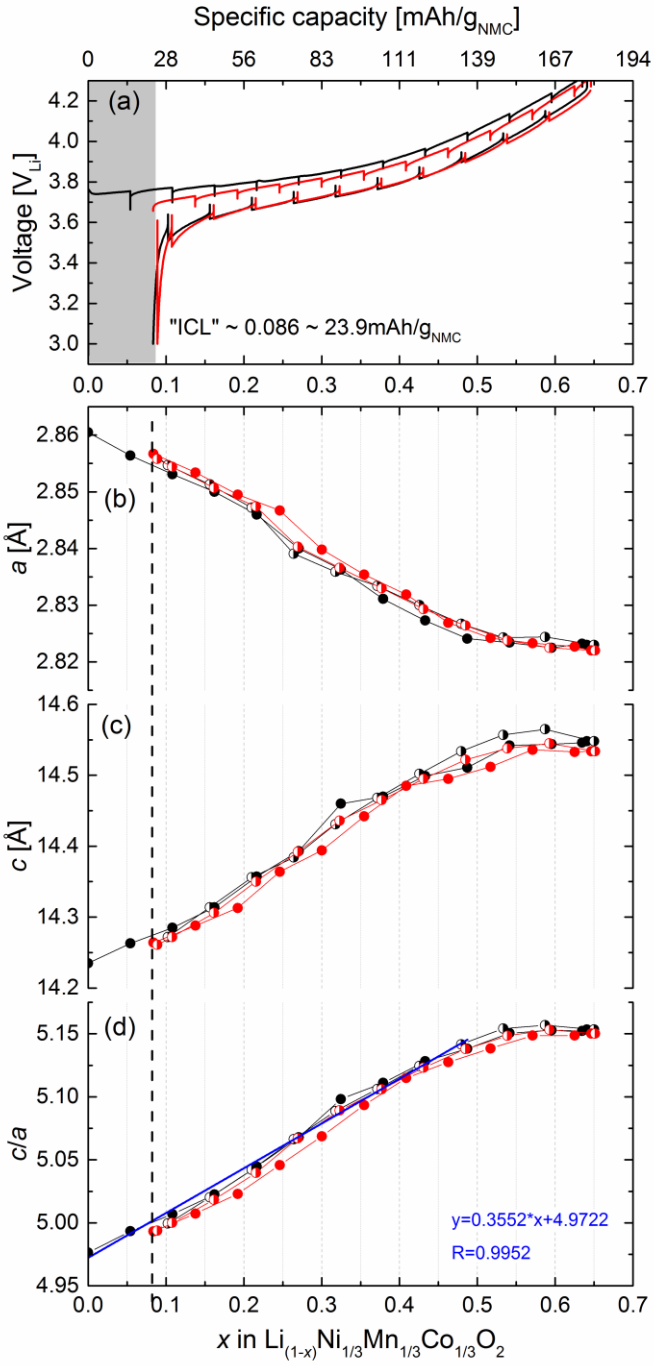

Figure 4.28: Charge and discharge curves of $Li/Li_{(1-x)}Ni_{1/3}Mn_{1/3}Co_{1/3}O_2$ recorded in the *in situ* XRD half-cell operated at a rate of 0.1C between 3.0 and 4.3 V (a). Spikes indicate the OCV period during which XRD diffraction patterns were collected. The black curves are the very first charge and discharge; the red curves are the second charge and discharge. (b), (c), and (d) Fitted lattice parameters *a* and *c* in hexagonal space group together with the ratio of *c/a* as a function of *x* (in $Li_{1-x}Ni_{1/3}Mn_{1/3}Co_{1/3}O_2$) during the first two charge/discharge cycles. The linear regression fit between *x*=0 and 0.5 gives *c/a* = 0.3552**x* + 4.9722 with R^2 = 0.9952.

Multiple groups[215,220,240] have observed the occurrence of an ICL, but only few groups[241–244] have proposed a mechanism for it. Figure 4.29 shows results from an *in situ* XRD Li/NMC half-cell experiment, in which the charging time was gradually increased by 1 h and the discharge terminated at 3.0 V, *i.e.*, initially, pristine NMC was charged for 1 hour at a rate of 15 mA/g_{NMC} (corresponding to a C-rate of 0.1 h^{-1} for a commonly used NMC capacity of 150 mAh/g_{NMC}) and then discharged to 3.0 V; subsequently, the same electrode was charged for 2 hours at a rate of 15 mA/g_{NMC} followed by another discharge to 3.0V, etc. It is apparent from Figure 4.29a that after the initial 1 hour charge (left-most black symbol at 15 mAh/g_{NMC}), essentially no discharge capacity is observed (left-most red symbol at. 2.5 mAh/g_{NMC}); after the following 2 hour charge to 30 mAh/g_{NMC} (second black symbol from the left), a discharge capacity of only ~18.9 mAh/g_{NMC} is obtained (second red symbol from the left). Only after the following 3 hour charge to 45 mAh/g_{NMC}, the subsequent discharge capacity essentially equals the preceding charge capacity. Thus, the accumulated irreversible capacity loss (ICL) in the first two cycles of this sequence amounts to ~23.6 mAh/g_{NMC} (*i.e.*, the sum of the difference between the charge and discharge capacity in the first two cycles) or ~0.085 mol Li, which is essentially identical to the ICL observed in the full charge/discharge shown in Figure 4.28a (black lines).

It is obvious from these data that the ICL only occurs in the initial delithiation process and that the extraction of the first 0.085 mol lithium per mol of NMC is irreversible under these cycling conditions, which is evidenced by the fact that the *c/a* value in the discharged state does not return to its initial value of ~4.975, but takes on a minimum value of ~5.00 (see red symbols in Figure 4.29b). These data suggest that a fraction of the discharged lithium ions, viz., 0.085 mol lithium per mol of NMC (or ~8.5% of the active lithium in NMC), cannot be intercalated back into the layered NMC structure and that the maximum reversible lithium content corresponds to $Li_{0.915}$NMC under these conditions. Analogous observations have already been reported.[243]

One of the tentative explanations for the first-cycle irreversible capacity loss of NMC is that it could be based on parasitic reactions occurring on the NMC surface, as was suggested by Choi *et al.*,[241] who had observed that NMC with lower BET area (produced by calcining at higher temperature) showed a lower ICL. On the other hand, Kang *et al.*[242,243] related the ICL to a very sluggish lithium diffusion into the layers of the oxide structure, caused by the lack of lithium ion vacancies as the lithium content (1-*x*) approaches 1 (*x*~0) in the Li_{1-x}NMC structure, *i.e.*, near the end of discharge; by allowing the discharge voltage to go below 1.5 V leading to the formation of an overlithiated phase "Li_2MO_2" (*M*=transition metal), they were able to completely recover the ICL. Therefore, if the latter hypothesis were correct, it should be possible to recover the full capacity of NMC, if the discharge is not terminated by a voltage limit but continued at constant voltage to compensate for the slow lithium ion diffusion.

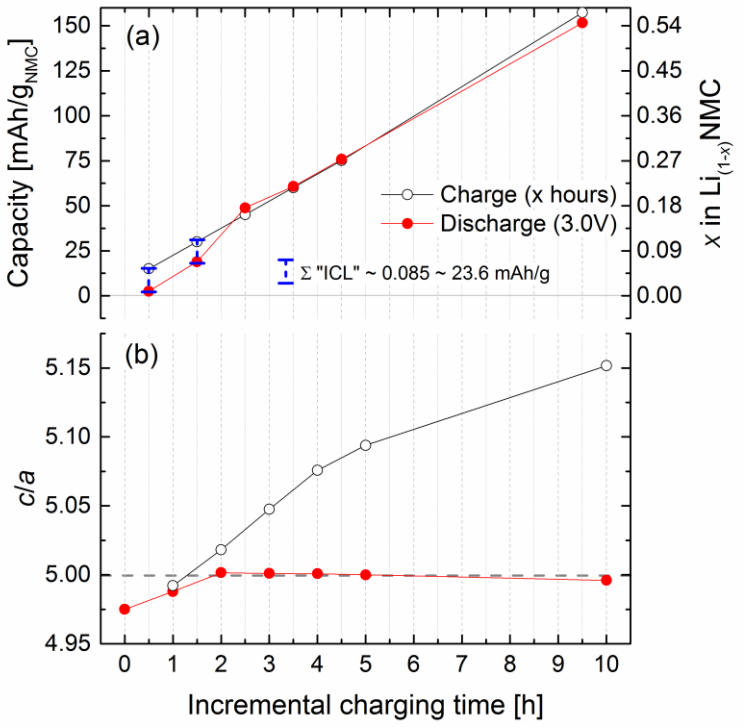

Figure 4.29: NMC charge (black symbols) and discharge (red symbols) capacity obtained with incrementally increasing NMC charging times (followed by discharge to 3.0 V) at a rate of 15 mA/g_{NMC} (corresponding to 0.1C if referenced to a conventionally used capacity value of 150 mAh/g_{NMC}) (a): 1 h charge followed by discharge to 3.0 V; then 2 h charge followed by discharge to 3.0 V; etc. (b) the corresponding parameter *c/a* determined at the end of every charge and discharge, respectively; note that the left-most red symbol in (b) refers to the lattice parameter of the pristine, fully lithiated $Li_{1.00}$NMC.

The results of such an approach are shown in Figure 4.30: after an initial charge and discharge cycle at 0.1C in the *in situ* XRD half-cell, the potential was first held at 3.0 V for 12 h, then at 2.0 V for 10 h, and finally at 1.6 V for 8 h. Note that the potential is kept well above 1.5 V to prevent the formation of the overlithiated "Li_2MO_2" on the particle surface which would result in a two-phase coexistence and two different Li diffusion processes;[242,243] its absence is evidenced in Figure 4.30c, as the associated additional peak at ~8°2$\theta_{Mo,K\alpha}$[245,246] left to the (0 0 3) peak is not appearing. Holding the potential at 3.0 V for 12 hours results in a ~50% recuperation of the ICL (marked by the gray area in Figure 4.30a), concomitant with a close approach of the *c/a* value towards its initial value (second-to the left black vs. red symbol in Figure 4.30b). After the final constant voltage hold at 1.6 V, all of the ICL has been recuperated and the *c/a* value has returned to its initial value, while at the same time the (1 1 3) reflection has moved back to its original position (see Figure 4.30a and c).

These data clearly demonstrate that the intercalation process above a Li content of ~0.915 (=$Li_{0.915}$NMC) is dominated by very slow Li diffusion into the layers of the NMC host structure and that the initial structure can be retrieved given enough time for the lith-

ium diffusion process. On the contrary, increasing the rate of the discharge process (*e.g.*, 1C) may result in a higher value for the ICL as the kinetic barrier increases.

While such extended voltage hold periods are impractical for real cells, in graphite/NMC full-cells the ICL of the NMC can be used to match the lithium-consuming SEI formation reaction of the graphite anode.[45,247] This is illustrated in Figure 4.31 by comparing the anode and cathode voltages (referenced to a lithium metal reference electrode) of a graphite/NMC full-cell during the first charge/discharge cycle (Figure 4.31a) with that of the cell voltages of Li/NMC (Figure 4.31b) and Li/graphite (Figure 4.31c) half-cells

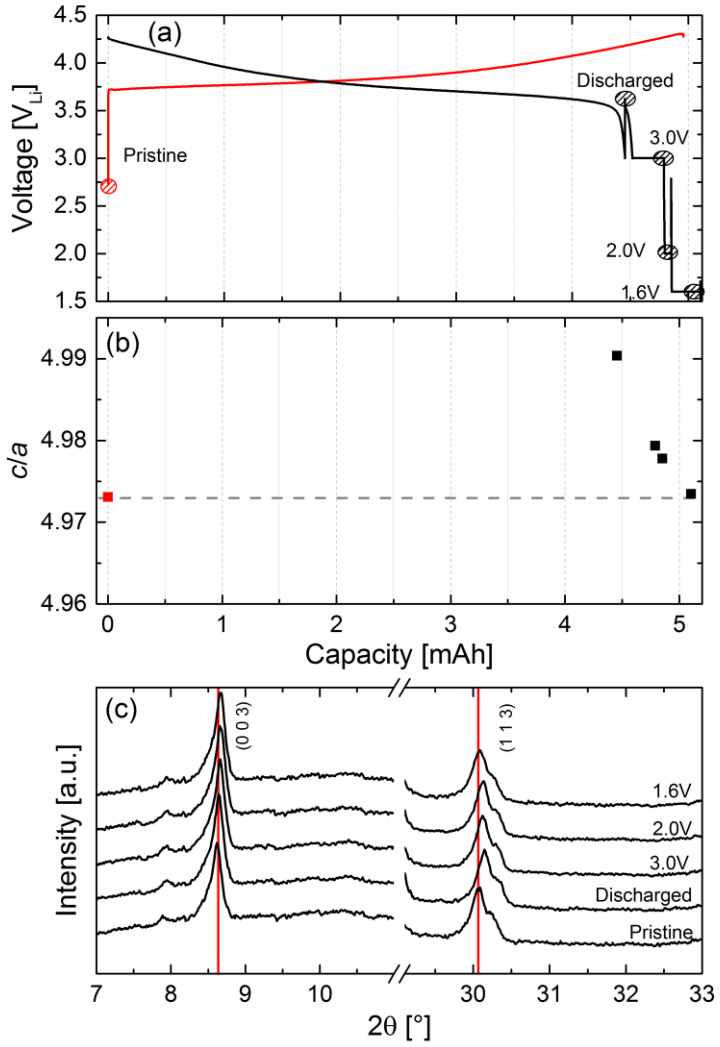

Figure 4.30: Initial charge/discharge cycle of Li/NMC in the *in situ* XRD half-cell at 0.1C to a positive cut-off potential of 4.3 V, with the discharge being followed by several constant voltage steps: for 12h at 3.0 V, then for 10h at 2.0 V, and finally for 8h at 1.6 V. (a) cell voltage versus capacity (XRD data collection is marked by dashed circles); (b) corresponding *c/a* values of the pristine structure of NMC (red symbol) and after the various potential holds following the first discharge cycle; (c) *in situ* XRD patterns in the 0 0 3 and 1 1 3 peak region.

made with comparable electrodes. Obviously, the first cycle irreversible capacity loss of the NMC cathode and the SEI loss of the graphite anode are not accumulative, since the sum of the ICL of the Li/NMC and the SEI loss of the Li/graphite half-cells do not match the full-cell first-cycle capacity loss (see Figure 4.31). Since the first-cycle capacity losses of both electrodes are very similar, the "excess" Li from NMC almost perfectly compensates the SEI loss of the graphite anode, so that the full-cell first-cycle capacity loss only amounts to the irreversible loss term of one of the electrodes, viz., the one with the larger first-cycle irreversible loss which in this case is the NMC cathode. Similar results were also confirmed by German *et al.*[244] This, of course, has to be considered when optimizing the balancing of graphite/NMC full-cells. In our study, cells based on these considerations were fabricated by us and tested at different operating conditions to investigate failure mechanisms.

4.5.6 Correlation of Li content in NMC with capacity fade

As the NMC cathode was chosen to be capacity limiting in the graphite/NMC full-cells (this can also be seen in Figure 4.31), its lithium content can be used to track the amount of active lithium in the cell ("lithium inventory"): if lithium ions are consumed by side reactions (e.g., SEI formation), they are lost for back-intercalation into the NMC cathode material during discharge, thereby limiting discharge capacity. To determine this active lithium loss, the cycled cells (s. Figure 4.25) were disassembled in the discharged state and XRD patterns of the harvested NMC electrodes were acquired to quantify their lithium content by means of the correlation established in Figure 4.28d. In the absence of active lithium loss during the cycling test, the NMC active material should be fully intercalated back to its lithium content after formation, i.e., to the stoichiometry corresponding to $Li_{0.916}NMC$ (x~0.084) as deduced from the analysis of the first cycle ICL (dashed line in Figure 4.28). Furthermore, a correction for changing the C-rate from 0.1 to 1C has to be applied to consider the higher kinetic barrier for Li re-intercalation at 1C, *i.e.*, $Li_{0.891}NMC$ (x~0.109). For comparison see rate performance in Figure 4.35.

Table 4.1 gives an overview of the capacity losses obtained from the electrochemical cycling data (ΔC_{cycing}) of cells aged for up to 300 cycles at different conditions. To obtain the capacity loss resulting from the loss of active lithium of the NMC electrode due to anode SEI formation[41,248,249] or other parasitic reactions ($\Delta C_{active\text{-}Li}$), *ex situ* XRD measurements were conducted on the harvested electrode in the discharged state to determine the lattice parameters and the *c*/*a* value (see Figure 4.26). From the linear part of the *c*/*a* plot obtained by *in situ* XRD (see Figure 4.28d), one can determine the lithium content *x* in $Li_{1-x}NMC$. The loss of active lithium ($\Delta C_{active\text{-}Li}$) can be quantified by subtracting the lithium loss due to the initial NMC ICL at 1C ($x = 0.109$) to yield the corrected value of $x_{ICL\text{-}corr}$. The latter can finally be converted into $\Delta C_{active\text{-}Li}$ by considering that the theoretical capacity of $Li_{1-x}NMC$ equates to 278 mAh/g_{NMC} for $x = 1$.

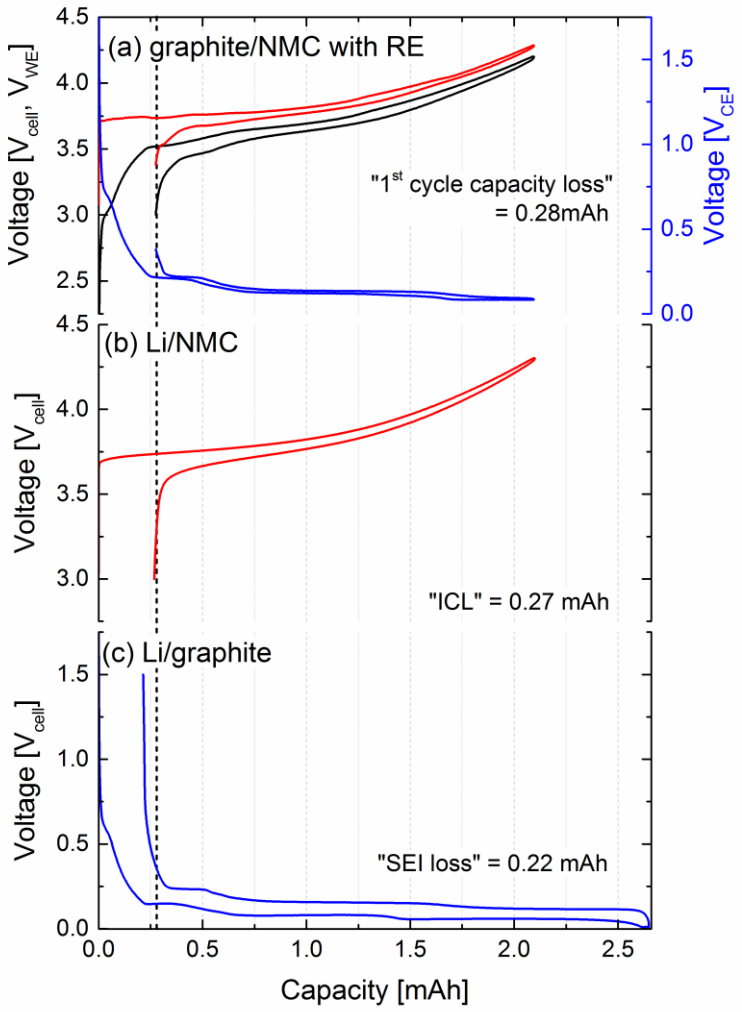

Figure 4.31: Initial charge/discharge cycle at 0.1C of (a) graphite/NMC full-cell with lithium reference electrode (RE) cycled between 3.0 V and 4.2 V (note that the NMC (WE) and the graphite (CE) potential are referenced to the lithium reference electrode potential). (b) Cell potential of a Li/NMC half-cell cycled between 3.0 V and 4.3 V. (c) Cell potential of a Li/graphite half-cell cycled between 0.01 V and 1.5 V. NMC loadings in the full- and the half-cell are 15.45 and 15.29 mg_{NMC}/cm^2, respectively; graphite loadings in the full- and the half-cell are 7.26 and 7.37 mg_C/cm^2, respectively.

Table 4.1 compares the capacity losses obtained from the cycling data (ΔC_{cycing}) to the capacity losses which can be ascribed to a loss of active lithium obtained from XRD analysis ($\Delta C_{active\text{-}Li}$), showing that the capacity loss of cells cycled with a positive cut-off potential of 4.2 V (cells 4.2V/25°C and 4.2V/60°C in Figure 4.25) are mainly due to the loss of active lithium (*i.e.*, $\Delta C_{cycing} \sim \Delta C_{active\text{-}Li}$). The gradual capacity loss with cycle number of these cells (s. Figure 4.25) is consistent with the literature,[226,227] which generally associates this behavior with a loss of active lithium. The loss of active lithium in the first cycle is associated with the SEI build-up on the graphite electrode, gradually passiv-

Table 4.1: Capacity losses of graphite/NMC cells after extended cycling at 1C (# of cycles is indicated) at different positive cut-off potentials (U) and temperatures (T). The electrochemically determined capacities at Beginning-of-Life (BoL), End-of-Life (EoL), and the thus determined capacity loss ($\Delta C_{cycling}$) are shown. The latter is compared to the capacity losses due to active lithium loss ($\Delta C_{active\text{-}Li}$), obtained from XRD analysis of harvested NMC electrodes via quantification of the *c/a*-value by *ex situ* XRD, conversion into *x* in $Li_{1-x}NMC$ using the *in situ* XRD calibration curve (Figure 4.28d), and subtraction of the lithium ion loss due to ICL to yield the ICL-corrected *x*-value ($x_{ICL\text{-}corr.}$); note that $x = 1$ marks the theoretical capacity of 278 mAh/g_{NMC}.

		Electrochemical Cycling Data			XRD Data Analysis		
		Capacity		$\Delta C_{cycling}$	*x* in $Li_{1-x}NMC$		$\Delta C_{active\text{-}Li}$
Condition	Cycle no.	BoL [mAh/g]	EoL [mAh/g]	[mAh/g]	*x* from *c/a*-fit	$x_{ICL\text{-}corr.}$ (-0.109)	[mAh/g]
4.2V/25°C	300	139.8	132.3	7.4	0.122	0.013	3.6
	300	139.6	132.7	6.9	0.121	0.012	3.3
4.2V/60°C	300	146.4	84.3	62.0	0.315	0.206	57.3
	300	149.8	85.3	64.5	0.328	0.219	60.9
4.6V/25°C	232	191.5	71.7	119.9	0.303	0.194	53.9
	228	187.4	59.9	127.5	0.321	0.212	58.9

ating its surface towards further reduction.[41,45,247] This quite effective surface passivation is indicated by the low capacity loss during extended cycling of the 4.2V/25°C cells. However, at elevated temperatures the SEI may partially dissolve in the electrolyte[45,250] and/or may be attacked by PF_5 which is formed as a decomposition product of $LiPF_6$ salt at higher temperatures.[221,251] Thus, the gradual SEI re-formation is the likely cause for the large active lithium loss in the cells cycled at a low cut-off voltage of 4.2 V at 60°C (s. Table 4.1).

In summary, the conclusion drawn from our XRD analysis that capacity losses during cycling of graphite/NMC cells at a low cut-off potential of 4.2 V are mostly due to the loss active lithium is consistent with the literature. This validates our here described experimental approach to quantify capacity losses due to active lithium loss by means of XRD analysis, providing an alternative method to the commonly used post-mortem quantification of the lithium content of discharged cathodes by means of chemical analysis.

On the other hand, cells cycled with a cut-off potential of 4.6 V exhibit a much higher total capacity loss (ΔC_{cycing} ~ 120-130 mAh/g_{NMC}) than what could be ascribed to the loss of active lithium ($\Delta C_{active\text{-}Li}$ ~ 54-59 mAh/g_{NMC}). This means, that the cathode still contains unused cyclable lithium and that the total capacity loss cannot be caused solely by a loss of active lithium. The additional large capacity loss might come from enhanced surface film formation on both anode and cathode active materials, concomitant with increased impedance and polarization losses. This would be consistent with the cycling profile of the 4.6V/25°C cells in Figure 4.25, exhibiting the typical "rapid rollover capacity loss" which has mainly been linked with excessive impedance growth and cell polarization.[226,227]

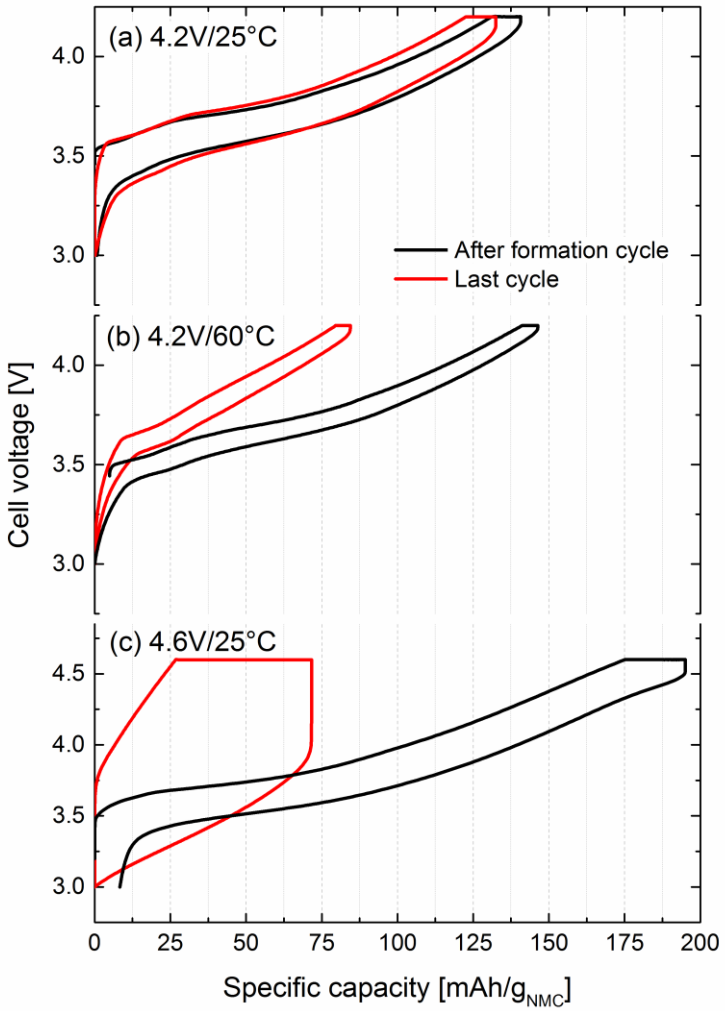

Figure 4.32: Cell voltage vs. specific capacity of the first cycle after formation and last cycle of the cycling test shown in Figure 4.25 of the aged graphite/NMC cells. Cells were charged (with a CV-step) and discharged at 1C at different temperatures (25°C, 60°C) and upper cut-off potentials (4.2 V, 4.6 V).

Increased cell polarization is indeed only observed for the 4.6V/25°C cells, as is shown in a comparison of the charge/discharge profiles after formation and at the end of the cycling test (s. Figure 4.32). Quite clearly, the capacity of the 4.6V/25°C cells becomes limited by cell polarization (Figure 4.32c), while the charge/discharge overpotentials of the 4.2V/25°C and 4.2V/60°C cells remains unchanged between the initial and the final cycles (Figure 4.32a and b). This further supports our above findings that the capacity loss for cells cycled with a cut-off voltage of 4.2 V is mainly due the loss of active lithium as inferred from our XRD analysis (Table 4.1)

As shown in the Nyquist plot in Figure 4.33, the increased charge/discharge cell voltage hysteresis for the 4.6V/25°C cells indicated in Figure 4.32c is also reflected in their nearly one order of magnitude larger AC impedance (red lines) compared to the

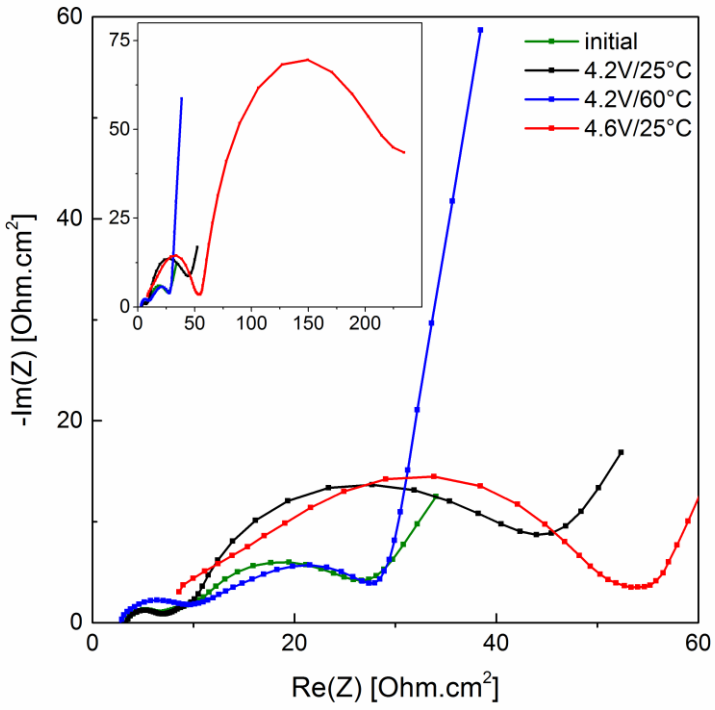

Figure 4.33: Nyquist plots of the fresh and aged graphite/NMC cells after long-term cycling at different temperatures (25°C, 60°C) and upper cut-off potentials (4.2 V, 4.6 V). The inset displays an expanded view in order to depict the complete AC impedance spectrum of the 4.6V/25°C cells. Spectra were collected at 25°C in the discharged state of the cell after at least 3h of OCV.

4.2V/25°C (black line) and 4.2V/60°C cells (blue line). Two semicircles can be observed in the graph that are generally attributed to surface film and charge transfer resistances.[252] Interestingly, the impedance of the aged 4.2V/60°C cell (blue line in Figure 4.33) is essentially identical with that of the pristine cell after formation (green line in Figure 4.33) and lower than that of the aged 4.2V/25°C (black line). This would actually be consistent with the above discussed hypothesis of partial anode SEI dissolution at 60°C compared to 25°C. Overall, however, the most pronounced impedance increase is observed for the 4.6V/25°C (red lines), which may be related to electrolyte oxidation/decomposition and/or the dissolution of transition metal from the NMC cathode.

4.5.7 Transition metal dissolution and deposition

One of the discussed reasons for accelerated capacity loss at high positive cut-off potentials and/or high temperatures is the dissolution of transition metals and their subsequent deposition on the graphite anode.[55,219,220,225,253] To examine the extent of transition metal deposition on the anode, PGAA was used to quantify the amount of deposited Ni, Mn, Co on harvested graphite anodes. Due to the large penetration depth of neutrons, PGAA examines the entire volume of the investigated anode samples. Figure 4.34 shows the

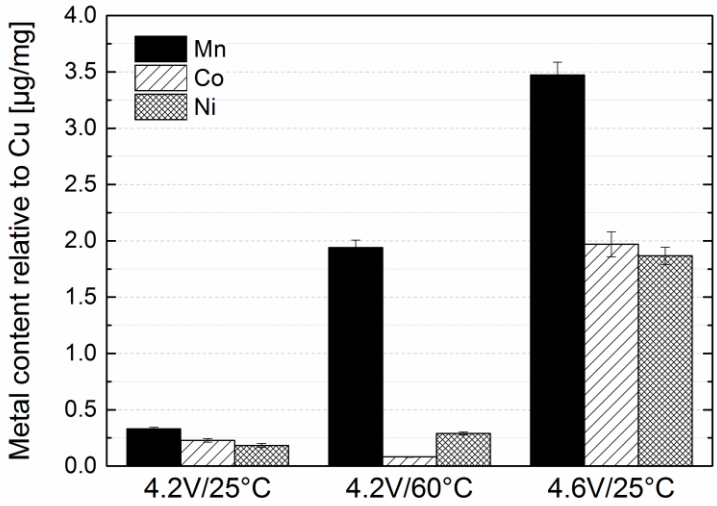

Figure 4.34: Concentration of Ni, Mn and Co deposited on harvested aged graphite electrodes determined by PGAA after cycling graphite/NMC cells up to 300 cycles at different temperatures (25°C, 60°C) and upper cut-off potentials (4.2 V, 4.6 V).

concentrations of Mn, Co, and Ni deposited on the graphite anodes after the long-term cycling test shown in Figure 4.25. Quite clearly, elevated temperatures and high positive cut-off voltages accelerate the loss of transition metal ions from the NMC electrode and their deposition on the graphite anode.[57] At 25°C, the amount of deposited Mn is 1.5- to 2-fold larger than that of Ni and Co, reasonably consistent with the report by Gallus *et al*.[55] On the other hand, at 60°C (4.2V/60°C cell), the amount of deposited manganese is almost an order of magnitude larger than that of Ni and Co, which implies preferential Mn dissolution at high temperature.

In general, two different mechanisms for transition metal dissolution are suggested in the literature: i) at lower voltages, disproportionation reactions according to $2Mn^{3+} \rightarrow Mn^{4+} + Mn^{2+}$ are supposed to be the main reason,[254,255] whereby trace amounts of Mn^{3+} in the NMC lattice due to defects or oxygen vacancies can trigger this reaction; ii) at higher potentials (>4.6 V), the hybridization of the electron orbitals of oxygen and the metals is hypothesized to take place[238,239] and lead to a reduction of the oxidation state of the metals. The manganese dissolution triggered by either mechanism is believed to be enhanced by an HF corrosion reaction according to Hunter´s reaction:[256,257]

$$4\ Li_{1-x}Mn_2O_4 + 8(1-x)\ HF \rightarrow (3+x)\ \lambda\text{-}Mn_2O_4 + 4(1-x)\ LiF + 4(1-x)\ H_2O + 2(1-x)\ MnF_2 \quad (4.4)$$

An analogous reaction can be formulated for NMC:

$$2\ Li_{(1-x)}Ni_{1/3}Mn_{1/3}Co_{1/3}O_2 + 4(1-x)\ HF \rightarrow (3x-1)\ Ni_{1/3}Mn_{1/3}Co_{1/3}O_2 + 2(1-x)\ H_2O + (1-x)\ MnF_2.+ 2(1-x)\ LiF + 2(1-x)\ Ni_{0.5}Co_{0.5}O_2 \quad (4.5)$$

It was shown that the HF required for this reaction is mainly formed by the decomposition reaction of $LiPF_6$ salt and H_2O:[55,221]

$$LiPF_6 \rightarrow LiF + PF_5 \quad (4.6)$$

$$PF_5 + H_2O \rightarrow 2HF + POF_3\uparrow \quad (4.7)$$

In a recent study by our group,[258] the detection of gaseous POF_3 at high positive potentials using online electrochemical mass spectrometry (OEMS) suggested that water may be formed during the oxidation of the electrolyte at high anodic potentials, thereby promoting the formation of HF.

The amount of metals deposited on the graphite electrode can be calculated using the copper current collector as internal standard. From this, the resulting loss of transition metals relative to the initial active mass of NMC can be determined and is shown in Table 4.2, whereby it is assumed that a loss (y) about 1% of transition metal in the NMC will result in a maximum loss of 4% ($4y$) of cyclable lithium due to charge compensation of the transition metal cation leaving the structure.

The data in Table 4.2 (right-most column) shows, that even for the cell cycled at the severest conditions of 4.6V/25°C, the loss of cyclable lithium due to a loss of active cathode material would be less than 5%, which cannot explain the huge capacity fade of these aged cells (~125mAh/g_{NMC} or ~65% loss of capacity). As a consequence, active NMC material loss due to transition metal dissolution seems to be negligible in the cells cycled in our study (Figure 4.25).

Based on this analysis, it is therefore more likely that the large capacity losses at either 4.6 V positive cut-off potential or at 60°C are due to excessive anode SEI growth caused by transition metal deposition as reported in the literature.[41,224,225,259] Generally, accelerat-

Table 4.2: Amounts of transition metals (TMs) deposited on the graphite electrodes for cells cycled at different positive cut-off potentials and temperatures after the experiments shown in Figure 4.25. Data are based on PGAA analysis.

Cells	Deposited TMs		Loss of TMs
	[µg]	[µmol]	[wt%]
4.2V/25°C	6.2	0.11	0.08
4.2V/60°C	19.3	0.35	0.26
4.6V/25°C	61.2	1.07	0.77

ed growth of the SEI may result from an increase of the electronic conductivity of the SEI due to the precipitation of transition metals into it.[41] For example, it was shown that the addition of transition metal salts to the electrolyte would decrease the cycle-life of full-cells, and surface analysis of the graphite anode revealed that the SEI layer growth was facilitated by transition metal addition.[225] It was also suggested that Mn undergoes several reactions at the anode (*i.e.*, $Mn^{2+} \rightarrow Mn^0 \rightarrow MnCO_3 + 2Li \rightarrow Mn^0 + Li_2CO_3$) which lead to cracks that favor electrolyte decomposition and further film growth. As a result, Mn contamination of the SEI should lead to the loss of active lithium.[224] This would be consistent with what we have observed for the aged 4.2V/60°C cells, where the loss of active lithium was very large (s. Table 4.1) and where a substantial amount of Mn was found to be deposited on the graphite anodes (s. Figure 4.34). On the other hand, in addition to a loss of active lithium, a substantial impedance growth was observed for the aged 4.6V/25°C cells (s. Figure 4.33), which results in capacity losses far beyond those related to active lithium loss (s. Table 4.1).

4.5.8 Half-Cell Studies

In an attempt to deconvolute the impedance growth observed by AC impedance measurements (without reference electrode) on the aged full-cells (s. Figure 4.33), electrodes were harvested from the aged full-cells in the discharged state and assembled in Li/NMC and Li/graphite half-cells. The rate-capability curves of fresh and aged Li/NMC and Li/graphite half-cells are presented in Figure 4.35a and b, respectively.

A comparison of half-cells with pristine NMC and graphite electrodes (grey lines in Figure 4.35) and half-cells with anodes/cathodes harvested from the aged 4.2V/25°C cells (black lines in Figure 4.35) clearly confirms that the observed full-cell capacity loss is mainly due to the loss of active lithium (s. Table 4.1), as the half-cell rate capability is unchanged. In the case of half-cells with anodes/cathodes harvested from the aged 4.2V/60°C cells (blue lines in Figure 4.35), significant differences to pristine electrodes can only be observed for the graphite anodes, indicating increased anode impedance. This is consistent with the study by Zheng *et al.*,[220] who upon extended cycling of graphite/NMC half-cells to 4.3 V found no indication for increased NMC impedance but observed increased graphite impedance.

However, the half-cell rate capability of the NMC electrode harvested from the aged 4.6V/25°C cells (red line in Figure 4.35a) is substantially reduced, indicating either a substantial loss of active material or substantially increased impedance. Since the total loss of active NMC material due to transition metal dissolution is minor (s. Table 4.2), the observed behavior must be due to increased charge transfer resistance and/or surface film resistance. While our XRD analysis does not detect any bulk structural changes of the NMC material aged in the 4.6V/25°C cells, the increased impedance might be due to surface structural changes which would not be detectable in our XRD measurements. While the rate capability of the graphite electrodes harvested from aged 4.6V/25°C cells is also substantially reduced (red line in Figure 4.35b), it is therefore quite clear that the capacity

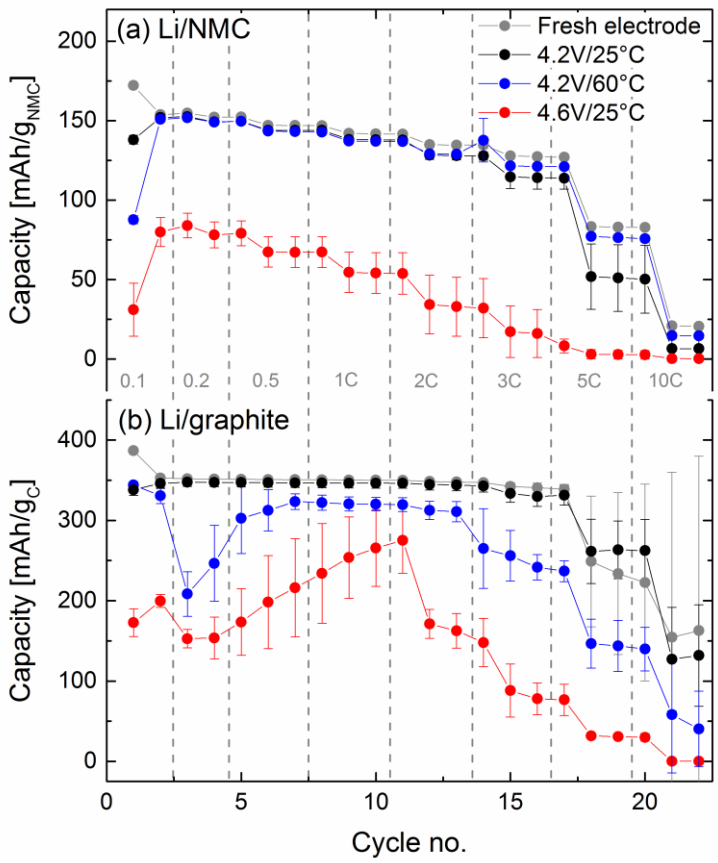

Figure 4.35: Rate performance of fresh and aged electrodes assembled in new half-cells at 25°C. (a) Li/NMC cells cycled between 3.0 and 4.3 V at 25°C, plotted is the lithiation capacity and (b) Li/graphite cells cycled between 0.01 and 1.5V at 25°C, plotted is the delithiation capacity. Results are averaged over two cells and the error bars represent the standard deviation.

loss in the 4.6V/25°C cells (s. Figure 4.25) is not only due to an impedance growth of the anode but also of the cathode (in addition to the loss of active lithium shown in Table 4.1).

The half-cell data in Figure 4.35 can also be used to try to compare the loss of active lithium obtained from XRD analysis (s. Table 4.1) with that which could be inferred from the first charge and discharge capacity of the harvested NMC half-cells. Table 4.3 shows the first cycle charge and discharge capacity at 0.1C of NMC cathodes harvested from aged cells in the discharged state in comparison to an NMC electrode just after formation. For the NMC cathodes harvested from the aged 4.2V/25°C and 4.2V/60°C cells, the half-cell discharge capacity corresponds to that of a pristine NMC electrode after formation (first row of Table 4.3) and the difference between the capacity in the first charge and the discharge should represent the amount of active lithium loss and, indeed, matches nicely the results from the *ex situ* XRD measurements (s. right-most column in Table 4.3). However, for the aged NMC cathode harvested from the 4.6V/25°C cell, the half-cell

discharge capacity is only 86 mAh/g_{NMC}, so that the difference between the first charge and discharge cycle half-cell capacity does not any more allow determining the loss of active lithium! Thus, in the case of severe impedance growth, the latter can only be determined from the XRD analysis or, alternatively, from chemical analysis of the lithium content of the harvested NMC sample.

Table 4.3: First cycle capacity at 0.1C of aged and fresh NMC electrodes assembled in new half-cells (data in Figure 11a) and comparison to capacity loss found with *ex situ* XRD measurements (from Table 4.1)

Cells	NMC new half-cell 1st cycle capacities			*Ex situ* XRD data
	Charge [mAh/g]	Discharge [mAh/g]	Li loss [mAh/g]	Li loss [mAh/g]
after formation	153	153	---	
4.2V/25°C	136	150	14	10.6
	140	149	9	10.3
4.2V/60°C	88	149	61	64.2
	85	149	64	67.8
4.6V/25°C	43	86	43	60.9
	20	71	51	65.9

4.5.9 Conclusion

Using *in situ* XRD analysis during the initial charge/discharge of graphite/NMC full cells, the first cycle irreversible capacity loss (ICL) of NMC was confirmed not to be caused by oxidative processes occurring on the NMC surface but to result from sluggish lithium diffusion into the host structure of $Li_{1-x}Ni_{1/3}Mn_{2/3}Co_{1/3}O_2$ when the lithium content (1-x) exceeds 0.915 (x < 0.085). Given enough time, *e.g.*, by holding the cell at constant voltage after the first discharge, the NMC can be nearly reversibly lithiated back to its initial lithium content. Consequently, in graphite/NMC full-cells, the loss of active lithium due to the ICL of NMC and the graphite SEI formation are not additive, and the loss of active lithium corresponds to the larger of the two contributions.

A correlation between the lithium content in NMC with its lattice parameters, *i.e.*, with the *c/a* ratio, allows a convenient quantification of the loss of active lithium during extended cycling by determining the *c/a* ratio of harvested NMC cathodes in their discharged state using *ex situ* XRD. With this new approach, it could be shown that the capacity loss of graphite/NMC cells cycled to a positive cut-off voltage of 4.2 V over 300 cycles is mainly due to the loss of active lithium, whereby these losses are minor at 25°C and rather large at 60°C. This strong temperature dependence is ascribed to the significant amount of predominantly Mn dissolution at 60°C, as demonstrated by Prompt Gamma Activation Analysis (PGAA) of harvested graphite anodes, which is also accompanied by partial anode SEI dissolution and re-formation

For graphite/NMC cells cycled at a positive cut-off voltage of 4.6 V at 25°C, a so-called "rapid rollover capacity loss" was observed and only about half of the capacity loss could be ascribed to a loss of active lithium, while significant amounts of Mn, Co, and Ni were found on the harvested graphite anodes. Full cell AC impedance and charge/discharge cell voltage profiles indicated a significant growth of cell impedance, which has commonly been ascribed to additional impedance growth of graphite electrodes in the presence of transition metal dissolution. However, half-cell measurements of harvested aged NMC and graphite electrodes clearly showed significant impedance growth of both electrodes.
In summary, increasing the temperature is less detrimental than applying high cut-off potentials as the latter one forces enhanced electrolyte oxidation and structural stresses in the positive active material.[63]

Acknowledgment: The authors thank the Heinz Maier-Leibnitz Zentrum (MLZ) for granting us beam time at the neutron source and express their thanks and gratitude to Z. Revay for helpful discussions during the PGAA data analysis. We also acknowledge the BMBF (Federal Ministry of Education and Research, Germany) for funding project "ExZell-TUM", grant number 03X4633A.

4.6 First-cycle defect evolution of $Li_{1-x}Ni_{1/3}Mn_{1/3}Co_{1/3}O_2$ lithium-ion battery electrodes investigated by positron annihilation spectroscopy

In this study, the structure and evolution of vacancy type defects in lithium-ion batteries are investigated using positron annihilation spectroscopy (PAS). The correlation between positron annihilation characteristics and structural changes during the delithiation/lithiation process of $Li_{1-x}Ni_{1/3}Mn_{1/3}Co_{1/3}O_2$ (NMC-111) electrodes, also in context of the electronic structure, is discussed. This work further continues the experiments on the so-called first-cycle irreversible capacity loss ("ICL") of NMC-111 examined in Chapter 4.5 and investigates possible reasons for the observed kinetic hindrance of lithium-ion reintercalation based on open-volume defects.

For this purpose, samples of NMC-111 electrodes with decreasing lithium content ($x = 0 – 0.7$), which covers a wide range of state of charge, were electrochemically prepared for the non-destructive analysis using positron coincidence Doppler broadening spectroscopy (CDBS). The positron measurements allowed us to observe the evolution of the defect structure caused by the delithiation process in the NMC electrodes. Furthermore, the combination of CDBS with X-ray diffraction for the characterization of the lattice structure enabled the analysis of the well-known kinetic-hindrance-effect in the first charge-discharge cycle and possible implications of vacancy ordering. In particular, CDBS revealed the highest degree of relithiation after discharge to 3.0 V at 55°C. For the first time, we report on the successful application of CDBS on NMC electrodes yielding new insights in the important role of defects caused by the delithiation process and the kinetic hindrance effect.

The following chapter is being prepared as manuscript for publication with the title *Defect evolution in the first charge/discharge cycle of $Li_{1-x}Ni_{1/3}Mn_{1/3}Co_{1/3}O_2$ lithium-ion battery electrodes investigated by positron annihilation spectroscopy*. The authors are Stefan Seidlmayer, Irmgard Buchberger, Markus Reiner, Thomas Gigl, Ralph Gilles, Hubert A. Gasteiger and Christoph Hugenschmidt, representing a collaboration between the Chair of Technical Electrochemistry, the Forschungsneutronenquelle FRM II and the Physics Department E21 at the Technische Universität München. The first three authors were contributing equally to this work regarding the discussion of results and the preparation of the manuscript. I was further declared as the corresponding author. My particular tasks in this work were the design of experiment and the electrochemical preparation of the cathode samples for the XRD measurements and for the CDBS analysis at the neutron source. Additionally, the evaluation of the XRD data was conducted together with Stefan Seidlmayer, whereas the interpretation of the CDBS results was rigorously discussed together with Markus Reiner, Thomas Gigl and Dr. Christoph Hugenschmidt.

4.6.1 Introduction

Layered-oxide materials (*e.g.*, $LiCoO_2$ (LCO), $LiNi_{1/3}Co_{1/3}Mn_{1/3}O_2$ (NMC-111) or $LiNi_{0.8}Co_{0.15}Al_{0.05}O_2$(NCA)) are the most popular cathode materials used in commercial lithium-ion batteries. By reducing cost and safety issues, NMC based materials have replaced standard $LiCoO_2$ and pushed forward the development of battery and hybrid electric vehicles (BEV, HEV).[13,14] NMC-111 could theoretically offer a capacity of 278 mAh g^{-1}, but owing to active material and electrolyte degradation processes, the upper potential window is typically limited to ≈4.3 V *vs.* Li/Li^+, resulting in a reversible capacity of only ≈150 mAh g^{-1} (corresponding to ≈54% of the available lithium ions).[55,214]

From our previous studies it is known that during the first charge-discharge cycle at 0.1 C up to a lithium content corresponding to $x = 0.62$, lithium ions can be removed from the $Li_{1-x}Ni_{1/3}Mn_{1/3}Co_{1/3}O_2$ structure but cannot be completely re-intercalated back into the material, resulting in a so-called irreversible capacity loss (ICL) corresponding to a value of $x \approx 0.08$.[63] The underlying process has been investigated by electrochemical methods and *in situ* X-ray diffraction (XRD), supporting the hypothesis of a kinetic barrier as the fully intercalated state is being approached, so that the initial structure with x = 0 can only be recovered after an extended voltage hold at low potentials. Similar results with $0.08 < x < 0.10$ have also been reported in the literature.[242,243,260]

In order to gain further insights into the underlying atomic processes and especially, into the role of defects during the charge and discharge process, we combine electrochemical analysis and XRD with positron annihilation spectroscopy (PAS) exhibiting outstanding sensitivity to open-volume defects. We have applied coincident Doppler broadening spectroscopy (CDBS)[110,261] of the electron-positron annihilation line using a slow positron beam provided at the neutron-induced positron source NEPOMUC at the Heinz Maier-Leibnitz Zentrum.[262,263] As sketched in Figure 4.36b, a positron implanted into a solid thermalizes rapidly within a few picoseconds (ps) and then diffuses through the solid until it annihilates with an electron after a characteristic mean lifetime in the order of 100 ps. The annihilating pair emits two γ-quanta with an energy of 511 keV in the center of mass system. In the lab scale, a Doppler shift, ΔE, of up to several keV is observed due to the momentum of the annihilating electrons.[264] Prior to its annihilation, the positron can be trapped in (metallic) vacancies which form an attractive potential for positrons due to the missing positively charged nucleus. In this case, the positron has a longer lifetime due to the locally reduced electron density. Moreover, the Doppler broadening of the annihilation line is reduced due to a lower contribution of high momentum core electrons. To our knowledge, only one work applying PAS on battery electrodes has been published so far, in which a 3-stage-mechanism for charging-induced defect evolution was proposed in bulk samples of Li_xCoO_2.[265]

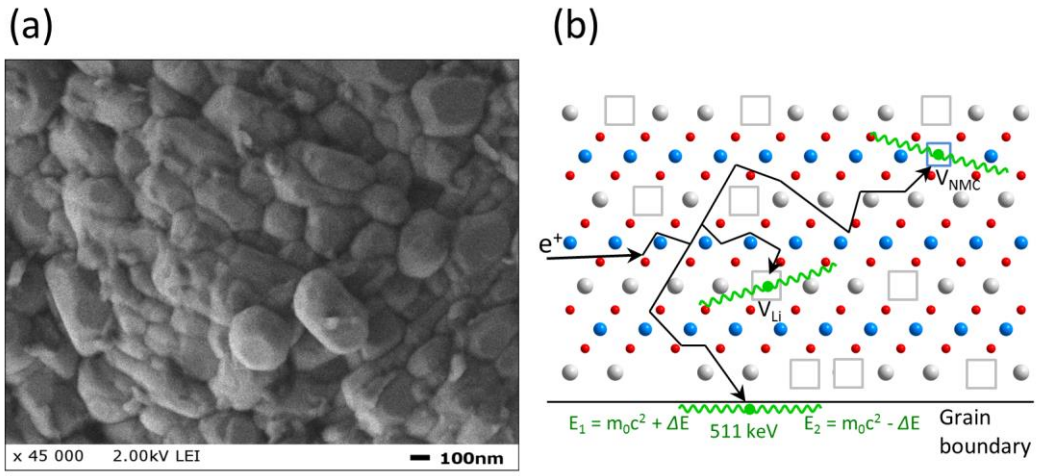

Figure 4.36: Positron annihilation spectroscopy on $Li_{1-x}Ni_{1/3}Mn_{1/3}Co_{1/3}O_2$ electrodes: (a) SEM image of a bulk sample of NMC-111, showing the primary particles of ≈100-200 nm size of a secondary particle agglomerate of ≈10 µm. The SEM characterization was carried out on a JEOL JSM 5900 LV SEM equipped with a tungsten cathode (b) Potential positron annihilation sites in NMC electrodes. Prior to annihilation, positrons (e^+) diffuse through the solid until being trapped in an open-volume defect such as Li or transition metal vacancies (V_{Li} and V_{NMC}, respectively; symbolized by a square □), or annihilating at grain surfaces.

In the present study we investigate the structurally related mixed layered oxide NMC-111 and carefully analyze the first-charge defect evolution with CDBS combined with complementary XRD. Furthermore, the results obtained for differently discharged NMC-111 samples will be compared in order to discuss the role of vacancies in the kinetic hindrance effect observed in the first charge-discharge cycle of NMC-111 half cells.

4.6.2 Experimental

(a) Sample preparation

The sample electrodes used for the PAS study are based on commercial $LiNi_{1/3}Mn_{1/3}Co_{1/3}O_2$ (NMC-111) active material. 96 wt.% NMC-111, 2 wt.% binder (polyvinylidene difluoride, PVDF, Kynar HSV 900, Arkema, France), and 2 wt.% conductive carbon (Super C65, TIMCAL, Switzerland) were dispersed in N-methyl-2-pyrrolidone (NMP, Sigma Aldrich, Germany) and mixed in a planetary centrifugal vacuum mixer (Thinky, USA) two times at 2000 rpm for 5 min. The resulting viscous slurry with a solid content of 1.9 g/ml_{NMP} was cast onto a thin aluminum foil (18 µm, MTI corporation, USA) using the doctor-blade method (RK, Print Coat Instruments, UK). The final coating was pre-dried at 50°C in a drying oven before punching electrodes of 10 mm diameter and then drying them at 120°C for 3 h under dynamic vacuum in a Büchi oven (B-580, Switzerland). All electrodes had an NMC loading of 14.64 ± 0.09 mg/cm^2, a thickness of 75 ± 1 µm and a porosity of 54%. Thus, only 4 wt.% of the electrode coating consists of non-active material.

For PAS and XRD measurements, NMC-111 electrodes with various degrees of lithium content were electrochemically fabricated by charging (*i.e.*, delithiating) or discharging (*i.e.*, re-lithiating) the electrodes in a 2-electrode Swagelok T-cell with a battery cycler (Maccor Series 4000, USA). A glass fiber separator (VWR, Germany) was used to separate the NMC-111 working electrode from the lithium counter electrode (Rockwood Lithium). The cell stack was soaked with 80 µl LP57 electrolyte (1 M $LiPF_6$ dissolved in EC:EMC(3:7), <20 ppm H_2O, BASF, Germany).

The delithiation was conducted under galvanostatic conditions with a current of 15 mA/g_{NMC} to a predefined amount of x in $Li_{1-x}Ni_{1/3}Mn_{1/3}Co_{1/3}O_2$. This current corresponds to a C-rate of ≈0.05 C if referenced to the theoretical capacity for complete delithiation. Thus, a charging (delithiation) time of 1 h corresponds to 15 mAh/g_{NMC} transferred charge, which equates to an extracted amount of Li^+ of $x = 0.054$, calculated from the total theoretical charge of 278 mAh/g_{NMC} ($x = 1$). With this approach eight samples with increasing Li extraction up to $x = 0.7$ were created, resulting in a charge end voltage of up to 4.4 V *vs.* Li/Li^+ (for details, see Table 4.4).

Furthermore, measurements were conducted on discharged NMC-111 electrodes. For these experiments, NMC-111 half cells were charged (delithiated) up to 4.3 V *vs.* Li/Li^+ and discharged to 3.0 V *vs.* Li/Li^+ (re-lithiated). For some samples, the discharge was continued by a constant voltage step, keeping the applied potential at 3.0 V for 12 h at 25°C or 55°C, or at 2.0 V for 12 h at 25°C.

After having obtained a defined lithium content as described above, the cells were carefully dissembled in an argon filled glovebox to harvest the NMC-111 electrode samples. For CDBS analysis, samples were rinsed with dimethyl carbonate (DMC, <1.4 ppm H_2O) to remove residual electrolyte and dried under vacuum at 120°C for 1h in the Büchi oven. The electrodes had to be cut into 5x5 mm pieces in order to accommodate several samples onto one CDBS sample holder. The sample holders were sealed into pouch foils in the glovebox under argon before transferring them to the CDBS instrument. These pouch foils were opened directly prior to introducing them into the CDBS measurement chamber to minimize contact with air (contact time <30 s).

Samples for XRD analysis were dissembled from the prepared T-cells and mounted directly in the XRD sample holder in an argon filled glovebox (see section XRD analysis). An overview of the examined samples is given in Table 4.4. Typical errors are given parenthesis.

(b) XRD analysis

The XRD patterns of the harvested NMC-111 electrodes were obtained in transmission mode with a STOE STADI P diffractometer (STOE & Cie GmbH, Germany) using Mo-$K_{\alpha 1}$ radiation ($\lambda = 0.70932$ Å, 50 kV, 40 mV) equipped with a Mythen 1K detector. The diffraction patterns were measured in repetition mode with two repetitions per sample. The obtained repetition data were then summed up. Patterns were collected in a 2θ-range between 6.5-52° with a step size of 0.015° and a step time of 5 s. For the XRD

Table 4.4: Lattice parameters obtained from XRD refinements of the samples prepared for PAS. *x* was calculated from the transferred charge (in mAh) divided by the mass of active material (in g) by considering that 278 mAh/g_{NMC} corresponds to $x = 1$. The error in quantifying *x* from the transferred charge is estimated to be ±0.01 (from the precision of the current measurement and the assumption that electrolyte oxidation in the examined potential window is negligible). CC = Constant Current; CV = Constant Voltage. The term "Pristine" refers to the measurement of an electrode as manufactured and before cell assembly.

Sample description	***x***	***a* [Å]**	***c* [Å]**	***V* [Å³]**
$LiNi_{1/3}Mn_{1/3}Co_{1/3}O_2$ (Yin *et al.*[233])	0	2.860	14.227	100.8
Sample #1 "Pristine"	0	2.857	14.220	100.5
Charged samples				
Sample #2	0.04(1)	2.854(1)	14.235(1)	100.4(2)
Sample #3	0.20(1)	2.841(1)	14.312(1)	100.0(2)
Sample #4	0.40(1)	2.825(1)	14.438(1)	99.8(2)
Sample #5	0.50(1)	2.820(1)	14.480(1)	99.7(2)
Sample #6	0.55(1)	2.819(1)	14.485(1)	99.7(2)
Sample #7	0.60(1)	2.818(1)	14.480(1)	99.6(2)
Sample #8	0.65(1)	2.819(1)	14.455(1)	99.5(2)
Sample #9	0.70(1)	2.820(1)	14.438(1)	99.4(2)
Discharged samples				
Sample #10 (CC 3.0V)	0.07(1)	2.852(1)	14.248(1)	100.4(2)
Sample #11 (CV 3.0V/25°C)	0.02(1)	2.856(1)	14.228(1)	100.5(2)
Sample #12 (CV 3.0V/55°C)	0.02(1)	2.857(1)	14.221(1)	100.5(2)
Sample #13 (CV 2.0V/25°C)	0.02(1)	2.856(1)	14.227(1)	100.5(2)

measurement, sample preparation was performed in an argon filled glovebox. The electrodes were placed inside a PTFE ring, enclosed by two sheets of Mylar foils and pressed together by two stainless steel rings. Data analysis was performed by Rietveld refinement using Highscore software packages.[87] All diffraction patterns could be refined with two phases only, NMC-111 active material with the $R\,\bar{3}\,m$ structure and Al current collector. Structure data for fitting were taken from the literature.[233,266] Thompson-Cox-Hastings profile functions[267] including scale factors, width parameters *W* and *X*, and a mixing parameter for peak shape were used. Profile asymmetry was corrected with the Finger-Cox-Jephcoat approach[268] and constrained for both phases. Lattice parameters, coordinate *z*(O) for NMC-111, and an isotropic thermal displacement parameter *B* for each phase were refined. The Li occupancy for Li1 position was adjusted to a fixed value according to values calculated from the coulombic charge passed during the electrochemical (de-) lithiation for each sample. Finally, using the Al current collector as an internal standard with fixed cell parameters, 2θ zero shift and specimen displacement were taken into account.

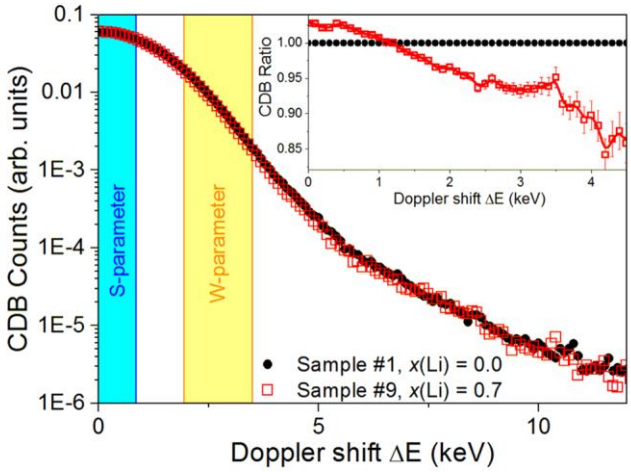

Figure 4.37: CDB spectra exemplarily shown for the samples #1 (x=0.00) and #9 (x=0.70) as a function of the Doppler shift Δ*E*. The respective CDB ratio obtained after division by the CDB spectrum of sample #1 as reference is shown in the inset. The *S*- and *W*-parameters are obtained by integrating the counts in the marked intervals of Δ*E* and further used for data evaluation.

(c) CDBS measurement

CDBS was conducted at the high-intensity positron beam NEPOMUC at MLZ.[269,270] The incident beam energy was set to 29 keV corresponding to a mean positron implantation depth of 2 µm. A quick sweep with depth dependent DBS confirmed that all positrons implanted in this depth annihilate in the bulk. A collinear set-up of high-purity Ge detectors was then used to record the CDB spectra. Valid coincident events stemming from the detection of both annihilation quanta can be easily filtered, since the sum of their energy must amount to 1022 keV. On average 8.3 x 10^6 counts in the coincident photopeak were accumulated for each sample. The Doppler broadening line shape parameter *S* and the wing parameter *W* were determined for the quantitative evaluation of the data (see Figure 4.37). The *S*-parameter is defined as the fraction of events with Doppler shifts $\Delta E < 0.85$ keV in the central region of the coincident photopeak. Hence, this parameter mainly reflects the annihilation with low momentum electrons which largely contribute to the annihilation in open-volume defects. The *W*-parameter is defined as the fraction of counts with $2 < \Delta E < 3.5$ keV in the wing region of the coincident photopeak. This parameter is sensitive to the annihilation with high momentum core electrons which is more dominant in a defect free lattice than in open-volume defects.

4.6.3 Results and discussion

Figure 4.38 shows the electrochemical sample preparation for the CDBS and XRD measurements. Identical Li/NMC-111 half cells were built in which a predefined amount of lithium *x* was removed from $Li_{1-x}Ni_{1/3}Mn_{1/3}Co_{1/3}O_2$ by galvanostatic charging of the cells at a rate of 15 mA/g for a certain time or galvanostatically discharging the cells to 3.0 V

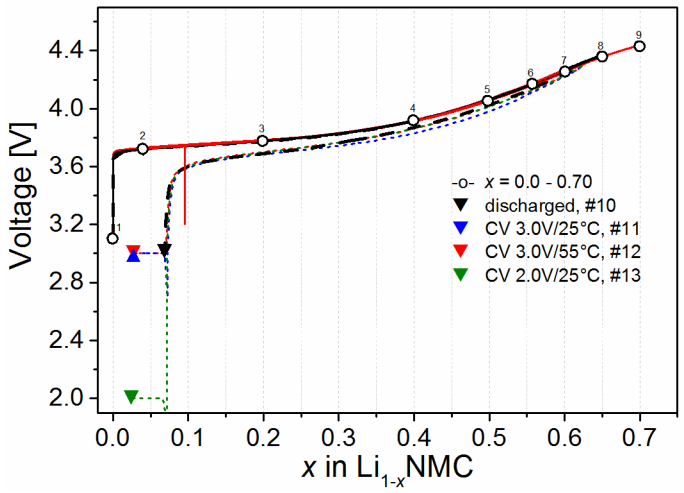

Figure 4.38: Galvanostatic charge (delithiation) and discharge (lithiation) of Li/NMC-111 half cells (14.64 ±0.09 mg_{NMC}/cm^2, 75 µm coating thickness) prepared for PAS and XRD measurements. The graph shows the superposition of all measured voltage curves of cells cycled with a current of 15 mA/g_{NMC}. The voltage is plotted against the amount of removed lithium x in $Li_{1-x}Ni_{1/3}Mn_{1/3}Co_{1/3}O_2$. Each position, at which NMC-111 electrode samples were taken, is either indicated by a circle (charge experiment) or a triangle (discharge experiment). Sample numbering is in accordance with Table 4.4.

with a final constant voltage hold. The kinetic hindrance of complete lithium intercalation is visible in the capacity difference between the first charge and discharge cycle (solid *vs.* dotted black lines in Figure 4.38).[63,242,243] Thus, the full capacity of NMC-111 could not be recovered during discharge, which leads to a loss of cyclable lithium ($x \approx 0.07$ ≈19.5 mAh/g_{NMC}), often referred to as irreversible capacity loss (ICL). However, by adding a constant voltage step with 12 h duration, the ICL could be reduced to ≈5.5 mAh/g_{NMC} ($x \approx 0.02$) in for all examined conditions, *viz.*, at potential holds at 3.0 V/25°C (blue triangle in Figure 4.38), at 3.0 V/55°C (red triangle in Figure 4.38), and at 2.0 V/25°C (green triangle in Figure 4.38), see also Ref.[260]

In order to investigate the structural dynamics, we performed XRD on the recovered NMC-111 electrodes during the delithiation and the re-lithiation process. The obtained crystallographic structure parameters from XRD pattern refinement of the prepared samples are listed in Table 4.4 and the results are plotted in Figure 4.39. Our results are consistent with previous literature data (*e.g.*, Ref.[231,271–273]).

In accordance with the electrochemical data, the XRD data shown in Figure 4.39, indicates that all NMC-111 electrode samples from the discharge experiments with a final constant voltage hold for 10 h at different temperatures and lower cut-off voltages show structural reversibility (*e.g.*, no additional phases in XRD). They coincide very closely with the lattice parameter values obtained by XRD for the pristine NMC-111 before charging (see especially blue, red and green triangles in the zoomed inset for *c*-axis). In the standard discharge to 3.0 V without constant voltage hold step (black triangle), however, the initial structure of NMC-111 could not be fully recovered, which is in

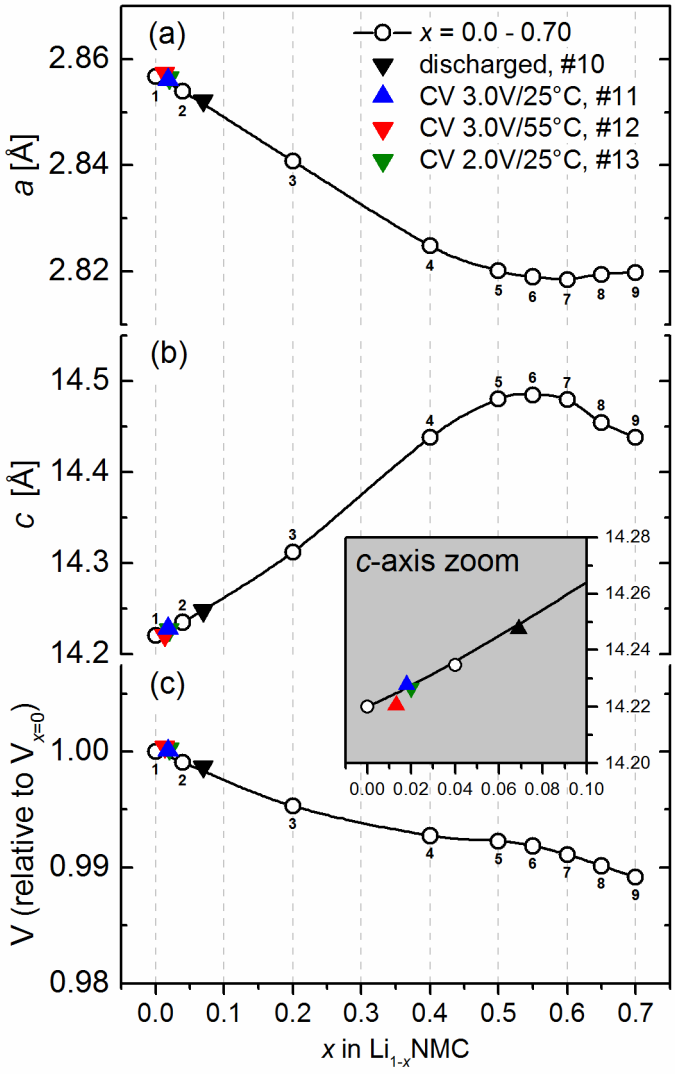

Figure 4.39: . Lattice parameters *a*, *c* and relative unit cell volume of $Li_{1-x}Ni_{1/3}Mn_{1/3}Co_{1/3}O_2$. (normalized to $V_{x=0}$ = 100.57 Å^3) as function of the lithium extraction degree *x*. Samples for XRD measurements are prepared according to Figure 4.38, the green triangle is nearly hidden behind the blue and red triangle. The inset shows a zoom of the *c vs. x*. Solid lines are guides to the eyes. Samples are labelled according to Table 4.4.

accordance with the observed capacity loss in Figure 4.38 (black dotted line) and this is due to the kinetic hindrance effect.[63,242,243,260]

The structure of $Li_{1-x}Ni_{1/3}Mn_{1/3}Co_{1/3}O_2$ is best described as a cubic closest packing of O atoms (6c site) in which the octahedral voids are filled with Li (3a site) or transition metal ions *M* = Ni, Mn, Co (3b site). The cations thus occupy slightly distorted edge-sharing octahedra ordered in alternating layers of LiO_6 and MO_6, respectively, as demonstrated in Figure 4.40. The transition metals are randomly distributed among the 3b site. The extraction of lithium from NMC-111 results first in an increase of lattice parameter *c* and in a decrease of lattice parameter *a* up to *x* = 0.5. This has been rationalized (see also Ref. [231,271–273]) by the removal of Li from the 3a site (grey in Figure 4.40) leading to an

increase of the O-O interlayer distance due to the increased repulsion of the partially negatively charged O atoms and thus to an elongation of the *c*-axis. At the same time, the gradual increase in oxidation number decreases the ionic radii of the transition metals of the 3b site and leads to a shrinking of the *M*-O bond lengths that are mostly oriented in the *a*-*b* plane and thus a decrease of the *a* parameter, consistent with Vegard's law for lattice parameter dynamics in solid-solution series.[235,236] Due to the reversed trends for *a*- and *c*-lattice parameters, the unit cell volume is effectively constant (only ≈1-2% volume change).

At higher Li extraction degrees ($x \geq 0.5$), a strong deviation from Vegard-like solid-solution behavior occurs. Between $x \approx 0.5$ and $x \approx 0.6$, both *a* and *c* parameter remain nearly constant and beyond $x \geq 0.6$, the *c*-axis starts to shrink again. This is an intriguing observation as no abrupt structural phase transition occurs (*e.g.*, a jump in lattice parameters or creation of a new additional phase or change in unit cell symmetry) and the unit cell and structure remains in the space group $R\,\bar{3}\,m$. Vegard-type behavior can strictly be expected only for solid-solution systems in which isoelectronic substitution occurs (*i.e.*, substitution of monovalent ions, for example Li^+/Na^+), but the de-intercalation of lithium from $Li_{1-x}Ni_{1/3}Mn_{1/3}Co_{1/3}O_2$ is in effect a non-isoelectronic substitution (the transition metals are oxidized during the process) a change in the electronic state occurs and this strongly influences the lattice parameter dynamics as observed by XRD. This change in electronic state has been investigated by many groups in the past *e.g.*, Hwang *et al.*[238] with computational studies and Tsai *et al.*[274] with X-ray absorption spectroscopy (XAS). According to Hwang and Tsai the effect is most likely associated with the differences in orbital hybridization between the metals and oxygen atoms when the Ni oxidation state is shifted between the initial Ni^{2+} to the final Ni^{4+} in the range x=0 and x≈0.7 and especially when the oxidation of Co^{3+} to Co^{4+} takes place beyond $x = 0.5$ as confirmed in Ref.[274] with XAS. According to the XRD patterns due to the change in the lattice parameter evolution this electronic state transition seems to take place between $x = 0.5$ and $x = 0.6$. This also fits very well with the observed plateau in the CDBS *S*- and *W*-parameters in Figure 4.41, as will be shown in the discussion below.

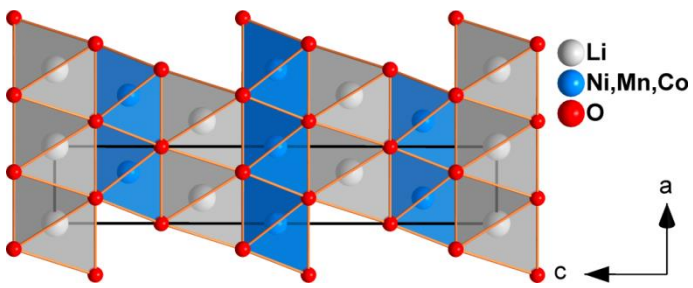

Figure 4.40: View of the $LiNi_{1/3}Mn_{1/3}Co_{1/3}O_2$ structure. Projection along *b*. LiO_6 and MO_6 octahedrons are emphasized in grey and blue color, respectively.

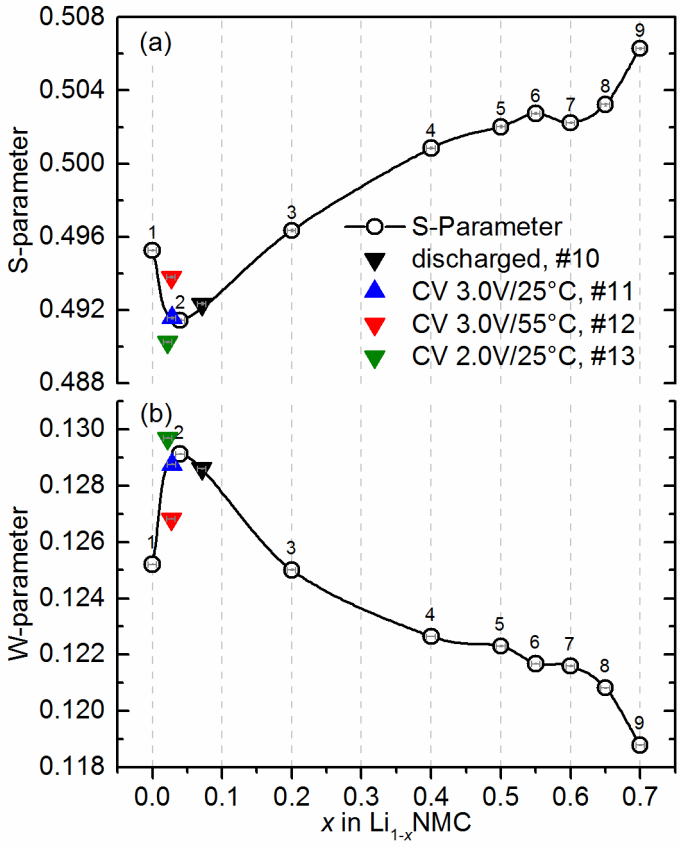

Figure 4.41: Doppler broadening shape *S*-parameter and wing *W*-parameter measured on $Li_{1-x}Ni_{1/3}Mn_{1/3}Co_{1/3}O_2$. Electrode samples in dependence of removed lithium *x*. Samples are prepared according to Figure 4.38. Soild lines are guides to the eyes. The instrumental error of the CDBS-parameters is shown as tiny circles, and the standard deviation in *x* as small bar inside the data symbols. Samples are numerated according to Table 4.4.

The *S*-parameter exhibits a pronounced dependency on *x* which can be separated into four sections as shown in Figure 4.41a, t: (i) Initially, the *S*-parameter decreases rapidly between $x = 0.00$ and $x = 0.04$ (samples #1 and #2). This behavior allows us to distinguish the defect structure of the discharged samples (#10-13; triangles) as discussed later. (ii) For $0.04 \leq x \leq 0.5$ (samples #2-5), an increase in the *S*-parameter by more than 2 % is observed, followed by (iii) a plateau for $0.5 \leq x \leq 0.65$ (samples #5-8). (iv) Finally, the *S*-parameter clearly increases further beyond to $x = 0.65$ (samples #8 and #9). Compared to the *S*-parameter the *W*-parameter displays a very similar behavior in the inverse direction (see Figure 4.41b), which is expected, *e.g.*, for a linear combination of two different positron states. For this reason, we only discuss the behavior of *S* and the underlying physics of its dependency on *x* in the following.

In order to explain the initial steep decrease in region(i) for $x \leq 0.04$, the positron states in the as-received material have to be considered first. At x=0.00, Li vacancies V_{Li} and, more likely, vacancies on the NMC sublattice V_{NMC} lead to positron trapping but also a certain fraction of positrons would diffuse to grain boundaries, which is very likely

due to the primary particle size of NMC in the order of ≈200 nm (see also Figure 4.36a and b). Thus, the observed *S*-parameter (and *W*-parameter) represents a superposition of these various positron states at $x \approx 0.00$. By increasing *x*, *i.e.*, by introducing V_{Li} as positron trapping centers, the predominant fraction of positrons will annihilate there, since already at a vacancy concentration of a few atomic percent (at.%) saturation trapping in these vacancies is expected. Consequently, the variation of the *S*-parameter for very low *x* reflects the change of the preferred annihilation site from a superposition of V_{Li}, V_{NMC} and grain boundaries for $x = 0.00$ to only V_{Li} for $x = 0.04$.

At higher *x* (region(ii)), the positrons are highly sensitive on changing lattice constants, as becomes obvious by plotting the *S*-parameter against the lattice parameter c in Figure 4.42a. For $0.04 \leq x \leq 0.50$ (samples #2-#5), the *S*-parameter exhibits an almost linear dependency on *c*. Since the increase of *c* reflects the increase in concentration of V_{Li} which therefore diminishes the contribution of high momentum electrons to the annihilation, a higher *S*-parameter (and a lower *W*-parameter) is observed.

Accordingly, in region(iii) for $0.50 < x \leq 0.65$, the almost constant parameter *c* leads to only small variation in the *S*-parameter. Consequently, we want to emphasize that our data do not give any hint for ordering phenomena of V_{Li} in the range $x \leq 0.65$, since any abrupt transition between ordering states of Li vacancies is expected to lead to a discontinuous change of the lattice parameters or the *S*-parameter as a function of *x*.

The steep increase of the *S*-parameter in regime (iv) at $x > 0.65$ shows apparently no clear correlation to the changes of the lattice parameter *c* obtained from XRD. Thus, this behavior seems to be caused by two effects, namely, changes in the free volume created by the Li vacancies and the variation of the electronic environment of the positron annihilation site. It is noteworthy that at such high values of *x* the positron could also occupy a delocalized state which extends over an agglomeration of several vacancies, V_{Li}, as observed in oxygen deficient YBCO.[275] Therefore, an ordering mechanism of V_{Li} leading to changes of the S parameter cannot be excluded. However, more important seems to be the change of the electronic structure in this regime. Using various techniques it was shown[218,238,271,274,276] the change of oxidation states of transition metal atoms directly modifies the electronic structure. In accordance, XRD also shows this electronic transition as a deviation from linear solid-solution behavior beyond $x > 0.5$. A detailed understanding of the contribution of the various processes such as electronic or ordering effects, would require theoretical modelling of the electronic structure for various defect structures in $Li_{1-x}Ni_{1/3}Mn_{1/3}Co_{1/3}O_2$ at $x > 0.65$, which is well beyond the scope of this paper.

Finally we combine the results of the applied methods in order to further investigate the discharged samples at low *x* values, in which the kinetic hindrance effect is observed during discharge. For commonly applied constant current discharge down to the cut-off potential of 3.0 V without subsequent potential hold, one reaches a re-lithiation degree of $x = 0.07$ (sample #10). This reflects the capacity loss due to kinetic limitations. On the other hand, when a final constant potential hold of 12 hours is applied (samples #11-13) additional capacity can be recovered, *i.e*, the ICL is reduced. As listed in Table 4.4, the

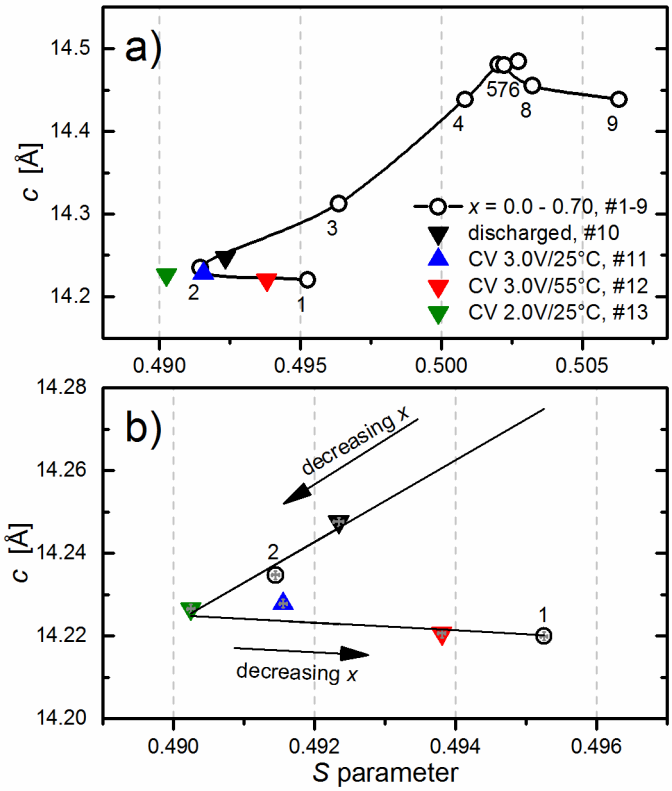

Figure 4.42: (a) Correlation between lattice parameter *c* and S-parameter. (b) Detailed view in the region of low $x < 0.04$. Samples are prepared according to Figure 4.38. Solid lines are guides to the eyes. Lower part: Zoom on low *x* region. Standard deviations of the samples are displayed as very small grey crosses inside the data symbols.

lithiation degree of samples #11-13, which is determined by the electrochemical method, is lower than that of sample #10, but cannot be distinguished from each other. On the other hand, XRD seems to indicate that sample #12 (discharged to 3.0 V at 55°C) has the highest lithiation degree because its structure is closest to the pristine sample (#1) (compare lattice parameters in Table 4.4), whereas the other samples (#10, 11, and 13) cannot be distinguished by XRD.

It has to be emphasized that in contrast to XRD and electrochemistry, the CDBS *S*-parameter reveals significant differences of all the discharged samples The respective analysis is therefore based on Figure 4.42, in which the lattice parameter *c* from XRD, which is most sensitive on *x*, is plotted against the obtained *S*-parameter. For a clearer representation, the zoom into the highly lithiated region is given in Figure 4.42b. Apparently, sample #12 exhibits the highest *S*-parameter compared to all discharged samples (#10, 11, and 13). This observation is explained by the partial (re)occupation of V_{Li} with Li atoms leading to positron annihilation in the still remaining V_{Li} and bulk V_{NMC}. A similar behavior has been noticed for the pristine sample (sample #1), in which the higher *S*-parameter was attributed to the superposition of these trapping states at very low *x* values. Thus, the degree of lithiation of sample #12 is closest to the pristine sample, in

agreement with the observation by XRD. Sample #13, however, provides the lowest S-parameter of all measured samples, which is interpreted as the onset of positron trapping only in V_{Li} sites. The transition of the S-parameter between both samples (#12 and #13) is expected to very abrupt, since already a very low vacancy concentration V_{Li} leads to saturation trapping in these vacancies. Based on these assumptions, sample #13 represents an extrapolation of the S *vs*. x curve of samples #2-#5 established in Figure 4.41, which finally results in a higher lithiation degree compared to sample #2 and a lower lithiation degree compared to sample #1 and #12. The degree of relithiation of sample #11, however, cannot be determined unambiguously, since the corresponding *S*-paramter lies between those of samples #12 and #13, and is also similar to sample #2 (see Figure 4.42).

In summary, our results allow us to evaluate the impact of temperature and discharge voltage on the degree of relithiation. Elevating the temperature to 55°C at 3.0 V is more efficient than applying a deep discharge voltage of 2.0 V. We thus confirm the findings of Kasnatscheew *et al*.[260] We conclude that slow Li-diffusion in the crystallites causes the kinetic hindrance for very low *x*. In this regime, hardly any vacancies are available and thus the relithiation of the crystallite is efficiently suppressed. Thus, increasing the mobility of lithium atoms and vacancies at elevated temperature accelerates relithiation.

4.6.4 Conclusion

We have applied defect sensitive PAS on charged and discharged $Li_{1-x}Ni_{1/3}Mn_{1/3}Co_{1/3}O_2$ electrodes for the first time. The aim was to reveal and understand the reasons for the 1st cycle irreversible capacity loss (ICL) of the cathode active material. A series of sample electrodes with decreasing lithium content as a reference were prepared from dismantled Swagelok T-cells. Additionally, samples after the 1st discharge were prepared using various 12 h potential hold steps (at 2.0 V/25°C, at 3.0 V/25°C, and at 3.0 V/55°C) after galvanostatic discharge to examine the evolution of lattice defects and especially of the Li-vacancies. In contrast to standard techniques, *e.g.*, XRD and electrochemistry, CDBS was shown to be highly sensitive at low *x* values ($x<0.04$). The Doppler broadening of the annihilation radiation exhibits a clear correlation to the degree of delithiation *x*, emerging from the microscopic behavior of the positrons, mainly their annihilation in Li vacancies and their sensitivity on changing lattice constants. It was shown that at very low *x* annihilation from competing states such as V_{Li} and V_{NMC} becomes relevant. With the interplay of CDBS, XRD, and electrochemistry we further confirned that, indeed, the 1st cycle capacity loss of the cathode material is governed by a kinetic effect. This is demonstrated by the primary dependence of the vacancy evolution on temperature rather than on discharge voltage. At high delithiation in the range beyond $x>0.5$, changes of the electronic structure affect both the *S*-parameter measured by PAS and the *c*-parameter obtained by XRD, which clearly shows a deviation from linearity of solid-solution behavior. *Ab initio* modelling of the electronic structure and further experimental studies in the range beyond $x>0.5$ are expected to lead to a deeper understanding of the underlying process. In future,

the different types of vacancies are envisaged to be characterized by complementary positron annihilation lifetime spectroscopy (PALS).

Acknowledgment: The authors thank the Heinz Maier-Leibnitz Zentrum (MLZ) for granting us beam time at the neutron source and express their thanks and gratitude to Z. Revay for helpful discussions during the PGAA data analysis. We also acknowledge the BMBF (Federal Ministry of Education and Research, Germany) for funding project "ExZell-TUM", grant number 03X4633A.

4.7 *In situ* XRD cell for transmission geometry

4.7.1 Performance of pouch cells

In addition to the custom-built *in situ* XRD cell for Bragg-Brentano geometry introduced in Chapter 4.2, single-layered pouch cells proved to be very useful in measuring XRD during operation at a laboratory diffractometer. Beside Swagelok T-cells and coin cells, pouch cells are also established as a laboratory test cell for electrochemical characterization.[44,277,278] Thus, performances can be easily compared among each cell design as well as to the literature. Furthermore, the pouch cell design is close to commercial cells with regard to the amount of electrolyte, electrode design and choice of separator. This enables the easy projection of electrochemical-structural results obtained from a laboratory pouch cell onto large-sized cells. Since pouch cells consist of a single-layered or multi-layered electrode stack encased in a thin laminated-polymer-aluminum foil, they can be directly used for XRD analysis in transmission mode without any necessary modifications. However, for this type of experiment, the highly penetrating X-rays from a Mo source are essential to minimize intensity losses by the absorption of the pouch foil and the cell components. The absorption is mainly caused by the aluminum component of the pouch foil and the aluminum and copper current collectors. Additionally, the entire bulk of the electrode material is probed in transmission geometry, which is preferable to reflection geometry, in which X-rays penetrate only few microns into the surface of the active material. With this setup, both cathode and anode materials can be investigated as discussed previously in Section 3.4.2.

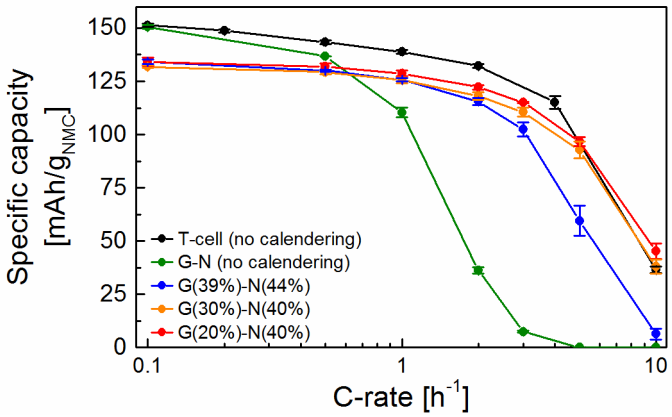

Figure 4.43: Electrochemical rate performance of pouch cells with graphite (G) and NMC (N) electrodes at different porosities (numbers in brackets). A Celgard separator is used in all pouch cells, which have an average NMC loading of 13.5 ±0.7 mg_{NMC}/cm^2 and a graphite to NMC areal-capacity ratio of 1.0 ±0.1. All tests are compared to laboratory Swagelok T-cells equipped with glass fiber separators and an average NMC loading of 15.1 ±0.3 mg_{NMC}/cm^2 and a graphite to NMC areal-capacity ratio of 1.2 ±0.1. Error bars indicate the standard deviation between three cells.

Despite these benefits, the manufacturing process of pouch cells is rather complex and depends on various parameters.[138,279] Important production steps include the cutting of electrodes and separators, calendering, electrolyte filling and sealing. Since pouch cells have been recently introduced in our group, the investigation of relevant parameters for a stable and comparable cycling performance is still in progress. One of those parameters concerns the calendering of electrodes. It has been found on the basis of a graphite-NMC system that electrodes need to be compressed to a porosity of ≈30% to achieve a competitive rate performance compared to Swagelok T-cells as shown in Figure 4.43. While graphite electrodes could easily be compressed to a porosity of 20%, cathode electrodes tend to undergo a relaxation process, in which the porosity again increases from 30% to 40% after calendering (see legend in Figure 4.43, in which equal porosity between anode and cathode was aimed at). Due to the calendering process, the particle to particle contact as well as the adhesion to the current collector is enhanced, which seems to be crucial characteristics for a good performance of pouch cells. It has to be noted, that in contrast to the spring compression in a T-cell, the pouch-cell electrode stack is only externally compressed by atmospheric pressure due to the applied vacuum during the sealing pro-

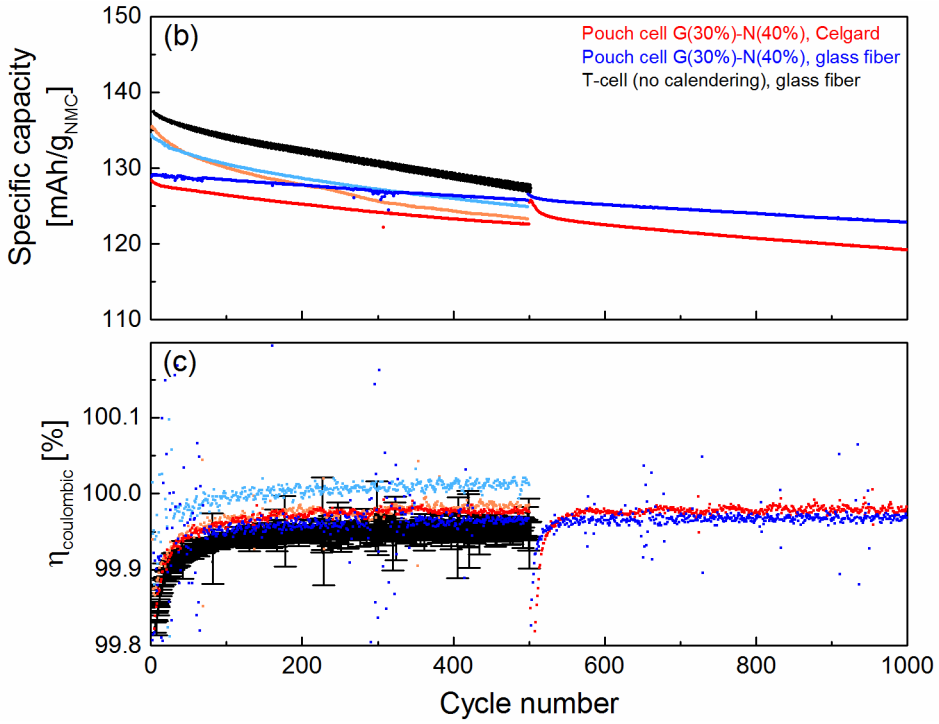

Figure 4.44: (a) Cycling performance of different pouch cells with glass fiber or Celgard separator at 1C between 3.0 and 4.2 V (CCCV) for 500 or 1000 cycles at 25°C. Comparable T-cell data represent an average of three cells for 500 cycles (error bars can only be reflected by a thicker line). (b) Corresponding coulombic efficiency. The pouch cells have an average NMC loading of 13.5 ±0.7 mg_{NMC}/cm^2 and a graphite to NMC areal-capacity ratio of 1.0 ±0.1. All tests are compared to laboratory Swagelok T-cells equipped with glass fiber separators and an average NMC loading of 15.1 ±0.3 mg_{NMC}/cm^2 and a graphite to NMC areal-capacity ratio of 1.2 ±0.1.

cess. Despite these improvements in rate capability, pouch cells with calendered electrodes always showed a lower capacity at 0.1C compared to a Swagelok T-cell. A possible reason might be a change in the reversible capacity of the electrodes due to the calendering process, but tests on calendered electrodes in coin-cell half cells did not confirm this assumption. Some improvements were made by a more precise alignment of the electrode stack, but the origin of lower capacity still remains to be solved.

The cycling stability of pouch cells for 500 cycles at 1C is similar to the T-cell (Figure 4.44). On trial, some pouch cells were even cycled for 1000 cycles with a capacity retention of 93% compared to the initial capacity at 1C. In contrast to T-cells, where only tests with glass fiber separators are possible, pouch cells could be operated reliably either with a glass fiber or a Celgard separator (trilayer separator with PP/PE/PP) as demonstrated in Figure 4.44a, whereas the latter separator is commonly used in commercial cells. The coulombic efficiency of pouch cells and hence the reversibility of the cell reaction is slightly improved using the Celgard separator as shown in Figure 4.44b. One pouch cell with glass fiber separator (light blue dots), however, seems to be an outlier, since the coulombic efficiency exceeds the 100%, which must be caused by an improper counting of coulombs during charge and discharge for this specific cell. Yet, issues with cell-to-cell variation exist, which can be observed best in the capacity deviation of different pouch cells in Figure 4.44a. The T-cells, on the contrary, are very reproducible and almost no deviation between the three tested cells is observed. Improvements on pouch cell reproducibility will be expected from a special-designed compression tool with adjustable spring pressure, which provides a constant loading of ≈0.15 – 0.2 MPa on each pouch cell (see Figure 4.50 in Section 4.7.4 “Conclusion and outlook”). Tests are planned in near future, so that results cannot be discussed here. Based on this approach, a possible variability in cell compression by evacuating the cell is thus assumed to be the main cause for the scatter of the pouch cells.

XRD measurements were conducted on a pouch cell with calendered electrodes directly after assembly. The pouch cell was therefore mounted on a transmission diffractometer equipped with a Mo source and the diffraction pattern was collected in the range 6.5-53°2θ (details on the measurement and refinement procedure are provided in Section 3.4.2). The Rietveld refinement of the measured diffractogram in Figure 4.45 shows a good agreement between measured and calculated pattern as illustrated in the difference plot below the patterns. Four phases, *i.e.*, Al, NMC, graphite, and Cu, were necessary to completely describe the measured pattern. Spikes in the difference plot are mainly attributed to Al, because the fitting of Al reflections was the most difficult task due to preferred orientation issues within the foil. The remaining phases, however, could be fitted with sufficient quality for pattern evaluation.

Despite the more difficult reproducibility and lower precision, pouch cells demonstrated to be feasible for XRD measurements on a laboratory diffractometer equipped with a Mo source. The provided intensity from the source was sufficient to allow for a proper Rietveld refinement and analysis, whereas the electrochemical performance and

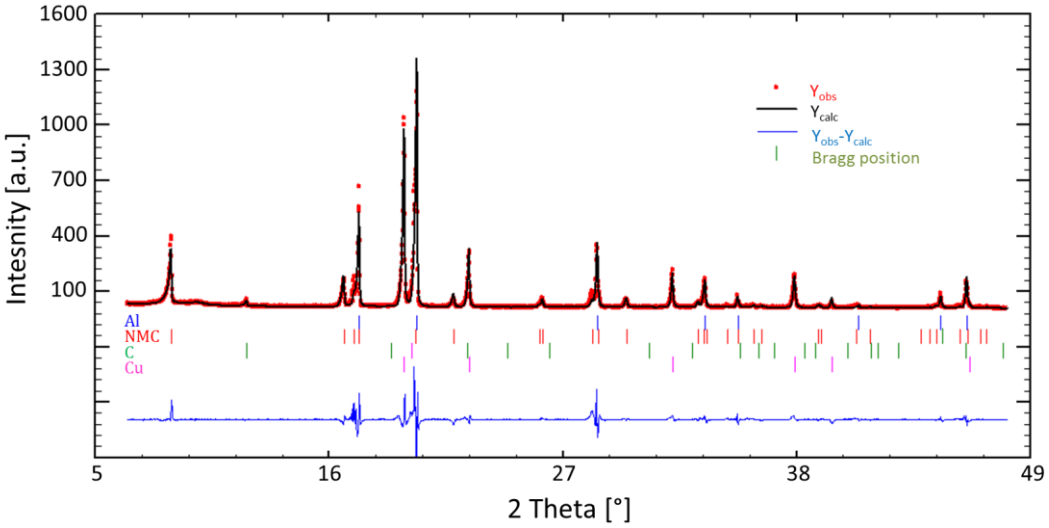

Figure 4.45: Rietveld refinement of the XRD pattern of a graphite-NMC pouch cell containing a glass fiber separator and LP57 electrolyte. Shown is the measured pattern (red dots, Y_{obs}), the calculated pattern (black line, Y_{calc}) and the difference plot (blue line). Ticks below the pattern refer to the refined phases Al ($Fm\bar{3}m$), NMC ($R\bar{3}m$), C ($P6_3/mmc$), and Cu ($Fm\bar{3}m$) denoted with the according space group.

stability of the pouch cell competed with our Swagelok T-cell. Due to the application of Celgard separators and the flexibility in cell design, the pouch cell represented an attractive system for a combined electrochemical and structural analysis. Therefore, a small insight into the applicability of pouch cells for XRD analysis will be given by the investigation of the graphite reflection evolution in a Li-graphite and a graphite-NMC cell. The investigation emphasizes on the advantageous analysis of anode materials and the parallel evaluation of both cathode and anode materials.

4.7.2 Experimental setup for XRD

Standard single-layered pouch cells were used for this study. The according electrode and cell preparation followed a conventional procedure which is described in the experimental Sections 3.2.2 and 3.3.1. Since pouch cells were cycled under atmospheric compression, a simple device was only necessary to fix and mount them on the XRD diffractometer. This device is shown in Figure 4.46a. The principle components comprised an ω-table which could be fixed to the diffractometer, a linear positioning stage with micrometer screw for fine-adjustment of the sample position, and the pouch cell sample holder (detailed technical drawings of the pouch-cell holder can be found in the appendix). During the complete test, *e.g.*, successive electrochemical cycling and XRD measurements, the pouch cell had to reside inside the sample holder to ensure XRD measurements at the same position of the pouch cell (*in situ*). The pouch cell sample holder consisted of 1 cm thick aluminum plates with 8 mm diameter holes for the X-ray beam. The plate facing the X-ray source had a cylindrical hole, whereas the plate facing the detector had a conical opening, which allows the diffraction of the X-ray beam in a 2θ range of 0 - 45°. Plates

and pouch cell were assembled with four screws and could then be mounted onto the linear positioning stage. The complete sample arrangement at the STOE STADI P transmission diffractometer is shown in Figure 4.46b. XRD measurements were conducted at a fixed incident beam angle of $\omega = 0°$ (relative to the surface normal) while the detector scanned over the whole 2θ range. With this set-up, a rotation of the sample around the sample axis was not possible, which resulted in preferred orientation issues as seen in the Rietveld refinement of the aluminum phase in Figure 4.45.

Single-layered pouch cells were either built in half-cell (Li-graphite) or in full-cell configuration (graphite-NMC). The corresponding graphite electrodes consisted of 95 wt% graphite and 5 wt% PVdF binder and the loading was adjusted between 6.2 and 6.5 mg_C/cm^2 (2.2-2.3 mAh/cm^2). NMC electrodes consisted of 96 wt% NMC, 2 wt% PVdF binder and 2 wt% Super C65 conductive carbon resulting in a loading of 13.7 mg_{NMC}/cm^2 (2.05 mAh/cm^2). Thus, an anode-to-cathode areal-capacity ratio of 1.1 could be achieved for the graphite-NMC system. In graphite half cells, metallic lithium (450µm, Rockwood lithium) was used as a counter electrode, which was only contacted at the edge by a thin strip of copper foil to minimize the amount of copper in the beam. To separate anode and cathode, a single sheet of glass fiber separator soaked with LP57 electrolyte (≈20 $\mu l/cm^2_{separator}$, 1 M $LiPF_6$ in EC:EMC, 3:7, w:w) was used. A portable potentiostat (SP 200, Biologic) is utilized when electrochemical experiments have to be conducted directly at the diffractometer. Details on the electrochemical experiments are given in the text.

For tests on the Li-graphite pouch cell, XRD scans were performed between 10- 20.2°2θ with a step size of 0.25° and a step time of 5 s in repetition mode (continuous data collection) resulting in a data-collection time of ≈11 min for one pattern. Five successive patterns, which had been collected during an OCV period, were added for data analysis using the $WINX^{POW}$ software resulting in a total of 55 min for the final averaged diffractogram. For the graphite-NMC system, XRD scans were performed in the charged

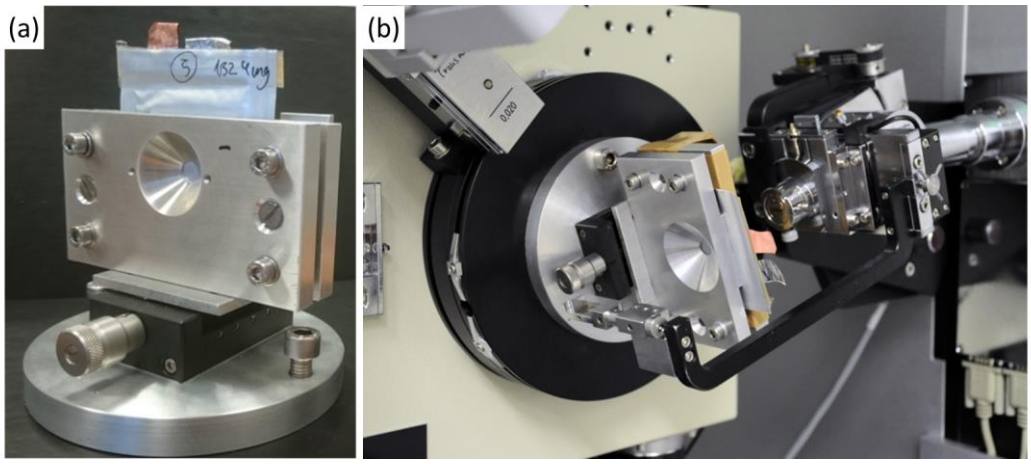

Figure 4.46: (a) Pouch cell mounting device for the STOE STADI P diffractometer in transmission geometry. (b) STOE STADI P transmission diffractometer equipped with the pouch cell mounting device.

state between 10 - 20.2° 2θ with a step size of 0.15° and a step time of 12 s, which resulted in a total of ≈42 min for the pattern. XRD scans in the discharged state were performed between 6.5 – 53.0°2θ with a step size of 0.15° and a step time of 5 s, which resulted in a total of ≈42 min for the pattern. The choice of two different 2θ ranges was related to the phase to be analyzed: While a restricted 2θ range is sufficient for the analysis of the most intense graphite reflection, a broad 2θ range is necessary for the Rietveld analysis of the NMC reflections.

Integrated reflection intensities for graphite were determined using the WINX^{POW} pattern fitting package. Rietveld refinement was only conducted on patterns collected in the discharged state of the full cell using the FullProf software package. Al (F$m\bar{3}m$), NMC (R$\bar{3}m$), graphite ($P6_3/mmc$), and Cu (F$m\bar{3}m$) were refined according to their space group. Refined parameters were scale factor, specimen displacement, background, lattice parameters, profile parameters *W* and *X*, asymmetry, preferred orientation for Al, and overall temperature factor. Atomic coordinates and occupancies were kept constant.

4.7.3 *In situ* XRD analysis of graphite and NMC in pouch cells

To study the phase transition during lithiation of graphite, *in situ* XRD on a pouch cell in transmission mode is possible because X-rays can penetrate the copper current collector of 9 µm thickness in this geometry. The goal of this experiment was the detection and evaluation of the LiC_{12} and LiC_6 phase transition in the second half of the graphite lithiation process. Due to the presence of the light elements Li and C, the interaction of graphite or lithiated graphite with X-rays is very weak. Thus, only the most intense reflection of each graphite phase could be evaluated.

From the literature it is known, that graphite undergoes several phase transitions during lithiation and delithiation.[280] It was observed that lithium intercalation proceeds through a series of staged graphite intercalation compounds, classified by a stage index *n*, which represents the number of graphene layers separating the layers of intercalated lithium-ions.[281] Based on *ex situ* and *in situ* XRD, several stages (single phases) were determined, which could be attributed to well-defined *x* values (Li_xC_6).[280,282,283] The phase transition between each stage, however, can occur in two different manners: (i) Coexistence of two phases expressed in the presence of two phases in the diffractogram with opposing intensity ratio or (ii) solid-solution like phase-transition expressed in a continuous shift of the *c*-axis parameter in the XRD pattern. These transitions are well supported by electrochemical data, in which a flat plateau in the voltage-profile curve represents the two-phase system.[282] This can also been seen in the experimental data of the Li-graphite pouch cell shown in Figure 4.47a. For XRD analysis, only the phase transition between LiC_{12} and LiC_6 ($0.5 < x < 1$) was investigated, which follows the two-phase reaction mechanism. The aim was to establish a correlation between reflection intensity ratio and lithium content *x* in Li_xC_6, similar to a procedure described for the mechanistically-related LFP.[284] With this approach, the determination of the remaining capacity in a graphite

electrode in the charged/lithiated state of a lithium-ion battery by XRD should be possible.

Before XRD analysis, Li-graphite pouch cells were cycled four times at 0.1C between 0.01 and 1.5 V *vs.* Li/Li^+ to build up a proper and stable SEI layer on graphite as demonstrated in Figure 4.47a. Since already after the first cycle a stable cycling without any capacity shift of the voltage-capacity curve was observed (≡ a shift corresponds to an ongoing parasitic SEI reaction), it can be assumed that in the fifth cycle the complete applied current is transferred into the electrochemical reaction of graphite intercalation/deintercalation. This is important for a clear correlation between electrochemical charge (x in Li_xC_6) and structural evolution in the XRD data. Successive XRD measure-

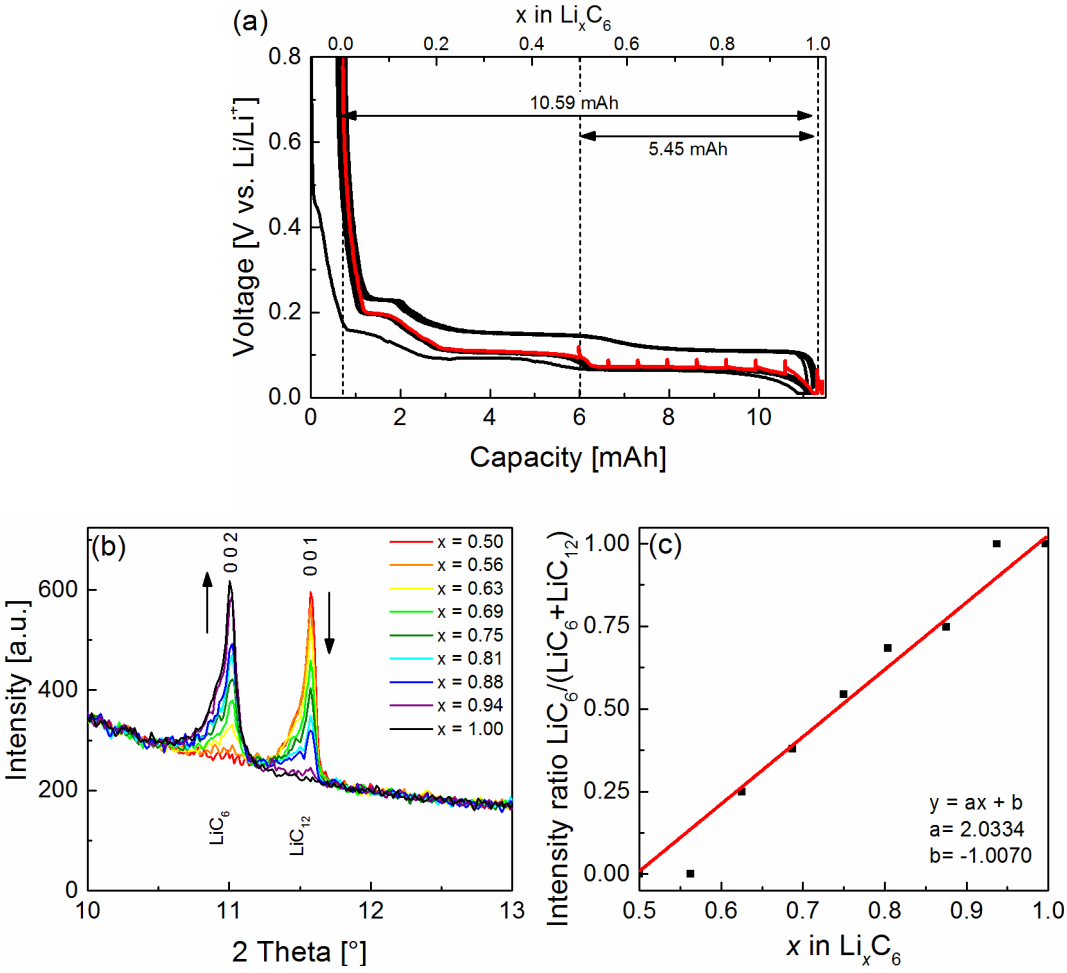

Figure 4.47: Combined electrochemical and *in situ* XRD investigation of a Li-graphite pouch cell. (a) Galvanostatic formation cycles at 0.1C between 0.01 and 1.5 V *vs.* Li/Li^+ with a CCCV procedure during discharge. The red line corresponds to the last discharge of the formation process. Spikes in the second half of discharge indicate an OCV period of 1 h, in which XRD patterns were collected for the analysis. Numbers in mAh correspond to the total reversible capacity and the obtained capacity during the XRD experiment. (b) Evolution of the 0 0 1 and 0 0 2 reflections of LiC_{12} and LiC_6 phases during the second half of discharge. Arrows indicate the lithiation process (c) Evaluation of the integral reflection intensity ratio of the 0 0 2 and 0 0 1 reflections (black markers) and linear regression of the data (red line).

ments were conducted in the fifth discharge (red curve) after the formation of LiC_{12} at $x = 0.5$ had been completed. Spikes in the plot represent an 1 h OCV interruption of the galvanostatic discharge to allow for phase equilibration and subsequent XRD data collection.

In Figure 4.47b the phase transition between LiC_{12} and LiC_6 can be followed by the most intense reflections of both phases between 10 and 13°2θ. When lithium intercalation proceeds, the 0 0 1 reflection of LiC_{12} decreases in intensity, while the 0 0 2 reflection of LiC_6 increases, which is characteristic for the two-phase reaction mechanism. These reflections were used as a simple means for phase quantification purposes, by forming an integral intensity ratio normalized to the total integral intensity of both reflections. Thus, issues with background or different pattern intensities can be neglected. A calibration curve is obtained by plotting the intensity ratio y against the lithium content x in Li_xC_6 and applying a linear fit as illustrated in Figure 4.47c: $y = 2.0334x - 1.0070$. For the fit, the second and penultimate data points were omitted because the integrated reflection intensity of the smallest phase present could not be distinguished from the background and therefore was assumed to be zero. This leads to a restricted lithium-content determination with high uncertainties in regions close to the single phase.

Despite these limitations, the calibration curve could be utilized to estimate the lithium content and capacity of a graphite electrode in the charged state of a full cell. In contrast to elemental analysis such as ICP-OES, no disassembly of the cell would be necessary using *in situ* XRD. Furthermore, this method is complementary to the lithium content determination from NMC in the discharged state as introduced in Chapter 4.5. When both analysis methods are applied, an overview of the intercalated lithium inventory in a pouch cell and a determination of active lithium-loss can be provided. The accuracy of the method, however, is limited due to the weak interaction of graphite with X-rays and its resulting low intensities. An alternative would be neutron diffraction, which is increasingly applied to investigate carbonaceous materials in commercial cylindrical lithium-ion cells,[285–287] but the access to the facility is limited, cost intensive and the method is not applicable to thin pouch cells.

In the next experiment, a pouch cell in full-cell configuration was investigated using *in situ* XRD to demonstrate the simultaneous analysis of both anode and cathode materials. For this purpose, a graphite-NMC pouch cell was assembled and a rate capability test up to 5C was performed. With increasing current, the ohmic resistance will be enhanced according to Ohm's law, resulting in a higher cell polarization. Limited by the cut-off potential, less charge or lithium ions are expected to be transferred between each electrode, thus remaining lithium ions must be left in one of the electrodes. The SEI reaction during the first formation cycle is considered as the main source for active lithium loss, while following losses are only attributed to kinetic losses.

Charge-discharge cycles were performed between 3.0 and 4.2 V two-times at a rate of 0.1C, 1C, and 5C with a CV step in the charged state (cut-off current 0.05C). The voltage profile of the rate capability test is shown in Figure 4.48c. Except for the first cycle, ca-

pacity losses can mainly be attributed to increased overpotentials and cell polarization as seen in the voltage difference between each C-rate. The first-cycle irreversible capacity loss is then caused by the SEI-formation reaction on graphite, which consumes active lithium provided by the cathode material.

In situ XRD measurements were conducted both in the charged and discharged state of the cell. A close-up of the XRD patterns in the charged state between 10 and 13° 2θ for graphite and between 15.5 and 17.5° 2θ for NMC are depicted in Figure 4.48a and b, respectively. In this state, graphite electrodes are intercalated with lithium ions, whereas NMC electrodes are delithiated up to a certain voltage-dependent degree. Obviously, graphite returns to the same particular structure in the charged state of the cell because no shift in reflection position or change in intensity is visible. NMC, however, shows a slight increase in intensity in the very last diffraction pattern, which reflects a small distortion in this material at higher rates. Since the structure of the active material is influenced by the amount of intercalated lithium, it is concluded that each active material is charged to the same degree of lithiation at any C-rate. The amount of lithium ions transferred between the electrodes, however, decrease with increasing C-rate. This can be observed in the according capacities for the charging process in Figure 4.48c, which decrease from 19.8 mAh to 9.0 mAh. These numbers strictly depend on the capacity obtained in the preceding discharge. The position and intensity of the graphite reflection at ≈11° 2θ in Figure 4.48a indicates a completely lithiated graphite with the composition LiC_6, when comparing the reflection position to those in Figure 4.47b. Further evaluations based on the graphite calibration line (Figure 4.47c) are not necessary due to the defined experimental conditions in the charged state.

In the discharged state, however, huge structural changes can be observed for both anode and cathode materials (see Figure 4.48d and e). In this state, graphite electrodes get delithiated, whereas NMC electrodes get lithiated by lithium ions. If no losses occur, both graphite and NMC should return to their initial structures as indicated by the black lines in Figure 4.48d and e. However, it was found that, *e.g.*, the initial graphite reflection 0 0 1 (black line) shifts to lower 2θ values as the C-rate increases. This shift is related to an expansion of the graphite layers in c-direction due to remaining intercalated lithium ions. Apparently, the amount of remaining lithium ions within the graphite structure increases with increasing C-rate. At 5C, the reflection is at a position which corresponds to the 0 0 1 reflection of LiC_{12} suggesting that half of the graphite material is intercalated with lithium ions. For NMC, a similar trend can be observed. With increasing C-rate, the initial NMC reflection 1 0 1 (black line) shifts to higher 2θ values, which indicates a lower intercalated state for NMC.

If only kinetic effects are the reason for the observed capacity losses of the cell, the remaining lithium in graphite should match with the reduced amount of lithium found in the NMC electrodes. For the quantification of lithium in graphite, the calibration curve established in Figure 4.47c cannot be applied, because it represents lithiation degrees

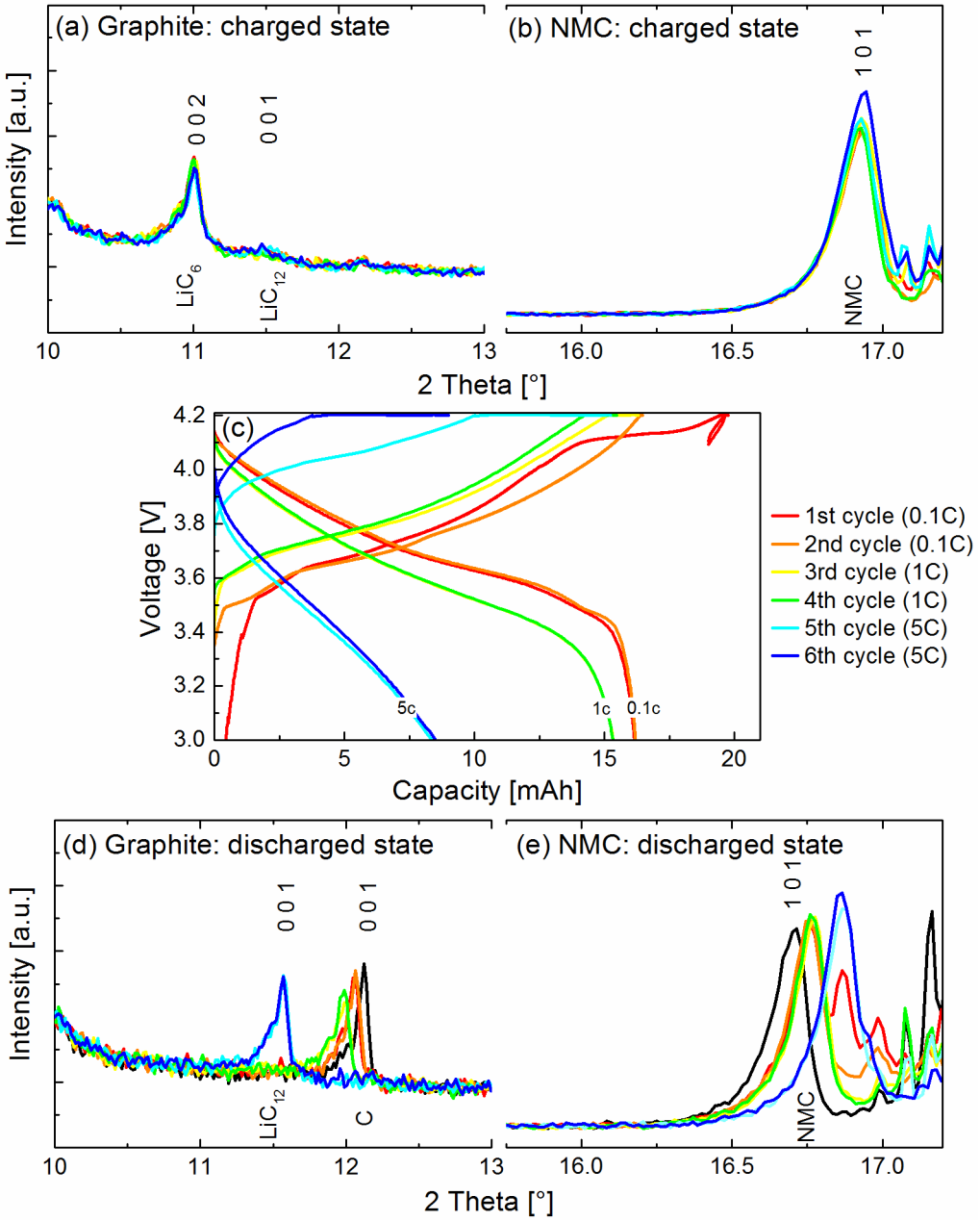

Figure 4.48: Combined electrochemical and *in situ* XRD investigation of a graphite-NMC pouch cell during a rate capability test. (c) Voltage profile of the charge and discharge at 0.1C, 1C, and 5C between 3.0 and 4.2 V with a CCCV procedure during charge. (a) and (b) Selected regions of the XRD patterns of graphite and NMC in the charged state of the cell. (d) and (e) Selected regions of the XRD patterns of graphite and NMC in the discharged state of the cell. Black line corresponds to the pristine state directly after assembly.

higher than $x = 0.5$. Thus, results from Dahn *et al.*[280] were used to estimate the lithium content in graphite at low lithiation degrees. In this study, a phase diagram of Li_xC_6 was accurately established. By comparing reflection positions at certain voltages, the lithiation degree could be determined from the provided voltage-composition curve. The quantification of lithium in NMC is based on a calibration method already described in detail in Chapter 4.5. By refining the lattice parameters *a* and *c* for each diffraction pattern, the *c*/*a* value can be calculated, which can directly be correlated to the lithium content *y* (≡1-*x*) in L_yNMC according to a conversion of the established calibration curve in Figure 4.28 of Chapter 4.5: $y = 1-[(c/a-4.972)/0.355]$. Note the difference between *x* and *y*: While *x* represents the amount of Li removed from NMC, *y* is the amount of Li residing in the NMC. Calculated and converted capacity values for both graphite and NMC are provided in Table 4.5.

Table 4.5 is also illustrated in Figure 4.49a, in which the quantified capacities in mAh are plotted against cycle number of the rate capability test. The unit mAh was chosen to have the same absolute scale for both graphite and NMC, which is based on their weighed masses. In accordance with the observations in Figure 4.48d and e, the capacity of graphite (blue line) accumulates with increasing C-rate/cycle number, while the capacity of NMC decreases (red solid line). The red dashed line represents the respective capacity losses in the NMC material, which is the difference between the fully lithiated NMC capacity and the capacities from the red solid line. By adding the existing capacities of graphite and NMC (green solid line) the initial capacity value of NMC should be recovered as it is the capacity (lithium) providing electrode in the cell. However, in the first cycle at 0.1C little losses to the initial NMC capacity are present, which can be attributed to the irreversible SEI formation reaction. With increasing C-rate/cycle number these losses keep almost constant, whereas at 5C (cycle 5 and 6) they seem to have paradoxically disappeared. The discrepancies are mainly related to the capacity determination of graphite. According to the reflection position, a pure composition of $Li_{0.5}C_6$ was assumed, which gives half of the graphite capacity. Since the transition from lower lithiated graphite $Li_{0.33}C_6$ to $Li_{0.5}C_6$ follows a two-phase coexistence mechanism,[280,282] a shift in reflection position is not expected for this transition but a change in intensity ratios. Due to limited intensity resolution of the graphite reflection close to a pure phase, which is similar to the established calibration curve in Figure 4.47b, the amount of lithium must be slightly overestimated. Despite these difficulties in capacity determination, the large capacity loss of NMC at 5C is primarily buffered by graphite, which retains almost all lost lithium ions. Thus, a clear kinetic effect of capacity loss for the full cell can be concluded because no lithium ions are lost, except for the SEI formation reaction. Due to the increasing ohmic resistances with C-rate, less lithium ions are transferred between each electrode. The remaining lithium ions consequently reside in the graphite electrode and lead to the observed capacity loss.

Table 4.5: Quantification of lithium content in graphite and NMC electrodes based on *in situ* XRD analysis of a graphite-NMC pouch cell during a rate capability test. XRD measurements were conducted in the discharged state of the cell, which had been cycled two times at 0.1C, 1C, and 5C. Lithium-content quantification for graphite is based on a phase diagram provided by Dahn *et al.*[280] For NMC, the calibration curve established in Chapter 4.5 is used (y = 1-[(c/a-4.972)/0.355]). $[mAh]_{NMC} = y*278\ mAh/g_{NMC}*m_{NMC}$. $[mAh]_C = x*360\ mAh/g_C*m_C$; m_{NMC}=123 mg and m_c=60 mg.

Cycle	C-rate	Graphite			NMC		
		2θ	x in Li_xC_6	[mAh]	c/a	y in Li_yNMC	[mAh]
Assembly	--	12.13	0	0	4.978	0.983	33.6
1	0.1	12.07	0.10	2.2	5.007	0.901	30.8
2	0.1	12.07	0.10	2.2	5.008	0.898	30.7
3	1C	11.99	0.11	2.4	5.013	0.883	30.2
4	1C	11.99	0.11	2.4	5.015	0.878	30.0
5	5C	11.57	0.50	10.8	5.094	0.656	22.5
6	5C	11.57	0.50	10.8	5.095	0.654	22.4

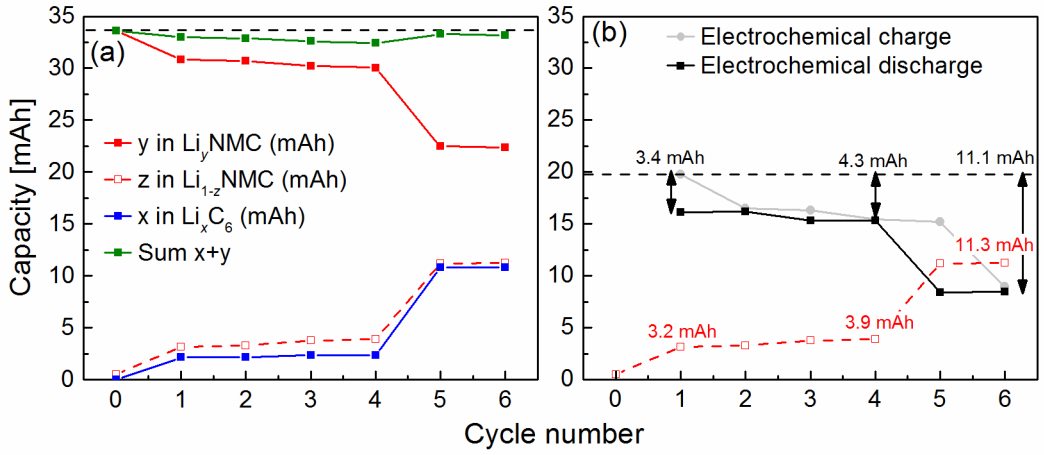

Figure 4.49: Evaluation of the *in situ* XRD measurement and rate capability test of the graphite-NMC pouch cell. (a) Determination of the capacity (in mAh) of graphite and NMC electrodes in the discharged state based on the *in situ* XRD analysis. For graphite, capacities were estimated from reflection positions by comparing to Ref.[280] For NMC, capacities were obtained by Rietveld refinement of the diffraction pattern and inserting the refined lattice parameters into the calibration curve established in Figure 4.28 in Chapter 4.5. (b) Comparison of capacity losses measured during the electrochemical rate capability test and capacity losses found in the NMC electrode.

Since NMC is the capacity (lithium) delivering electrode, its losses including irreversible SEI and kinetic losses (illustrated in the red dashed line in Figure 4.49a as well as in Figure 4.49b) must be directly reflected in the transferred charge losses of the pouch-cell full-cell. A comparison of both is performed in Figure 4.49b. For the pouch cell, charge/discharge capacities are calculated from the applied electric current and the corresponding time. The black numbers given in the plot correspond to the capacity losses of the discharge and are determined relative to the capacity of the first charge (black dashed line) because in this step all active/usable lithium-ions are transferred from the NMC to

the graphite electrode. By correlating the given capacity loss values at the same cycle number, the losses determined for NMC via *in situ* XRD (red numbers) indeed match those losses observed in the full cell.

4.7.4 Conclusion and outlook

The presented *in situ* XRD cell, which is based on a pouch-cell design, demonstrated to be very suitable for XRD measurements in transmission geometry on a laboratory diffractometer equipped with a Mo source. With this setup, it is possible to conduct preliminary mechanistic or failure studies independent from the availability of a synchrotron source. The evaluation of half and full cells based on the graphite-NMC system revealed a sufficient data quality of the measured XRD patterns for phase and lattice parameter analysis. On this basis, a calibration curve for the determination of the lithiation degree in graphite in the range $0.5 < x < 1$ (x in Li_xC_6) in dependence on reflection intensity ratios was established. Furthermore, the lithium inventory variations in both graphite and NMC electrodes could be reasonably followed during a rate capability test. These initial studies suggest that the investigation of more complex correlations in lithium-ion batteries is feasible by this method. Due to the stable performance of pouch cells, which is comparable to our established Swagelok T-cell, fatigue processes of the active material or changes in the lithium inventory can be further investigated. With respect to electrolyte amount, electrode design or choice of separator, the pouch cell system comes very close to commercial cell designs, which enables an easy projection of results on the large scale.

Nevertheless, the present cell-to-cell variation of our pouch cells on the long-term scale is still an important issue that has to be solved in our laboratory. A possible approach would be the special-designed compression tool with adjustable spring pressure, which provides a constant loading on each cell (see Figure 4.50 and the technical drawing provided in the Appendix). In this setup, the pouch cell is placed between the two stainless-steel plates and a constant pressure of ≈0.15 MPa or ≈0.2 MPa is applied by compressing the springs by a defined length. The current-collector tabs are connected by test pins (spring contact) to the potentiostat. The holder for the test pins and for the banana-plug connectors, which is movable in the vertical direction, was designed by our engineering and electronics workshop. This setup can be further modified according to Figure 4.46 in order to be suitable for XRD measurements in transmission geometry.

The pouch-cell system seems to be superior compared to the Bragg-Brentano *in situ* XRD cell. Pouch cells can be directly used for XRD analysis without any modifications. Due to their in principle more even compression by atmospheric pressure, inhomogeneous current distributions can be prevented in contrast to the XRD cell in reflection geometry with its indispensable XRD window design. The cycling stability is therefore much better. Furthermore, pouch cells provide the opportunity to investigate anode materials. However, the overall intensity of the diffracted X-ray beam in transmission geometry is markedly reduced because the beam has to additionally penetrate the pouch

foil as well as both current collector foils; but a reasonably quantitative analysis of the XRD pattern is still possible.

Figure 4.50: Photos of the special-designed pouch-cell compression tool with adjustable spring pressure. The loading can be adjusted between 0.15 and 0.2 MPa.

5 Conclusion

The introduction of the lithium-ion battery technology in the automotive field has boosted the electrification of the drive system over the last decade. Promoted by government and industrial funding, an important step towards climate protection is thus performed by reducing the dependence on fossil fuels. The development towards complete electromobility is only feasible by providing an appropriate electrical infrastructure, but also by meeting the consumer's expectations and requirements concerning costs, driving range and durability of the EV. In this respect, a continuous improvement in cathode and anode materials is necessary in order to increase their specific energies and hence the driving range of the EV. Furthermore, a key understanding of the individual electrode processes in the lithium-ion battery is essential in order to explain complex correlations not only related to novel electrode materials but also to degradation phenomena, which might benefit the life time of the battery. Therefore, the central focus of this work presented in this thesis was the introduction and development of analytical approaches to investigate different active materials and their related degradation processes.

Conventional XRD has been a basic tool since the beginning of lithium-ion battery research and helped a lot in developing electrode materials and revealing insertion or fatigue mechanisms. For this purpose, an electrochemical cell for *in situ* XRD analysis has been developed for both Bragg-Brentano (reflection mode) and transmission geometry of the laboratory diffractometer system. In reflection mode, a specially designed cell, which directly utilizes the thin electrode current-collector foil as XRD window, is necessary to perform diffraction experiments on cathode materials, although the XRD window of this system introduces a weak point of non-uniform cell compression. While showing poor rate and cycling performance on longer time scales, which could be improved to a large extent by using either a FEC-containing electrolyte or an adapter for the X-ray opening, the *in situ* XRD cell behaved very reliable during the initial cycles at slow rates. To close the gap on the long-term performance, single-layered pouch cells have been introduced, which can be operated in transmission geometry to analyze both cathode and anode materials.

Related to efforts to increase energy density, not only improved battery active materials are developed but also new cell chemistries such as the Li-S system are considered. Among various cathode materials, $LiCoPO_4$ represents an interesting candidate to increase specific energies by offering high charge/discharge voltages. The analysis of the

first cycle with *in situ* XRD revealed a two two-phase transition ($LiCoPO_4$ ↔ "$Li_{0.7}CoPO_4$" and "$Li_{0.7}CoPO_4$" ↔ "$CoPO_4$"), which is structurally reversible. However, a huge capacity loss can be observed during the first cycle, which is attributed to degraded electrolyte species at the cathode surface at high potentials. The Li-S system, on the contrary, which is based on Li_2S cathodes and Si/C anodes in this work, provides high specific energies that result from the low weight of the active material and the two-electron process. Structural investigations with *in situ* XRD half-cells showed that Li_2S could be completely decomposed during the first charge leading to the formation of crystalline sulfur, which was not that obvious based on contradictory literature data. It was further confirmed that Si/C anodes are superior to metallic lithium due to the improved rate capability of the anode material. Although both cathode materials (LCP, Li_2S) exhibit promising structural properties for electrochemical cycling, their commercial application is still impeded, which is mainly caused by undesired side reactions, *i.e.* enhanced electrolyte oxidation in LCP containing cells and the polysulfide-shuttle in Li-S cells.

By systematically combining (*in situ*) XRD with neutron-induced PGAA, PAS and EIS, the kinetic origin of the first-cycle capacity loss of NMC-111 and the main degradation processes in graphite-NMC-111 cells under different operating conditions could be identified. In these studies, investigative methods were established that are not always common in lithium-ion battery research: (i) By combing *in situ* with *ex situ* XRD, the amount of active-lithium loss in NMC-111 was determined, which could in future be extended to pure *in situ* XRD analysis by using the developed pouch-cell system. (ii) Neutrons were successfully utilized to quantify the amount of transition metals deposited on the graphite anodes with the possibility to recycle the electrode samples. (iii) The use of positrons for electrode analysis is almost new to lithium-ion battery research. Their particular sensitivity for open-volume defects helped to understand the first-cycle defect evolution in NMC-111. The experiences obtained in this work could be further applied to similar materials having a more complex charge/discharge characteristic or to aged electrodes samples, in which the defect type and ordering might play a critical role in material degradation.

This work clearly accentuates the strength in using different or even complementary analytical methods to elucidate fundamental processes in lithium-ion batteries. The close collaboration with the neutron source and the physics department further demonstrated the importance of combining different facilities at various areas of expertise in order to tackle issues by utilizing their different approaches. Thus, it is not surprising that currently emerging research projects increasingly resemble a cluster of diverse working groups, research facilities and industry partners. One example is the ExZELLTUM project (by which main of the work presented in this thesis is funded), which reflects the expertise of electrochemical, electrical and mechanical engineering as well as the knowledge from the neutron facility and relevant industry partners.

References

[1] Van Noorden, R. *Nature* **2014**, *507*, 26–28.

[2] Cluzel, C.; Douglas, C. *Cost and performance of EV batteries: Final report for The Committee on Climate Change*; Element Energy Limited: Cambridge, **2012**.

[3] *Nationaler Entwicklungsplan Elektromobilität*, Deutsche Bundesregierung, **2009**, https://www.bmbf.de/files/nationaler_entwicklungsplan_elektromobilitaet.pdf, accessed May 17, 2016.

[4] *Auswertungstabellen zur Energiebilanz Deutschland 1990 bis 2014*, AG Energiebilanzen e.V., **2015**, http://www.ag-energiebilanzen.de, accessed May 18, 2016.

[5] *Fortschrittsbericht 2014 - Bilanz der Marktvorbereitung*, Nationale Plattform Elektromobilität (NPE), **2014**, https://www.bmbf.de/files/NPE_Fortschrittsbericht_2014_barrierefrei.pdf, accessed May 18, 2016.

[6] *Nationales Innovationsprogramm Wasserstoff- und Brennstoffzellentechnologie*, Deutsche Bundesregierung, **2006**, https://www.bmvi.de/SharedDocs/DE/Artikel/G/nationales-innovationsprogramm-wasserstoff-und-brennstoffzellentechnologie-nip.html, accessed May 24, 2016.

[7] Winter, M.; Brodd, R. J. *Chem. Rev.* **2004**, *104*, 4245–4269.

[8] Thackeray, M. M.; Wolverton, C.; Isaacs, E. D. *Energy Environ. Sci.* **2012**, *5*, 7854.

[9] Mitzushima, K.; Jones, P. C.; Wiseman, P. J.; Goodenough, J. B. *Mater. Res. Bull.* **1980**, *15*, 783–789.

[10] Mohri, M.; Yangisawa, N.; Tajima, Y.; Tanaka, H.; Mitate, T.; Nakajima, S.; Yoshida, M.; Yoshimoto, Y.; Suzuki, T.; Wada, H. *J. Power Sources* **1989**, *26*, 545–551.

[11] Nagaura, T.; Tozawa, K. *Prog. Batteries Solar Cells* **1990**, *9*, 209–217.

[12] Ozawa, K. *Solid State Ionics* **1994**, *69*, 212–221.

[13] Andre, D.; Kim, S.-J.; Lamp, P.; Lux, S. F.; Maglia, F.; Paschos, O.; Stiaszny, B. *J. Mater. Chem. A* **2015**, *3*, 6709–6732.

[14] Croy, J. R.; Abouimrane, A.; Zhang, Z. *MRS Bull.* **2014**, *39*, 407–415.

[15] Noh, H. J.; Youn, S.; Yoon, C. S.; Sun, Y. K. *J. Power Sources* **2013**, *233*, 121–130.

[16] Liu, W.; Oh, P.; Liu, X.; Lee, M. J.; Cho, W.; Chae, S.; Kim, Y.; Cho, J. *Angew. Chemie - Int. Ed.* **2015**, *54*, 4440–4457.

[17] Thackeray, M. M.; Kang, S.-H.; Johnson, C. S.; Vaughey, J. T.; Benedek, R.; Hackney, S. A. *J. Mater. Chem.* **2007**, *17*, 3112.

[18] Liu, D.; Zhu, W.; Trottier, J.; Gagnon, C.; Barray, F.; Guerfi, A.; Mauger, A.; Groult, H.; Julien, C. M.; Goodenough, J. B.; Zaghi, K. *Rsc Adv.* **2014**, *4*, 154–167.

[19] Obrovak, M. N.; Christensen, L. *Electrochem. Solid-State Lett.* **2004**, *7*, A93–A96.

[20] Beaulieu, L. Y.; Beattie, S. D.; Hatchard, T. D.; Dahn, J. R. *J. Electrochem. Soc.* **2003**, *150*, A419.

[21] Gallagher, K. G.; Goebel, S.; Greszler, T.; Mathias, M.; Oelerich, W.; Eroglu, D.; Srinivasan, V. *Energy Environ. Sci.* **2014**, *7*, 1555–1563.

[22] Wagner, F. T.; Lakshmanan, B.; Mathias, M. F. *J. Phys. Chem. Lett.* **2010**, *1*, 2204–2219.

[23] Xu, W.; Wang, J.; Ding, F.; Chen, X.; Nasybulin, E.; Zhang, Y.; Zhang, J.-G. *Energy Environ. Sci.* **2014**, *7*, 513–537.

[24] Amine, K.; Kanno, R.; Tzeng, Y. *MRS Bull.* **2014**, *39*, 395–401.

[25] Christensen, J.; Albertus, P.; Sanchez-Carrera, R.; Lohmannn, T.; Kozinsky, B.; Liedtke, R.; Ahmed, J.; Kojic, A. *J. Electrochem. Soc.* **2012**, *159*, 1–30.

[26] Gröger, O.; Gasteiger, H. A.; Suchsland, J.-P. *J. Electrochem. Soc.* **2015**, *162*, A2605–A2622.

[27] Wagner, R.; Preschitschek, N.; Passerini, S.; Leker, J.; Winter, M. *J. Appl. Electrochem.* **2013**, *43*, 481–496.

[28] *Technology Roadmap: Electric and plug-in hybrid electric vehicles*, International Energy Agency (IEA), **2011**, https://www.iea.org/publications/freepublications/publication/EV_PHEV_Roadmap.pdf, accessed May 22, 2016.

[29] Barré, A.; Deguilhem, B.; Grolleau, S.; Gérard, M.; Suard, F.; Riu, D. *J. Power Sources* **2013**, *241*, 680–689.

[30] Broussely, M.; Biensan, P.; Bonhomme, F.; Blanchard, P.; Herreyre, S.; Nechev, K.; Staniewicz, R. J. *Sel. Pap. Press. 12th Int. Meet. Lithium Batter. 12th Int. Meet. Lithium Batter.* **2005**, *146*, 90–96.

[31] Hausbrand, R.; Cherkashinin, G.; Eherenberg, H.; Gröting, M.; Albe, K.; Hess, C.; Jaegermann, W. *Mater. Sci. Eng. B* **2015**, *192*, 3–25.

[32] Novák, P.; Panitz, J.-C.; Joho, F.; Lanz, M.; Imhof, R.; Coluccia, M. *J. Power Sources* **2000**, *90*, 52–58.

[33] Novák, P.; Goers, D.; Hardwick, L.; Holzapfel, M.; Scheifele, W.; Ufheil, J.; Würsig, A. *J. Power Sources* **2005**, *146*, 15–20.

[34] Bloom, I.; Jansen, A. N.; Abraham, D. P.; Knuth, J.; Jones, S. A.; Battaglia, V. S.; Henriksen, G. L. *J. Power Sources* **2005**, *139*, 295–303.

[35] Kassem, M.; Delacourt, C. *J. Power Sources* **2013**, *235*, 159–171.

[36] Kubiak, P.; Edström, K.; Morcrette, M. *JPS power D* **2013**, *12*, 03691.

[37] Mohanty, D.; Li, J.; Nagpure, S. C.; Wood, D. L.; Daniel, C. *MRS Energy Sustain.* **2015**, *2*, 1–24.

[38] Vetter, J.; Novák, P.; Wagner, M. R.; Veit, C.; Möller, K.-C.; Besenhard, J. O.; Winter, M.; Wohlfahrt-Mehrens, M.; Vogler, C.; Hammouche, A. *J. Power Sources* **2005**, *147*, 269–281.

[39] Xu, K. *Chem. Rev.* **2014**, *114*, 11503–11618.

[40] Gauthier, M.; Carney, T. J.; Grimaud, A.; Giordano, L.; Pour, N.; Chang, H.-H.; Fenning, D. P.; Lux, S. F.; Paschos, O.; Bauer, C.; Maglia, F.; Lupart, S.; Lamp, P.; Shao-Horn, Y. *J. Phys. Chem. Lett.* **2015**, *6*, 4653–4672.

[41] Peled, E. *J. Electrochem. Soc.* **1979**, *126*, 2047.

[42] Peled, E. *J. Electrochem. Soc.* **1997**, *144*, L208.

[43] Aurbach, D. *J. Power Sources* **2000**, *89*, 206–218.

[44] Edström, K.; Herstedt, M.; Abraham, D. P. *J. Power Sources* **2006**, *153*, 380–384.

[45] Verma, P.; Maire, P.; Novák, P. *Electrochim. Acta* **2010**, *55*, 6332–6341.

[46] Aurbach, D.; Zinigrad, E.; Cohen, Y.; Teller, H. *Solid State Ionics* **2002**, *148*, 405–416.

[47] Smith, A. J.; Burns, J. C.; Zhao, X.; Xiong, D.; Dahn, J. R. *J. Electrochem. Soc.* **2011**, *158*, S23.

[48] Spotnitz, R. *J. Power Sources* **2003**, *113*, 72–80.

[49] Richard, M. N.; Dahn, J. R. *J. Electrochem. Soc.* **1999**, *146*, 2078.

[50] Andersson, A. M.; Edström, K. *J. Electrochem. Soc.* **2001**, *148*, A1100.

[51] Agubra, V.; Fergus, J. *Materials* **2013**, *6*, 1310–1325.

[52] Wohlfahrt-Mehrens, M.; Vogler, C.; Garche, J. *J. Power Sources* **2004**, *127*, 58–64.

[53] Zhou, J.; Notten, P. H. L. *J. Power Sources* **2008**, *177*, 553–560.

[54] Choi, W.; Manthiram, A. *J. Electrochem. Soc.* **2006**, *153*, A1760.

[55] Gallus, D. R.; Schmitz, R.; Wagner, R.; Hoffmann, B.; Nowak, S.; Cekic-Laskovic, I.; Schmitz, R. W.; Winter, M. *Electrochim. Acta* **2014**, *134*, 393–398.

[56] Kleiner, K.; Dixon, D.; Jakes, P.; Melke, J.; Yavuz, M.; Roth, C.; Nikolowski, K.; Liebau, V.; Ehrenberg, H. *J. Power Sources* **2015**, *273*, 70–82.

[57] Blyr, A.; Amatucci, G.; Guyomard, D.; Chabre, Y.; Tarascon, J.-M. *J. Electrochem. Soc.* **1998**, *145*, 194–209.

[58] Bernhard, R.; Metzger, M.; Gasteiger, H. A. *J. Electrochem. Soc.* **2015**, *162*, A1984–A1989.

[59] Bramnik, N. N.; Nikolowski, K.; Baehtz, C.; Bramnik, K. G. *Chem. Mater.* **2007**, *19*, 908–915.

[60] Yang, Y.; Zheng, G.; Misra, S.; Nelson, J.; Toney, M. F.; Cui, Y. *J. Am. Chem. Soc.* **2012**, *134*, 15387–15394.

[61] Nelson, J.; Misra, S.; Yang, Y.; Jackson, A.; Liu, Y.; Wang, H.; Dai, H.; Andrews, J. C.; Cui, Y.; Toney, M. F.; Andrews, J. C. *J. Am. Chem. Soc.* **2012**, *134*, 6337–6343.

[62] Jha, H.; Buchberger, I.; Cui, X.; Meini, S.; Gasteiger, H. A. *J. Electrochem. Soc.* **2015**, *162*, A1829–A1835.

[63] Buchberger, I.; Seidlmayer, S.; Pokharel, A.; Piana, M.; Hattendorff, J.; Kudejova, P.; Gilles, R.; Gasteiger, H. A. *J. Electrochem. Soc.* **2015**, *162*, A2737–A2746.

[64] Linden, D.; Reddy, T. B. *Handbook of Batteries*, 3rd ed.; McGraw-Hill: United States of America, **2002**.

[65] Bard, A.; Faulkner, L. *Electrochemical Methods: Fundamentals and Applications*, 2nd ed.; John Wiley & Sons, **2001**.

[66] Haynes, W. M. *Electrochemical Series in Handbook of Chemistry and Physics*, 95th ed.; CRC press, **2014**.

[67] Hamann, C. H.; Vielstich, W. *Elektrochemie*; WILEY-VCH Verlag GmbH: Weinheim, **2005**.

[68] Vincent, C. A.; Scrosati, B. *Modern Batteries: An introduction to electrochemical power sources*, 2nd ed.; Butterworth-Heinemann: London, **1997**.

[69] Marks, T.; Trussler, S.; Smith, A. J.; Xiong, D.; Dahn, J. R. *J. Electrochem. Soc.* **2010**, *158*, A51–A57.

[70] Chen, Z.; Christensen, L.; Dahn, J. R. *J. Appl. Polym. Sci.* **2004**, *91*, 2958–2965.

[71] Aurbach, D. *Nonaqueous Electrochemistry*; Marcel Dekker Inc., **1999**.

[72] Lux, S. F.; Schappacher, F.; Balducci, A.; Passerini, S.; Winter, M. *J. Electrochem. Soc.* **2010**, *157*, A320–A325.

[73] Wissler, M. *J. Power Sources* **2006**, *156*, 142–150.

[74] Garbe, S. *Untersuchung des irreversiblen Kapazitätsverlustes im ersten Zyklus von NMC- und Graphit-Elektroden und der Einfluss auf das Balancing von Vollzellen*, Bachelor's Thesis, Technische Universität München, **2015**.

[75] Honkura, K.; Takahashi, K.; Horiba, T. *ECS Trans.* **2008**, *13*, 61–73.

[76] Bernhard, R. J. *Novel Electrolyte Solvents and Additives for Lithium-Ion Batteries and Different Materials Degradation Phenomena*, Ph.D. Thesis, Technische Universität München, **2014**.

[77] Ende, D.; Mangold, K. *Chemie unserer Zeit* **1993**, *27*, 134–140.

[78] Lvovich, V. F. *Impedance Spectroscopy: Applications to Electrochemical and Dielectric Phenomena*; John Wiley & Sons: New Jersey, **2012**.

[79] Illig, J. N. *Physically based Impedance Modelling of Lithium-Ion Cells*; PhD Thesis, KIT Scientific Publishing, **2014**.

[80] Abraham, D. P.; Poppen, S. D.; Jansen, A. N.; Liu, J.; Dees, D. W. *Electrochim. Acta* **2004**, *49*, 4763–4775.

[81] Burns, J. C.; Krause, L. J.; Le, D.-B.; Jensen, L. D.; Smith, A. J.; Xiong, D.; Dahn, J. R. *J. Electrochem. Soc.* **2011**, *158*, A1417–A1422.

[82] Ender, M.; Weber, A.; Ivers-Tiffée, E. *J. Electrochem. Soc.* **2012**, *159*, A128.

[83] Walter Umrath. *Fundamentals of Vacuum Technology*, Oerlikon leybold vacuum, **2012**, http://www.oerlikon.com, accessed May 28, 2016.

[84] Giacovazzo, C.; Monaco, H. L.; Artioli, G.; Viterbo, D.; Ferraris, G.; Gilli, G.; Zanotti, G.; Catti, M. *Fundamentals of Crytallography*, second edi.; Oxford University Press: New York, **2002**.

[85] Rietveld, H. M. *J. Appl. Crystallogr.* **1969**, *2*, 65–71.

[86] Hammond, C. *The Basics of Crystallography and Diffraction*, third edit.; Oxford University Press: New York, **2009**.

[87] Degen, T.; Sadki, M.; Bron, E.; König, U.; Nénert, G. *Powder Diffr.* **2014**, *29*, S13–S18.

[88] Rodríguez-Carvajal, J. *Physica B* **1993**, *192*, 55–69.

[89] Rodríguez-Carvajal, J. *Recent developments of the program FULLPROF*; **2001**.

[90] McCusker, L. B.; Dreele, R. B. Von; Cox, D. E.; Louer, D.; Scardi, P. *J. Appl. Crystallogr.* **1999**, *32*, 36–50.

[91] Meini, S.; Tsiouvaras, N.; Schwenke, K. U.; Piana, M.; Beyer, H.; Lange, L.; Gasteiger, H. a. *Phys. Chem. Chem. Phys.* **2013**, *15*, 11478–11493.

[92] Meini, S. *The Influence of Irreversible Electrochemical Reactions on the Fundamental Mechanisms Governing Capacity and Cycle Life of Li-O2 Batteries*, Ph.D. Thesis, Technische Universität München, **2013**.

[93] Hubbell, J. H.; Seltzer, S. M. *Tables of X-Ray Mass Attenuation Coefficients and Mass Energy-Absorption Coefficients*, **2004**, http://physics.nist.gov/xaamdi, accessed Apr 2, 2016.

[94] Henke, B. L.; Gullikson, E. M.; Davis, J. C. *Hompage of the Center for X-ray Optics - Lawrence Berkley National Laboratories*, **1993**, http://henke.lbl.gov/optical_constants/atten2.html, accessed Apr 9, 2015.

[95] McMaster, W. H.; Del Grande, N. K.; Mallett, J. H.; Hubbell, J. H. *Homepage of the Center for Synchrotron Radiation Research and Instrumentation*, http://www.csrri.iit.edu/periodic-table.html, accessed Apr 9, 2016.

[96] Perry, D. L.; Firestone, R. B.; Molnar, G. L.; Revay, Z.; Kasztovszky, Z.; Gatti, R. C.; Wilde, P. *J. Anal. At. Spectrom.* **2002**, *17*, 32–37.

[97] Alfassi, Z. B.; Chung, C. *Prompt Gamma Neutron Activation Analysis*; CRC Press, Inc., **1995**.

[98] Heinz Maier-Leibnitz Zentrum (MLZ). *PGAA Prompte Gamma Aktivierungs-Analyse*; Skript zum Physikalischen Fortgeschrittenenpraktikum am FRMII, Technische Universität München, **2010**.

[99] Canella, L.; Kudejova, P.; Schulze, R.; Türler, A.; Jolie, J. *Nucl. Instrum. Methods Phys. Res., Sect. A* **2011**, *636*, 108–113.

[100] Révay, Z.; Kudějová, P.; Kleszcz, K.; Söllradl, S.; Genreith, C. *Nucl. Instrum. Methods Phys. Res., Sect. A* **2015**, 1–10.

[101] Révay, Z. *J. large-scale Res. Facil.* **2015**, *1*, 19–21.

[102] Kudejova, P.; Révay, Z.; Kleszcz, K.; Genreith, C.; Rossbach, M. *EPJ Web Conf.* **2015**, *93*, 08001–08002.

[103] Révay, Z. *Anal. Chem.* **2009**, *81*, 6851–6859.

[104] Harrich, A.; Jagsch, S.; Riedler, S.; Rosinger, W. *Am. J. Undergrad. Res.* **2003**, *2*, 13–18.

[105] Procházka, I. *Mater. Struct.* **2001**, *8*, 55–60.

[106] Tuomisto, F.; Makkonen, I. *Rev. Mod. Phys.* **2013**, *85*, 1583–1631.

[107] Heinz Maier-Leibnitz Zentrum (MLZ). *NEPOMUC-neutron induced positron source munich*, http://www.mlz-garching.de/nepomuc, accessed May 6, 2016.

[108] Hugenschmidt, C.; Ceeh, H.; Gigl, T.; Lippert, F.; Piochacz, C.; Pikart, P.; Reiner, M.; Weber, J.; Zimnik, S. *J. Phys. Conf. Ser.* **2013**, *443*, 012079.

[109] Hugenschmidt, C.; Piochacz, C. *J. large-scale Res. Facil. JLSRF* **2015**, *1*, A22.

[110] Hugenschmidt, C.; Löwe, B.; Mayer, J.; Piochacz, C.; Pikart, P.; Repper, R.; Stadlbauer, M.; Schreckenbach, K. *Nucl. Instrum. Methods Phys. Res., Sect. A* **2008**, *593*, 616–618.

[111] Hugenschmidt, C. *J. large-scale Res. Facil.* **2015**, *1*, A23.

[112] Chianelli, R. R.; Scanlon, J. C.; Rao, B. M. L. *J. Electrochem. Soc.* **1978**, *125*, 1563–1566.

[113] Dahn, J. R.; Haering, R. R. *Solid State Commun.* **1981**, *40*, 245–248.

[114] Dahn, J. R.; Py, M.; Haering, R. R. *Can, J. Phys.* **1982**, *60*, 307–313.

[115] Tarascon, J. M.; Hull, G. W. *Solid State Ionics* **1986**, *22*, 85–96.

[116] Tarascon, J. M.; Hull, G. W.; Marsh, P.; Haar, T. *J. Solid State Chem.* **1987**, *66*, 204–224.

[117] Reimers, J. N.; Dahn, J. R. *J. Electrochem. Soc.* **1992**, *139*, 2–8.

[118] Li, W.; Reimers, J.; Dahn, J. *Solid State Ionics* **1993**, *67*, 123–130.

[119] Amatucci, G.; Tarascon, J.; Klein, L. *J. Electrochem. Soc.* **1996**, *143*, 1114–1123.

[120] Roberts, G. A.; Stewart, K. D. *Rev. Sci. Instrum.* **2004**, *75*, 1251–1254.

[121] Richard, M. N., Koetschau, I. , Dahn, J. R. *J. Electrochem. Soc.* **1997**, *144*, 554–557.

[122] Fell, C. R.; Chi, M.; Meng, Y. S.; Jones, J. L. *Solid State Ionics* **2012**, *207*, 44–49.

[123] Meulenkamp, E. A. *J. Electrochem. Soc.* **1998**, *145*, 2759–2762.

[124] Myung, S.-T.; Komaba, S.; Hirosaki, N.; Kumagai, N.; Arai, K.; Kodama, R.; Nakai, I. *J. Electrochem. Soc.* **2003**, *150*, A1560.

[125] Cañas, N. a.; Wolf, S.; Wagner, N.; Friedrich, K. A. *J. Power Sources* **2013**, *226*, 313–319.

[126] Gustafsson, T.; Thomas, J. O.; Koksbang, R.; Farrington, G. C. *Electrochim. Acta* **1992**, *37*, 1639–1643.

[127] Tarascon, J. M.; Gozdz, A. S.; Schmutz, C.; Shokoohi, F.; Warren, P. C. *Solid State Ionics* **1996**, *86-88*, 49–54.

[128] Thurston, T. R.; Jisrawi, N. M.; Mukerjee, S.; Yang, X. Q.; McBreen, J.; Daroux, M. L.; Xing, X. K. *Appl. Phys. Lett.* **1996**, *69*, 194.

[129] Mukerjee, S.; Thurston, T. R.; Jisrawi, N. M.; Yang, X. Q.; McBreen, J.; Daroux, M. L.; Xing, X. K. *J. Electrochem. Soc.* **1998**, *145*, 466.

[130] Strobel, P.; Anne, M.; Chabre, Y.; Palacín, M. R.; Seguin, L.; Vaughan, G.; Amatucci, G.; Tarascon, J. M. *J. Power Sources* **1999**, *81-82*, 458–462.

[131] Palacín, M. R.; Amatucci, G. G.; Anne, M.; Chabre, Y.; Seguin, L.; Strobel, P.; Tarascon, J. M.; Vaughan, G. *J. Power Sources* **1999**, *81-82*, 627–631.

[132] Palacín, M. R.; Chabre, Y.; Dupont, L.; Hervieu, M.; Strobel, P.; G, R.; Masquelier, C.; Anne, M.; Amatucci, G. G.; J.M. *J. Electrochem. Soc.* **2000**, *147*, 845–853.

[133] Balasubramanian, M.; Sun, X.; Yang, X. Q.; Mcbreen, J. *J. Power Sources* **2001**, *92*, 1–8.

[134] Li, Z. G.; Harlow, R. L.; Gao, F.; Lin, P.; Miao, R.; Liang, L. *J. Electrochem. Soc.* **2003**, *150*, A1171.

[135] Holzapfel, M.; Strobel, P.; Darie, C.; Wright, J.; Morcrette, M.; Chappel, E.; Anne, M. *J. Mater. Chem.* **2004**, *14*, 94–101.

[136] Baehtz, C.; Buhrmester, T.; Bramnik, N. N.; Nikolowski, K.; Ehrenberg, H. *Solid State Ionics* **2005**, *176*, 1647–1652.

[137] Nikolowski, K.; Baehtz, G.; Bramnik, N. N.; Ehrenberg, H. *J. Appl. Crystallogr.* **2005**, *38*, 851–853.

[138] Rosciano, F.; Holzapfel, M.; Kaiser, H.; Scheifele, W.; Ruch, P.; Hahn, M.; Kötz, R.; Novák, P. *J. Synchrotron Radiat.* **2007**, *14*, 487–491.

[139] Leriche, J. B.; Hamelet, S.; Shu, J.; Morcrette, M.; Masquelier, C.; Ouvrard, G.; Zerrouki, M.; Soudan, P.; Belin, S.; Elkaïm, E.; Baudelet, F. *J. Electrochem. Soc.* **2010**, *157*, A606.

[140] Borkiewicz, O. J.; Shyam, B.; Wiaderek, K. M.; Kurtz, C.; Chupas, P. J.; Chapman, K. W. *J. Appl. Crystallogr.* **2012**, *45*, 1261–1269.

[141] Villevieille, C.; Sasaki, T.; Novák, P. *RSC Adv.* **2014**, *4*, 6782.

[142] Johnsen, R. E.; Norby, P. *J. Appl. Crystallogr.* **2013**, *46*, 1537–1543.

[143] *Rigaku J.* **2011**, *27*, 32–35.

[144] Kishi, A. *Rigaku J.* **2012**, *28*, 28–30.

[145] EL-CELL GmbH. *ECC-Opto-Std - Test cell for optical and X-ray characterization in the reflective mode*, http://el-cell.com/products/test-cells/ecc-opto-std, accessed Apr 4, 2016.

[146] MTI Corporation. *Provider of lab equippment*, http://www.mtixtl.com/about-us.aspx, accessed Apr 4, 2016.

[147] Pokharel, A. *Design and performance optimization of an in-situ X-ray powder diffraction cell for electrochemical and crystal structure investigations*, Master's Thesis, Technische Universität München, **2014**.

[148] Gireaud, L.; Grugeon, S.; Laruelle, S.; Yrieix, B.; Tarascon, J.-M. *Electrochem. commun.* **2006**, *8*, 1639–1649.

[149] Mikhaylik, Y.; Kovalev, I.; Schock, R.; Kumaresan, K.; Xu, J.; Affinito, J. *ECS Trans.* **2010**, *25*, 23–34.

[150] Steiger, J.; Kramer, D.; Mönig, R. *Electrochim. Acta* **2014**, *136*, 529–536.

[151] Cheng, X.-B.; Zhang, R.; Zhao, C.-Z.; Wei, F.; Zhang, J.-G.; Zhang, Q. *Adv. Sci.* **2016**, *3*, 1–20.

[152] McMillan, R.; Slegr, H.; Shu, Z. .; Wang, W. *J. Power Sources* **1999**, *81-82*, 20–26.

[153] Mogi, R.; Inaba, M.; Jeong, S.-K.; Iriyama, Y.; Abe, T.; Ogumi, Z. *J. Electrochem. Soc.* **2002**, *149*, A1578–A1583.

[154] Choi, N. S.; Yew, K. H.; Lee, K. Y.; Sung, M.; Kim, H.; Kim, S. S. *J. Power Sources* **2006**, *161*, 1254–1259.

[155] von Cresce, A.; Selena, M. R.; Baker, D. R.; Gaskell, K. J.; Xu, K. *Nano Lett.* **2014**, *14*, 1405–1412.

[156] Shkrob, I. A.; Wishart, J. F.; Abraham, D. P. *J. Phys. Chem. C* **2015**, *119*, 14954–14964.

[157] Markevich, E.; Fridman, K.; Sharabi, R.; Elazari, R.; Salitra, G.; Gottlieb, H. E.; Gershinsky, G.; Garsuch, A.; Semrau, G.; Schmidt, M. a; Aurbach, D. *J. Electrochem. Soc.* **2013**, *160*, A1824–A1833.

[158] Wandt, J.; Marino, C.; Gasteiger, H. A.; Jakes, P.; Eichel, R.-A.; Granwehr, J. *Energy Environ. Sci.* **2015**, *14*, 1358–1367.

[159] Zhao, X.; Zhuang, Q. C.; Xu, S. D.; Xu, Y. X.; Shi, Y. L.; Zhang, X. X. *Int. J. Electrochem. Sci.* **2015**, *10*, 2515–2534.

[160] Zhang, S. S. *J. Power Sources* **2006**, *162*, 1379–1394.

[161] Zhuang, G. V.; Ross, P. N. *Electrochem. Solid-State Lett.* **2003**, *6*, A136–A139.

[162] Padhi, A. K.; Nanjundaswamy, K. S.; Goodenough, J. B. *J. Electrochem. Soc.* **1997**, *144*, 1188–1194.

[163] Goodenough, J. B.; Armand, M.; Padhi, A. K.; Nanjundaswamy, K. S.; Maquelier, C.; Kirakodu, S. Cathode materials for secondary (rechargeable) lithium ion batteries. U.S. patent no. US5910382 and US6514640, **1997**.

[164] Brutti, S.; Panero, S. In *Nanotechnology for Sustainable Energy*; ACS Symposium Series, **2013**; Chap. 4, pp 67–99.

[165] Andersson, A. S.; Kalska, B.; Häggström, L.; Thomas, J. O. *Solid State Ionics* **2000**, *130*, 41–52.

[166] Li, D.; Zhou, H. *Mater. Today* **2014**, *17*, 451–463.

[167] Amine, K.; Yasuda, H.; Yamachi, M. *Electrochem. Solid-State Lett.* **2000**, *3*, 178–179.

[168] Eftekhari, A. *J. Electrochem. Soc.* **2004**, *151*, A1456.

[169] Bramnik, N. N.; Bramnik, K. G.; Baehtz, C.; Ehrenberg, H. *J. Power Sources* **2005**, *145*, 74–81.

[170] Nakayama, M.; Goto, S.; Uchimoto, Y.; Wakihara, M.; Kitajima, Y. *Chem. Mater.* **2004**, *16*, 3399–3401.

[171] Bramnik, N. N.; Bramnik, K. G.; Buhrmester, T.; Baehtz, C.; Ehrenberg, H.; Fuess, H. *J. Solid State Electrochem.* **2004**, *8*, 558–564.

[172] Freiberg, A.; Metzger, M.; Haering, D.; Bretzke, S.; Puravankara, S.; Nilges, T.; Stinner, C.; Marino, C.; Gasteiger, H. A. *J. Electrochem. Soc.* **2014**, *161*, A2255–A2261.

[173] *WinXPOW Powder diffraction software*, Version 3.0.2.2, STOE & Cie GmbH, **2011**.

[174] Strobridge, F. C.; Clement, R. J.; Leskes, M.; Middlemiss, D. S.; Borkiewicz, O. J.; Wiaderek, K. M.; Chapman, K. W.; Chupas, P. J.; Grey, C. P. *Chem. Mater.* **2014**, *26*, 6193.

[175] Kaus, M.; Issac, I.; Heinzmann, R.; Doyle, S.; Mangold, S.; Hahn, H.; Chakravadhanula, V. S. K.; Kuebel, C.; Ehrenberg, H.; Indris, S. *J. Phys. Chem. C* **2014**, *118*, 17279–17290.

[176] Manthiram, A.; Fu, Y.; Su, Y.-S. *Acc. Chem. Res.* **2013**, *46*, 1125–1134.

[177] Kasavajjula, U.; Wang, C.; Appleby, A. J. *J. Power Sources* **2007**, *163*, 1003–1039.

[178] Bruce, P. G.; Freunberger, S. A.; Hardwick, L. J.; Tarascon, J.-M. *Nat Mater* **2012**, *11*, 19–29.

[179] Abraham, K. M.; Jiang, Z. *J. Electrochem. Soc.* **1996**, *143*, 1–5.

[180] Rao, B. M. L. Organic Electrolyte Cells. U.S. Pat. 3413154, **1968**.

[181] Rauh, R. D.; Abraham, K. M.; Pearson, G. F.; Surprenant, J. K.; Brummer, S. B. *J. Electrochem. Soc.* **1979**, *126*, 523–527.

[182] McCloskey, B. D.; Valery, A.; Luntz, A. C.; Gowda, S. R.; Wallraff, G. M.; Garcia, J. M.; Mori, T.; Krupp, L. E. *J. Phys. Chem. Lett.* **2013**, *4*, 2989–2993.

[183] Luntz, A. C.; Mccloskey, B. D. *Chem. Rev.* **2014**, *114*, 11721–11750.

[184] Adams, B. D.; Black, R.; Williams, Z.; Fernandes, R.; Cuisinier, M.; Berg, E. J.; Novak, P.; Murphy, G. K.; Nazar, L. F. *Adv. Energy Mater.* **2015**, *5*, 1–11.

[185] Bryantsev, V. S.; Giordani, V.; Walker, W.; Uddin, J.; Lee, I.; Duin, A. C. T. Van; Chase, G. V; Addison, D. *J. Phys. Chem. C* **2013**, 1–7.

[186] Freunberger, S. A.; Chen, Y.; Drewett, N. E.; Hardwick, L. J.; Bardé, F.; Bruce, P. G. *Angew. Chemie Int. Ed.* **2011**, *50*, 8609–8613.

[187] Thotiyl, M. M. O.; Freunberger, S. a; Peng, Z.; Bruce, P. G. *J. Am. Chem. Soc.* **2013**, *135*, 494–500.

[188] Nazar, L. F.; Cuisinier, M.; Pang, Q. *MRS Bull.* **2014**, *39*, 436–442.

[189] Ji, X.; Lee, K. T.; Nazar, L. F. *Nat. Mater.* **2009**, *8*, 500–506.

[190] Elazari, R.; Salitra, G.; Garsuch, A.; Panchenko, A.; Aurbach, D. *Adv. Mater.* **2011**, *23*, 5641–5644.

[191] Pang, Q.; Kundu, D.; Cuisinier, M.; Nazar, L. F. *Nat. Commun.* **2014**, *5*, 4759.

[192] Liang, X.; Hart, C.; Pang, Q.; Garsuch, A.; Weiss, T.; Nazar, L. F. *Nat. Commun.* **2015**, *6*, 5682.

[193] Aurbach, D.; Pollak, E.; Elazari, R.; Salitra, G.; Kelley, C. S.; Affinito, J. *J. Electrochem. Soc.* **2009**, *156*, A694–A702.

[194] Dokko, K.; Tachikawa, N.; Yamauchi, K.; Tsuchiya, M.; Yamazaki, A.; Takashima, E.; Park, J.; Ueno, K.; Seki, S.; Serizawa, N.; Watanabe, M. **2013**, *160*, 32–37.

[195] Schuster, J.; He, G.; Mandlmeier, B.; Yim, T.; Lee, K. T.; Bein, T.; Nazar, L. F. *Angew. Chemie - Int. Ed.* **2012**, *51*, 3591–3595.

[196] Tarascon, J.-M.; Armand, M. *Nature* **2001**, *414*, 359–367.

[197] Zhang, W. J. *J. Power Sources* **2011**, *196*, 13–24.

[198] Etacheri, V.; Geiger, U.; Gofer, Y.; Roberts, G. a; Stefan, I. C.; Fasching, R.; Aurbach, D. *Langmuir* **2012**, *28*, 6175–6184.

[199] Li, H.; Li, H.; Huang, X.; Huang, X.; Chen, L.; Chen, L.; Wu, Z.; Wu, Z.; Liang, Y.; Liang, Y. *Electrochem. Solid-State Lett.* **1999**, *2*, 547–549.

[200] Zu, C.; Klein, M.; Manthiram, A. *J. Phys. Chem. Lett.* **2014**, *5*, 3986–3991.

[201] Hassoun, J.; Scrosati, B. *Angew. Chemie Int. Ed.* **2010**, *49*, 2371–2374.

[202] Elazari, R.; Salitra, G.; Gershinsky, G.; Garsuch, A.; Panchenko, A.; Aurbach, D. *Electrochem. commun.* **2012**, *14*, 21–24.

[203] Liu, N.; Hu, L.; McDowell, M. T.; Jackson, A.; Cui, Y. *ACS Nano* **2011**, *5*, 6487–6493.

[204] Brückner, J.; Thieme, S.; Böttger-Hiller, F.; Bauer, I.; Grossmann, H. T.; Strubel, P.; Althues, H.; Spange, S.; Kaskel, S. *Adv. Funct. Mater.* **2014**, *24*, 1284–1289.

[205] Li, J.; Dahn, J. R. *J. Electrochem. Soc.* **2007**, *154*, A156–A161.

[206] Bommier, C.; Luo, W.; Gao, W. Y.; Greaney, A.; Ma, S.; Ji, X. *Carbon N. Y.* **2014**, *76*, 165–174.

[207] Meini, S.; Tsiouvaras, N.; Schwenke, K. U.; Piana, M.; Beyer, H.; Lange, L.; Gasteiger, H. A. *Phys. Chem. Chem. Phys.* **2013**, *15*, 11478.

[208] Meini, S.; Elazari, R.; Rosenman, A.; Garsuch, A.; Aurbach, D. *J. Phys. Chem. Lett.* **2014**, *5*, 915–918.

[209] Yang, Y.; McDowell, M. T.; Jackson, A.; Cha, J. J.; Hong, S. S.; Cui, Y. *Nano Lett.* **2010**, *10*, 1486–1491.

[210] Cai, K.; Song, M. K.; Cairns, E. J.; Zhang, Y. *Nano Lett.* **2012**, *12*, 6474–6479.

[211] Mulder, G.; Omar, N.; Pauwels, S.; Meeus, M.; Leemans, F.; Verbrugge, B.; Nijs, W.; van den Bossche, P.; Six, D.; van Mierlo, J. *Electrochim. Acta* **2013**, *87*, 473–488.

[212] Belharouak, I.; Sun, Y.-K.; Liu, J.; Amine, K. *J. Power Sources* **2003**, *123*, 247–252.

[213] Whittingham, M. S. *Chem. Rev.* **2004**, *104*, 4271–4302.

[214] Choi, J.; Manthiram, A. *J. Electrochem. Soc.* **2005**, *152*, A1714–A1718.

[215] Yabuuchi, N.; Makimura, Y.; Ohzuku, T. *J. Electrochem. Soc.* **2007**, *154*, A314–A321.

[216] Gabrisch, H.; Yi, T.; Yazami, R. *Electrochem. Solid-State Lett.* **2008**, *11*, A119.

[217] Kim, M. G.; Shin, H. J.; Kim, J.-H.; Park, S.-H.; Sun, Y.-K. *J. Electrochem. Soc.* **2005**, *152*, A1320.

[218] Yabuuchi, N.; Ohzuku, T. *J. Power Sources* **2005**, *146*, 636–639.

[219] Amine, K.; Chen, Z.; Zhang, Z.; Liu, J.; Lu, W.; Qin, Y.; Lu, J.; Curtis, L.; Sun, Y.-K. *J. Mater. Chem.* **2011**, *21*, 17754.

[220] Zheng, H.; Sun, Q.; Liu, G.; Song, X.; Battaglia, V. S. *J. Power Sources* **2012**, *207*, 134–140.

[221] Lux, S. F.; Lucas, I. T.; Pollak, E.; Passerini, S.; Winter, M.; Kostecki, R. *Electrochem. commun.* **2012**, *14*, 47–50.

[222] Ochida, M.; Domi, Y.; Doi, T.; Tsubouchi, S.; Nakagawa, H.; Yamanaka, T.; Abe, T.; Ogumi, Z. *J. Electrochem. Soc.* **2012**, *159*, A961–A966.

[223] Zhan, C.; Lu, J.; Jeremy Kropf, A.; Wu, T.; Jansen, A. N.; Sun, Y.-K.; Qiu, X.; Amine, K. *Nat. Commun.* **2013**, *4*.

[224] Delacourt, C.; Kwong, A.; Liu, X.; Qiao, R.; Yang, W. L.; Lu, P.; Harris, S. J.; Srinivasan, V. *J. Electrochem. Soc.* **2013**, *160*, A1099.

[225] Joshi, T.; Eom, K.; Yushin, G.; Fuller, T. F. *J. Electrochem. Soc.* **2014**, *161*, A1915–A1921.

[226] Dubarry, M.; Truchot, C.; Liaw, B. Y.; Gering, K.; Sazhin, S.; Jamison, D.; Michelbacher, C. *J. Power Sources* **2011**, *196*, 10336–10343.

[227] Burns, J. C.; Kassam, A.; Sinha, N. N.; Downie, L. E.; Solnickova, L.; Way, B. Â. M.; Dahn, J. R. *J. Electrochem. Soc.* **2013**, *160*, A1451–A1456.

[228] Xiao, X.; Liu, Z.; Baggetto, L.; Veith, G. M.; More, K. L.; Unocic, R. R. *Phys. Chem. Chem. Phys.* **2014**, *16*, 10398–10402.

[229] Shkrob, I. A.; Kropf, A. J.; Marin, T. W.; Li, Y.; Poluektov, O. G.; Niklas, J.; Abraham, D. P. *J. Phys. Chem.* **2014**, *118*, 24335–24348.

[230] Xu, K. *Chem. Rev.* **2004**, *104*, 4303–4418.

[231] Li, J.; Zhang, Z.; Guo, X.; Yang, Y. *Solid State Ionics* **2006**, *177*, 1509–1516.

[232] Li, D.-C.; Muta, T.; Zhang, L.-Q.; Yoshio, M.; Noguchi, H. *J. Power Sources* **2004**, *132*, 150–155.

[233] Yin, S.-C.; Rho, Y.-H.; Swainson, I.; Nazar, L. F. *Chem. Mater.* **2006**, *18*, 1901–1910.

[234] Rodriguez, A. M.; Ingersoll, D.; Doughty, D. H. *Adv. X-Ray Anal.* **2002**, *45*, 182–187.

[235] Vegard, L. *Zeitschrift für Phys.* **1921**, *5*, 17–26.

[236] Vegard, L.; Dale, H. *Zeitschrift für Krist. - Crystaline Mater.* **1928**, *67*, 148–162.

[237] Denton, A. R.; Ashcroft, N. W. *Phys. Rev. A* **1991**, *43*, 3161–3164.

[238] Hwang, B. J.; Tsai, Y. W.; Carlier, D.; Ceder, G. *Chem. Mater.* **2003**, *15*, 3676–3682.

[239] Koyama, Y.; Yabuuchi, N.; Tanaka, I.; Adachi, H.; Ohzuku, T. *J. Electrochem. Soc.* **2004**, *151*, A1545.

[240] Shaju, K. M.; Bruce, P. G. *Adv. Mater.* **2006**, *18*, 2330–2334.

[241] Choi, J.; Manthiram, A. *Electrochem. Solid-State Lett.* **2005**, *8*, C102–C105.

[242] Kang, S.-H.; Abraham, D. P.; Yoon, W.-S.; Nam, K.-W.; Yang, X.-Q. *Electrochim. Acta* **2008**, *54*, 684–689.

[243] Kang, S.-H.; Yoon, W.-S.; Nam, K.-W.; Yang, X.-Q.; Abraham, D. P. *J. Mater. Sci.* **2008**, *43*, 4701–4706.

[244] German, F.; Hintennach, A.; LaCroix, A.; Thiemig, D.; Oswald, S.; Scheiba, F.; Hoffmann, M. J.; Ehrenberg, H. *J. Power Sources* **2014**, *264*, 100–107.

[245] Dahn, J. *Solid State Ionics* **1990**, *44*, 87–97.

[246] Johnson, C. S.; Kim, J.; Kropf, A. J.; Kahaian, A. J.; Vaughey, J. T.; Fransson, L. M. L.; Edström, K.; Thackeray, M. M. *Chem. Mater.* **2003**, *2*, 2313–2322.

[247] Winter, M.; Novák, P.; Monnier, A. *J. Electrochem. Soc.* **1998**, *145*, 428–436.

[248] Peled, E.; Bar Tow, D.; Merson, a.; Gladkich, a.; Burstein, L.; Golodnitsky, D. *J. Power Sources* **2001**, *97-98*, 52–57.

[249] Eshkenazi, V.; Peled, E.; Burstein, L.; Golodnitsky, D. *Solid State Ionics* **2004**, *170*, 83–91.

[250] Du Pasquier, A.; Disma, F.; Bowner, T.; Gozdz, A. S.; Amatucci, G.; Tarascon, J.-M. *J. Electrochem. Soc.* **1998**, *145*, 472–476.

[251] Lee, H. H.; Wan, C. C.; Wang, Y. Y. *J. Electrochem. Soc.* **2004**, *151*, A542.

[252] Liu, T.; Garsuch, A.; Chesneau, F.; Lucht, B. L. *J. Power Sources* **2014**, *269*, 920–926.

[253] Komaba, S.; Kumagai, N.; Kataoka, Y. *Electrochim. Acta* **2002**, No. 47, 1229–1239.

[254] Xia, Y.; Yoshio, M. *J. Electrochem. Soc.* **1996**, *143*, 825–833.

[255] Jang, D. H.; Shin, Y. J.; Oh, S. H. *J. Electrochem. Soc.* **1996**, *143*, 2204–2211.

[256] Aurbach, D.; Levi, M. D.; Gamulski, K.; Markovsky, B.; Salitra, G.; Levi, E.; Heider, U.; Heider, L.; Oesten, R. *J. Power Sources* **1999**, *81-82*, 472–479.

[257] Hunter, J. C. *J. Solid State Chem.* **1981**, *39*, 142–147.

[258] Metzger, M.; Sicklinger, J.; Haering, D.; Kavakli, C.; Stinner, C.; Marino, C.; Gasteiger, H. A. *J. Electrochem. Soc.* **2015**, *162*, A1227–A1235.

[259] Tsunekawa, H.; Tanimoto, a. S.; Marubayashi, R.; Fujita, M.; Kifune, K.; Sano, M. *J. Electrochem. Soc.* **2002**, *149*, A1326–A1331.

[260] Kasnatscheew, J.; Evertz, M.; Streipert, B.; Wagner, R.; Klöpsch, R.; Vortmann, B.; Hahn, H.; Nowak, S.; Amereller, M.; Gentschev, A.-C.; Lamp, P.; Winter, M. *Phys. Chem. Chem. Phys.* **2016**, *18*, 3956–3965.

[261] Asoka-Kumar, P.; Alatalo, M.; Ghosh, V. J.; Kruseman, a C.; Nielsen, B.; Lynn, K. G. *Phys. Rev. Lett.* **1996**, *77*, 2097–2100.

[262] Schultz, P. J.; Lynn, K. G. *Rev. Mod. Phys.* **1988**, *60*, 701–779.

[263] Hugenschmidt, C.; Ceeh, H.; Gigl, T.; Lippert, F.; Piochacz, C.; Reiner, M.; Schreckenbach, K.; Vohburger, S.; Weber, J.; Zimnik, S. *J. Phys. Conf. Ser.* **2014**, *505*, 012029.

[264] West, R. N. *Adv. Phys.* **1973**, *8*, 1823–1825.

[265] Parz, P.; Fuchsbichler, B.; Koller, S.; Bitschnau, B.; Mautner, F.; Puff, W. *Appl. Phys. Lett.* **2014**, *102*, 151901.

[266] Cooper, A. S. *Acta Crystallogr.* **1962**, *15*, 578–582.

[267] Thompson, P.; Cox, D. E.; Hastings, J. B. *J. Appl. Crystallogr.* **1987**, *20*, 79–83.

[268] Finger, L. W.; Cox, D. E.; Jephcoat, A. P. *J. Appl. Cryst.* **1994**, *27*, 892–900.

[269] Stadlbauer, M.; Hugenschmidt, C.; Schreckenbach, K. *Appl. Surf. Sci.* **2008**, *255*, 136–138.

[270] Reiner, M.; Pikart, P.; Hugenschmidt, C. *J. Phys. Conf. Ser.* **2013**, *443*, 012071.

[271] Yabuuchi, N.; Makimura, Y.; Ohzuku, T. *J. Electrochem. Soc.* **2007**, *154*, A314.

[272] Yabuuchi, N.; Makimura, Y.; Ohzuku, T. *J. Electrochem. Soc.* **2005**, *154*, A314.

[273] Igawa, N.; Taguchi, T.; Fukazawa, H.; Yamauchi, H.; Utsumi, W. *J. Am. Ceram. Soc.* **2010**, *93*, 2144–2146.

[274] Tsai, Y. W.; Hwang, B. J.; Ceder, G.; Sheu, H. S.; Liu, D. G.; Lee, J. F. *Chem. Mater.* **2005**, *17*, 3191–3199.

[275] Reiner, M.; Gigl, T.; Jany, R.; Hammerl, G.; Hugenschmidt, C. *Appl. Phys. Lett.* **2015**, *106*.

[276] Yabuuchi, N.; Koyama, Y.; Nakayama, N.; Ohzuku, T. *J. Electrochem. Soc.* **2005**, *152*, A1434–A1440.

[277] Trask, S. E.; Pupek, K. Z.; Gilbert, J. A.; Klett, M.; Polzin, B. J.; Jansen, A. N.; Abraham, D. P. *J. Electrochem. Soc.* **2016**, *163*, A345–A350.

[278] Gallagher, K. G.; Trask, S. E.; Bauer, C.; Woehrle, T.; Lux, S. F.; Tschech, M.; Lamp, P.; Polzin, B. J.; Ha, S.; Long, B.; Wu, Q.; Lu, W.; Dees, D. W.; Jansen, A. N. *J. Electrochem. Soc.* **2016**, *163*, A138–A149.

[279] Liu, G.; Zheng, H.; Battaglia, V. S. *Fabrication procedure for LiMn2O4/Graphite-based Lithium-ion Rechargeable Pouch Cells*; Lawrence Berkley National Laboratory, **2007**.

[280] Dahn, J. R. *Phys. Rev. B* **1991**, *44*, 9170–9177.

[281] Yazami, R.; Reynier, Y. *J. Power Sources* **2006**, *153*, 312–318.

[282] Ohzuku, T.; Iwakoshi, Y.; Sawai, K. *J. Electrochem. Soc.* **1993**, *140*, 2490.

[283] Billaud, D.; Henry, F. X.; Lelaurain, M.; Willmann, P. *J. Phys. Chem. Solids* **1996**, *57*, 775–781.

[284] Safari, M.; Delacourt, C. *J. Electrochem. Soc.* **2011**, *158*, A1436.

[285] Senyshyn, A.; Mühlbauer, M. J.; Nikolowski, K.; Pirling, T.; Ehrenberg, H. *J. Power Sources* **2012**, *203*, 126–129.

[286] Senyshyn, A.; Dolotko, O.; Muhlbauer, M. J.; Nikolowski, K.; Fuess, H.; Ehrenberg, H. *J. Electrochem. Soc.* **2013**, *160*, A3198–A3205.

[287] Zinth, V.; Von Lüders, C.; Hofmann, M.; Hattendorff, J.; Buchberger, I.; Erhard, S.; Rebelo-Kornmeier, J.; Jossen, A.; Gilles, R. *J. Power Sources* **2014**, *271*, 152–159.

List of Figures

List of Tables

List of Publications

Manuscripts

1. Seidlmayer, S.; **Buchberger, I.**; S.; Reiner, M.; Gigl, T.; Gilles, R.; Gasteiger, H. A.; Hugenschmidt; C., First-Cycle-Defect Evolution of $Li_{1-x}Ni_{1/3}Mn_{1/3}Co_{1/3}O_2$ Lithium-Ion Battery Electrodes Investigated by Positron Annihilation Spectroscopy, *in preparation*
2. **Buchberger, I.**; Seidlmayer, S.; Pokharel,A.; Piana, M.;Hattendorff, J.; Kudejova, P.; Gilles, R.; Gasteiger, H. A., Aging Analysis of Graphite/$LiNi_{1/3}Mn_{1/3}Co_{1/3}O_2$ Cells Using XRD,PGAA, and AC Impedance *J. Electrochem. Soc.*, **2015**, 162 (14), A2737-A2746.
3. Jha, H.; **Buchberger, I.**; Cui, X.; Meini, S.; Gasteiger, H. A., Li-S Batteries with Li_2S Cathodes and Si/C Anodes *J. Electrochem. Soc*., **2015**, 162 (9), A1829-A1835.
4. Seidlmayer, S.; Hattendorff, J.; **Buchberger, I.**; Karge, L.; Gasteiger, H. A.; Gilles, R., In Operando Small-Angle Neutron Scattering (SANS) on Li-Ion Batteries *J. Electrochem. Soc.* ,**2015**, 162 (2), A3116-A3125.
5. Zinth, V.; von Lüders, C.; Hofmann, M.; Hattendorff, J.; **Buchberger, I.**; Erhard, S.; Gilles, R., Lithium Plating in Lithium-Ion Batteries at Sub-ambient Temperatures Investigated by In Situ Neutron Diffraction *J. PowerSources,* **2014**, 271, 152-159.
6. Piana, M.; Wandt, J.; Meini, S.; **Buchberger, I.**; Tsiouvaras, N.; Gasteiger, H.A., Stability of a Pyrrolidonium-Based Ionic Liquid in Li-O_2 Cells *J. Electrochem. Soc.*, **2014**, 161 (14) A1992-A2001.
7. Tsiouvaras, N.; Meini, S.; **Buchberger, I.**; Gasteiger, H. A., A Novel On-Line Mass Spectrometer Design for the Study of Multiple Charging Cycles of a Li-O2 Battery, *J. Electrochem. Soc.*, **2013**, 160(3), A471-A477.

Conference talks

1. *X-rays, Neutrons and Positrons: Strong Contributors in Revealing Fundamental Processes in Lithium-Ion Batterie* 6th MSE Colloquium (July 7th, 2016) in Garching, Germany
2. *Aging Analysis of Graphite/$LiNi_{1/3}Mn_{1/3}Co_{1/3}O_2$ Cells using XRD, PGAA, and AC Impedance* 228th ECS Meeting of the Electrochemical Society (October 11-15, 2015) in Phoenix, Arizona, Abstract number # 452.

Poster presentations

1. **Buchberger, I.**; Seidlmayer, S.; Kudejova, P.; Hattendorff, J.; Schuster, J.; Zinth, V.; Gilles, R.; Gasteiger, H.A., Anodic transition metal deposition (Ni, Mn, Co) investigated by Prompt Gamma Activation Analysis (PGAA); Poster at Kraftwerk Batterie 2014, Münster.
2. **Buchberger, I.**; Pokharel, A.; Piana, M., Gasteiger, H.A., Design and Performance of an In situ X-ray diffraction cell for long-term electrochemical studies; Poster at Electrochemistry 2014, Mainz.
3. Pokharel, A.; **Buchberger, I.**; Piana, M.; Gasteiger, H.A., Design and Performance of an In situ X-ray Diffraction Li-ion Cell for Electrochemical/Crystal Structure Investigations; Poster at 4th Colloquium of the Munich School of Engeneering, 2014, Garching.
4. Hattendorff J.; **Buchberger, I.**; Schuster, J.; Seidlmayer, S; Zinth, V.; Kudejova, P; Gasteiger, H.A.; Gilles, R., Untersuchungen von Elektrodendesign, -alterung & -sicherheit im Projekt ExZellTUM; Poster at Batterieforum Deutschland 2014, Berlin.

Appendix

Technical drawings:

A *In situ* XRD cell version1
B *In situ* XRD cell version2
C Pouch-cell holder for XRD in transmission mode
D Pouch-cell compression tool

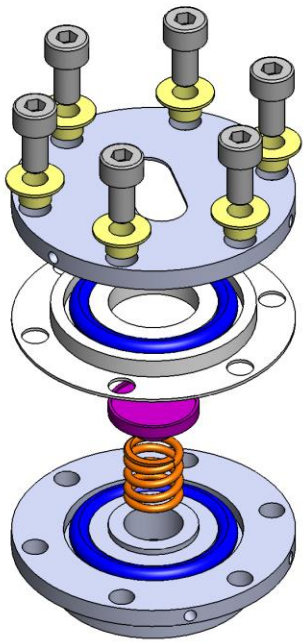

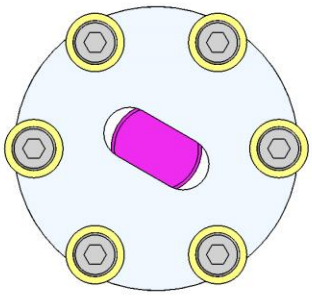

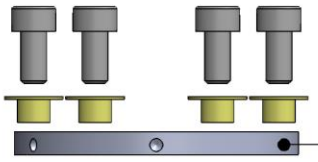

Top positive current-collector plate (p. 2)

Insulating sealing unit (p.3)

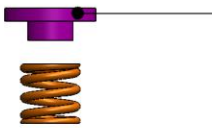

Anode plate (p.5)

Bottom negative current-collector plate (p.4)

Adapter for XRD sample holder (p. 6)

WENN NICHT ANDERS DEFINIERT: BEMASSUNGEN SIND IN MILLIMETER OBERFLÄCHENBESCHAFFENHEIT: TOLERANZEN: LINEAR: WINKEL:	OBERFLÄCHENGÜTE:			ENTGRATEN UND SCHARFE KANTEN BRECHEN	ZEICHNUNG NICHT SKALIEREN	ÄNDERUNG
	NAME	SIGNATUR	DATUM		BENENNUNG: Overall view	
GEZEICHNET						
GEPRÜFT						
GENEHMIGT						
PRODUKTION						
QUALITÄT				WERKSTOFF:	ZEICHNUNGSNR. In situ XRD (version 1)	A4
GEWICHT:					MASSSTAB: 3:2	BLATT 1 VON 6

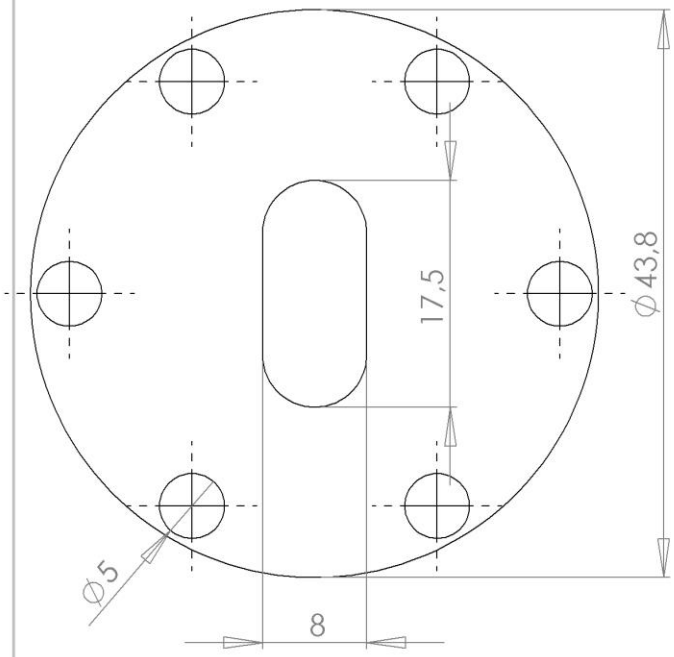

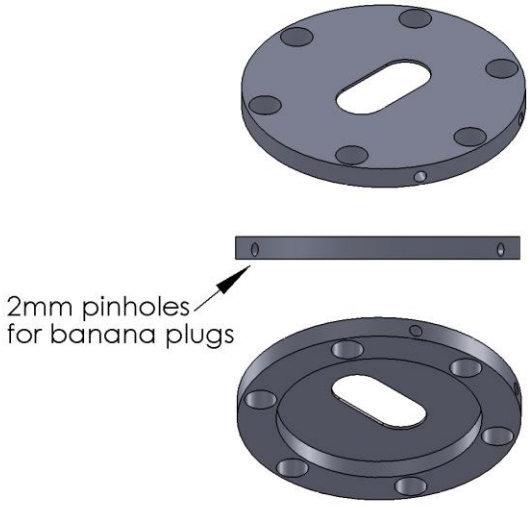

Scale 1:1

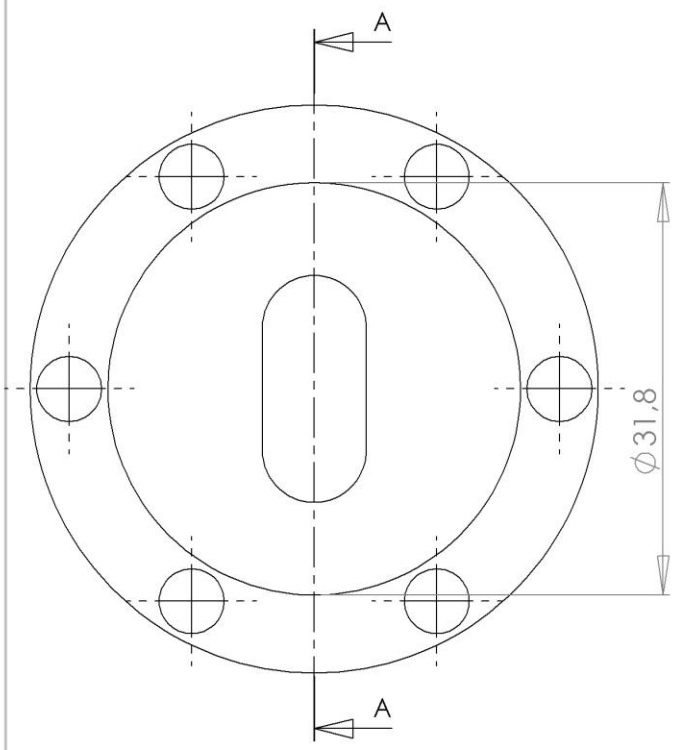

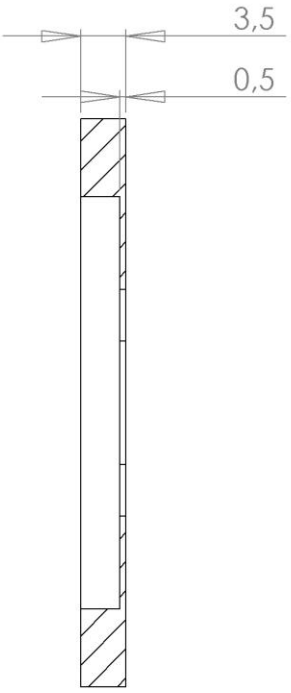

PROFILE A-A
Scale 2 : 1

WENN NICHT ANDERS DEFINIERT: BEMASSUNGEN SIND IN MILLIMETER OBERFLÄCHENBESCHAFFENHEIT: TOLERANZEN: LINEAR: WINKEL:	OBERFLÄCHENGÜTE:		ENTGRATEN UND SCHARFE KANTEN BRECHEN	ZEICHNUNG NICHT SKALIEREN	ÄNDERUNG	
	NAME	SIGNATUR	DATUM	BENENNUNG:		
GEZEICHNET				Top positive current-collector plate		
GEPRÜFT						
GENEHMIGT						
PRODUKTION						
QUALITÄT				WERKSTOFF: stainless steel 1.4571	ZEICHNUNGSNR. In situ XRD (version 1)	A4
				GEWICHT:	MASSSTAB:1:1	BLATT 2 VON 6

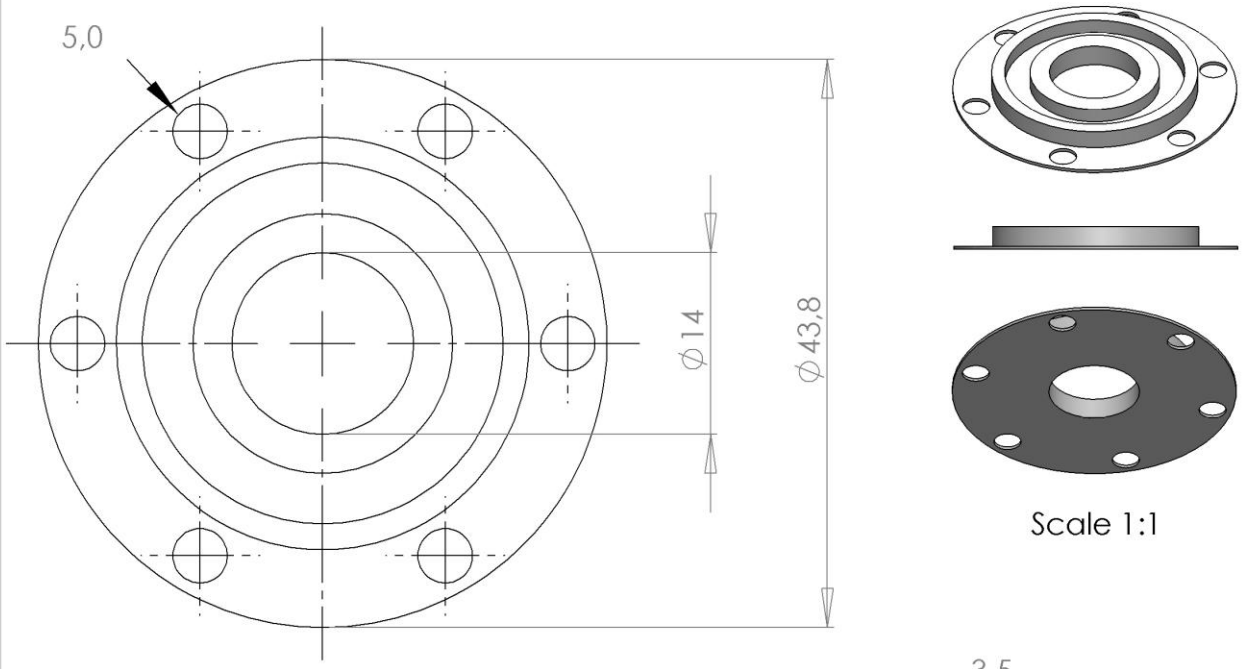

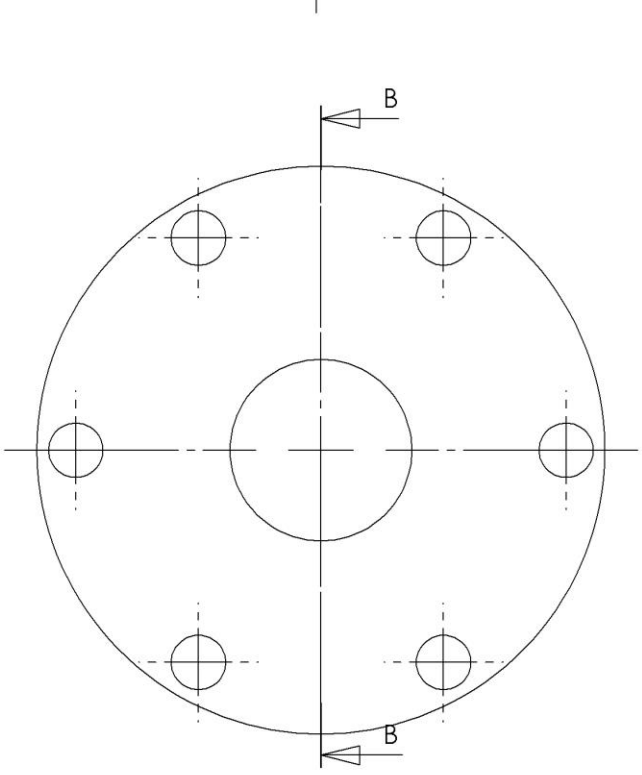

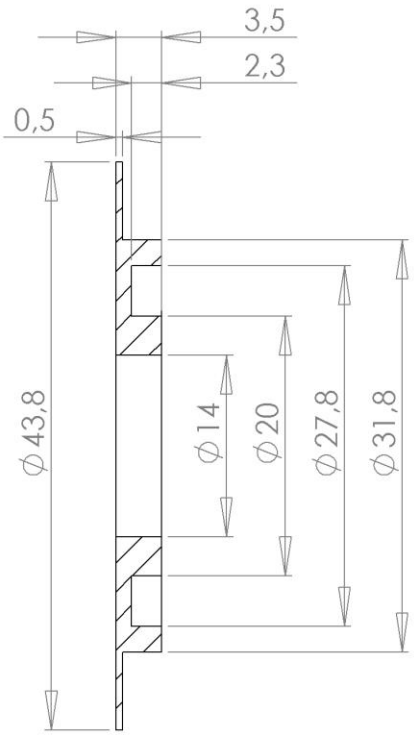

PROFILE B-B
Scale 2 : 1

WENN NICHT ANDERS DEFINIERT: BEMASSUNGEN SIND IN MILLIMETER OBERFLÄCHENBESCHAFFENHEIT: TOLERANZEN: LINEAR: WINKEL:	OBERFLÄCHENGÜTE:		ENTGRATEN UND SCHARFE KANTEN BRECHEN	ZEICHNUNG NICHT SKALIEREN	ÄNDERUNG	
	NAME	SIGNATUR	DATUM	BENENNUNG:		
GEZEICHNET				Insulating sealing unit		
GEPRÜFT						
GENEHMIGT						
PRODUKTION						
QUALITÄT				WERKSTOFF:	ZEICHNUNGSNR.	A4
				PTFE	In situ XRD (version 1)	
				GEWICHT:	MASSSTAB:1:1	BLATT 3 VON 6

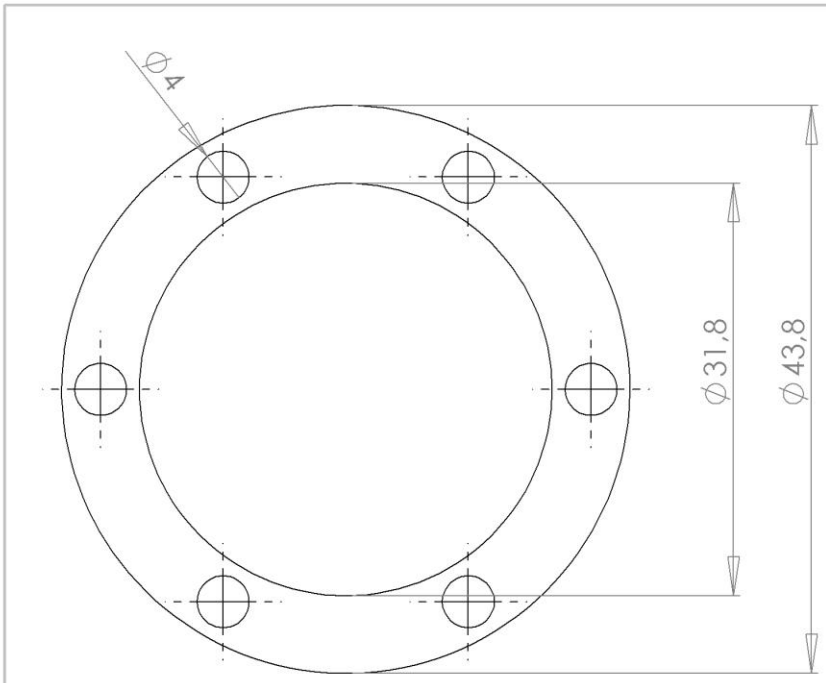

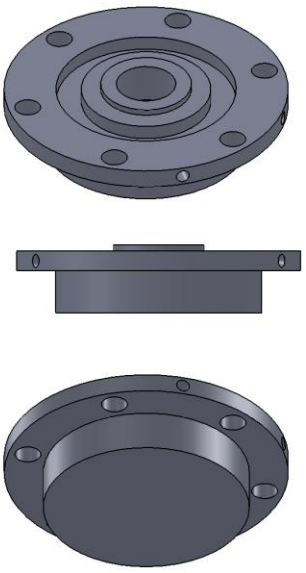

Scale 1:1

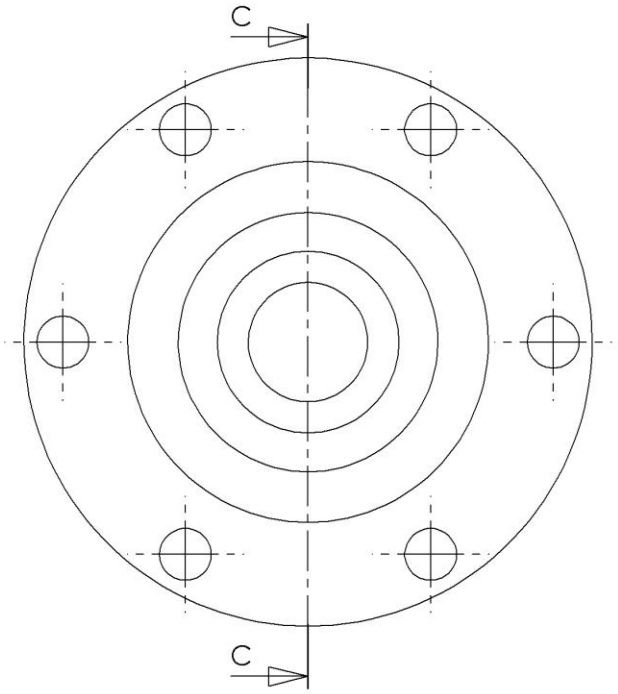

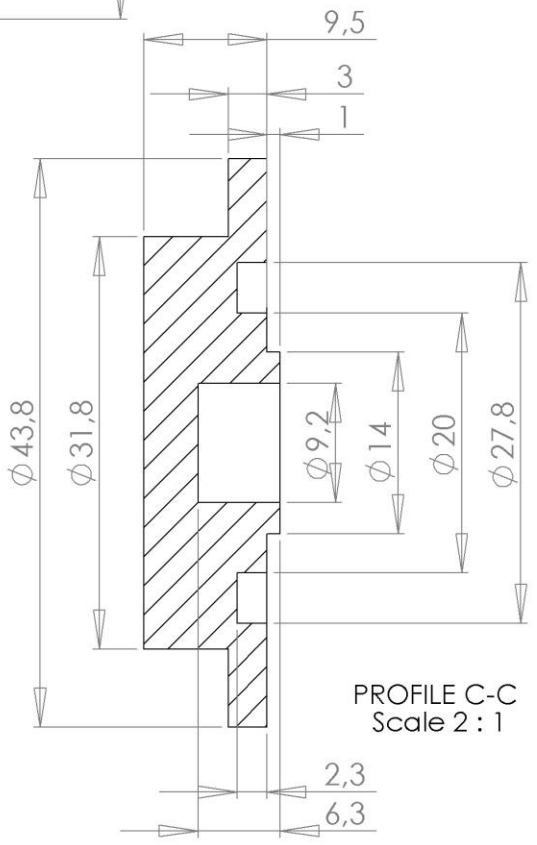

PROFILE C-C
Scale 2 : 1

WENN NICHT ANDERS DEFINIERT: BEMASSUNGEN SIND IN MILLIMETER OBERFLÄCHENBESCHAFFENHEIT: TOLERANZEN: LINEAR: WINKEL:	OBERFLÄCHENGÜTE:		ENTGRATEN UND SCHARFE KANTEN BRECHEN	ZEICHNUNG NICHT SKALIEREN	ÄNDERUNG	
	NAME	SIGNATUR	DATUM	BENENNUNG:		
GEZEICHNET				Bottom negative current-collector plate		
GEPRÜFT						
GENEHMIGT						
PRODUKTION						
QUALITÄT				WERKSTOFF: stainless steel 1.4571	ZEICHNUNGSNR. In situ XRD (version 1)	A4
				GEWICHT:	MASSSTAB:1:1	BLATT 4 VON 6

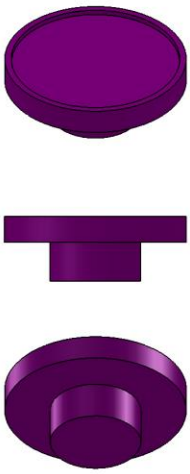

Scale 2:1

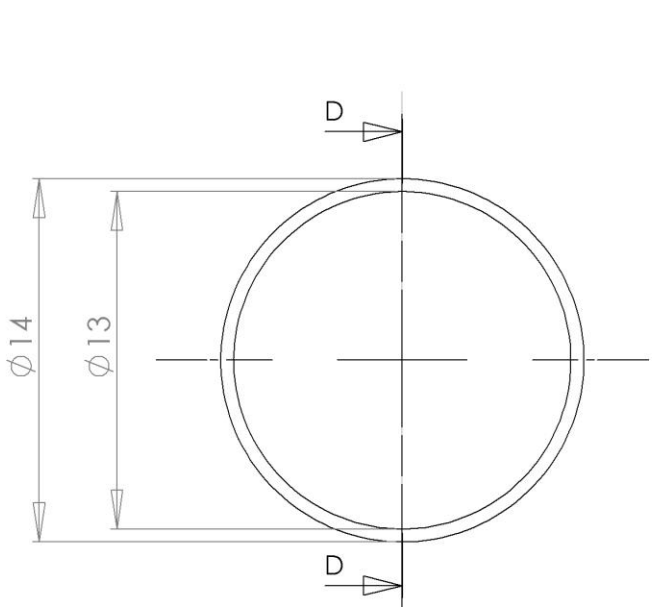

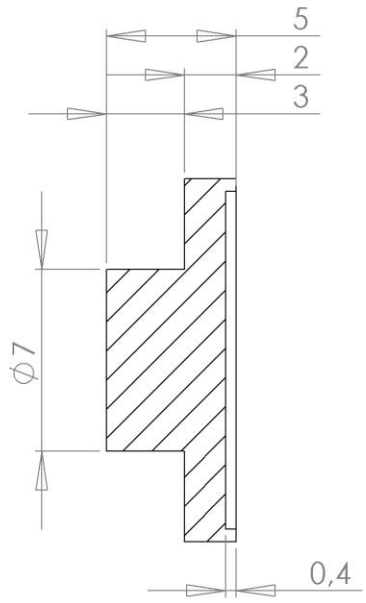

PROFILE D-D
Scale 4 : 1

WENN NICHT ANDERS DEFINIERT: BEMASSUNGEN SIND IN MILLIMETER OBERFLÄCHENBESCHAFFENHEIT: TOLERANZEN: LINEAR: WINKEL:	OBERFLÄCHENGÜTE:				ENTGRATEN UND SCHARFE KANTEN BRECHEN	ZEICHNUNG NICHT SKALIEREN / ÄNDERUNG
	NAME	SIGNATUR	DATUM			BENENNUNG: Anode plate
GEZEICHNET						
GEPRÜFT						
GENEHMIGT						
PRODUKTION						
QUALITÄT				WERKSTOFF: stainless steel 1.4571		ZEICHNUNGSNR.: In situ XRD (version 1) / A4
				GEWICHT:		MASSSTAB:2:1 / BLATT 5 VON 6

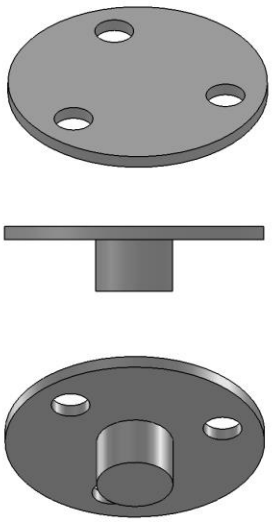

Scale 2:1

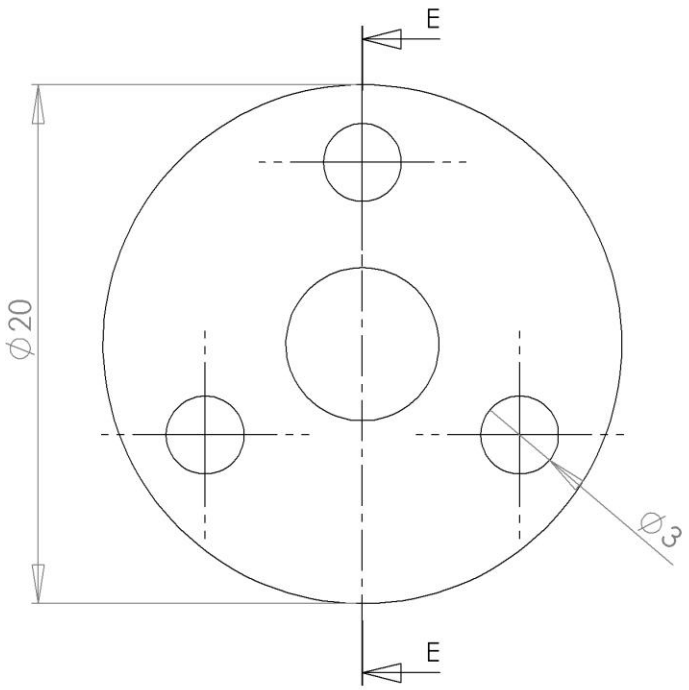

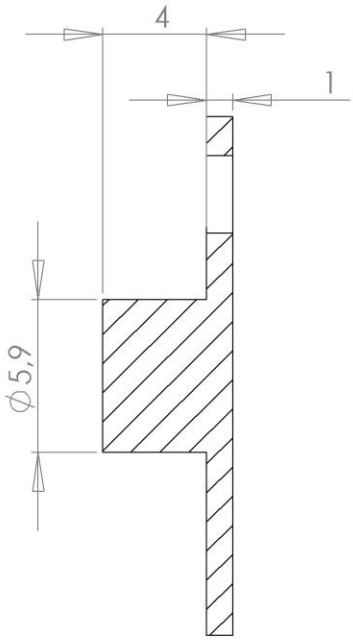

PROFILE E-E
Scale 4 : 1

WENN NICHT ANDERS DEFINIERT: BEMASSUNGEN SIND IN MILLIMETER OBERFLÄCHENBESCHAFFENHEIT: TOLERANZEN: LINEAR: WINKEL:	OBERFLÄCHENGÜTE:			ENTGRATEN UND SCHARFE KANTEN BRECHEN	ZEICHNUNG NICHT SKALIEREN	ÄNDERUNG
	NAME	SIGNATUR	DATUM		BENENNUNG: Adapter for XRD sample holder	
GEZEICHNET						
GEPRÜFT						
GENEHMIGT						
PRODUKTION						
QUALITÄT				WERKSTOFF: polyethylene/ polypropylene	ZEICHNUNGSNR. In situ XRD (version 1)	A4
				GEWICHT:	MASSSTAB:1:1	BLATT 6 VON 6

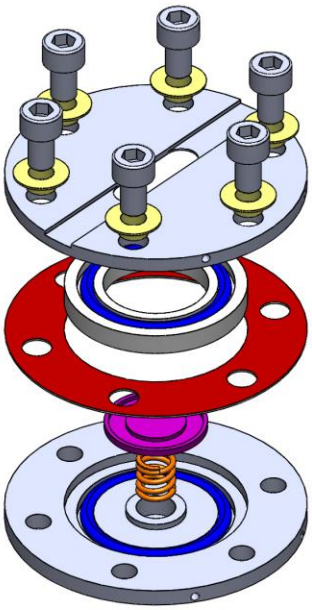

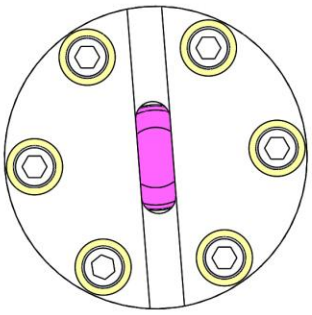

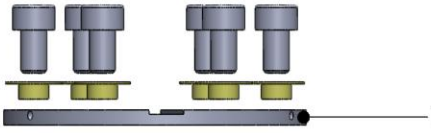

Top positive current-collector plate (p. 2)

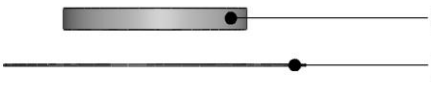

Sealing unit (p. 3)

Insulating rubber (p. 4)

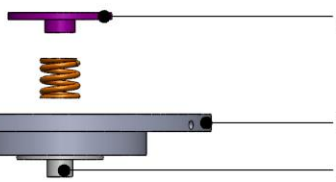

Anode plate (p. 6)

Bottom negative current-collctor plate (p. 5)

Adapter for XRD sample holder (p. 7)

WENN NICHT ANDERS DEFINIERT: BEMASSUNGEN SIND IN MILLIMETER OBERFLÄCHENBESCHAFFENHEIT: TOLERANZEN: LINEAR: WINKEL:	OBERFLÄCHENGÜTE:		ENTGRATEN UND SCHARFE KANTEN BRECHEN	ZEICHNUNG NICHT SKALIEREN	ÄNDERUNG		
	NAME	SIGNATUR	DATUM	BENENNUNG:			
GEZEICHNET				Overall view			
GEPRÜFT							
GENEHMIGT							
PRODUKTION							
QUALITÄT				WERKSTOFF:	ZEICHNUNGSNR.	A4	
					In situ XRD cell version2		
				GEWICHT:	MASSSTAB:1:1		

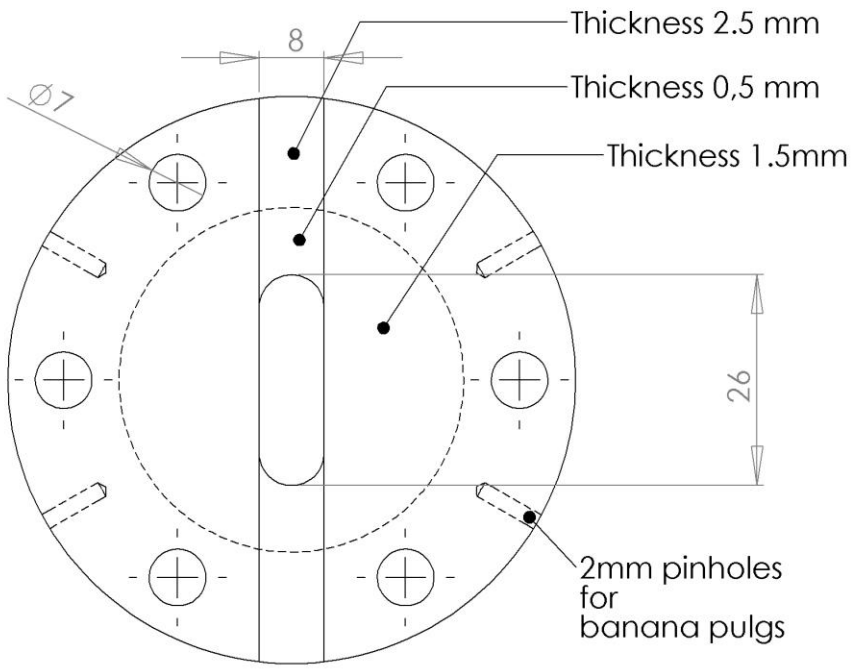

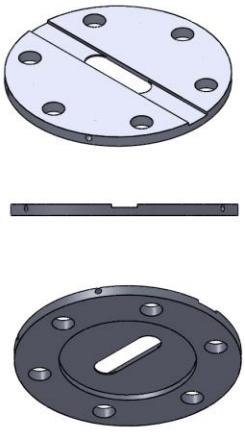

Scale 1:2

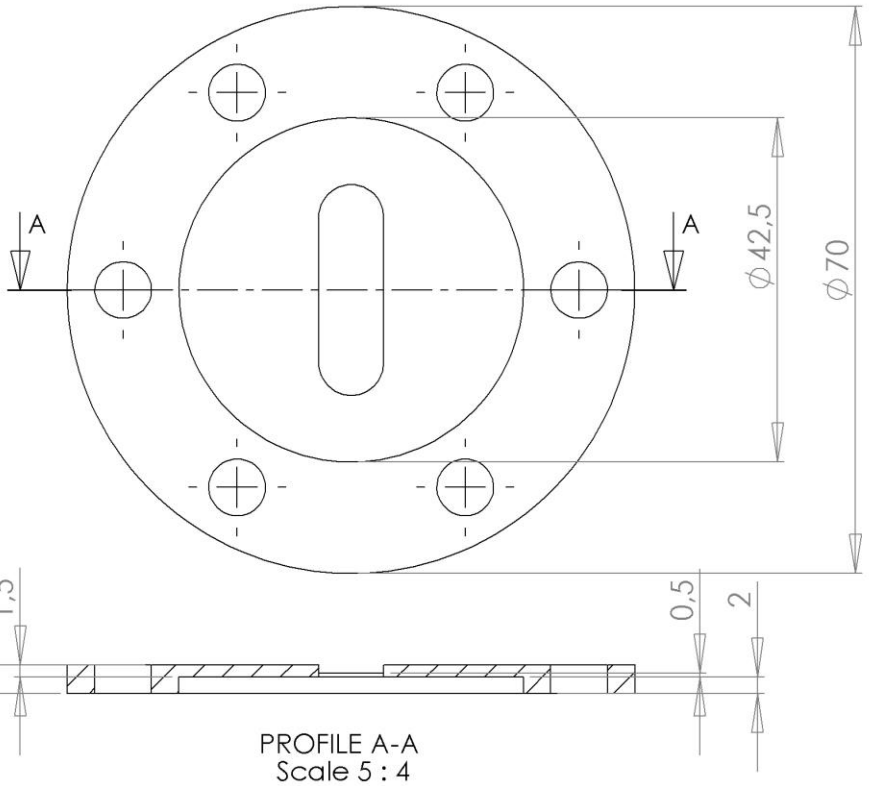

PROFILE A-A
Scale 5 : 4

WENN NICHT ANDERS DEFINIERT: BEMASSUNGEN SIND IN MILLIMETER OBERFLÄCHENBESCHAFFENHEIT: TOLERANZEN: LINEAR: WINKEL:	OBERFLÄCHENGÜTE:		ENTGRATEN UND SCHARFE KANTEN BRECHEN	ZEICHNUNG NICHT SKALIEREN	ÄNDERUNG	
	NAME	SIGNATUR	DATUM	BENENNUNG:		
GEZEICHNET				Top positive current-collector plate		
GEPRÜFT						
GENEHMIGT						
PRODUKTION						
QUALITÄT				WERKSTOFF: stainless steel 1.4571	ZEICHNUNGSNR. In situ XRD cell version2	A4
GEWICHT:					MASSSTAB:1:1	BLATT 2 VON 7

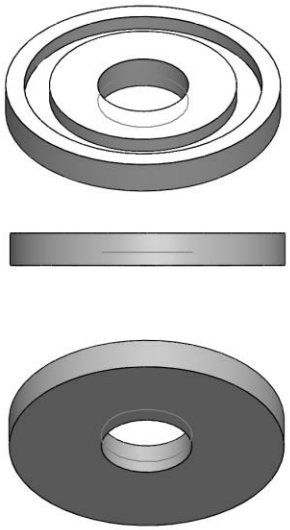

Scale 1:1

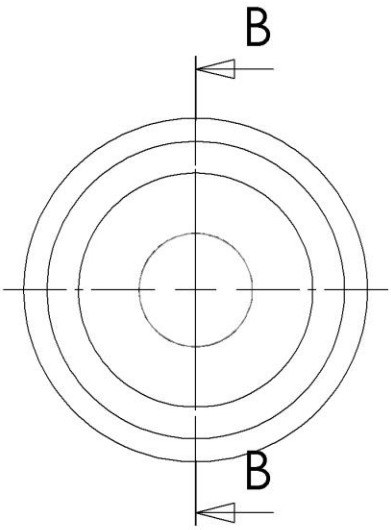

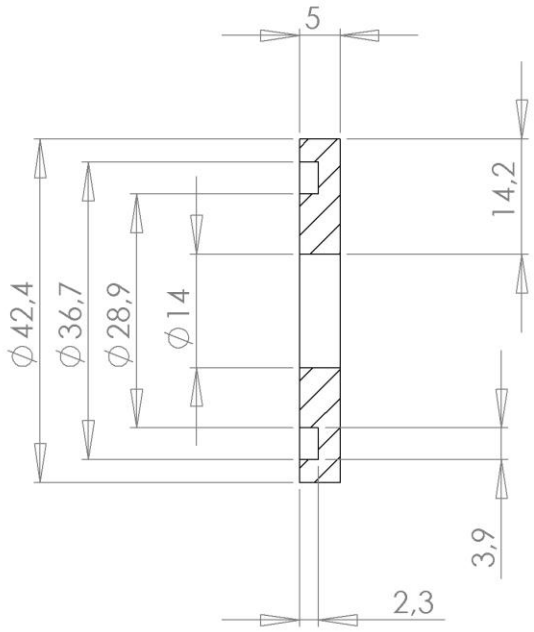

PROFILE B-B
Scale 5 : 4

WENN NICHT ANDERS DEFINIERT: BEMASSUNGEN SIND IN MILLIMETER OBERFLÄCHENBESCHAFFENHEIT: TOLERANZEN: LINEAR: WINKEL:	OBERFLÄCHENGÜTE:		ENTGRATEN UND SCHARFE KANTEN BRECHEN	ZEICHNUNG NICHT SKALIEREN	ÄNDERUNG	
	NAME	SIGNATUR	DATUM	BENENNUNG:		
GEZEICHNET				Sealing unit		
GEPRÜFT						
GENEHMIGT						
PRODUKTION						
QUALITÄT				WERKSTOFF: PE	ZEICHNUNGSNR. In situ XRD cell version2	A4
GEWICHT:				MASSSTAB:1:1	BLATT 3 VON 7	

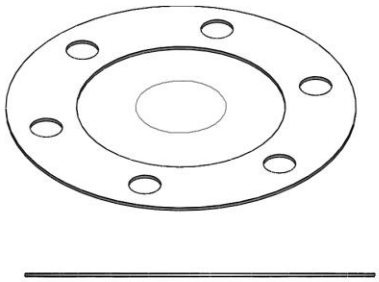

Scale 1:1

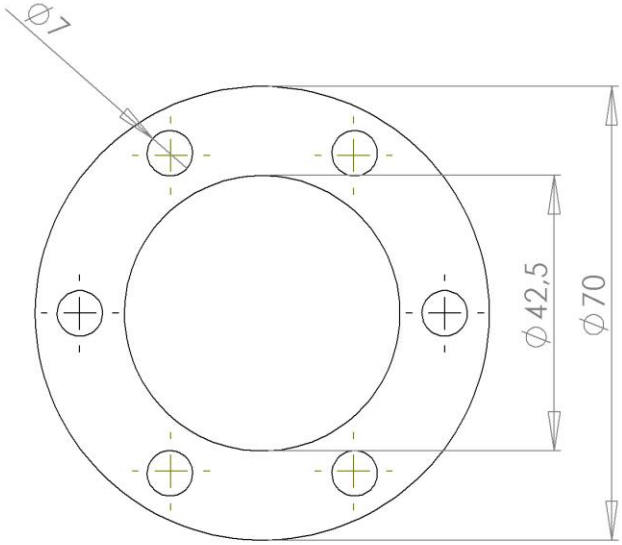

Scale 5:4

WENN NICHT ANDERS DEFINIERT: BEMASSUNGEN SIND IN MILLIMETER OBERFLÄCHENBESCHAFFENHEIT: TOLERANZEN: LINEAR: WINKEL:	OBERFLÄCHENGÜTE:				ENTGRATEN UND SCHARFE KANTEN BRECHEN	ZEICHNUNG NICHT SKALIEREN / ÄNDERUNG
	NAME	SIGNATUR	DATUM			BENENNUNG: Insulating rubber
GEZEICHNET						
GEPRÜFT						
GENEHMIGT						
PRODUKTION						
QUALITÄT				WERKSTOFF: silicon rubber		ZEICHNUNGSNR.: In situ XRD cell version2 / A4
GEWICHT:						MASSSTAB:1:1 / BLATT 4 VON 7

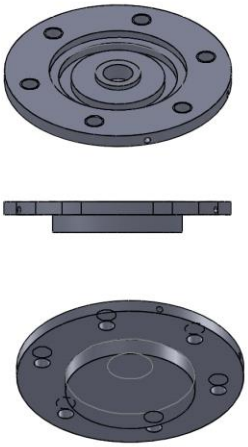

Scale 1:2

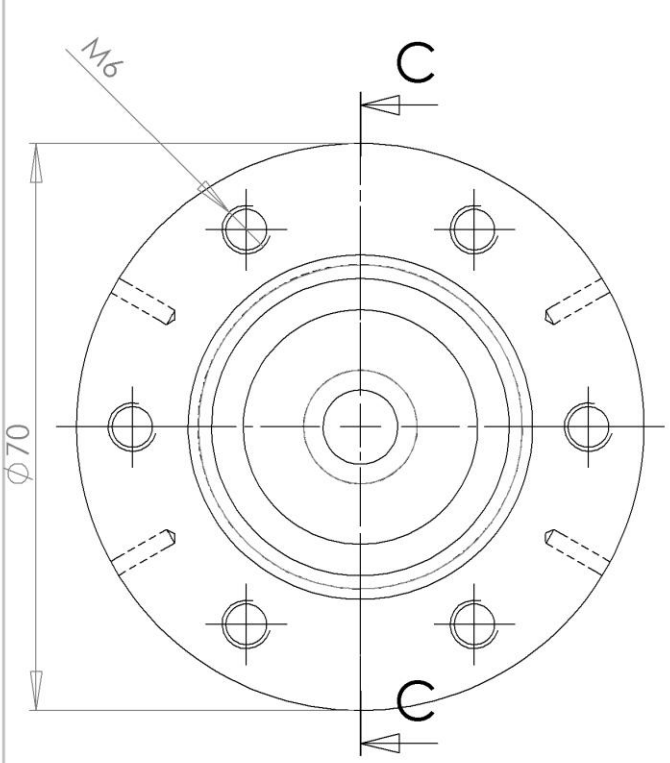

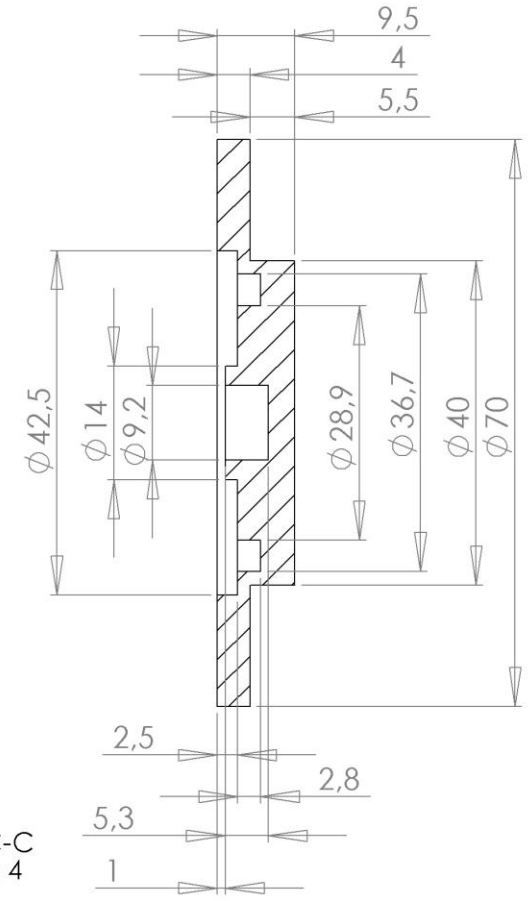

PROFILE C-C
Scale 5 : 4

WENN NICHT ANDERS DEFINIERT: BEMASSUNGEN SIND IN MILLIMETER OBERFLÄCHENBESCHAFFENHEIT: TOLERANZEN: LINEAR: WINKEL:	OBERFLÄCHENGÜTE:		ENTGRATEN UND SCHARFE KANTEN BRECHEN	ZEICHNUNG NICHT SKALIEREN	ÄNDERUNG	
	NAME	SIGNATUR	DATUM	BENENNUNG:		
GEZEICHNET				Bottom negative current-collector plate		
GEPRÜFT						
GENEHMIGT						
PRODUKTION						
QUALITÄT				WERKSTOFF: stainless steel 1.4571	ZEICHNUNGSNR. In situ XRD cell version2	A4
GEWICHT:				MASSSTAB:1:1	BLATT 5 VON 7	

Scale 1:1

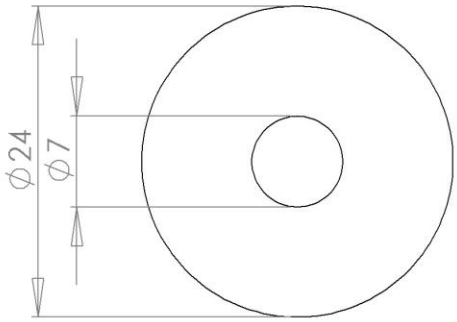

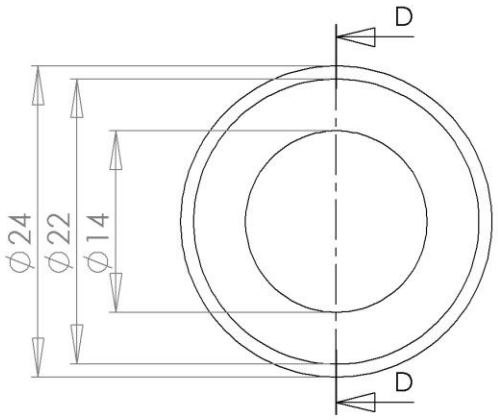

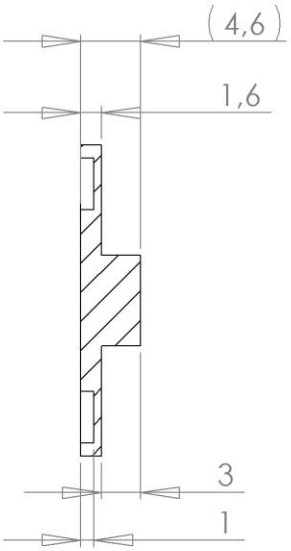

PROFILE D-D
Scale 2 : 1

WENN NICHT ANDERS DEFINIERT: BEMASSUNGEN SIND IN MILLIMETER OBERFLÄCHENBESCHAFFENHEIT: TOLERANZEN: LINEAR: WINKEL:	OBERFLÄCHENGÜTE:		ENTGRATEN UND SCHARFE KANTEN BRECHEN	ZEICHNUNG NICHT SKALIEREN	ÄNDERUNG	
	NAME	SIGNATUR	DATUM	BENENNUNG: Anode plate		
GEZEICHNET						
GEPRÜFT						
GENEHMIGT						
PRODUKTION						
QUALITÄT				WERKSTOFF: stainless steel 1.4571	ZEICHNUNGSNR. In situ XRD cell version2	A4
				GEWICHT:	MASSSTAB:1:1	BLATT 6 VON 7

Scale 1:1

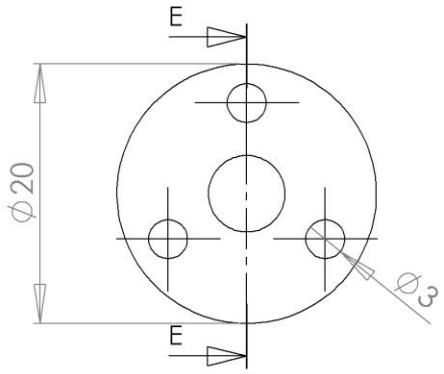

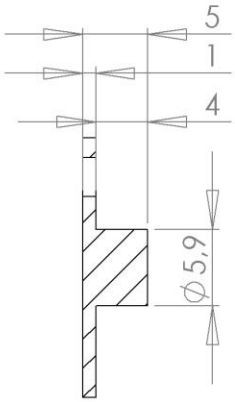

SCHNITT E-E
MAßSTAB 2 : 1

WENN NICHT ANDERS DEFINIERT: BEMASSUNGEN SIND IN MILLIMETER OBERFLÄCHENBESCHAFFENHEIT: TOLERANZEN: LINEAR: WINKEL:	OBERFLÄCHENGÜTE:		ENTGRATEN UND SCHARFE KANTEN BRECHEN	ZEICHNUNG NICHT SKALIEREN	ÄNDERUNG	
	NAME	SIGNATUR	DATUM	BENENNUNG:		
GEZEICHNET				Adapter for XRD sample holder		
GEPRÜFT						
GENEHMIGT						
PRODUKTION						
QUALITÄT				WERKSTOFF:	ZEICHNUNGSNR.	A4
				polyethylene/ polypropylene	In situ XRD cell version2	
				GEWICHT:	MASSSTAB:1:1	BLATT 7 VON 7

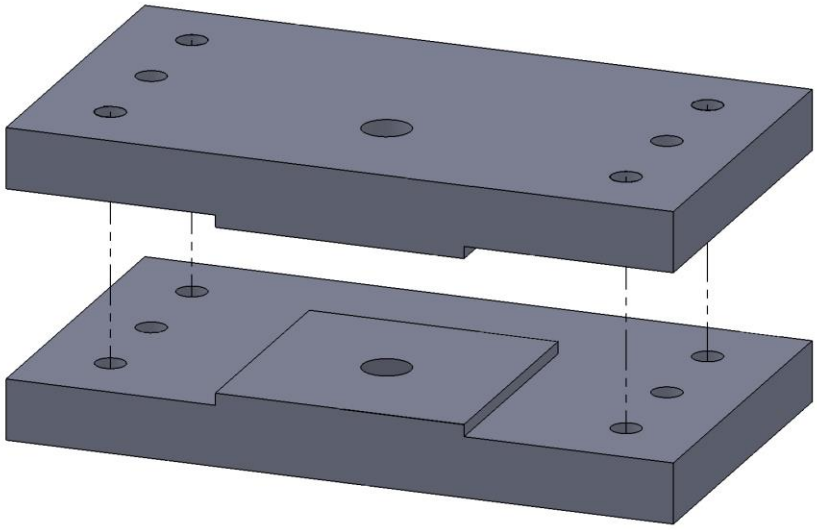

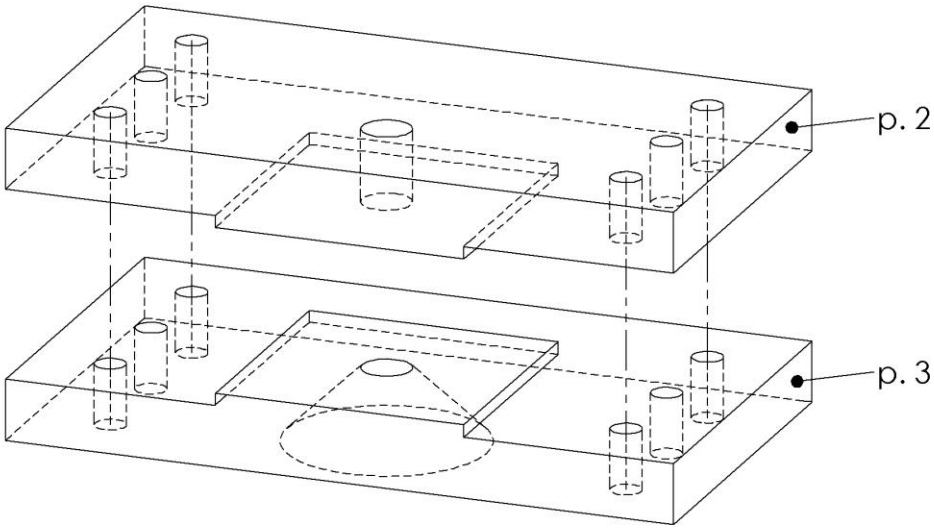

WENN NICHT ANDERS DEFINIERT: BEMASSUNGEN SIND IN MILLIMETER OBERFLÄCHENBESCHAFFENHEIT: TOLERANZEN: LINEAR: WINKEL:	OBERFLÄCHENGÜTE:				ENTGRATEN UND SCHARFE KANTEN BRECHEN	ZEICHNUNG NICHT SKALIEREN / ÄNDERUNG
	NAME	SIGNATUR	DATUM			BENENNUNG: Overall view
GEZEICHNET						
GEPRÜFT						
GENEHMIGT						
PRODUKTION						
QUALITÄT				WERKSTOFF:		ZEICHNUNGSNR. Pouch cell holder for transmission mode / A4
				GEWICHT:		MASSSTAB:1:2 / BLATT 1 VON 4

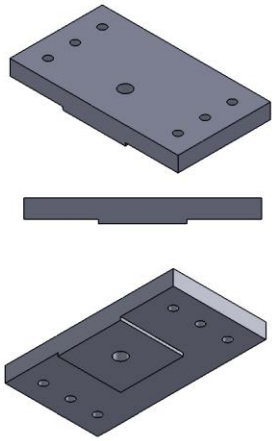

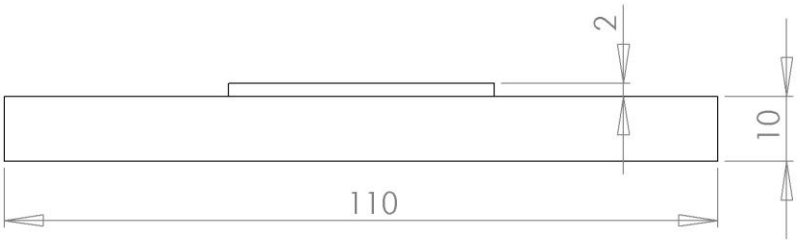

Scale 1:3

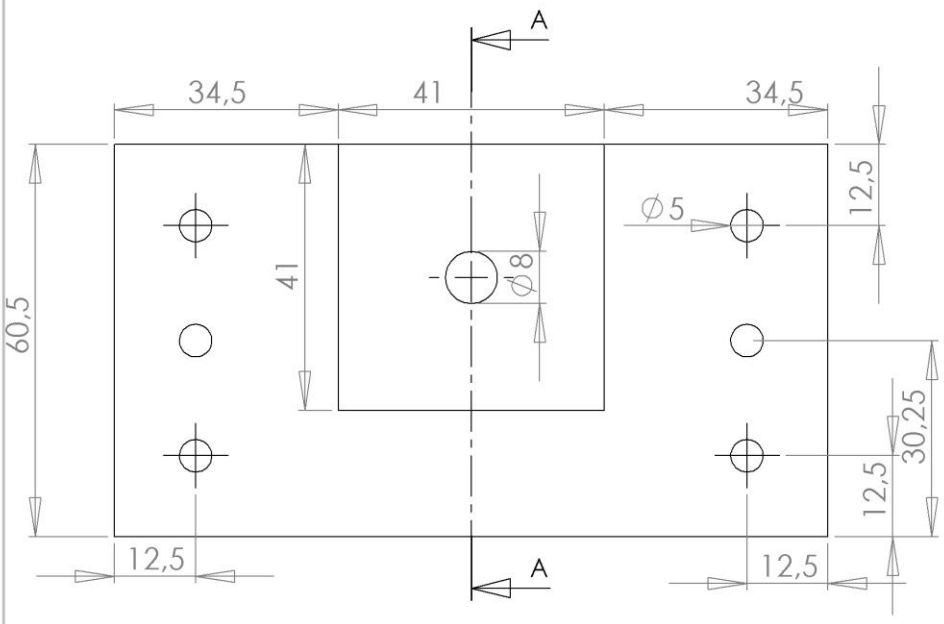

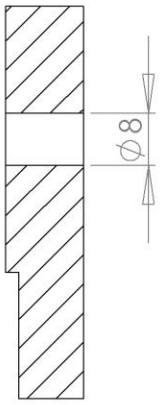

SCHNITT A-A
MAßSTAB 1 : 1

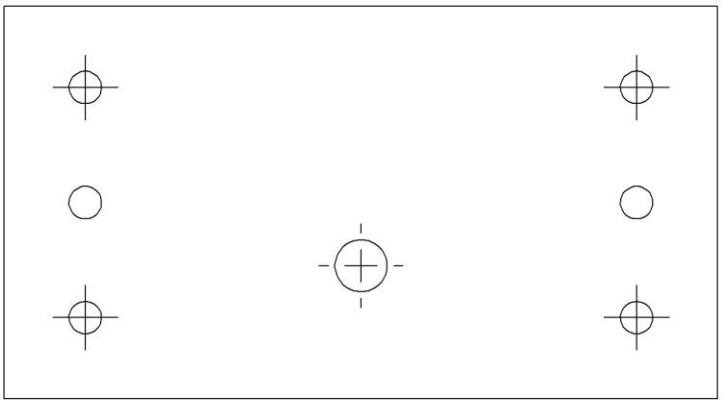

WENN NICHT ANDERS DEFINIERT: BEMASSUNGEN SIND IN MILLIMETER OBERFLÄCHENBESCHAFFENHEIT: TOLERANZEN: LINEAR: WINKEL:	OBERFLÄCHENGÜTE:		ENTGRATEN UND SCHARFE KANTEN BRECHEN	ZEICHNUNG NICHT SKALIEREN	ÄNDERUNG	
	NAME	SIGNATUR	DATUM	BENENNUNG:		
GEZEICHNET				Plate - detector side		
GEPRÜFT						
GENEHMIGT						
PRODUKTION						
QUALITÄT				WERKSTOFF: aluminum	ZEICHNUNGSNR. Pouch cell holder for transmission mode	A4
GEWICHT:				MASSSTAB:1:2	BLATT 2 VON 4	

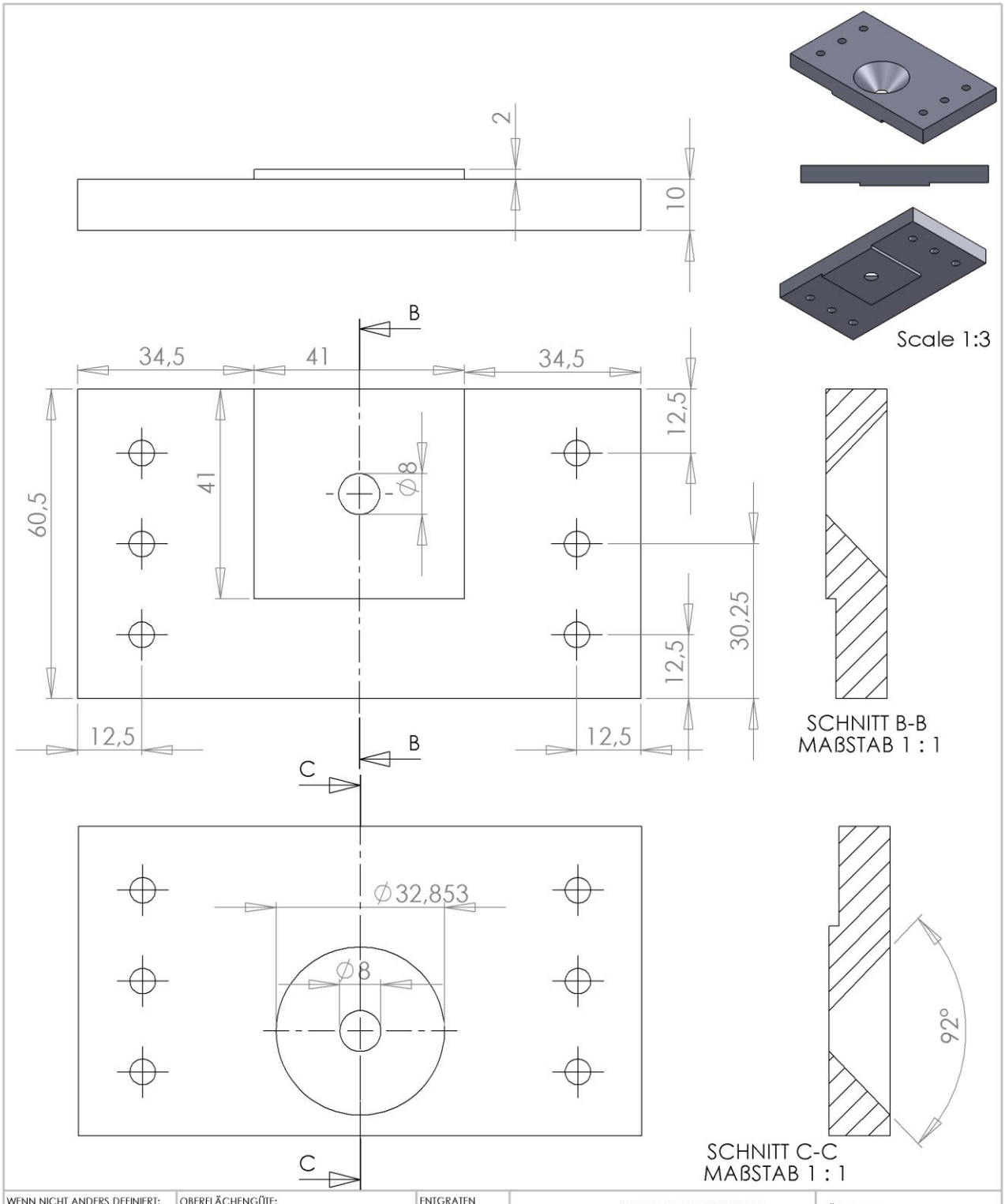

WENN NICHT ANDERS DEFINIERT: BEMASSUNGEN SIND IN MILLIMETER OBERFLÄCHENBESCHAFFENHEIT: TOLERANZEN: LINEAR: WINKEL:	OBERFLÄCHENGÜTE:		ENTGRATEN UND SCHARFE KANTEN BRECHEN	ZEICHNUNG NICHT SKALIEREN	ÄNDERUNG	
	NAME	SIGNATUR	DATUM	BENENNUNG:		
GEZEICHNET				Plate - beam side		
GEPRÜFT						
GENEHMIGT						
PRODUKTION						
QUALITÄT				WERKSTOFF: aluminum	ZEICHNUNGSNR. Pouch cell holder for transmission mode	A4
GEWICHT:					MASSSTAB:1:2	BLATT 3 VON 4

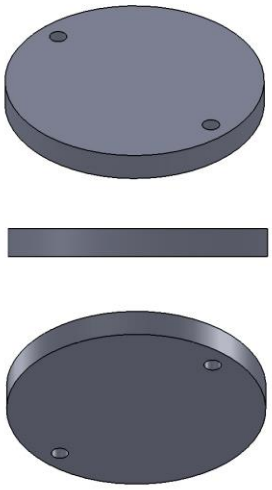

Scale 1:3

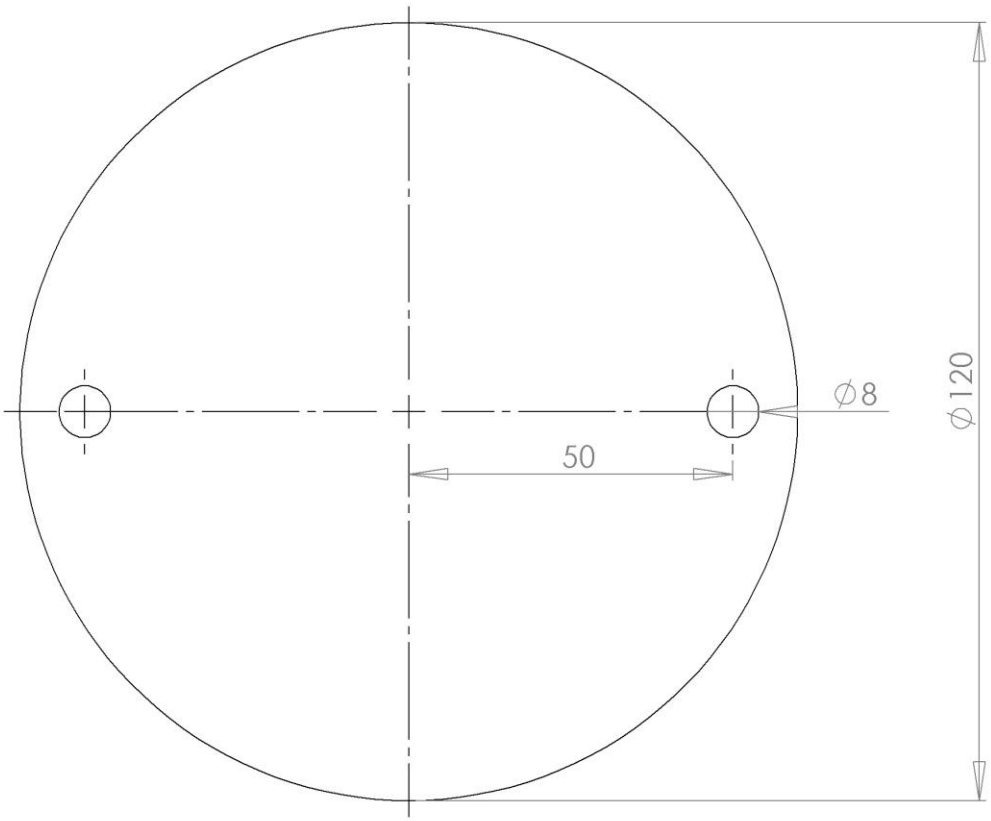

WENN NICHT ANDERS DEFINIERT: BEMASSUNGEN SIND IN MILLIMETER OBERFLÄCHENBESCHAFFENHEIT: TOLERANZEN: LINEAR: WINKEL:	OBERFLÄCHENGÜTE:			ENTGRATEN UND SCHARFE KANTEN BRECHEN	ZEICHNUNG NICHT SKALIEREN	ÄNDERUNG
	NAME	SIGNATUR	DATUM		BENENNUNG:	
GEZEICHNET					omega table	
GEPRÜFT						
GENEHMIGT						
PRODUKTION						
QUALITÄT				WERKSTOFF: stainless steel	ZEICHNUNGSNR. Pouch cell holder for transmission mode	A4
GEWICHT:					MASSSTAB:1:5	BLATT 4 VON 4

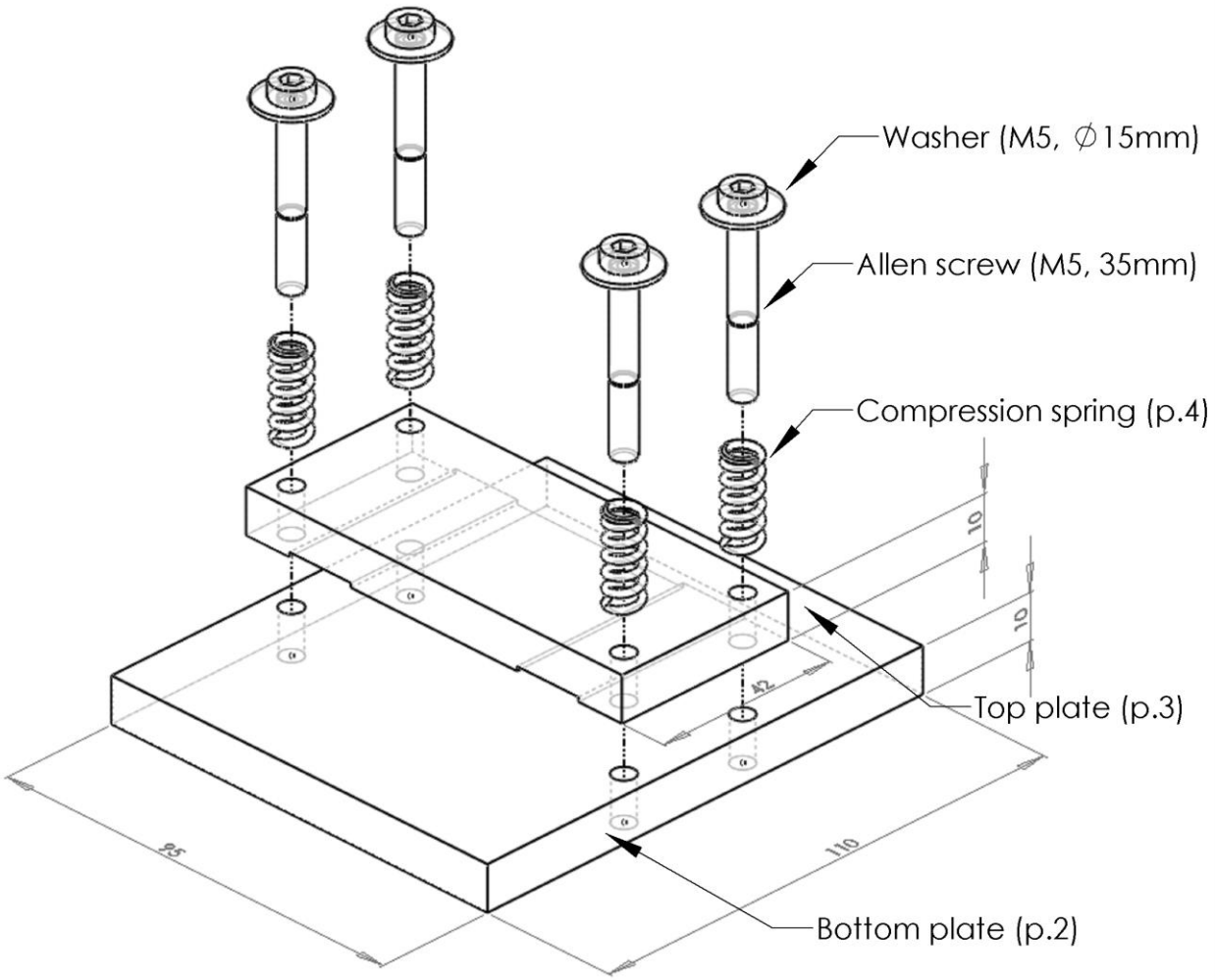

WENN NICHT ANDERS DEFINIERT: BEMASSUNGEN SIND IN MILLIMETER OBERFLÄCHENBESCHAFFENHEIT: TOLERANZEN: LINEAR: WINKEL:	OBERFLÄCHENGÜTE:		ENTGRATEN UND SCHARFE KANTEN BRECHEN	ZEICHNUNG NICHT SKALIEREN	ÄNDERUNG	
	NAME	SIGNATUR	DATUM	BENENNUNG: Overall view		
GEZEICHNET						
GEPRÜFT						
GENEHMIGT						
PRODUKTION						
QUALITÄT				WERKSTOFF:	ZEICHNUNGSNR. Pouch-cell compression tool	A4
GEWICHT:					MASSSTAB:1:1	BLATT 1 VON 4

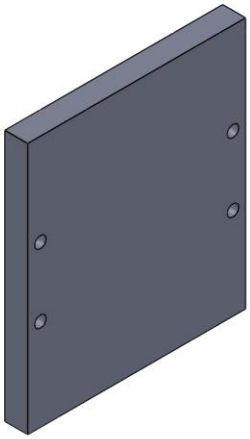

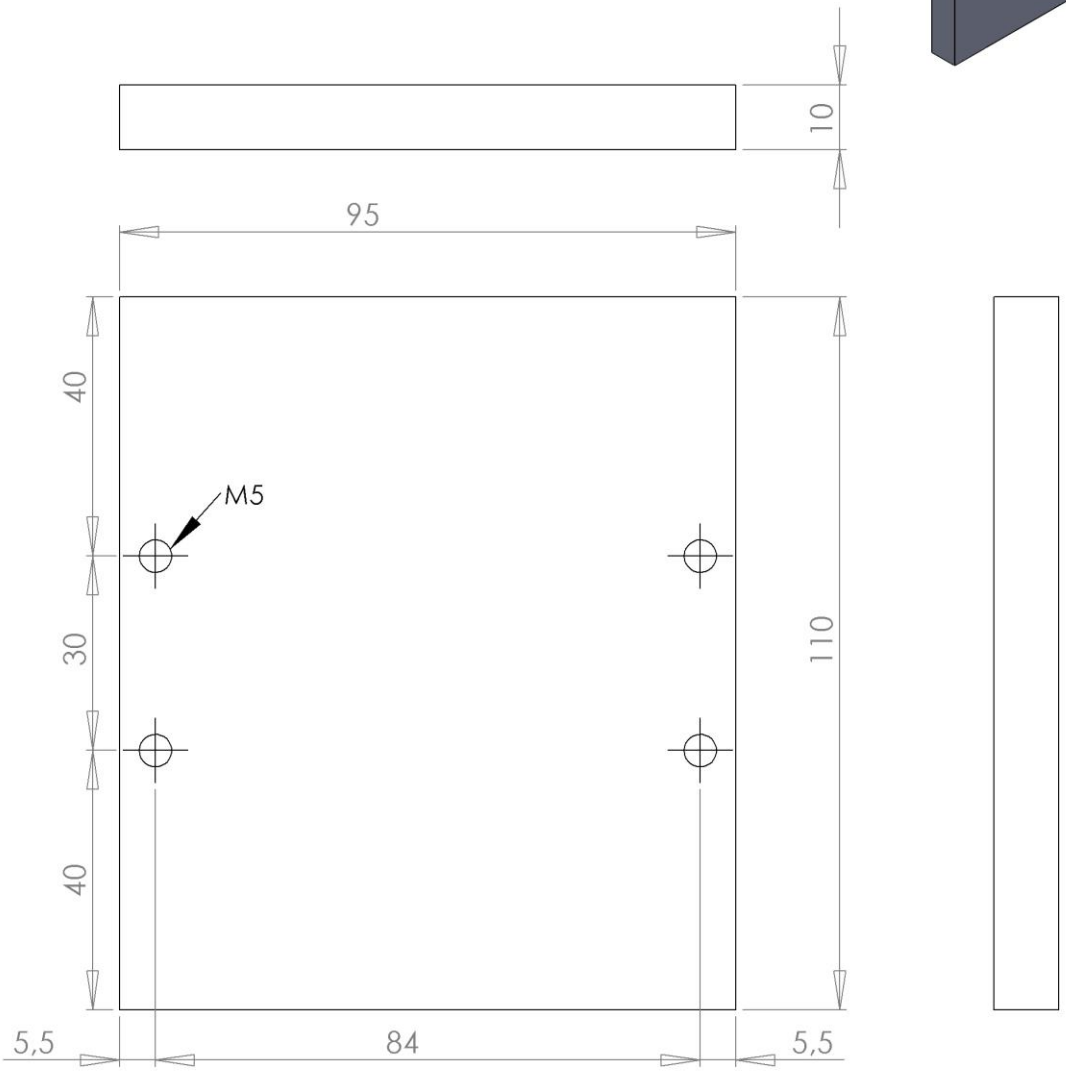

WENN NICHT ANDERS DEFINIERT: BEMASSUNGEN SIND IN MILLIMETER OBERFLÄCHENBESCHAFFENHEIT: TOLERANZEN: LINEAR: WINKEL:	OBERFLÄCHENGÜTE:		ENTGRATEN UND SCHARFE KANTEN BRECHEN	ZEICHNUNG NICHT SKALIEREN	ÄNDERUNG	
	NAME	SIGNATUR	DATUM	BENENNUNG:		
GEZEICHNET				Bottom plate		
GEPRÜFT						
GENEHMIGT						
PRODUKTION						
QUALITÄT				WERKSTOFF:	ZEICHNUNGSNR.	A4
				stainless steel	Pouch-cell compression tool	
				GEWICHT:	MASSSTAB:1:1	BLATT 2 VON 4

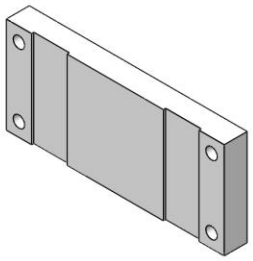

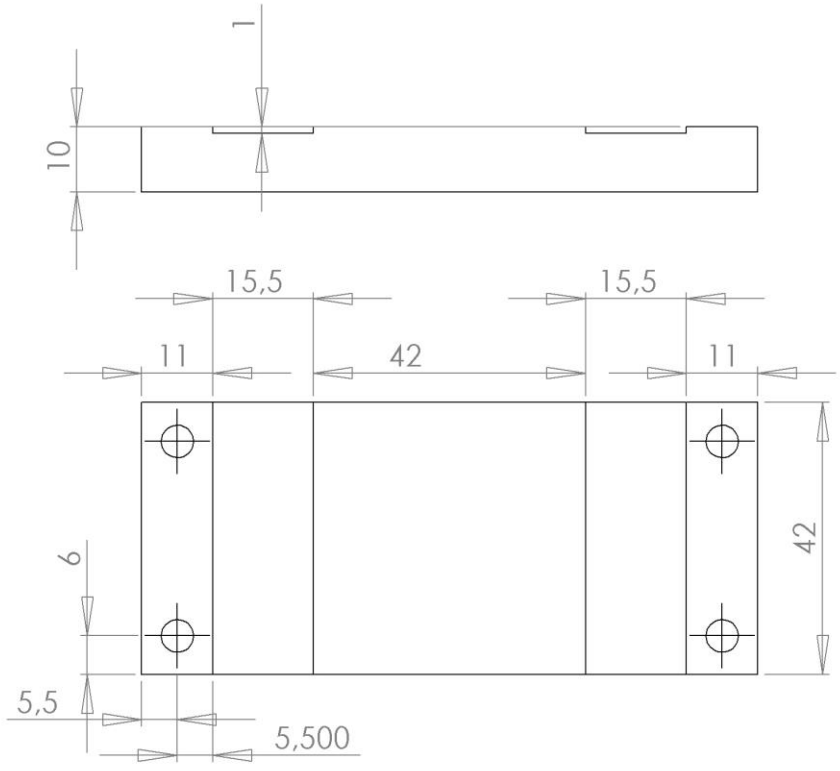

WENN NICHT ANDERS DEFINIERT: BEMASSUNGEN SIND IN MILLIMETER OBERFLÄCHENBESCHAFFENHEIT: TOLERANZEN: LINEAR: WINKEL:	OBERFLÄCHENGÜTE:		ENTGRATEN UND SCHARFE KANTEN BRECHEN	ZEICHNUNG NICHT SKALIEREN	ÄNDERUNG	
	NAME	SIGNATUR	DATUM	BENENNUNG: Top plate		
GEZEICHNET						
GEPRÜFT						
GENEHMIGT						
PRODUKTION						
QUALITÄT				WERKSTOFF: stainless steel	ZEICHNUNGSNR. Pouch-cell compression tool	A4
GEWICHT:					MASSSTAB:1:1	BLATT 3 VON 4

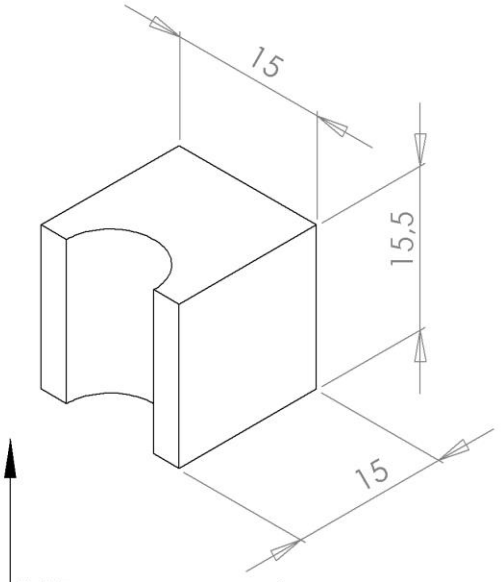

5.15mm compression
33.4N

> 0.15MPa

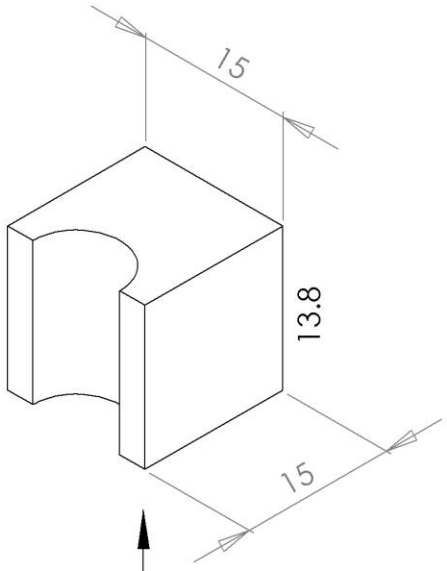

6.85mm compression
44.4N

> 0.20MPa

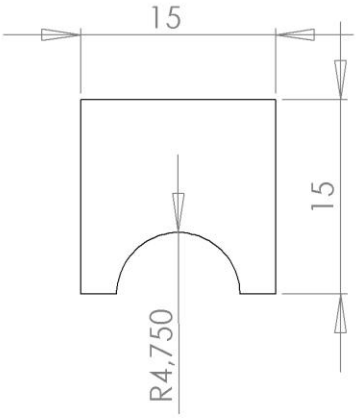

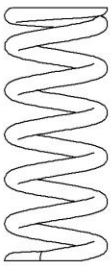

Compression spring (LeeSpring)
LC047E07S

Free length 20.65mm
Rate 6.48N/mm

WENN NICHT ANDERS DEFINIERT: BEMASSUNGEN SIND IN MILLIMETER OBERFLÄCHENBESCHAFFENHEIT: TOLERANZEN: LINEAR: WINKEL:		OBERFLÄCHENGÜTE:			ENTGRATEN UND SCHARFE KANTEN BRECHEN	ZEICHNUNG NICHT SKALIEREN	ÄNDERUNG
	NAME	SIGNATUR	DATUM			BENENNUNG: Metal block to adjust spring compression Compression spring	
GEZEICHNET							
GEPRÜFT							
GENEHMIGT							
PRODUKTION							
QUALITÄT				WERKSTOFF: stainless steel		ZEICHNUNGSNR. Pouch-cell compression tool	A4
				GEWICHT:		MASSSTAB:1:1	BLATT 4 VON 4